Triplet-Triplet Annihilation Upconversion at Model Biomembrane

Amrutha Prabhakaran, M.Sc.

A thesis submitted for the award of Ph.D.

Supervisor: Prof. Tia E. Keyes

School of Chemical Sciences

Dublin City University

August 2023

Declaration

I hereby certify that this material, which I now submit for assessment on the programme of study leading to the award of Doctor of Philosophy (Ph.D.) is entirely my own work, and that I have exercised reasonable care to ensure that the work is original, and does not to the best of my knowledge breach any law of copyright, and has not been taken from the work of others save and to the extent that such work has been cited and acknowledged within the text of my work.

Signed: ID No.: 19212651 Date: 14.08.2023

This thesis is dedicated to my parents,

Ramadevi and Prabhakaran,

My brother, Aneesh, and

My late grandmother, Leelavathy Amma.

Acknowledgements

First and foremost, I would like to express my sincere and immense gratitude to my supervisor, Prof. Tia Keyes. Thank you for selecting me to do this work, for your continuous support, guidance, and endless encouragement for the past 3.5 years, and for making this journey a great experience.

Next, I would like to thank Dr. Nirod Kumar Sarangi for his dedicated involvement in every step throughout my Ph.D. period. I learned many things from you, and your suggestions were always helpful. You are an excellent researcher, lab mate, and friend, thank you for all the help and support.

Thank you, Ruben, for everything. You are a wonderful friend and colleague. All our memories will be delightfully cherished. Our research symbiosis was amazing and thanks to BODIPY.

I would like to extend my sincere acknowledgment to Prof. Fiona Regan for all her suggestions on my writing during the transfer viva. Many thanks to Julie for the timely help, support, and kindness. I would like to thank the technical staff of the school of Chemical sciences, particularly Veronica, Ambrose, John, Vinny, and Damien. Thanks to Una, Leah, and Josephine for all the training and support.

I acknowledge Prof. Benjamin Dietzek-Ivanšić, Friedrich Schiller University Jena, for his valuable suggestions, collaboration and for providing the opportunity to work in his research group during the secondment. I am thankful to Keshav Kumar Jha for the collaboration, fruitful discussions, and all the help during my secondment. I would like to thank Dr. Anja Schulz for all her support throughout the Ph.D. period. Thanks to Tingxiang Yang for her help during my research visit to Jena. I would extend my sincere thanks to Prof. Sylvestre Bonnet and David M. Klein, Leiden University for their collaboration. I would like to express my gratitude to all the early stage researchers and PIs of LogicLab for all the scientific discussions and all the memories.

I take this opportunity to express my heartfelt thanks to all the past and present members of Keyes research group. Dr. Guilherme Berselli, thank you for introducing me to the land of

lipids and FCS. I acknowledge Dr. Christopher Burke for providing me with the ruthenium complex, for all the training, and for the scientific discussions. Thanks to Dr. Arpita Roy for all the fun we had in the lab. I would like to express my sincere thanks to Dr. Vadde Ramu for sharing a vast area of knowledge, for the lunchtime talks, and for our friendship. I would extend my gratitude to David; I will remember the fun moments we had during our Friday brunch time. I would like to thank Jack, Shane, and John for all their help. Thanks, Philip for all your support during our visit to Jena and for inviting me to Vienna. Thank you Dr. Meenaxi Saini for all the support. Thanks to Dr. Karmel Gkika for all the kind and motivating words. Many thanks to Rhianne for introducing me to cell culture. I would like to thank Darragh for sharing his knowledge of GUVs. Thank you Dr. Surajit Ghosh for all the scientific discussions. Thanks to Lorcan and Ryan for always welcoming me whenever I go to the synthesis lab. Thanks to Kho and Rokas for all the little things in the lab.

Now I would like to gratefully acknowledge all the people outside Chemistry, those who were with me during the Ph.D. period. Many thanks to Visakh for making my Dublin life easier and for being a good friend. Devika, you are such an amazing friend, and thank you for every little to big thing. Thanks to all my housemates, Sweta, Paul, Deval, and Anushka. I would like to thank Greta for all the memories we made. Thanks to Rengesh and Purabi for their companionship during lunchtime.

I take this opportunity to thank all my teachers and friends from school, BSc, MSc, and CECRI. Thanks to Saranya, Nivi akka and Krati for their support from miles away. I would like to thank Athira for always being there for me. I also thank Indher and Suganya for their wonderful friendship. A special thanks to Aswin Babu for listening to all my stories and for the timely support.

Last but not least, I would like to thank my family for all their love and support. I thank Amma and Achan for everything, none of this would have been possible without your support. Most importantly my brother Aneesh, you are my greatest inspiration, you are the one who taught me to dream, you always gave me the strongest support whenever required, you wanted me to be independent in every aspect and I can't thank you with my words, you are the best part of my life.

Research Outcomes

Publications

2023	Radwan B., **Prabhakaran A.**, Rocchetti S., Matuszyk E., Keyes T. E., Baranska M., Uptake and anti-inflammatory effects of liposomal astaxanthin on endothelial cells tracked by Raman and fluorescence imaging. *Microchimica Acta*. **2023**, 190 (8), 332.
2023	Jha K. K.,[#] **Prabhakaran A.**,[#] Sia R. C. E., Reyes R. A. A., Sarangi N. K., Yang T., Kumar K., Kupfer S., Guthmuller J., Keyes T. E., Ivanšić B. D., Triplet Formation and Triplet-Triplet Annihilation Upconversion in Iodine Substituted Non-Orthogonal BODIPY-Perylene Dyads. *ChemPhotoChem*. **2023**, e202300073. ([#]equally contributed)
2023	Roy A., Sarangi N. K., Ghosh S., **Prabhakaran A.**, Keyes T. E., Leaflet by Leaflet Synergistic Effects of Antimicrobial Peptides on Bacterial and Mammalian Membrane Models. *J. Phys. Chem. Lett.* **2023**, 14 (16), 3920–3928.
2023	Reyes R. A. A., **Prabhakaran A.**, Sia R. C. E., Guthmuller J., Jha K. K., Yang T., Ivanšić B. D., McKee V., Keyes T. E., BODIPY-perylene Charge Transfer Compounds: Sensitizers for triplet-triplet annihilation up-conversion. *Chem. - A Eur. J*. **2023**, 29 (24), e202300239.
2022	Sarangi N. K., **Prabhakaran A.**, Keyes T. E., Multimodal investigation into the interaction of quinacrine with microcavity-supported lipid bilayers. *Langmuir* **2022**, *38* (20), 6411–6424.
2022	Jha K. K., **Prabhakaran A.**, Burke C. S., Schulze M., Schubert U. S., Keyes T. E., Jäger M., Ivanšić B. D., Triplet-Triplet Annihilation Upconversion by Polymeric Sensitizers. *J. Phys. Chem. C* **2022**, *126* (8), 4057–4066.
2021	Klein D. M., Rodríguez-Jiménez S., Hoefnagel M. E., Pannwitz A., **Prabhakaran A.**, Siegler M. A., Keyes T. E., Reisner E., Brouwer A. M., Bonnet S., Shorter Alkyl Chains Enhance Molecular Diffusion and Electron Transfer Kinetics between Photosensitisers and Catalysts in CO2-Reducing Photocatalytic Liposomes. *Chem. - A Eur. J*. **2021**, *27* (68), 17203–17212.
2020	Sarangi N. K., **Prabhakaran A.**, Keyes T. E., Interaction of Miltefosine with Microcavity Supported Lipid Membrane: Biophysical Insights from Electrochemical Impedance Spectroscopy. *Electroanalysis* **2020**, *32* (12), 2936–2945.

Conference Presentations

2022	**MSMLG 2022** 7th International Conference on Molecular Sensors and Molecular Logic Gates, **Poster**, ''BODIPY derivatives Sensitized Triplet-Triplet Annihilation in Solution and Model Biomembranes''. (Dublin, Ireland)

2022	**BBS Biennial Meeting**: from Molecular Machines to Materials, **Oral presentation**, ''Bodipy Derivatives Sensitized Triplet-Triplet Annihilation Upconversion in Solution and Liposomes''. (Galway, Ireland)
2021	International symposium "Molecular Biosensing: From Theory to Practice'', **Oral presentation**, ''Bodipy Derivatives Sensitized Triplet-Triplet Annihilation Upconversion in Solution and Liposomes''. (Online)
2020	**IBICS-4** Symposium of the Irish Biological Inorganic Chemistry Society, **Oral presentation**, ''Inorganic complex sensitized Triplet-Triplet Annihilation Upconversion''. (Online)
2020	**ICI** Institute of Chemistry of Ireland- Postgraduate Chemistry Research Symposium, **Oral presentation**, ''Photon Upconversion by Triplet-Triplet Annihilation in Lipid Membranes''. (Online)

Thesis Outline

Chapter 1

Chapter 1 covered background to this thesis, with an overview of the TTA-UC process's mechanism and fundamental principles. This part will also discuss the importance of membrane composition and its impact on the TTA-UC process. The application of other reported photosensitizers in cell membrane models are explained and there are few examples of TTA-UC in membrane models. Even though TTA-UC has been reported in liposomes, only a little is known about how the physicochemical properties of the membrane affect TTA-UC efficiency. Model membranes can be helpful to investigate the TTA-UC efficiency towards biological applications, but they must be fluidic and interrogable. This chapter also gives general basic concepts, terms, and definitions related to the presented work, as well as various surface sensitive experimental techniques for taping various intrinsic properties of lipid bilayer membranes, are thoroughly explained.

Chapter 2

Chapter 2, entitled *BODIPY Charge Transfer Dyad Sensitized Triplet-Triplet Annihilation Upconversion in Solution and Model Membranes* presents and discusses two BODIPY-based photosensitizers, with and without iodine substitution in combination with annihilator, perylene, for the first time to investigate TTA-UC in solution and liposome membranes of varying fluidity, lipid's head group charge, and phase separated membrane. Additionally, the excited state properties of the photosensitizer and annihilator in the membrane have also been investigated and compared with that in the solution. To better understand the photophysical behaviour of the photosensitizer in the lipid environment as a function of viscosity, specifically its lateral diffusivity, the diffusion behaviour of the BODIPY in a two-dimensional model lipid membrane was investigated.

Chapter 3

Chapter 3, entitled *Role of phospholipase A_2 modulating Triplet-Triplet Annihilation Upconversion of B2PI-perylene pair within model biomembrane* presents and discusses the effect of enzyme catalysed phospholipid membrane hydrolysis on TTA-UC in liposome. The efficiency of TTA-UC in presence of phospholipase A_2 (PLA$_2$) in the liposomal membrane is studied as a function of PLA$_2$ hydrolysis. The effects are discussed in terms of impact on membrane organization, underlying phospholipase kinetics, role of Ca^{2+} and inhibition etc. at a more biomimetic microcavity supported lipid bilayer (MSLB) model membrane using

various surface sensitive techniques such as single molecule-based fluorescence lifetime correlation spectroscopy, fluorescence lifetime imaging, and label-free electrochemical impedance spectroscopy etc.

Chapter 4

Chapter 4, entitled *Ruthenium(II) Polypyridyl Complex Sensitized Triplet-Triplet Annihilation Upconversion* presents a Ru(II) polypyridyl complex with strong triplet ligand-centred character as a potential photosensitizer for TTA-UC. The investigation involves the study of photosensitizer in combination with different annihilators in a number of solvents. Time resolved photophysical characterization was performed to study the triplet state properties of the photosensitizer. Finally, this chapter includes the confirmation of doping of the molecule into the lipid bilayer and TTA-UC studies in liposomes and makes the interesting observation that efficient solution TTA-UC does not guarantee the same effect in liposome.

Chapter 5

Chapter 5, entitled *Microcavity Supported Lipid Bilayers: Versatile Tools for understanding Membrane Fluidity Responses to Drug and Fluorophores* presents and discusses the versatility of MSLB for investigating how small molecule drugs interact and modulate the fluidity of different membranes using fluorescence lifetime imaging (FLIM) and fluorescence lifetime correlation spectroscopy (FLCS). This chapter discusses the diffusion study of a photosensitizer using MSLB which helped to establish a route for evaluating the lateral diffusion of photosensitizers used for triplet-triplet annihilation upconversion. This chapter also includes the comparison of leaflet-by-leaflet diffusivity of MSLB to supported lipid bilayer (SLB) to validate the use of MSLB as a better biomimetic bilayer versus conventional glass SLB.

Chapter 6

Chapter 6 presents the overall conclusions and future perspectives.

Table of Contents

Table of Figures

ATTO655 (0.01 mol%) present at the upper leaflet of bilayer on PDMS microcavity array. Panels c, f and i shows the respective fluorescence lifetime images obtained after 30 min of incubation with quinacrine (~10 µM). The scale bar at each panel is 20 µm. Inset in panel (h) and (i) are the expanded regions showing a modest membrane homogenization caused by quinacrine, which is highlighted in yellow square box

Table of Schemes

List of Tables

List of Abbreviations

TTA-UC	Triplet-triplet annihilation upconversion
TPA	Two photon absorption
TTA	Triplet-triplet annihilation
TTET	Triplet-triplet energy transfer
PDT	Photodynamic therapy
PACT	Photoactivated chemotherapy
ISC	Intersystem crossing
SOCT	Spin-orbit charge transfer
BODIPY	Boron dipyrromethene
ε	Molar absorption coefficient

$^1O_2$	Singlet oxygen
ROS	Reactive oxygen species
$^1S*$	First excited singlet state of photosensitizer
$^3S*$	Excited triplet state of photosensitizer
$^3A*$	Excited triplet state of annihilator
^3CT	Triplet charge transfer state
PS	Photosensitizer
Φ	Quantum yield
B2P	Ph-2-BODIPY-2-Perylene
B2PI	Ph-2-BODIPY-Perylene-Iodine
DPA	Diphenylanthracene
9-ACA	9-anthracenecarboxylic acid
SAM	Self assembled monolayer
DOPC	1,2-Dioleoyl-sn-glycero-3-phosphocholine
DPPC	1,2-dipalmitoyl-sn-glycero-3-phosphocholine
DMPC	1,2-dimyristoyl-sn-glycero-3-phosphocholine
DLPC	1,2-dilauroyl-sn-glycero-3-phosphocholine
POPC	1-palmitoyl-2-oleoyl-glycero-3-phosphocholine
DOTAP	1,2-dioleoyl-3-trimethylammonium-propane
DOPE	1,2-dioleoyl-sn-glycero-3-phosphoethanolamine
DOPS	1,2-dioleoyl-sn-glycero-3-phospho-L-serine
DOPG	1,2-dioleoyl-sn-glycero-3-phospho-(1'-rac-glycerol)
DSPE-MPEG2000	1,2-distearoyl-sn-glycero-3-phosphoethanolamine-N-[amino(polyethylene glycol)-2000]
SM	Sphingomyelin
Chol	Cholesterol
SUV	Small unilamellar vesicle
LUV	Large unilamellar vesicle
GUV	Giant unilamellar vesicle
ITO	Indium tin oxide

DiD	DiIC18(5); 1,1′-dioctadecyl-3,3,3′,3′- 4-tetramethylindodicarbocyanine, chlorobenzenesulfonate salt
SLB	Supported lipid bilayer
MSLB	Microcavity supported lipid bilayer
L_o	Liquid ordered phase
L_d	Liquid disordered phase
T_m	Phase transition temperature
LB	Langmuir-Blodgett
VF	Vesicle fusion
PLA_2	Phospholipase A_2
PDMS	Polydimethylsiloxane
THF	Tetrahydrofuran
ε_r	Dielectric constant
λ	Wavelength
λ_{ex}	Excitation wavelength
λ_{em}	Emission wavelength
PBS	Phosphate buffered saline
DLS	Dynamic light scattering
AFM	Atomic force microscopy
SEM	Scanning electron microscope
EIS	Electrochemical impedance spectroscopy
ECM	Equivalent circuit model
R_s	Solution resistance
R_M	Membrane resistance
C	Capacitance
C_M	Membrane capacitance
IBS	Interface binding site
CPE	Constant phase element
I_{th}	Threshold power density
CW	Continuous-wave

TCSPC	Time correlated single photon spectroscopy
FLIM	Fluorescence lifetime imaging
FLCS	Fluorescence lifetime correlation spectroscopy
ACF	Autocorrelation function
D	Diffusion coefficient
2D	Two dimensional
3D	Three dimensional
τ_D	Diffusion time/transit time
α	Anomaly coeffcient
FRAP	Fluorescence recovery after photobleaching
ns-TA	Nanosecond transient absorption spectroscopy
GSB	Ground state bleach
ESA	Excitaed state absorption
NIR	Near-infrared
MLCT	Metal-to-ligand charge transfer
LC	Ligand centred transition
K_{SV}	Stern-Volmer quenching constant
k_q	Bimolecular energy transfer quenching rate constant
TCA	Tricyclic antidepressant drugs

List of Units of measurements

M	Molar
mM	Millimolar
μM	Micromolar
nM	Nanomolar
g	Gram
mg	Milligram
cm	Centimetre
mm	Millimetre
nm	Nanometre

μm	Micrometre
min	Minutes
s	Seconds
μs	Miceoseconds
ns	Nanoseconds
mL	Millilitre
μL	Microlitre
°C	Celcius
V	Volt
mV	Millivolt
Hz	Hertz
MHz	Megahertz
mJ	Milli joules
mW	Milliwatts
mW cm^{-2}	Milliwatts per centimetre square (unit of power density)
μms^{-1}	Micrometre per second (unit of diffusion coefficient)
kΩ	Kilo ohm
MΩ	Mega ohm
MΩcm^{-2}	Mega ohm per centimetre square
mN/m	Milli Neuton per metre
F	Farad
μFcm^{-2}	Micro Farad per centimetre square
μFs^{m-1}	Unit of capacitance in terms of constant phase element

Amrutha Prabhakaran

Triplet-Triplet Annihilation Upconversion at Model Biomembrane

Thesis Abstract

Light addressable machinery translation to lipid membrane structures is highly desirable for a variety of uses such as liposome drug or imaging agent delivery, membrane-bound photosynthesis analogues, etc., but little is known in this area. This thesis focuses on two objectives: the translation of triplet-triplet annihilation upconversion (TTA-UC) to liposomal systems and the use of MSLBs as tools to interrogate the behaviour of photosensitizers in these systems using surface sensitive methods. TTA-UC produces high-energy photon from low-energy excitation via Dexter energy transfer mechanism between photosensitizer and annihilator. TTA-UC uses low-power non-coherent light sources to produce anti-Stokes emission. It thus holds significant potential for photoactivated drug delivery and biological imaging since it can be stimulated using low-frequency light that penetrates biological tissue. Incorporating molecular elements into liposomes and TTA-UC in cell membranes can help biological applications and treatment without harming other organs. However, TTA-UC in a liposome or cell membrane is difficult and requires appropriate photosensitizer and annihilator that can be co-confined to the membrane and where their collisional energy transfer is supported.

This thesis explores TTA-UC in solution and lipid bilayer membrane using BODIPY- and Ru(II) complex-based photosensitizers. Using new BODIPY-perylene-based photosensitizers, heavy atom effects that increase intersystem crossing via spin-orbit coupling and other heavy atom-free photosensitizers that support triplet state formatting for efficient TTA-UC are investigated. TTA-UC efficacy in cell membrane models is assessed by incorporating the molecules into liposomes, which emit intense oxygen sensitive blue/violet emission upon green excitation. The liposome-based TTA-UC further expanded into various membrane compositions with varying membrane's physicochemical properties to simulate the effects of viscosity/fluidity on TTA-UC. TTA-UC's response to enzyme-catalysed membrane hydrolysis was examined. A thorough study using MSLB provides insights into the photosensitizer's lateral diffusion and membrane fluidity. MSLB's versatility is assessed for comprehending membrane fluidity responses to drugs and photosensitizers.

Chapter 1: Introduction

The use of multifunctional nanocarriers enables simultaneous and real-time sensing of particular cellular parameters. Multifunctional nanocarriers combine multiple properties in a single particle, allowing for minimally invasive and all-optical monitoring of particular physiological parameters at the cellular level with unprecedented efficiency and sensitivity. Recent years have seen a significant increase, at least on the in vitro level, in the use of nanocarriers (liposomes, polymer-drug conjugates, polymersomes, micelles, nanoshells etc.) as a diagnostic, prognostic, and therapeutic platform for a wide range of biomedical applications.[1–3] New nanoscale biosensing methods have been developed thanks to recent advances in nanocarrier engineering. These methods have the potential to shed light on the cellular mechanisms of disease, aid in early disease diagnosis, and allow for early response monitoring and therapy efficacy evaluation.

Designing and optimising an experimental working state of reporter molecules and the selection of a carrier vehicle to carry the reporter molecule to the target sites is essential for the development of biomedical sensing methods and devices. In terms of spectral mismatch, optical sensing has an extra requirement: there are highly contradictory demands for the wavelength of the excitation light. Tissue transparency by light occurs between 650 and 940 nm, allowing light to pass through easily, whereas light with sufficient energy, at or less than 700 nm, can initiate biochemical reactions and be used as a sensing tool. Triplet-triplet annihilation aided upconversion (TTA-UC) is a technique that may help solve these sensing issues. In this method, low-intensity and low-spectral-power-density optical sources can be used to generate high-energy photons from lower-energy excitation photons. TTA-UC is highly sensitive to environmental parameters including temperature, viscosity, and the presence of heavy metal atoms or oxidising agents.

This chapter provides a brief overview of the TTA-UC process's mechanism and fundamental principles, which will help readers comprehend the research presented in the thesis. The rationale for using BODIPY based photosensitizers, heavy-metal effect, and liposome based nanocarriers are discussed. The physicochemical properties of biomembranes, their fluidity, and phase separation are discussed as it is essential for the reconstitution and optimal performance of TTA-UC. The methodology and underlying theory for estimating diffusion coefficients of lipid membrane and photosensitizer using single molecule-based fluorescence fluctuation spectroscopy are described.

The primary aim of this thesis is to demonstrate how membrane physicochemical properties influence efficient TTA-UC. This work was part of a larger project aimed at using liposome to deliver TTA-UC as a sensing vehicle to endothelial cells. To avoid the complexities of working with live cells to understand membrane behaviour and also because the system is implemented in liposome this thesis investigates the role of membrane physicochemical properties in TTA-UC using a model membrane system, either liposomal or micropore suspended. The main focus of this work was not only on designing a functional TTA-UC pair(s) that could operate in a membrane, but also on optimising TTA-UC pair working concentrations for efficient photon upconversion (UC) intensity at both the solution and membrane environments. Furthermore, this study investigates if TTA-UC responds to the diffusivity/viscosity of the local nanocarrier environment, as membrane viscosity is important in signalling adhesion and changes are associated with disease states such as endothelial dysfunction.[4] This work demonstrate for example how TTA-UC is influenced by enzyme activity at a liposome where the main impact is changes to the membrane viscosity. Furthermore, it has shown that microcavity supported lipid bilayers (MSLB) can be used as true biomimetic model membranes when combined with a single molecule-based fluorescence approach to predict how membrane fluidity/viscosity determines passive permeation of small molecules and vice versa. The MSLB was further extended to show a metal (ruthenium) complex-based photosensitizer reconstitution and its optimal mobility in order to provide proof of its diffusive effectiveness for artificial photosynthesis machines.

1.1 Triplet-Triplet Annihilation Upconversion (TTA-UC): Mechanism and fundamental principles

The emitted light in conventional fluorescence is always Stokes shifted. Photon upconversion, on the other hand, is an anti-Stokes emission process that occurs when lower energy photons are converted into higher energy photons. Photon upconversion is the process by which the absorption of two or more photons leads in the emission of radiation with a lower wavelength than the excitation wavelength.

Photon upconversion can occur by either a two photon absorption (TPA) mechanism or by triplet-triplet annihilation (TTA).[5] In TPA, a molecule in the ground state is excited to the 1st excited singlet state or to the 2nd excited singlet state through the simultaneous absorption of two photons via a virtual state.[6–8] When this molecule is promoted to the excited state, its relaxation generates the emission of a photon of higher energy frequency than the absorbed photon.[9] Since a virtual state is involved, TPA requires a high excitation power density,

typically greater than MWcm^{-2}, that can only be produced by an ultrafast laser.[10,11] TTA-based photon upconversion, also known as p-type delayed fluorescence process follows anti-stokes law process since the emission exceeds the excitation energy violating the basic statement of Stokes law.[12]

Triplet-Triplet Annihilation Upconversion (TTA-UC) generally operates in a bichromophore system where an emitter (typically aromatic hydrocarbons) and a photosensitizer (metallated macrocycles or organic chromophores) which must be energetically tuned to enable the process. Typically, TTA-UC is a photophysical process that occurs through an energy transfer, usually Dexter energy transfer, between two molecules in their triplet state excited .[13] The process is described in the Jablonski diagram shown in Figure 1.1.
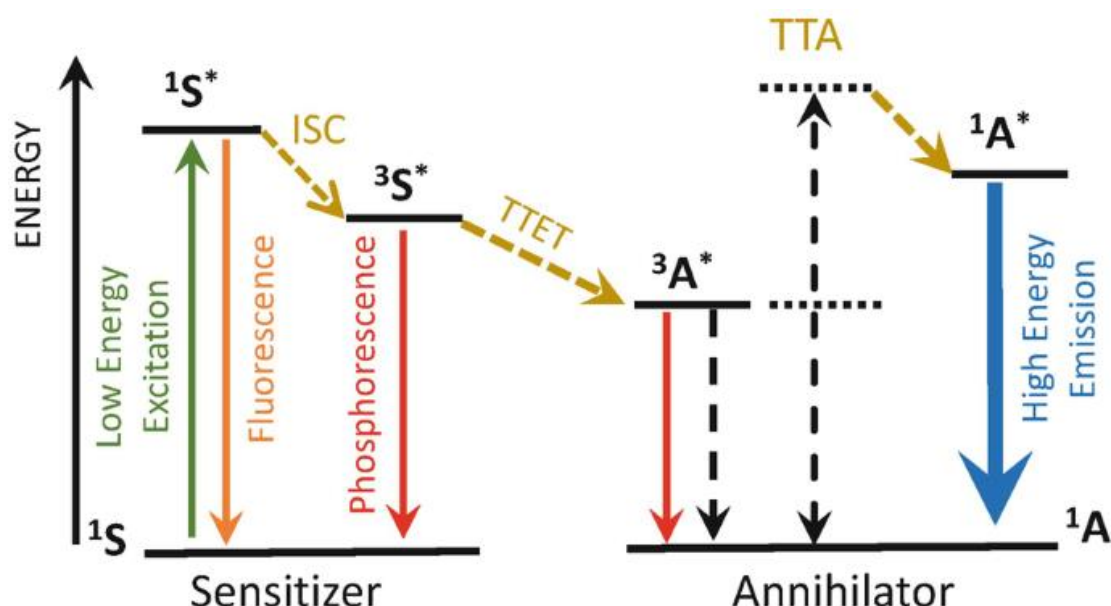
Figure 1.1 Jablonski diagram depicting the mechanism of TTA-UC. Adapted from Springer.[14]

TTA-UC requires a photosensitizer that serves as the light absorbing donor, and an annihilator, that is not excited in the primary step but serves as the energy transfer acceptor and the emitter.[15,16] The photosensitizer absorbs low energy photons, and then undergo intersystem crossing (ISC) from excited singlet state to triplet state.[17,18] In the triplet state, the photosensitizer transfers its energy to the annihilator molecule through triplet-triplet energy transfer (TTET). Then two annihilator molecules in the triplet state collide with each other through which one molecule transfers its energy to the other molecule and this process is called triplet-triplet annihilation (TTA). The molecule that gained energy is promoted to the higher energy excited singlet state, whereas the molecule that donated its energy in this process returns to the ground state. The excited annihilator molecule, now in the singlet excited state returns

to the ground state by emitting a high energy photon through fluorescence and this is the mechanism behind TTA-UC as shown in figure 1.1.[19–23] The entire process can be summarized as follows:

$$2^1S + 2h\nu_1 \rightarrow 2^1S* \xrightarrow{ISC} 2^3S* \xrightarrow{2^1A, TTET, -2^1S} 2^3A* \xrightarrow{TTA} {}^1A + {}^1A* \rightarrow 2^1A + h\nu_2$$
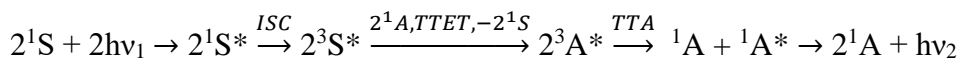
with the net reaction $2h\nu_1 \rightarrow h\nu_2$, where $h\nu_1 < h\nu_2$. TTA-UC relies on the spin-forbidden process of ISC and tightly constrained thermodynamics of the photosensitizers and annihilators. Some thermodynamic and kinetic restrictions for efficient TTA-UC are:

i. The triplet energy of the annihilator should be lower than, or at least equal to, that of the photosensitizer (i.e., ${}^3A* \leq {}^3S*$) to ensure the presence of an energetic pathway for the TTET process.

ii. The energy of the first excited singlet state of the annihilator should be higher than, or at least equal to, twice that of its triplet state (i.e., $2 \times {}^3A* \geq {}^1A*$) to enable the TTA process.

iii. The triplet states involved should be long-lived (at least on the order of several μs) to facilitate both TTET and TTA which are diffusion-controlled processes.

iv. Ideally, both the ISC quantum yield of the photosensitizer and the fluorescence quantum yield of the annihilator should be close to unity.[24,25]

Synthetic modification can be made to photosensitizers and annihilators to tune their molecular properties in order to try to meet the above requirements.[26,27] TTA-UC, unlike other upconversion processes, does not require a coherent excitation source to enable upconversion and it can even happen with incoherent sunlight.[28] The low energy radiation such as red light has high penetration through biological tissue or various media and harmful UV light irradiation is not required for TTA-UC but it can be produced locally, which leads to its exciting applications in biological and material chemistry.[29,30]

TTA-UC is highly sensitive towards molecular oxygen as it is a triplet molecule that readily quenches the triplet state of donor and acceptor and hence the competes with upconversion.[31] Careful selection of the photosensitizer and annihilator must be made to fulfil the constraints described.

Below is a snapshot (Figure 1.2) captured in our lab that illustrates this above TTA-UC phenomenon, when excited by low-energy radiation like red light, the sample emits high-energy blue light.

Figure 1.2 Digital photograph of oxygen sensitive blue emission occurred from 100 µM perylene combined with 5 µM palladium tetraphenyltetrabenzoporhyrin in deaerated toluene by 630 nm laser (1 mW) irradiation.

In recent years, TTA-UC has attracted increasing attention due to the high efficiency accomplishable at relatively low excitation intensities. TTA requires an excitation power density, typically of less than 100 mWcm^{-2}.[32–35] TTA was described initially by Parker and Hatchard in the early 1960s with proposed applications in bioimaging, photocatalysis, photovoltaics and OLEDs, and also potentially in drug delivery/release.

1.2 TTA-UC Photosensitizers

To date most photosensitizers used in TTA-UC have been macrocycles porphyrins, protoporphyrin, and phthalocyanine. Photosensitizers are mainly of four types; red absorbing photosensitizers like meso-tetraphenyl-tetrabenzoporphyrin platinum/palladium (PtTPTBP/PdTPTBP), green absorbing photosensitizers like platinum/palladium octaethylporphyrin (PtOEP/PdOEP), near IR absorbing photosensitizers like palladium(II) octabutoxyphthalocyanine (PdPc(OBu)$_8$) and metal free BODIPY photosensitizers[36,37] which have poor aqueous solubility because they are hydrophobic. In the TTA-UC process, a photosensitizer should have the following characteristics:

- high absorption coefficient;
- close to quantitative triplet yield;
- long-lived triplet state (>10 µs);
- small singlet-triplet splitting minimizing energy losses.[38]

In recent years, photosensitizer molecules have diversified to include both organic photosensitizers and noble metal complexes such as Ru(II), Ir(III), Re(I), and Pt(II). Heavy metal complexes have the advantage of very high, typically 100% conversion to triplet state upon photoexcitation, i.e., with no competing fluorescence, as well as quite long lived triplet

states at room temperature,.[39] Figure 1.3 depicts some commercially available photosensitizers and annihilators/emitters/acceptors that have been used in TTA-UC.
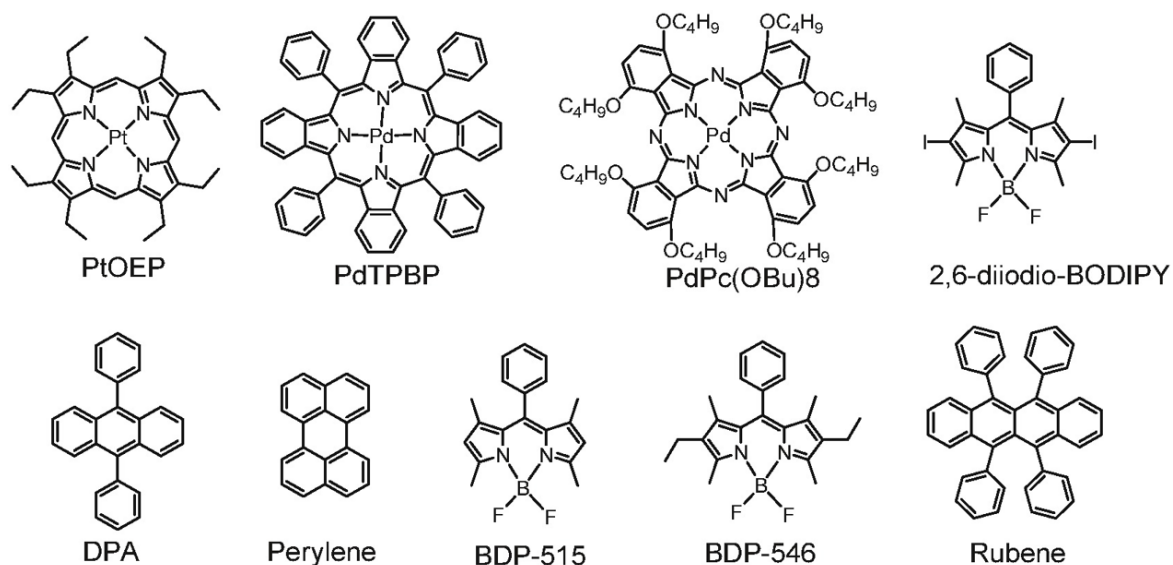
Figure 1.3 Structures of some commercially available photosensitizers (PtOEP, PdTPTBP, PdPc(OBu)$_8$, 2,6-diiodo-BODIPY) and annihilators (DPA, perylene, BDP-515, BDP-546, rubrene) used in TTA-UC. Adapted from Biomaterials 2019, 201, 77–86.[40]

The photosensitizers used in this thesis are BODIPY or Ru(II) polypyridyl based, so the properties of these materials are explored here.

1.2.1 BODIPY

For efficient TTA-UC, it is important to choose appropriate chromophores for the preparation of organic triplet photosensitizers for reasons such as simple derivatization and photostability. Boron-dipyrromethene stands out as a promising candidate because of these qualities.

In 1968, 4,4-difluoro-4-bora-3a,4a-diaza-s-indacene (henceforth referred to as BODIPY) dyes were found by Treibs and Kreuzer.[41] Tricyclic fusions are made up of two dipyrrole units joined by a methine (i.e. carbon at the meso position) or an aza-methine unit (i.e. nitrogen at the meso position) to form a six-membered ring with a boron at its core to bind the ring together and two five-membered units on either side (cf. Figure 1.4). BODIPY including their chemistry, synthesis, reactivity, chemical modification, and spectral specifics of compounds have been widely studied and reviewed by Burgess et al. and Ziessel et al.[42–45] Their optical properties include high fluorescence quantum yields (suppressed non-radiative decay), sharp, high extinction excitation (usually visible light) and emission spectra, and high photo- and chemo stability. They are usually highly lipophilic but can be substituted, e.g., sulfonated, to improve

water solubility if required.[46] BODIPY molecules are small and stable to changes in physiological conditions such as pH and media polarity; they also show excellent photostability in general.[47,48]

Fluorescent molecular sensors[49–53], light-harvesting arrays[54,55], molecular logic gates[56,57], dye-sensitized solar cells, and photovoltaics[58–62] are just a few of the many fields that made use of BODIPY to study the singlet excited state. Research into BODIPY's triplet charged state is in its infancy.
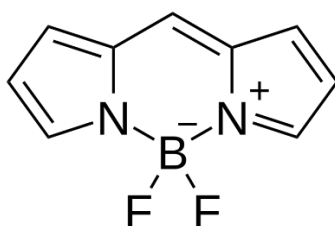
Figure 1.4 Structure of BODIPY.

The ability to be derivatized is one of the many important features of the BODIPY chromophore.[43,44,63,64] Changing the absorption/emission wavelength[64], hydrophilicity[65,66], or redox characteristic[67,68] of BODIPY is as simple as adding a new substituent. It is possibly the most investigated chromophore for triplet state production than any other chromophore, except for the conventional porphyrin derivatives, thanks to its easy derivatization and potential use in the development of a novel triplet photosensitizer.[69] Triplet excited state research employs BODIPY.[70–72] Photocatalysis[73,74], photodynamic therapy[75–77], and TTA-UC have all benefited from the use of new organic triplet photosensitizers based on BODIPY.

As a result of its wide range of practical uses, the BODIPY framework has gained a reputation as a reliable and robust fluorophore including as photostable alternative to fluorescein and rhodamine that can be used for biological labelling by fluorescent conjugates of proteins, nucleotides, fatty acids, and other biological units to gain insight into biological systems and processes.[78,79] Through structural modification of BODIPY, the sharp absorption and emission bands can be adjusted from wavelengths (excitation and emission) of about 500 nm to NIR wavelengths.[80]

However, BODIPYs are brightly fluorescent dyes, meaning they generally are do not efficiently form strong triplet excited state, i.e., ISC is typically weak in such compounds. ISC where $S_n \rightarrow T_m$ ISC is a non-radiative transition during which the electron spin flips or reverts.[81] It is an electron spin forbidden process, and so perturbation to lift the spin selection

rule is required to facilitate electron spin flipping.[82] It is therefore necessary to apply a magnetic torque to the electron spin. A charge transfer state is generated when photoinduced electron transfer (PET) happens within donor-acceptor molecules, resulting in ISC.[83] PET involves the electron transfer between photo-excited and ground state molecules.[84] The most common mechanisms of ISC by PET are the spin-orbital coupling (SOC) and hyperfine interaction.[85] In SOC, the spin angular momentum of the atom interacts with the orbital angular momentum, and examples of this process include the heavy atom effect, the El Syed's rule ($n\pi* \leftrightarrow \pi\pi*$ transition), the spin orbital charge transfer, etc.[86] In hyperfine interaction, the radical pair ISC (RP ISC) in electron donor/acceptor dyads occurs through the magnetic coupling between the electron and the magnetic nucleus.[87] And, these mechanisms can be used to promote intersystem crossing in BODIPY derivatives.[88]

In this thesis, one of the primary focuses is on the investigation of BODIPY-based compounds and their liposome-based bio-delivery as potential triplet photosensitizers for TTA-UC.

1.2.1.1 Heavy atom effect in BODIPY derivatives

One way to assess triplet formation in luminophores, in the absence of ultra-fast spectroscopy is to assess their capability to photosensitize singlet oxygen formation, which can be evaluated by studying the resulting phosphorescence from the $^1O_2$ (1270 nm).[75] For example, Liu et al. showed use of mono- and diiodo-BODIPY derivatives with different absorption wavelengths and efficient $^1O_2$ was used to verify the ISC, and the relative efficiency of $^1O_2$ generation was measured with reference to Rose Bengal under the same conditions and the diiodo-BODIPY has better photostability high singlet oxygen quantum yield.[89] Wu et al. taking advantage of the amenability of the BODIPY framework for derivatization, prepared a library of iodinated BODIPY derivatives with absorption extending from 510 to 629 nm; using time-dependent density functional theory (TD-DFT), they estimated the T_1 state energy level of these derivatives to lie between 1.5 to 1.15 eV.[72] These derivatives have high visible light absorption efficiencies ($59,400$–$180,000\, M^{-1}\, cm^{-1}$). The compounds' triplet-state lifetimes were measured using nanosecond transient absorption spectra in the range of 26-66 µs. Because of the self-quenching effect of triplet-triplet annihilation (TTA), apparent triplet-state lifetimes were shorter than intrinsic triplet-state lifetimes. Based on Zhao and Dick's kinetic model, the intrinsic triplet-state lifetimes of diiodo-BODIPY were calculated to be up to 276 µs.[90,91] Until the work descried by Lou et al. and Wang et al. the intrinsic triplet state lifetime of BODIPY derivatives has never been studied. According to Wu et al. the TTA upconversion process was

facilitated by these diiodo-BODIPY derivatives due to their strong visible light absorption, efficient ISC, and a long-lived triplet state.[72] Following 532 nm CW-laser excitation using perylene as the triplet acceptor/emitter, significant upconverted blue emission of about 450 nm was observed, with upconversion quantum yields of up to 6%. As a result, these compounds can be used with alternative excitation wavelengths for TTA upconversion.[92]

1.2.2 Ruthenium complex as photosensitizer

Recently, light-sensitive ruthenium(II) polypyridyl compounds have been suggested as prodrugs in photoactivatable anticancer therapy (PACT), making them classic tools in photochemistry.[93–95] In PACT, ruthenium-functionalized liposomes, for instance, could be activated with visible light.[96] However, the "phototherapeutic window," a spectrum of wavelengths (600-900 nm) that permeate mammalian tissues optimally, does not include blue light (400-500 nm), which is needed to activate most ruthenium(II) polypyridyl compounds. Upconverting drug carriers can overcome this shortcoming by locally converting red photons into blue photons within a tumour, allowing the phototherapeutic drug to be activated without first having to travel great lengths through the tissue. For instance, in-situ generation of blue light particles via TTA-UC of green or red-light using liposomes was achieved. Clinical grade photodynamic therapy laser sources (630 nm) were able to initiate photodissociation of ruthenium polypyridyl compounds from PEGylated liposomes containing red-to-blue upconverting pair of photosensitizer and annihilator.[93]

TTA-UC has been shown to work in a number of different mediums, including organic solvent, liposomes, ionic liquid, polymer matrix, functionalized polymer, and to name a few. All these systems rely solely on radiative energy transfer to further utilise the upconverted light, such as to activate ruthenium complex-based prodrug, because the molecule sensitive to high-energy light is too far, at the nanoscale (>10 nm), from the annihilator. In order for non-radiative energy transfer to occur, the medium must be bioactive and flexible enough to accommodate the photoactive molecules within it while still allowing them to diffuse, with an average distance of less than 5-8 nm between photochemically active components (photosensitizers, annihilators, and/or prodrug molecules).[97] In this context, liposome models as organic nanocarriers are useful. Organic nanocarriers are promising drug delivery devices because they can load molecules by conjugation on the surface or in the core or by physical encapsulation.

1.3 Cell Membranes

This thesis investigates liposome and pore-suspended lipid bilayer made up of various lipid types as an in vitro model for reconstituting photoactive sensitizers and annihilators and demonstrating their TTA-UC. The inherent physicochemical characteristics of the cell membrane, such as degrees of fluidity, head group charge, local alkyl chain packing ordered and disordered domain, and so on, were studied to see how they influence TTA-UC occurrence and efficiency. The following section describes cell membranes in depth and classifies various lipids, some of which were used in this work to prepare liposomes using a bottom-up approach.

The cell membrane, also known as plasma membrane, are thin, flexible barriers that protect and are essential components of all cells. It is composed of lipids, proteins, and carbohydrates and provides a semi permeable barrier separating the inside and outside of the cell. In a constantly changing external environment, cell membranes are essential for maintaining homeostasis.[98]
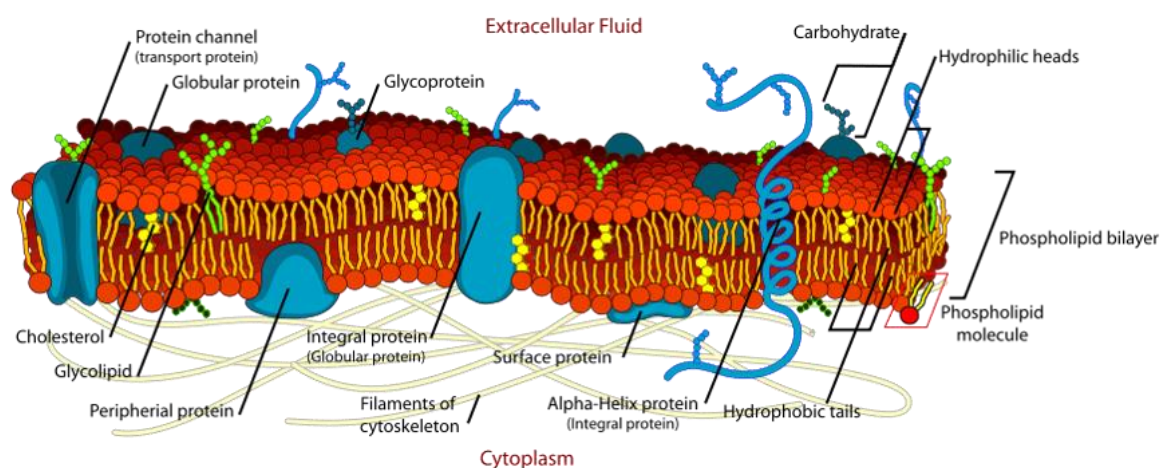
Figure 1.5 Schematic illustration of the structure of cell membrane. Figure is adapted from teachmepsychology.com.

The membrane serves several functions, including transporting nutrients into the cell and removing toxic substances from it. Plasma membrane has proteins in it, up to 50% by weight and they are involved mainly in signalling adhesion and transport. Double-chained phospholipids, cholesterol and glycolipids, make up the majority of the cell's membrane, which is structured in a bilayer with embedded proteins.[99] There are hydrophobic and hydrophilic lipid chains on each side of the membrane, with hydrophilic heads face towards the aqueous environment outside.[100] The thickness of a typical mammalian cell is approximately 4-6 nm which is about two thousand times smaller than the radius of a typical mammalian cell.[101]

Because the current thesis makes use of various lipids to form a biomembrane that reconstitutes the TTA-UC pair, a detailed explanation of the various lipid types is given below.

1.3.1 Glycerophospholipids

This class of lipids is the most prevalent in the biological membranes of living organism.[102] Fatty acids are joined to glycerol's carbon 1 and 2 by an ester oxygen in glycerophospholipids.[103] The phosphate moiety is attached to carbon 3 through an ester bond, whereas the phosphate moiety can be coupled to any of a number of different substituents. This architecture is amphipathic in nature, with glycerol and phosphate at the polar end of the molecule, and hydrocarbon chains at the nonpolar end.[104] Typically the major abundance of glycerophospholipids in biological systems are those where carbon 1 is normally saturated and carbon 2 is usually unsaturated, but the hydrocarbons can be any of the common ones.[105] The various combinations of two fatty acid with respect to its chain length, degree of unsaturation as well as the position of unsaturation etc. can give rise to thousands of such glycerophospholipids.[106] Additionally, the head group structures also make different molecules differ greatly in their physical properties due to the various size, chemistry and overall difference in their electrical charges.[107,108] Phosphatidylcholines and phosphatidylethanolamines are zwitterionic, which means that the substituent group has one positive and one negative charge.[109] However, the overall net charge of phosphatidylserine, phosphatidylinositol, phosphatidic acid etc. is negative and trimethylammonium propane is positively charge.[110,111]

In bilayers, glycerophospholipids and sphingomyelin (Figures 1.6 and 1.7) can be gel or liquid-crystalline.[112] In gel state, the lipid molecules are tightly packed with extended acyl chain organized in a two-dimensional lattice.[113] Upon heating, the gel state turns liquid-crystalline and in such cases bilayer stays in a two-dimensional lattice but gain more conformational freedom laterally as well as along the bilayer axis.[114,115] The packing of acyl chain is also lost compared to gel state behaving as a quasi-liquid.[116]
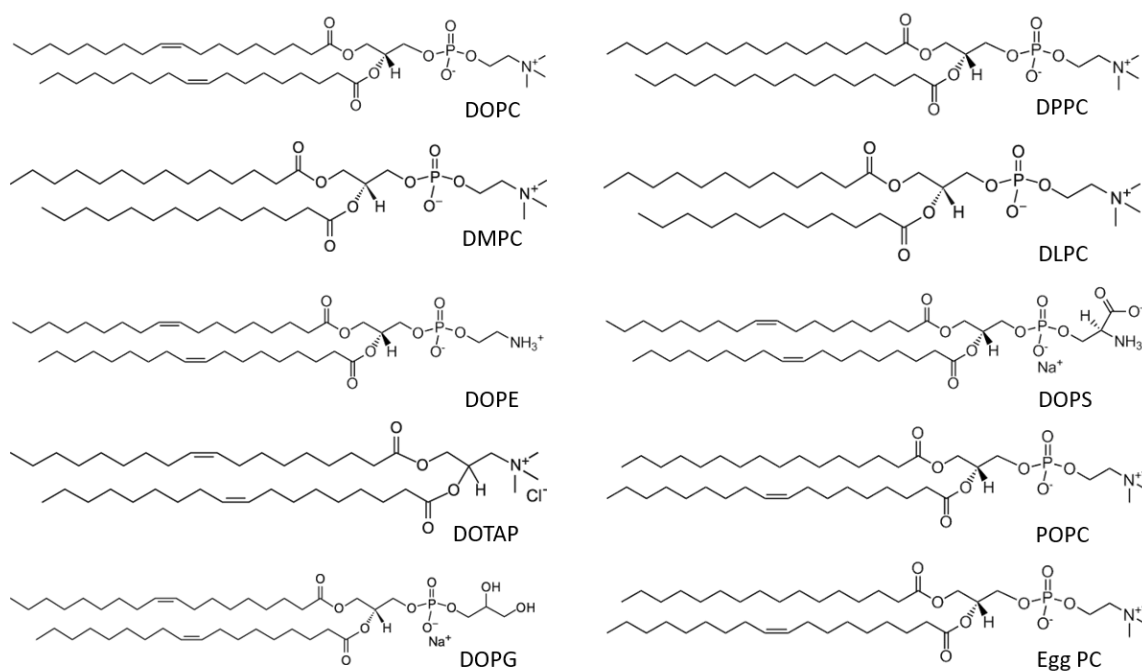
Figure 1.6 Chemical structure of different phospholipids used in this work, DOPC, DPPC, DMPC, DLPC, DOPE, DOPS, DOTAP, POPC, DOPG, and egg PC. All lipid structures are adapted from the website of Avanti polar lipids. Egg PC is a mixture of 16 to 22 carbon atoms long acyl chain containing multiple double bonds and the structure shown is only representative of one possible structure present in egg PC.

1.3.2 Sphingolipids

Sphingolipids are another type of membrane-bound lipids. Sphingolipids are based on more abundant sphingosine (18-carbon amine alcohol) and less abundant phytosphingosine (20-carbon analog).[117] Sphingomyelin is an analog of phosphatidylcholine because it has phosphorylcholine group instead of the sugar moiety.[118] All sphingolipids have a fatty acid linked to the sphingosine's amino group. Sphingomyelin is the most common sphingolipid found in biological membranes.[119]

Mainly substituents connected to sphingosine's carbon 1 determine sphingolipid characteristics and minor variations in properties also depend upon the fatty acid component.[120] Asymmetrically placed on the cell membrane's outer leaflet, glycosphingolipids often serve as a role of receptor, which all have a sugar linked to sphingosine's carbon-1.[121,122] Neutral glycosphingolipids contain only neutral sugars, while gangliosides contain one or more sialic acid residues linked to the sugar.[123]

Figure 1.7 Chemical structure of sphingomyelin.

1.3.3 Cholesterol

Sterols are key components of eukaryotic membranes but are scarce in prokaryotes.[124] Mammalian's main sterol content is cholesterol, while fungi's is ergosterol and plants' is sitosterol.[125] Each of these three key compounds has four fused carbon rings creating the steroid nucleus and an associated hydroxyl (OH) group attached to the first ring. Carbon-carbon double bonds and the hydrocarbon side chain on the fourth ring differentiate the sterol molecules.[126,127]

Figure 1.8 Chemical structure of cholesterol.

Cholesterol and related compounds are hydrophobic and water-insoluble.[128] It is a major component of the mammalian plasma membrane, where its concentration can reach 50% by weight.[129]Cholesterol's rigid fused ring strengthens liquid crystalline phospholipid bilayers against mechanical rupture.[130] When the cholesterol concentration of a binary phospholipid-cholesterol mixture is increased, the liquid crystalline phospholipids (unsaturated hydrocarbon chain containing lipids such as DOPC, POPC, etc.) rigidifies the membrane while the gel-like phospholipid (DPPC, DMPC, etc.) fluidizes. In a ternary lipid mixture of glycerophospholipid, SM, and cholesterol at the proper mole percentages, cholesterol induces domain formation into liquid ordered domains (L_o) rich in SM and cholesterol and liquid disordered domains (L_d) rich in glycerophospholipid. The model membranes comprised of single component, binary and ternary lipid mixtures are used here to mimic different fluidity aspect of membranes and its interplay effect on TTA-UC and small molecule permeability assay.

1.4 Model Membranes

Much of our knowledge of cellular process such as lipid-lipid, lipid-protein, protein-protein understanding comes from model membrane, including liposomes and solid supported membranes because they provide a simpler system with fewer lipid constituents, that the real cell membrane which is incredibly complex containing1000's of lipids and proteins. Understanding the biomolecules that make up the cell is necessary for a quantitative description of live cells.[131] This is most simply addressed using a biophysical approach to either by attaching the membrane to a solid's surface or by suitably positing in the form of free-standing membrane.[132]

Using such membrane models one can answer several biologically important questions such as fluidity/viscosity of membrane constituents.[133] Monolayers, supported or free standing bilayers, and vesicles are the most studied membrane-based model systems.[134] Large unilamellar vesicles, or giant liposomes, are cell-sized.[135] Like cells, they have finite volume, area and are ideal as membrane model.[136] Attempting to create self-replicating artificial cells for evolutionary research is a fascinating use of giant unilamellar vesicles (GUVs).[137] Previously GUVs (>1000 nm diameter) have been used as minimum systems for cell-free protein synthesis or micro-reactors.[138] Small unilamellar vesicles (SUVs) of less than 100 nm and large unilamellar vesicles (LUVs) of sizes less than 1000 nm are easier to prepare in laboratory, however, due to its small size visualizing the membrane surface by microscopy is challenging.[139,140] However, with regard to upconversion studies, here, both LUVs and GUVs as cell models to examine membrane based phenomena will be employed. Due to its large size, and amenability to confocal microscopy, GUVs have been utilized to shed light on phase-separating domain formation, often refer as ''rafts'' and their relation to various membrane functions, including cell adhesion, endo and exocytosis, antimicrobial peptides, ion channels, antibody binding and more recently, cell division.[141,142]

An intrinsic property of the plasma membrane is that the composition of each bilayer leaflet is not same, referred to as transbilayer asymmetry.[143,144] In the mammalian plasma membrane sphingomyelin and phosphatidylcholine are actively sequester to the outer leaflet.[145] The inner leaflet contains phosphatidylethanolamine, phosphatidylserine, and phosphatidylinositol.[146] Cholesterol is present in both membrane leaflets.[147] This asymmetry in terms of charge and composition gives it special structural properties and is essential for some of its functions. Along with transversal asymmetry, lateral inhomogeneities, particularly in the outer leaflet of

plasma membrane, are thought to play a key role in how some membrane proteins signal, e.g. by concentrating of proteins along with their ligands into domains .[148]Lateral inhomogeneities include lipid rafts structures from cholesterol, SM and unsaturated lipids leading to phase separated domains where a pool of lipids segregated form another pool of lipids depending upon the composition and temperature.[149] Under these conditions, high-melting lipids like sphingomyelin and cholesterol form liquid-ordered (L_o) phase, with low mobility or high viscosity, whereas, low-melting lipids like unsaturated phosphatidylcholine form liquid-disordered phase which is of low viscous and has high mobility. These L_o domains are of nm to sub-micrometre in length and can be prepared in laboratory by mixing three such lipids in appropriate ratio at ambient temperature.[150]

Because cell membranes are complex and dynamic, to interrogate the role of fluidity in a given process (e.g., TTA-UC, small molecule permeation, and photosensitizer mobility across 2D) in such a crowded and dynamic environment is extremely difficult.[151] As described, model membrane systems offer the opportunity to understand membrane behaviour starting from a minimal single component lipid test cell to mixed lipid compositions, so the specifics of the biophysical process can be unravelled. The power of such a model systems rests in their simplicity, and ease of interrogation of controlled experimental conditions.[152] They rely upon the fact that in an aqueous environment, lipids tend to self-aggregate or assemble into liposomes or bilayers and this is the basis of the assembly of most models.

1.5 The self-assembly of lipids and model membranes

1.5.1 Liposomes

Liposomes are a type of spherical vesicles comprised of lipid bilayer or multilayer of phospholipids and they can easily be prepared in the laboratory. They have been used widely as models to study the characteristics of the cell membrane and also as delivery vehicles for molecular cargo to cells including drugs, imaging agents etc.[153] Liposomes are freestanding membrane models where both leaflets are in touch with water and they freely diffuse in solution.[154]

Liposomes are referred to as unilamellar if there is one phospholipid bilayer, bilamellar if there are two bilayers, and multilamellar vesicles (MLV) if there are several lipid bilayers.[155] According to their size, vesicles are divided into three categories: small, large and giant unilamellar vesicles. Giant unilamellar vesicles (GUV) are 1-100 μm size, small unilamellar vesicles (SUV) range in size from 20-100 nm, and large unilamellar vesicles (LUV) are 100

to1000 nm in size (Figure 1.9). Extrusion, sonication, or the quick injection of a phospholipid solution into an aqueous buffer solution can all be used to prepare a homogeneous phospholipid vesicle suspensions.[156] GUVs that are prepared by electroformation method are of large size and is suitable for confocal based imaging.[157]
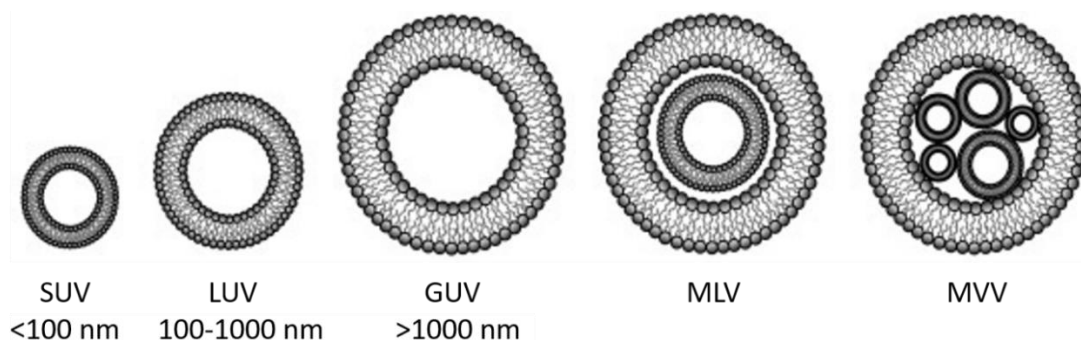
Figure 1.9 Schematic illustration of different size of vesicles with their diameter size and they are classified into small unilamellar vesicles (SUV), large unilamellar vesicle (LUV), giant unilamellar vesicle (GUV), multilamellar vesicle (MLV), and multi vesicular vesicles (MVV). Adapted and recreated from Adv. Colloid Interface Sci. 2017, 249, 163–180.[158]

Throughout this thesis, electro formation and extrusion methods are used to respectively prepare large and small size vesicles for TTA-UC studies. The details of these experimental methods are provided below.

1.5.1.1 Electroformation of GUVs

Electroformation is probably the most important technique for creating large vesicles. Angelova and Dimitrov provided the initial explanation of the electroformation procedure in 1986.[159] It entails coating a planar conductive electrode with lipids that have been dissolved in an organic solvent like chloroform, vacuum desiccating the solvent to create dry phospholipid film, immersing the coated electrode in an aqueous buffer solution, and then applying an electric A.C field across the lipid film within the surrounding buffer (Figure 1.10). By doing so, lipids ''peel off'' from the electrode surface in layers and self-assemble into giant yet polydisperse, multilamellar vesicles However, in this thesis the procedure to yield monodisperse GUVs of more than 10 μm size is slightly modified, and the detail procedure will be discussed in the experimental section.
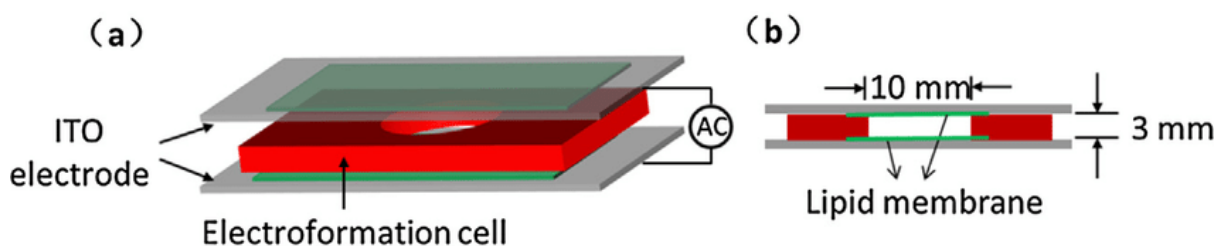
Figure 1.10 Schematic illustration of the GUV electroformation setup. (a) Two slides of ITO electrodes both coated with lipid film were separated face-to-face by a spacer. (b) Side view of the electroformation setup. Adapted from J. Mater. Chem. A, 2013, 1, 7125-7130.[160]

1.5.1.2 Preparation of monodisperse LUVs by Extrusion

When dried lipid films come into contact with aqueous solutions, they self-assemble into polydisperse vesicles of various sizes. After self-assembly, these vesicles are extruded, which changes their lamellarity, dimension, and size distribution. Olson et al. in 1979 has outline the procedure by passing lipid or vesicle solution via a polycarbonate membrane or other mesh of microscopic openings.[161] These days, it's simple to make vesicles of various sizes (typically smaller than 1000 nm) that are unilamellar and monodisperse using the extrusion kit from Avanti polar lipids. Filter papers' pore size, mechanical pressure, and the number of times the solution pass through the membrane filter determine the final diameters.[162] The extrusion method has been used extensively in this work with range of membrane compositions for TTA-UC studies and the schematic illustration of an extruder is shown in Figure 1.11.
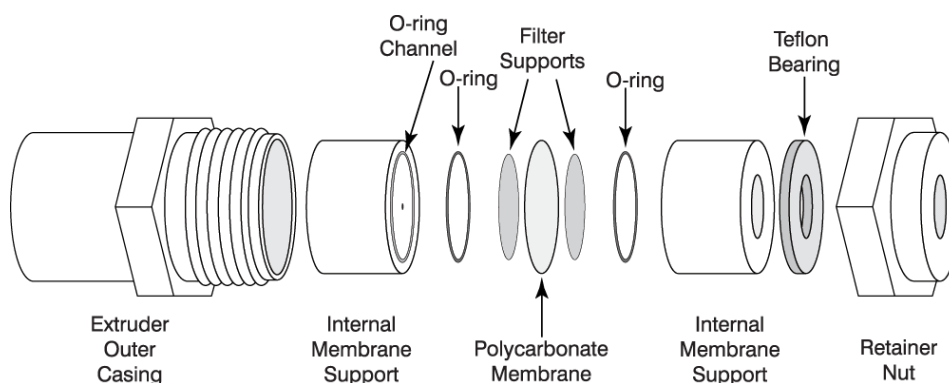
Figure 1.11 Schematic illustration of extruder assembly for liposomes preparation. Adapted from Avanti polar lipids.

1.5.2 Solid suspended lipid bilayer

Planar membrane models are not free-standing structures; instead, they are assembled on top of a solid support (Figure 1.12a).[163] Because of the solid support, their fluidity is compromised through both leaflets, and they are unsuitable for membrane protein reconstitution, yet they

are easily interrogated by surface sensitive analytical techniques.[164] Using such supported lipid bilayer platform, various studies such as membrane-protein, membrane-drug, membrane-peptide etc. have been reported.[165–167] But, as mentioned SLBs are generally not suitable for study of proteins of large transmembrane domain or cytoplasmic tails as when it inserts across the membrane, it will come in direct contact with the solid support and will eventually lose its functionality.[168] Much effort has been made to address these issues by creating space between the bilayer and solid support, so that the protein does not come into direct contact with the interface, so it remains functional and mobile. One such approach is to use polymer cushions(Figure 1.12b), where a polycation layer can be sandwiched between the solid substrate and the bilayer.[169] In another approach, tethered or spacer molecule are placed on the solid surface to decouple the bilayer from the solid support.[170] Although these methods have proven to be suitable for protein insertion where ligand binding, for example, shows that the proteins are functional. The transmembrane protein generally does not show lateral fluidity; either diffusion is highly restricted or the mobile fraction is very low, and the use of extra tethering organic molecules/polymer in the context of physiological membrane compositions remains an issue.[171] Nonetheless, the formation of solid supported lipid bilayers is relatively easy and can be achieved by various means such as unilamellar vesicle fusion (VF), two layers Langmuir-Blodgett (LB) deposition (Y-type), Langmuir-Blodgett followed by Langmuir-Schaefer (LB-LS) and combination of LB-VF methods.[172,173] Asymmetric bilayer with varying compositions across each leaflet can be prepared over the solid support using the above mentioned methods, except for VF.
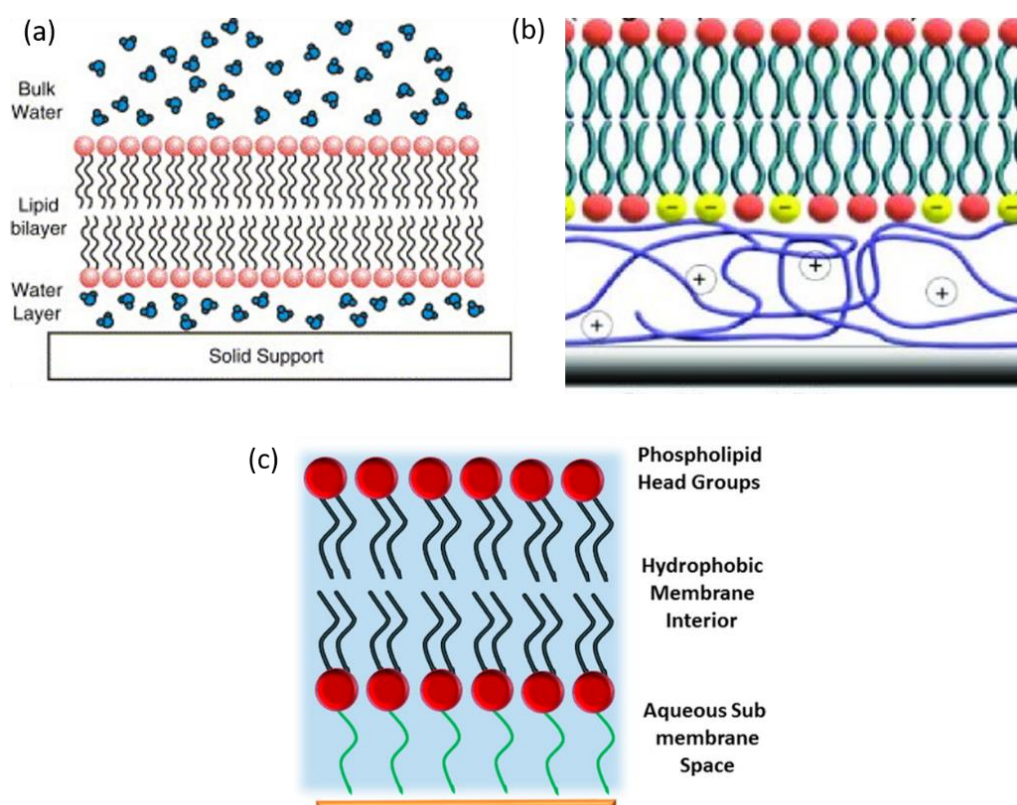
Figure 1.12 Schematic illustration of (a) solid supported lipid bilayer, (b) polymer cushion bilayer and (c) tethered bilayer. Adapted from Surf. Sci. Rep., 2006, 61, 429-444, Eur. Biophys. J., 2007, 36, 621-635.[170,174]

Solid substrates with high hydrophilicity are required for lipid bilayer assembly as the hydrophilic head group of the lower leaflet must adsorb at the substrate.[175] Various solid supports that have been commonly utilized to form SLBs are glass, silicon, mica, ITO and gold.[176] For example, mica and silicon are commonly used to prepare bilayer for atomic force microscopy (AFM) studies.[177] Transparent substrate such as glass is used for fluorescence studies.[178] Conducting gold or semiconducting ITO, Si etc. have been used for electrochemical studies.[179] The surface pre-treatment of the substrate is another important criterion for the successful formation of stable bilayer. Glass and silicon substrates are often treated by piranha for cleaning surface impurities and to render its surface hydrophilic, whereas mica is freshly cleaved.[180] Oxygen plasma cleaning procedures can also be used following the above treatment to make the surface more hydrophilic.[181] For conducting substrate such as gold, the surface is often treated with small molecule alkane thiols with terminal -OH, -NH$_2$ and -COOH group following electrochemical cleaning for increasing the surface hydrophilicity.[182]

1.5.3 Pore suspended lipid bilayer

Spanning the membrane over a pore is an alternative strategy that has only recently been developed to reduce membrane substrate interactions. Free-standing membranes, or pore suspended bilayers, have been proposed as a link between solid-supported lipid bilayers (SLBs) and BLMs.[183] Developed by Keyes group, the microcavity supported lipid bilayer (MSLB) system, schematically depicted here (Figure 1.13) is one of the key models used here. It comprises a lipid bilayer suspended over a small pore (typically <10 μm in diameter), which allows for the study of lipid bilayer properties without the restrictions imposed by membrane-substrate interactions (such as poor lipid diffusivity or protein denaturation).[184]
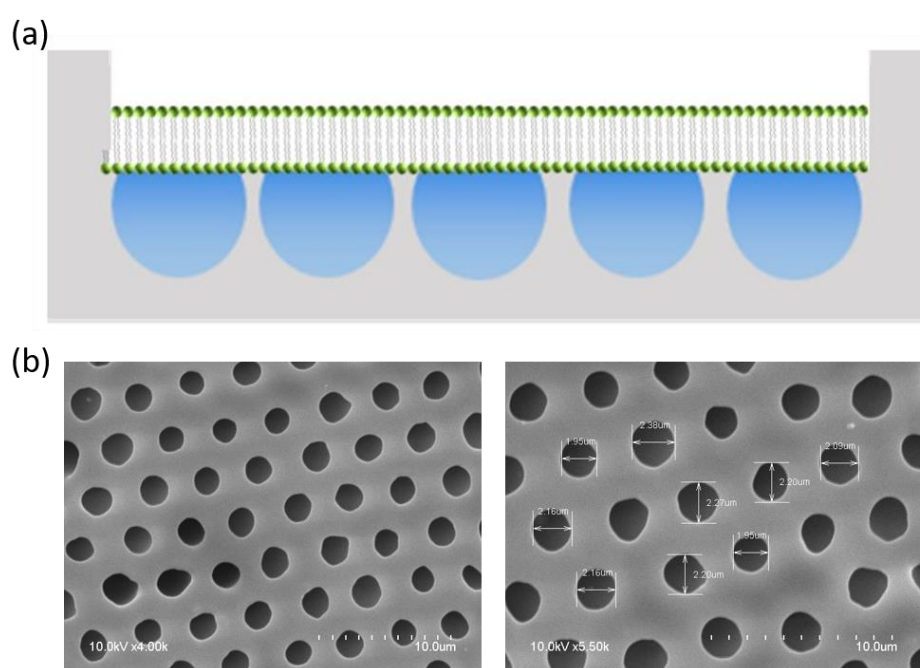
Figure 1.13 (a) Schematic illustration of microcavity suspended lipid bilayer. Adapted from Chem. – Eur. J., 2021, 27, 17203.[185] (b) Scanning electron microscopy (SEM) images of microcavity arrays of 2 μm diameter on PDMS substrate. The scale bar is 10 μm.

The substrates used in this thesis are a hexagonal close packed imprinted microporous array filled with buffer and the intestinal space is hydrophilic, bilayers can be spanned directly over hydrophilic porous substrates and remain suspended over the buffer-filled cavities. The scanning electron microscopy (SEM) images showing 2 μm sized pores over PDMS substrate is shown in Figure 1.13b. Multiple substrate materials, including porous silicon, alumina, silicon nitride, PDMS, gold-coated silicon nitride, and gold coated silicon substrate have been used to assemble pore-supported bilayers.[186,187] By increasing hydrophilicity, functionalizing the top intestinal surface of the substrates with hydrophilic molecules can increase affinity to

the membrane. Self-assembled monolayers (SAMs), such as -OH, -NH$_2$, and -COOH terminated thiols, can be covalently bound to the gold intestinal surface to improve the substrate's hydrophilicity.[152,188] Similarly, silicon and aluminium oxide-based substrates with terminal hydrophilic groups are compatible with silane chemistry.

Similar to solid supported lipid bilayers, pore suspended lipid bilayers can be created through a variety of methods, including, but not limited to, lipid transfer via Langmuir-Blodgett and/or Langmuir-Schafer, vesicle fusion, or a combination of LB/VF.[189,190] Some groups, who work with pores of small, (nanometre) dimensions use direct fusion of liposomes to porous substrates. Liposomes with a diameter greater than the aperture of the pores are required to obtain a pore-suspended membrane, limiting the use of SUVs and LUVs because they may become trapped in the cavities and assemble across the interior surface of the array rather than span across the pores. GUVs are a viable option for this purpose. Heinemann and Schwille, for example, reported on a free-standing membrane by directly fusing GUVs to a Si$_3$N$_4$ support with 2.5 µm pores.[191] Fluorescence correlation spectroscopy (FCS) was used to measure lipid lateral diffusion, and lipid bilayers made of DOPC demonstrated lipid diffusion of around 10 µm^{2}s^{-1}. A drawback of this approach is that the bilayers formed after GUV fusion did not cover the full substrate but rather create patches of lipid bilayer of few micrometres, and formation of asymmetric bilayer was not achieved.

Langmuir-Blodgett (LB) transfer has the advantage of covering larger areas than GUVs disruption but as the sole method has not been thoroughly investigated in the preparation of pore-suspended lipid membranes. Simon et al. successfully prepared pore-suspended membranes via Langmuir-Blodgett transfer. DOPC/DOPS (7:3 ratio) lipid bilayers were stretched across 1 µm pore-sized silicon arrays.[192] Although LB methods improve coverage of porous substrates, protein incorporation is limited. In addition, although asymmetric bilayer is achievable using LB-LB or LB-LS method, however, it requires extra effort to prepare independent monolayers which is time consuming, not cost-effective and prone to expose to air.

However, lipid bilayers prepared using a combination of LB followed by liposome/vesicle fusion (VF), can circumvent the above limitation and this is the approach used in this thesis. This is accomplished by exposing a lipid monolayer pre-transferred to the pore array by the LB method to a solution containing liposomes of the same or different composition, yielding symmetric and asymmetric lipid bilayers. The lipid monolayer acts as a seal, preventing the

liposomes from entering and rupturing inside the cavities. In contrast to SLBs, microcavity supported lipid bilayers (MSLB) prepared by the LB-VF method facilitate the reconstitution of integral proteins with biomimetic lateral mobility by generating a free-standing bilayer over the pore with a deep aqueous interface at both leaflets of the bilayer and any interaction with underlying solid support is confined to the interpore regions. Basit et al. reported membrane protein reconstitution into MSLBs of glycophorin A and integrin $\alpha_{II}\beta_3$,using FCS diffusion coefficients of 4 and 3.2 $\mu m^2 s^{-1}$ for the reconstituted proteins respectively, which matched the reported diffusion values in liposome, demonstrate their considerable mobility.[187] In addition, Keyes's team has created the microcavity array substrate using a variety of materials, including PDMS and gold, in which lipid membranes have been used to study the lateral mobility of lipids, to create asymmetric lipid bilayers, and to assess the passive permeability of small molecule therapeutics.[193–199] Incorporating membrane proteins into pore-supported lipid membranes and creating asymmetric lipid bilayers are both made possible by LB in combination with liposome fusion. In pore supported DOPC lipid bilayers, the diffusion coefficient of a lipid probe molecules is typically around 10 $\mu m^2 s^{-1}$, which is comparable to the values found for free suspended vesicles like GUVs.[191] Diffusion coefficients in SLBs are typically between 4 and 10 times lower than those in pore spanning membranes, demonstrating a significant benefit of pore-membranes over solid supported membranes.[200]

Overall, artificial membranes can provide new knowledge on lipid-lipid and lipid-protein interactions at the molecular level in the cell membranes environment because such models are simpler and the particular aspect can be studied without any complexity posed by cell. They are also far more addressable and easily studied than liposomes and can provide useful insights into electrical and dynamic properties of liposomal membranes as they can be made of exactly the same constituents. The MSLB as a true biomimetic platform was used in this thesis to support liposome studies to understand different bilayers integrity and underlying fluidity ranging from single component to binary to ternary compositions. In addition, the current thesis aid TTA-UC liposome development and as described later in the thesis to provide insight on membrane-drug interactions and evaluated other photosensitizer interactions in liposomes. Mainly for this work PDMS based MSLB was employed which was assembled in a microfluidic environment using a hybrid LB/VF technique that did not require the use of harsh organic solvents or more analyte concentrations.

1.6 Lipid Diffusivity

Cell membranes are dynamic and this is necessary to facilitate a range of processes at the membrane including permitting functional components such as proteins and glycolipids to diffuse to their reaction sites and allowing for aggregation and clustering processes involved in membrane signalling.[201–203] Small variations in cell membrane fluidity, e.g., due to different phases, domains or rafts in the membrane have been shown to impact cell properties and lead to variations in several functions, including protein expression, exposure of cell membrane receptors, and functional properties of the cell membrane.[204]

For example, the efficiency of a photosensitizer within the membrane is affected by different physical properties of the membrane and fluidity is critical among them.[205,206] The study of lipid mobility in biological and artificial lipid models can reveal details about membrane structure, viscosity and organisation. Regardless of whether photosensitizers play a role in TTA-UC or photocatalysis at membranes, both uses require collision, which at a membrane is in two dimensions and is intrinsically dependent on viscosity. One of the primary objectives of this thesis is to investigate how fluidity and viscosity affect TTA-UC intensities and whether the photosensitizer can freely diffuse across 2D to collide with the annihilator for effective UC.

A molecule's diffusion can be characterised as a random trajectory or random walk. A molecule in solution, for example, may diffuse unpredictably as a result of random collisions with water particles. The Einstein relation (Eq. 1.1) describes free Brownian motion as it relates to the movement of a molecule in a fluid, where $\langle r(t)^2 \rangle$ is the mean square displacement (MSD) that is proportionate to time t and diffusion coefficient D, as shown in Equation 1.1

$$\langle r^2(t) \rangle = \langle \left(r(t) - r(0) \right)^2 \rangle = 4Dt \tag{1.1}$$

Membrane constituents can easily diffuse according to Brownian motion in lipid models, particularly free-standing bilayers such as GUVs. The existence of lateral heterogeneities in the membrane can impair the diffusivity of its constituents, resulting in anomalous or sub-diffusion. This motion deviates from Brownian or "random walk" particle diffusion, and here the distance travelled by molecules is proportional to $4D\Gamma^\alpha$, the anomalous exponent α varying from 0 to 1. As per Stokes-Einstein equation, the diffusion of a molecule in a liquid with a low Reynolds number is characterised by the relationship between the radius (r), as shown in Equation 1.2.

$$D = \frac{k_B T}{6\pi\eta r} \tag{1.2}$$

Where k_B is the Boltzmann constant, T is the media temperature, and η is the mass solution viscosity. The Saffman-Delbrück model can be used to describe the lateral diffusion of molecules within a lipid membrane. According to this theory molecule treated as cylindrical inclusions diffusing in a viscous two-dimensional medium encircled by a less viscous fluid. The diffusivity (D_L) is defined as Equation 1.3.

$$D_L = \frac{k_B T}{4\pi\mu h}\left(ln\left(\frac{\mu h}{\mu' r}\right) - \gamma\right) \tag{1.3}$$

Where D_L is the lateral diffusion of the cylindrical inclusion of radius r, T is the absolute temperature, h is the thickness of the lipid membrane, γ is Euler-Mascheroni constant (approx. 0.577), μ and μ' are the membrane viscosity and the bulk solution viscosity, respectively. The Saffman-Delbrück model is commonly used in the literature to explain protein diffusion in lipid membranes.

1.6.1 Factors affecting lipid diffusivity

Many factors, such as the lipid composition of the membrane, lipid distribution, concentration of the doped molecule, and external factors such as temperature, pH etc, can impact the mobility of lipids and molecules reconstituted within free standing membranes. In the context of this thesis, the membrane composition is the parameter that varies, and so this is discussed in detail below.

1.6.1.1 Membrane composition

The physicochemical characteristics of membrane lipids, such as the length and degree of saturation of fatty acid tails influence lateral packing and fluidity and may result in the formation of distinct phases. The temperature of the transition phase of phospholipids is well defined and depends on the degree of unsaturation (double bond) of the backbone hydrophobic tail. Due to the higher hydrophobic bulk volume of unsaturated fatty acids, unsaturated tails decrease lateral lipid packing, resulting in a more flexible membrane with a lower phase transition temperature (T_m). This can result in the creation of more fluidic phases with high lipid mobility, which are referred to as liquid disordered (L_d) domains (Figure 1.14a). The degree of unsaturation of lipids is related to poorly packed membranes, which firmly suggests that membrane packing affects lateral diffusion.[207] Data from molecular dynamics simulations have been reasonably effective in predicting lateral diffusion coefficients.[208] Saturated fatty

acids, on the other hand, pack more tightly in membranes due to higher van der Waals interactions along the length of the lipid tail, resulting in more rigid phases, indeed they frequently form gel phases (L$_\beta$ or S), at room or physiological temperature as shown in Figure 1.14a.
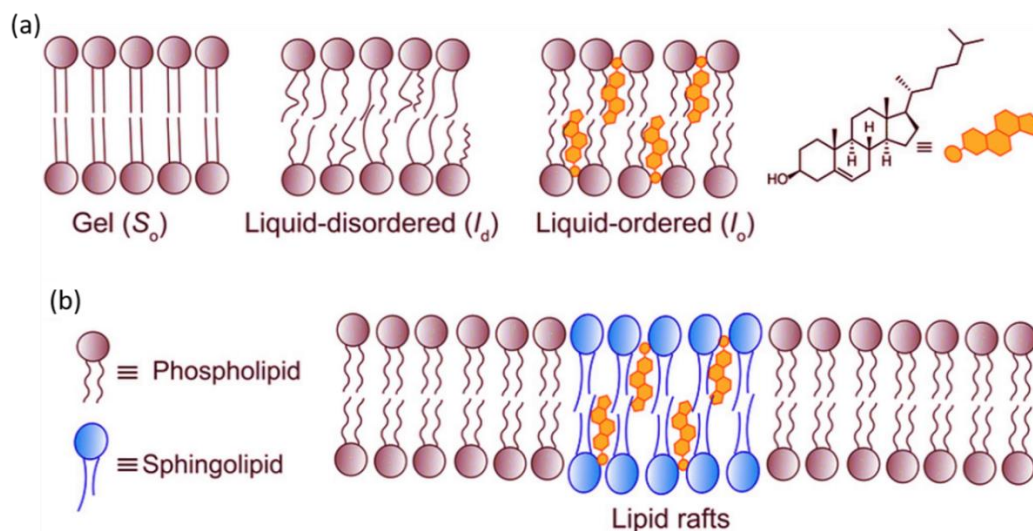
Figure 1.14 Schematic illustration of (a) the gel phase, liquid-disordered phase, and liquid-ordered phase containing cholesterol, of phospholipid membranes, and B) membrane phase separation, leading to the formation of lipid rafts. Adapted and recreated from ChemBioChem 2020, 21 (7), 886–910.[209]

In lipids models made up of lipid with a mix of low and high phase transition temperature constituents and sterol, they will often phase separate and cholesterol laterally segregates into ordered domains (L$_o$), which contain saturated phospholipids exclusively, as shown in Figure 1.14. Bezlyepkina et al. proposed a phase diagram, based on experimental studies of ternary lipid mixtures comprised of unsaturated DOPC, saturated sphingomyelin (SM) (T$_m$ DOPC ≈ -17 °C, T$_m$ SM ≈ 45 °C) and cholesterol (Figure 1.15).[210] Applied in this thesis in selecting lipid composition, this diagram allowed to predict the different phases that would be formed in our liposomes and MSLB. Lipid bilayers comprised primarily of SM, for example, will create gel phases (pink area). The addition of cholesterol can induce the formation of L$_o$ + S (red area) due to hydrogen bonding interaction between the SM and cholesterol or van der Waal interaction between saturated lipid and cholesterol. By combining DOPC/SM for example, two independent phases can be formed: a L$_d$ enriched in DOPC and a L$_o$ enriched with SM (blue area). As shown in the green and yellow areas, the addition of cholesterol can induce the gradual formation of L$_o$ phases.
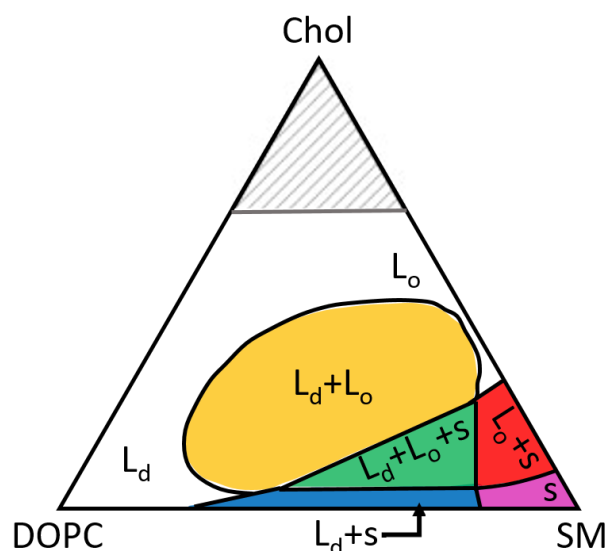
Figure 1.15 Phase diagram of ternary lipid mixture DOPC:SM:Chol at room temperature with rough estimated for the boundaries of one-, two-, and three-phase regions. Adapted and recreated from Biophys. J. 2013, 104 (7), 1456–1464.[210]

Using lipid models, a number of researchers have investigated the impact of lipid phases on the diffusivity of membrane components. Kahya et al. investigated the effect of cholesterol concentration on the formation different lipid phase domains in GUVs as shown in Figure 1.16 and used fluorescence correlation spectroscopy (FCS) to evaluate the spatial and dynamic organization of lipids in GUVs.[211] Heikal et al. used an integrated fluorescence-dynamic assay of monophasic, biphasic and ternary composition of GUVs to demonstrate the impact of L_d and S phases on the diffusivity of fluorescently labelled bodipy-cholesterol.[212] From FCS, the diffusion coefficient of cholesterol in monophasic lipid bilayers comprised of DOPC was 7.4 ± 0.3 $\mu m^2 s^{-1}$. SM containing lipid bilayers, on the other hand, had a diffusion coefficient of 0.35 $\mu m^2 s^{-1}$. This difference is due to the partitioning of cholesterol to more viscous ordered phases enriched with SM. Comparable findings were reported by Sezgin et al. when using DOPC/SM/Chol GUVs. The diffusion coefficient measured by FCS was 10 times greater for L_d (5 $\mu m^2 s^{-1}$) domains than for L_o domains (0.5 $\mu m^2 s^{-1}$), associated with the greater fluidity for L_d phases of GUVs.[213]
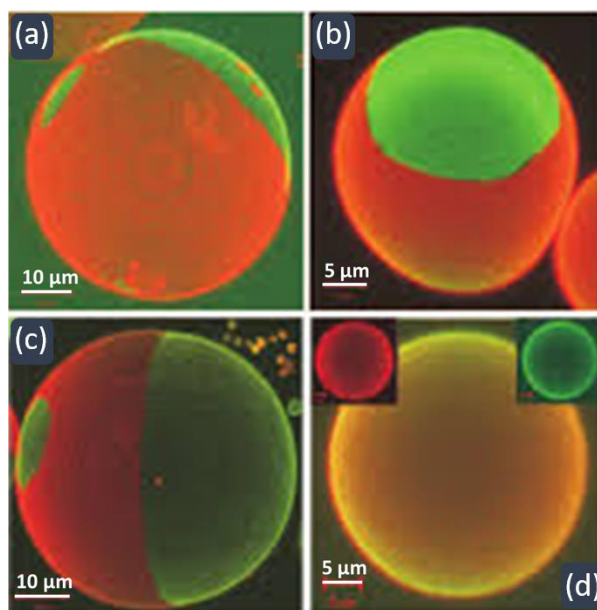
Figure 1.16 Confocal images of GUVs showing the phase separation from ternary mixture of DOPC:SM 0.5/0.5 with increasing concentrations of cholesterol at (a) 10 mol%, (b) 20 mol%, (c) 33 mol%, and (d) 50 mol%. The GUVs are labelled with Dil-C_{18} (red channel) which goes to DOPC enriched liquid disordered phase and AF-CTB (green channel). Upon increasing the concentration of cholesterol, the total green surface has increased. A homogeneous distribution of both green and red (L_o & L_d) regions are observed at increased cholesterol concentration of 50 mol% as shown in insets of (d). Figure reproduced from J. Biol. Chem. 2003, 278 (30), 28109–28115.[211]

SLBs have also been used to investigate the effect of lipid phases on particle/label diffusion coefficient. Woodward and Kelly, for example, used FCS to calculate the diffusion coefficient of lipid in the L_d and L_o phases on glass supported lipid bilayers. The diffusion of DPPE-TR was 4.9±0.2 $\mu m^2 s^{-1}$ in POPC (L_d) lipid bilayers and 2.5±0.8 $\mu m^2 s^{-1}$ for DiPhyPC (L_o) bilayers.[214] The addition of DiPhyPC and cholesterol to POPC caused the formation of L_d and L_o phases, which altered the diffusion of DPPE in L_d phase. The diffusion was faster for the L_d vs. L_o phases, although not significantly for the cholesterol-rich DiPhyPC:POPC:cholesterol (1:1:2) SLB; diffusivity was (1.6 ± 0.5)x faster for L_d vs. L_o phases in the 2:2:1 SLBs and (1.1 ± 0.4)x for the 1:1:2 SLBs. Their result was consistent in demonstrating a greater difference in diffusion between the L_d and L_o phases for a membrane that has less cholesterol and a longer tie-line, but notably the diffusion values at SLBs are notably slower and encompass narrower diffusion ranges than liposomes.

Along with domain formation, it has been proposed that membranes may rearrange the lipid membranes in such a manner that the special registration of domains at both leaflets is maintained. This interdigitation is thought to be involved in the organization of nanodomains

as well as signalling, protein co-localization, immunological reactions, and protein sorting into the membrane. Computation modelling using phenomenological free energies is typically used to study phase separation and co-localization. For example, Reigada and Sagués investigated the impact of carbon tails of saturated lipids on domain registration.[215] The lipid bilayers were made up of unsaturated DUPC, saturated DLPC or DSPC and cholesterol. They observed that bilayer containing short-tailed DLPC resulted in domain registration, whereas a bilayer containing long-tailed DSPC results in anti-registration. However, the diffusion of PC lipids in ordered phases was found to be higher in the anti-registration configuration, at 5.1 $\mu m^2 s^{-1}$, than in the registration configuration, 4.3 $\mu m^2 s^{-1}$. Lipid diffusion in L_d phases was 8.8 $\mu m^2 s^{-1}$ for DLPC and 8.1 $\mu m^2 s^{-1}$ for DSPC membranes.

Transmembrane asymmetry is a crucial physical feature of membranes that play a role in regulating cellular processes. Protein-protein, protein-lipid, and lipid-lipid interactions are all possible in the dynamic milieu of lipid membranes. To learn how proteins, lipids, drugs and other molecules like photosensitizers work in artificial lipid membranes, it is necessary to comprehend lateral asymmetry, lipid mobility, and factors influencing membrane fluidity.

1.6.2 Techniques used to measure the lateral diffusion of membrane constituents

The diffusion coefficient of lipid membrane has been experimentally investigated using a number of different methods, as it is an important variable in studies of membrane dynamics and organisation. Single Particle Tracking (SPT), Fluorescence Recovery After Photobleaching (FRAP), and Fluorescence Correlation Spectroscopy (FCS) are some of the key microscopy methods that have been used over the years to measure the diffusivity of membrane constituents.[216–219]

SPT tracks the movement and resting place of a fluorescent tracer molecule over time. A camera-based device captures images of the molecule and plots its motion over time. Gold nanoparticles[220] or single fluorophores are typical optical tags used in SPT.[221,222] Particle trajectories are used to derive the mean square movement of the particle. If the particles are moving randomly, the SPT analysis reflects the type of diffusion occurring and the diffusion parameters.[223,224] In instances where particles are used though the size of the particles may affect the molecule's mobility in unexpected ways.

FRAP is probably the most widely used method for probing the diffusional properties of molecules in lipid membranes; it involves photobleaching fluorophore labels (e.g., tagged to lipid) with an intense laser beam focused on a relatively large region of interest (up to several

μm^2). The recovery of fluorescence from the bleached area is monitored. As this recovery is caused by diffusion of unbleached molecules into the focal area it directly reflects the diffusion coefficient. If we know how long it takes for the fluorescence signature of dye molecules to recover, the diffusion coefficient can be estimated. Although extensively used, as it is a method available on most confocal microscopes, a key limitation is that a high concentration of fluorophore is required which may alter the properties of the membrane and the spatial area is very large and temporal resolution low.[225–228]

Lastly and used in this work, is the single molecule fluorescence techniques FCS/FLCS. The FCS/FLCS experimental method is explored in greater depth in section 1.13. It overcomes the above limitations and has been successfully used for biomembrane studies for the last two to three decades. By analysing the time-dependent variations in fluorescence intensity of fluorophores diffusing into a femtolitre volume, FCS/FLCS can reveal information about the diffusivity of fluorescent molecules. Local information (on the size of the confocal volume) about parameters such as the diffusion coefficient, particle concentration, flow rate, aggregates formations, and triplet lifetimes can be gleaned from the autocorrelation of the temporal intensity. Therefore, FCS can be used to clarify kinetics, medium viscosity, and other observations. In particular, pore-supported lipid bilayer can be interrogated without interference from the substrate thanks to the confocal volume of FCS/FLCS, usually radii of 300-380 nm (depending on the laser used), being smaller than the aperture of microcavities, which equate to approximately 2 μm. In addition, the spatial resolved FCS measurements can provides additional information of the sample deciphering the heterogeneity of membrane as well as other biomolecule's spatial organization.[229–235]

1.6.2.1 Comparison of diffusivity values using different methods

FCS/FLCS has a number of benefits that make it stand out when compared to SPT or FRAP. First, FCS/FLCS's femtolitre confocal volume allows for much higher spatial and temporal precision than SPT and FRAP. This is especially significant for the cavity supported membranes used here as the narrow dimensions of the interrogation volume permits the examination of individual pores outside of the restricted diffusion imposed by the rim-supported bilayer. FCS/FLCS can also be used to probe the local molecule content and kinetic data without causing any harm (photobleaching) to the fluorescent molecules.[236] When compared to FRAP, FCS/FLCS also requires a much lower quantity of fluorophores (typically nanomolar concentration).

Comparing methods, there may be variations in the diffusion coefficients measured due to length scale of their interrogation. Using FRAP and FCS, Guo et al. determined the diffusion coefficient of NBD-PE in POPC bilayers mounted on glass (Figure 1.17).[217] In FCS and FRAP, the diffusion coefficients for the labelled NBD-PE were 3.1 and 1.0 $\mu m^2 s^{-1}$, respectively. They note that the methods' different observational spheres could be to blame for the observed discrepancies in diffusion values. In contrast to FCS, which, as described, measures diffusion on a diffraction-limited field of about 400 nm, the region of interest in FRAP is on the order of 5-6 μm. For this reason, FRAP volume is more likely to encompass discontinuities, domains or other features that can cause a lower average apparent diffusion coefficient.[217]
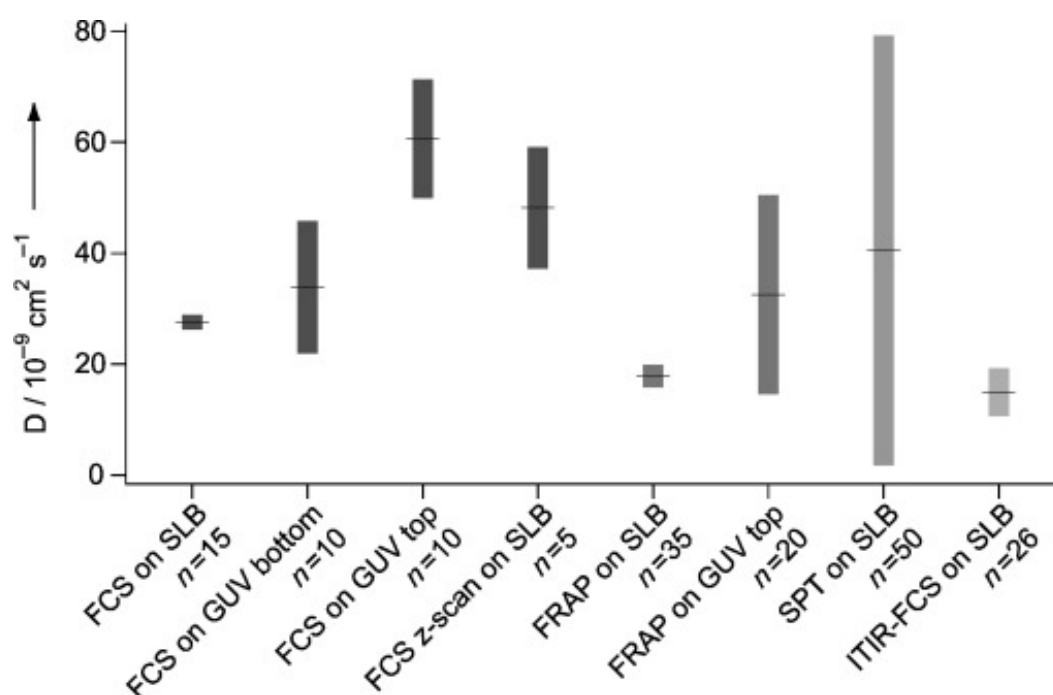
Figure 1.17 Comparison of the diffusion coefficients from SLBs and GUVs measured by FCS, FRAP, SPT, and ITIR–FCS. The number of measurements is given as n. Adapted from ChemPhysChem 2008, 9 (5), 721–728.[217]

One of the disadvantages of FCS and FLCS is that the procedure requires only a low concentration of fluorophores, and because of this, slower diffusing molecules may be more susceptible to photobleaching, depending on how photostable they are. In order for FCS/FLCS measurements to be successfully applied, sufficient mobility is a prerequisite.

1.7 Membrane Viscosity

In biological membranes, fluidity, stiffness, permeability and functionality are important and they are connected to each other with various biological effects.[237] Fluidity and viscosity have

specific meaning in physics: the viscosity is a dynamic property of matter and is defined as the skid resistance of two fluid layers between them, in a real system treated as a package of fluid layers superimposed (in slow linear motion), which can vary with temperature for the same molecules, while the fluidity is the opposite.[238]

Membrane viscosity reflects the ease of movement of a particle within the two-dimensional space of the cell membrane. The local viscosity directly affects the proper function of membrane proteins. Changes in membrane viscosity, or its reciprocal fluidity, is connected with disease states and they are useful indicators of cell viability.[239] Furthermore, increases in membrane viscosity have been reported with the onset of atherosclerosis, malignancy, diabetes, and hypercholesterolemia.[240] Conversely, an increase in membrane fluidity has been linked with amyloid precursor protein production in Alzheimer's patients.[241] In order to understand how some drugs influence membrane viscosity, alcohol and anaesthetics are considerable. Alcohol has viscosity reducing effect and some anaesthetics also decreases membrane viscosity at high concentrations by binding to the membrane.[239]

As discussed previously, fluorescence recovery after photobleaching (FRAP), fluorescence anisotropy, and fluorescence correlation spectroscopy can be used to monitor the fluidity of the membrane and associated dynamics of proteins or fluorophores by monitoring the diffusion of labelled species in the membrane.[242] Fluorescent molecular rotors, are a group of fluorophores can also be used to assess the viscosity of the membrane.[243] Molecular rotors belong to a group of fluorescent molecules, defined as twisted intermolecular charge transfer (TICT) complexes that have two de-excitation pathways.[244] A molecular rotor either assumes the twisted state with subsequent non-radiative de-excitation, or it emits a photon. Since TICT formation is hindered in environments of higher viscosity, the quantum yield increases.[245] Processes that require diffusion such as TTAUC, are also expected to be profoundly influenced by viscosity of the membrane.

1.8 Triplet-Triplet Annihilation Upconversion (TTA-UC) in Lipid Bilayer

There are relatively few studies to date of TTA-UC in liposome. Askes et al. have reported palladium tetraphenyltetrabenzoporphyrin and perylene as photosensitizer and annihilator that produce TTA-UC in liposomes. They used TTA-UC as a technique to activate photodissociation of a ruthenium complex in liposomes comprising of DMPC and DSPE-MPEG2000 lipids. Excitation of upconverting liposomes with a 630 nm laser triggered the

hydrolysis Ru-S bond using radiative energy transfer and this resulted in the release of the photoproduct.[93] Later they combined TTA-UC with Forster resonance energy transfer (FRET) for a photosubstitution reaction.[97] The imaging of giant unilamellar vesicles was achieved using red to blue upconversion light using the same palladium based photosensitizer and perylene annihilator and temperature dependence of TTA-UC was studied.[246,247] Additionally, they attempted to image A549 cell using red to blue upconversion under hypoxic conditions, but the less intense luminescence was a barrier for imaging .[248] The extent of tissue damage difference was compared with blue light, red light and red to blue upconverting light in real tissues and this study paved a path for TTA-UC mediated photoactivation of photochemotherapeutic drugs.[30]

1.9 Liposome Based Nanocarriers

Liposomes are colloidal particles whose aqueous-phase solubilized contents are encapsulated by a phospholipid bilayer membrane made of self-assembled amphiphilic molecules. Liposomes have been widely used and have tremendous potential as a nanocarriers for various biotechnology and pharmaceutical products because they can selectively target particular tissues and cells.[3,249–251] Typically, the liposomes are of fairly stable structures.[252] This is due to the fact that these systems are kinetically confined and not necessarily in a state of thermodynamic equilibrium.[251,253,254]
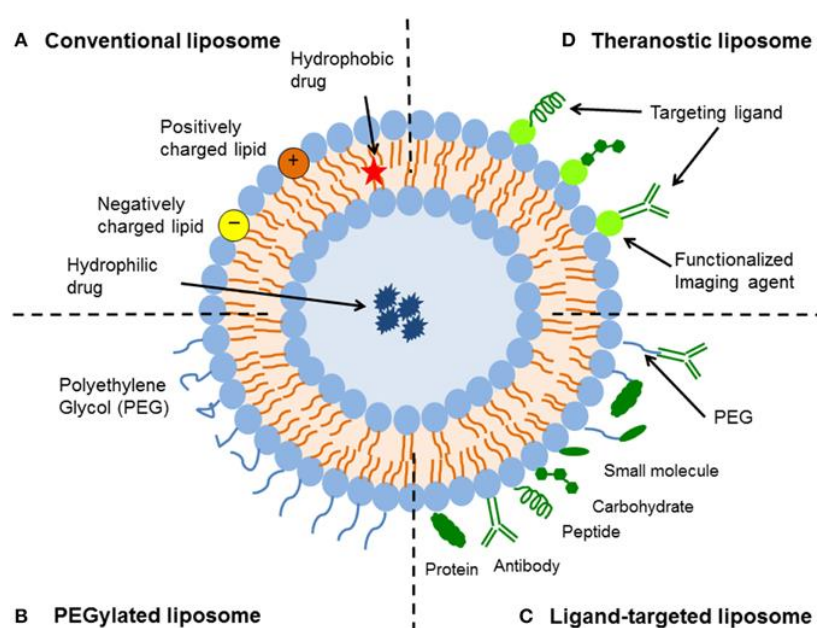
Figure 1.18 Schematic illustration of different types of liposomal drug delivery systems. (A) Conventional liposomes containing anionic/cationic lipids, (B) PEGylated liposomes, (C) ligand-

targeted liposomes, (D) theranostic liposomes containing targeting ligands and functionalized imaging agent. Adapted from Front. Pharmacol. 2015, 6.[255]

There are several types of liposomes in terms of interaction properties: conventional liposomes, which have nonspecific reactivity to the environment, sterically stabilised liposomes, which are relatively inert and thus nonreactive to the environment, immunoliposomes, and polymorphic liposomes, which are highly reactive to specific agents.[256–259] Cationic liposomes, for example, undergo structural changes when they engage with nucleic acids, while proton-sensitive liposomes become aggregated, destabilized, or fused at low pH.[260] These are types of liposomes that can respond to subtle environmental cues by altering the permeability, phase, or stability of their membranes. However, while the composition of liposomes has a smaller impact on their morphology, but a larger impact on functionality, their morphology is highly reliant on the preparation process.[261,262]

In drug delivery small (and medium-sized, 100-200 nm) unilamellar vesicles are typically used for systemic administration.[263] The quantity of encapsulated contents per mass of lipid is reduced, but the smaller size increases the blood circulation times, the volume of bio-distribution, and the possibility of extravasation through blood vessels. Therefore, the optimal size for different systemic applications may vary according to the target tissue.[264]

There are a number of manufacturing, physicochemical, and biological benefits unique to liposomes that set them apart from other delivery methods.[265] Biocompatibility, biodegradability, and minimal toxicity/immunogenicity are just a few of these.[266] A benefit of liposomes, from a physicochemical perspective, is that they reflect a kinetically trapped system and are therefore not in thermodynamic equilibrium. Liposomes and other kinetically trapped systems are not immediately impacted by a change in their environment, in contrast to thermodynamically stable systems. Dissimilar to micelles and microemulsions, which become unstable upon diluting to lower concentrations, liposomes remain stable. Unlike micelles and microemulsions, liposomes are able to maintain their original size and form, as well as their encapsulated contents under varying conditions.[249,267,268] Because of this outstanding properties of liposome, this nanocarriers platforms were used for TTA-UC based study. Furthermore, lipid bilayers provide a sturdy anchor for the binding of a wide range of functional molecules and ligands. Very cohesive bilayers, such as those made of DSPC and cholesterol, have mechanical properties that approach the Young modulus of van der Waals solids, such as polyethylene, when the small thickness of lipid membranes is taken into account.[269]

Liposomes' colloidal and molecular stability issues can be addressed through the addition of charged and primarily polymer-bearing lipids to the membrane, and for the latter, this is accomplished through the careful selection of lipids, the addition of antioxidants, the optimization of pH, and the addition of metal chelators.[270–272] For instance, saturated lipids with shorter and/or mixed hydrocarbon chains can replace unsaturated lipids to create fluid membranes free of the comparatively unstable double bonds.[273] Coating the surface of liposomes with inert hydrophilic polymers like polyethylene glycol and other glycolipids greatly enhanced their biological instability and their short circulation times in blood.[274]

Liposome encapsulation efficiency is often just as important as liposome stability in the context of bio-delivery uses.[275] Liposomes have the ability to concentrate molecules into their interior space in response to specific transmembrane gradients. These molecules include weak bases, potentially weak acids, and some permeable chelated metals. Precipitating the encapsulated drug can further improve its retention inside the liposome.[276] Liposomes can make surprising bonds with hydrophobic or electrostatic molecules during preparation. Dilution and protein interactions disrupt the liposome balance, releasing the drug/reporter molecule soon after injection. Liposomes can temporarily solubilize hydrophobically or electrostatically linked drug compounds. Liposomes change pharmacokinetics and bio-distribution, making stable encapsulated compounds easier to absorb by tissues and internalise by target cells.[277–279]

The section that follows explains in detail the experimental methods that have been used solely throughout this thesis. Although specific lipid-based membrane preparation and fluorescent-based imaging and spectroscopy are covered in separate chapters, the general methodologies and underlying theory are explained here to gain a better understanding before moving on to the actual examples.

1.10 Experimental methods and instrumentation

1.10.1 Langmuir-Blodgett method

The Langmuir-Blodgett technique, a method of layer by layer deposition on a solid substrate to form monolayer, bilayer or multilayers of amphiphilic molecules was discovered by Irving Langmuir and Katherine Blodgett.[280,281] It is a very well established method that has been widely used to create for diverse applications across physics, material science, biomembrane science and physical chemistry for fabrication of sensor device to liquid crystal display to lipid bilayer.[282] Water insoluble amphiphiles such as phospholipids and fatty acids produced

Langmuir monolayer at the air/water interface by decreasing its free energy, from which the LB films are transferred onto a solid support.
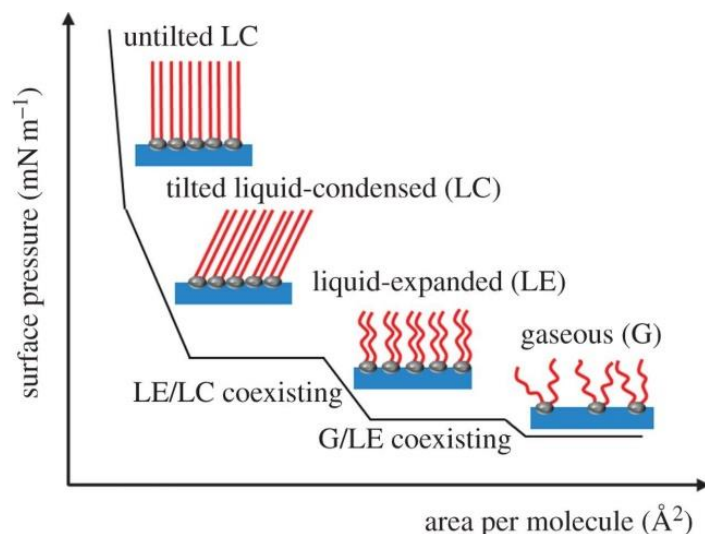
Figure 1.19 (a) Schematic representation of typical ∏-A isotherm with the phase changes associated during the compression of an amphiphile monolayer and organization of amphiphilic monolayers in different phases. Adapted from J. R. Soc. Interface 2017, 14 (130), 20161028.[283]

The phase behaviour of the LB isotherm is determined by the physical and chemical properties of the amphiphile, the subphase temperature and the subphase composition. The monolayers are in the gaseous state (G) at large molecular areas right before compression, and upon compression they go through a phase transition into the liquid-expanded state (LE). Upon further compression, the LE phase undergoes a transition to the liquid-condensed state (LC), and at even higher densities the monolayer finally enters the solid state (S). After reaching the S state, the monolayer will collapse into three-dimensional structures if it is further compressed, as shown in Figure 1.19. This behaviour is common for phospholipids and depending upon the nature of phospholipid, the isotherm and its associated phase can change. Often this phase change also dependent on external stimulant such as temperature, pH as well as in presence of additives in the subphase.[284,285]
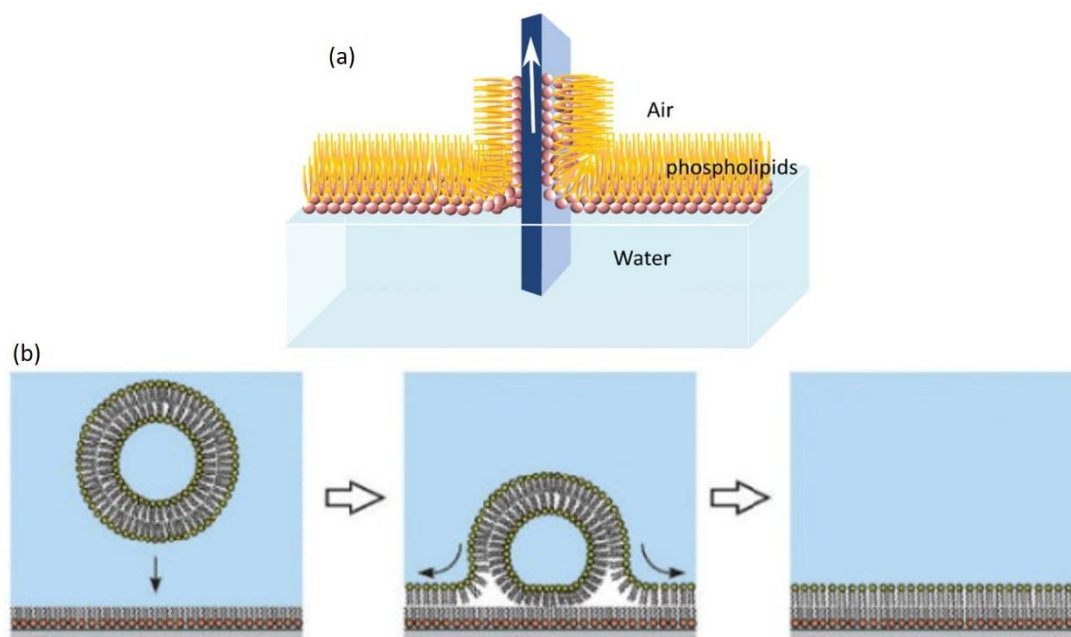
Figure 1.20 Schematic illustration of (a) lipid monolayer transfer using Langmuir-Blodgett technique followed by (b) vesicle fusion to form lipid bilayer. Adapted from Electrochem. Sci. Adv. 2021, 2 (2), e2100170 and Coatings 2020, 10 (10), 981.[286,287]

Typically, in this work a single component and/or mixed lipid compositions were sprayed dropwise on to the air/water interface of an LB trough (KSV NIMA L&LB system, KN 0002; Platinum Wilhelhmy plate: wetted perimeter, 39.24 mm, plate dimension W 19.62mm×H 10 mm) and at least two compression and two decompression cycles are performed within 0-35 mN/m range. By doing so, the monolayer is distributed over the entire water surface as a result, preventing any collapse that might otherwise result in the formation of multilayers. With the surface pressure held constant at 33 mN/m, the LB transfer was carried out by withdrawing the substrate at a rate of 5 mm/min. At this surface pressure, lipids are in liquid-condensed phase with higher packing, and they can successfully transfer on the solid substrate. A schematic illustration of lipid monolayer transfer followed by vesicle fusion is shown in Figure 1.20.

1.10.2 Time Correlated Single Photon Counting and Fluorescence Lifetime

Time correlated single photon counting method (TCSPC) used to determine the emission lifetime. The emission photons are detected one after the other using a single photon detector and a histogram is generated based on the number of events across all of these recorded points. The amount of time the molecule spends in the singlet excited state is directly related to this. Thousands of photons must be collected in order to provide statistically accurate information about the typical fluorescence lifetime of the excited state. A mono- or multi-exponential decay

can be used to describe the resulting histogram of photon arrival timings. The information about lifetime of individual components τ_i and their amplitude in sample A_i is obtained by fitting data to an exponential model using the expression, $I(t) = \sum A_i \, e^{-t/\tau_i}$, where $I(t)$ is fluorescence intensity profile i.e., histogram of photon arrival times.[288]
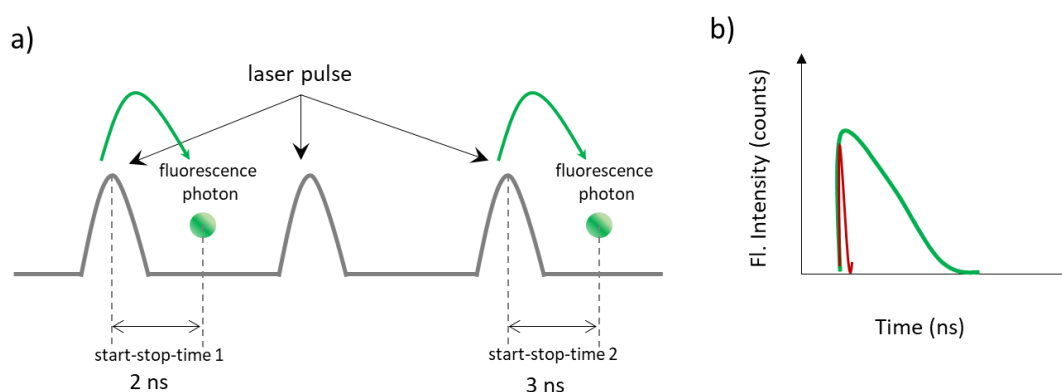
Figure 1.21 Schematic illustration showing an example of a) measurement of time intervals between the laser pulse and the detection of photon by TCSPC and b) photon arrival time histogram of a green fluorescent dye (green) and instrument response function, IRF (red). Adapted and recreated from PicoQuant.

In a TCSPC measurement, the measured fluorescence drop is the product of a convolution of an initial ''true'' decay and broadening in the order of tens or hundreds of picoseconds. This broadening, known as the Instrument Response Function (IRF), is caused by the electronics' constraints, particularly the non-zero temporal response of the detectors and the non-zero laser pulse width. Particularly for short decay times, IRF has an impact on the initial decay's shape. A scattering sample with no emission can be used to collect an IRF (e.g., ludox) and this IRF is deconvoluted mathematically from the decay. If the emission lifetime well exceeds the IRF, it is possible to determine lifetime by ignoring the early part of the emission decay and carrying out a tail-fitting approach .[289]

1.10.3 Fluorescence Lifetime Imaging Microscopy

Fluorescence Lifetime Imaging Microscopy (FLIM) can quantify fluorophores' excited state lifetimes for each pixel in a given image. Additional parameters such as location in an image region, wavelength (if additional spectral channels are recorded), and time from the commencement of an experiment are also recorded for each photon that is captured. A lifetime image can be created by capturing thousands of photons each pixel.[290]
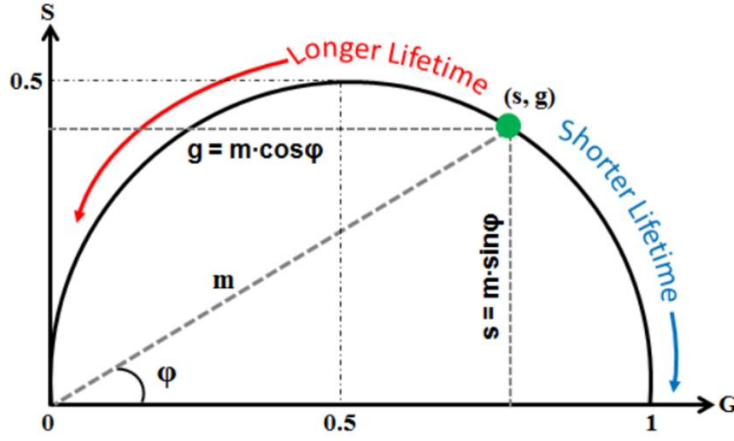
Figure 1.22 The phasor plot vector space and the universal circle. On the universal circle, a single decay component is represented by a point (s,g).

Typically, phasor plot analyses indicate the image's lifetime distribution and whether the image pixel intensity decays are mono- or multi-exponential. Fluorescence intensity profile $I(t)$ is created for each pixel based on the photons seen in time t. Then, phasor coordinates g and s are determined for every pixel [i, j] by using the equations x and y, at a laser repetition angular frequency (ω):

$$g_{i,j}(\omega) = \frac{\int_0^\infty I_{i,j}(t) \cos(\omega t) dt}{\int_0^\infty I_{i,j}(t) dt} \qquad (1.7)$$

$$s_{i,j}(\omega) = \frac{\int_0^\infty I_{i,j}(t) \sin(\omega t) dt}{\int_0^\infty I_{i,j}(t) dt} \qquad (1.8)$$

The phasor plot allows identification of single- or multi-exponential decay and selecting photons with a given lifetime distribution. Single-exponential decay appears on the universal circle with diameter 1 and centre [0.5, 0] in the g, s coordinates of the phasor plot. Inside the circle is multi-exponential decay. Experimental phasor plots are two-dimensional spectra with well-localized peaks. By selecting photons from around a phasor plot peak, we may set up a filter mask so that only molecules with certain decay characteristics of individual fluorophores and their surroundings. Local pH, temperature, and viscosity affect the fluorescence lifetime of several fluorophores, but generally concentration does not (unless it causes physicochemical changes such as aggregation or excimer formation). Hence, fluorophores can act as local environmental sensors. Fluorescence lifetime helps distinguishing between background noise

or autofluorescence and specific fluorescence signal based on differences between fluorescence decay profiles.[291]

1.10.4 Fluorescence Lifetime Correlation Spectroscopy (FLCS)

As a single-molecule approach FLCS studies the temporal fluctuations of fluorescence signals captured in a tiny observation area (typically 200-400 nm in diameter) or volume (typically femtolitres). Fluorophore translational and rotational diffusion, local concentration, binding constants, molecular weights or photodynamics among others can be obtained using FCS. It was not until 1972 that Madge, Elson and Webb came up with the concept of FCS. Initially, they applied FCS to assess the diffusion and chemical dynamic of DNA-ethidium bromide interaction in solution.[292] The combination of FCS with confocal microscopy has made the method highly versatile and extremely sensitivity as discussed by Rigler and his co-workers.[293–296]

FCS requires only nanomolar fluorophore concentration and interrogates only a very tiny volume (or area) (Figure 1.23a). Even at 1 nanomolar, there are 1011 particles per millilitre. Low concentration is essential, if more than a couple of molecules are excited in the interrogation volume at a time, there will be no fluctuation in the fluorescence intensity to measure with time (Figure 1.23b). A high numerical aperture objective focuses incoming laser light to a diffraction limited spot to achieve this. A confocal pinhole in the image plane blocks all off-focal-plane light, limiting the axial detection volume. Fluorescence intensity is multiplied by a time shifted replica (lag time, τ) for varying values. The temporal averages of these products are fair estimates of the autocorrelation function G(τ) (second order correlation function, ACF) for the respective lag time, τ (Figure 1.23c): The ACF in FCS is given by eq. (1.9).

$$G(\tau) = \frac{\langle F(t)\, F(t+\tau)\rangle}{\langle F(t)\rangle^2} \tag{1.9}$$

where $\langle \;\; \rangle$ represents the temporal average, $F(t)$ is the instantaneous fluorescence intensity at time t, and $F(t + \tau)$ is the intensity at time $t + \tau$.
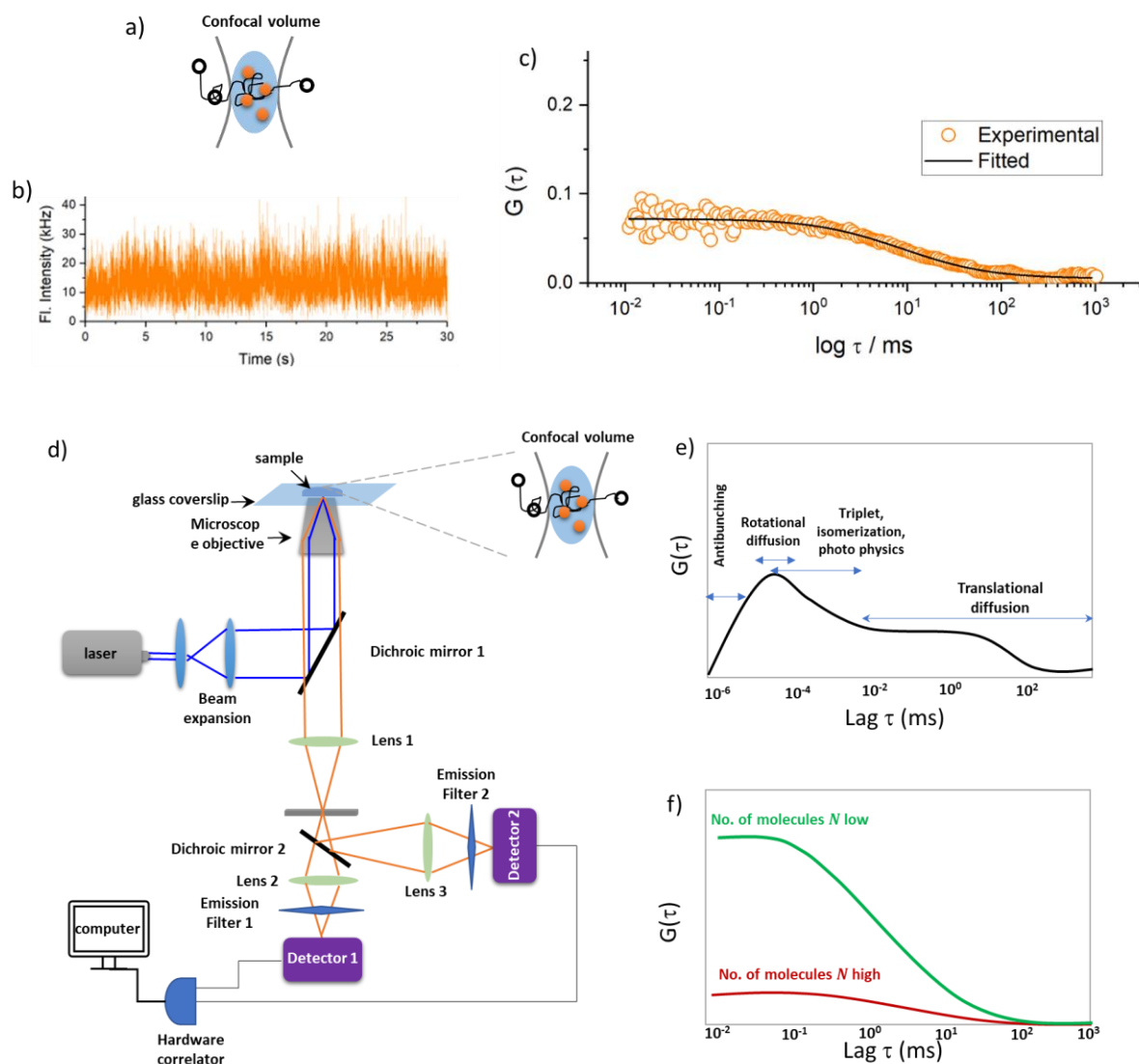
Figure 1.23 FCS measurement of fluorescent molecules in lipid bilayer membrane by FCS method. Fluorescent molecules moving in and out of the detection volume (a) is recorded as intensity versus time (b) to yield the autocorrelation function (c). The solid lines in panel c is the fit using 2D diffusion model equation 1.19. d) Illustrates the confocal FCS instrumentation setup. (e) A representative correlation curve of a fluorophore highlighting the processes occurring in different time scales. f) Represents how the ACF amplitude depends on the number of molecules (N): the sample with green ACF has lower number of particles than the sample with red ACF.[236]

The typical experimental set-up for FCS instrumentation is shown in Figure 1.23d. Autocorrelation reflects the likelihood of detecting a photon at time τ if one was detected at time zero. This probability has two different parts. A key term is correlated signal, which means that two photons from the same molecule are physically correlated. This reflects FCS's single molecule nature. The other term includes contributions from uncorrelated signals, i.e., the two

detected photons came from distinct fluorescent molecules or backscattered laser light and have no physical correlation. Uncorrelated events will contribute to a constant G(τ) offset that is independent of the time, τ. Each component of the ACF curve shows distinct processes based on their timescale (Figure 1.23e). Fluorophores blinking due to triplet transitions in μs can be an interference in FCS but as their diffusion through a diffraction-limited volume takes tens of μs the diffusion can be discriminated. A diffusing fluorophore in solution that shows triplet transitions would have two decays, one for blinking and one for molecule mobility. Antibunching and rotational diffusion also affect fluorescence. There is a correlation between the ACF's shape and its function. Hyperbolic decay and exponential decay are two examples of ACF shapes that can be found in diffusion and active transport processes, respectively. The calculated ACF can be fitted with theoretical models to estimate the various underlying physical parameters of the studied system.[297]

In terms of the fluctuation in fluorescence intensity $\delta F(t)$, the above eq. (1.9) can be rewritten as:

$$\delta F(t) = F(t) - \langle F(t) \rangle \qquad (1.10)$$

As mentioned above, for a stationary phase, the fluorescence intensity average over a time period t and do not change over $t + \tau$. Upon substitution of eq. (1.10) in eq. (1.9), one obtains,

$$G(\tau) = \frac{\langle (\delta F(t) + \langle F(t) \rangle)(\delta F(t+\tau) + \langle F(t) \rangle) \rangle}{\langle F(t) \rangle^2} \qquad (1.11)$$

In the numerator out of the four product terms, two are time average fluctuations in fluorescence intensity and hence are both zero. Hence, eq. (1.11) can be written as:

$$G(\tau) = \frac{\langle \delta F(t) \, \delta F(t+\tau) \rangle}{\langle F(t) \rangle^2} \qquad (1.12)$$

Despite a fixed bulk sample concentration, the number of fluorescence molecules randomly enter and exit the tiny observation volume, causing fluctuations in fluorescence intensity. Typically, freely diffusing molecules follow a Poisson distribution in the observation volume. At zero lag time, eq (1.12) shows,

$$G(0) = \frac{\langle \delta^2 F(t) \rangle}{\langle F(t) \rangle^2} \qquad (1.13)$$

There is a direct relationship between the fluorescence intensity and the number of particles in the confocal volume (N). In other words, it can be written as:

$$G(0) = \frac{\langle \delta N^2 \rangle}{\langle N \rangle^2} \qquad (1.14)$$

where $\langle \delta N^2 \rangle$ is the average square of particle fluctuation. In Poisson variables, the mean equals the variance, hence this is the mean number of particles. So, eq. (1.14) can become:

$$G(0) = \frac{1}{\langle N \rangle} \qquad (1.15)$$

The above eq. (2.12) indicates that the amplitude of the ACF is inversely proportional to the N i.e., number of fluorescent molecules (as reflected in Figure 1.23f). In this study, analytical formalism is shown for translational diffusion, the most commonly researched diffusion phenomena in soft mater and biomembrane studies using FCS. Furthermore, the FCS in lifetime modality (FLCS) will also be discussed briefly. In the case of three-dimensional diffusion (3D), the theoretical ACF model can be defined as:

$$G_{3D}(\tau) = \frac{1}{N}\left(1 + \frac{\tau}{\tau_D}\right)^{-1}\left(1 + \frac{\tau}{\kappa^2 \tau_D}\right)^{-1/2} \qquad (1.16)$$

Where τ_D is the transit time or the average diffusion time that takes to enter and exit from the confocal observation volume, κ (kappa) is the structure factor which is the ratio of the $1/e^2$ radius of the observation volume in the axial (z_0) and lateral (ω_0) directions. Upon fitting the ACF curve, one can obtain N and τ_D. After knowing the τ_D, the diffusion coefficient (D) can be determined by using the equation (1.17).

$$D = \frac{r_0^2}{4\tau_D} \qquad (1.17)$$

where r_0 is the lateral diameter of the confocal beam at $1/e^2$ of 0.135, and obtained by calibrating the microscope system with a fluorophore of known diffusion coefficient value diffusing freely in aqueous solution.

Fluorophores diffusing translationally in a two-dimensional (2D) plane e.g., at model bilayer membrane, the ACF can be theoretically fitted using eq. (1.18).

$$G_{2D}(\tau) = \frac{1}{N}\left[1 + \frac{f_T}{1-f_T}e^{-t/\tau_T}\right]\sum_{i=1}^{m}\left(1 + \left(\frac{\tau}{\tau_{Di}}\right)^{\alpha}\right)^{-1} \tag{1.18}$$

where f_T and τ_T are the fractions and the decay time of the triplet state respectively, τ_{Di} is the transit time of the ith diffusing molecules, and α is anomaly coefficient typically indicates when the diffusion is Brownian ($\alpha=1$) or not ($\alpha\neq1$). A representative fit using eq. (1.18) is shown in solid lines in Figure 1.23c. When there is no contribution from the triplet state, the above equation (1.18) can be simplified into the following expression.

$$G_{2D}(\tau) = \frac{1}{N}\sum_{i=1}^{m}\left(1 + \left(\frac{\tau}{\tau_{Di}}\right)^{\alpha}\right)^{-1} \tag{1.19}$$

As a variant of fluorescence correlation spectroscopy (FCS), fluorescence life time correlation spectroscopy (FLCS) employs differences in fluorescence decay rates to obtain autocorrelation functions (ACFs) of distinct fluorophore populations in a mixture. In FLCS, during ACF calculation, each photon is weighted with a statistical filter function. The arrival time of the photon must be known on two different time scales in order to use the fluorescence lifetime information in FCS: (1) the lifetime-scale (with picosecond resolution), which measures the time between the photon arrival and the appropriate excitation pulse; and (2) the FCS-scale (at least microsecond resolution), which measures the time between the photon arrival and the start of the experiment. As a result, the list of photon records with two timing figures is the main FLCS data output. By using TCSPC, the photons are often detected. The lifetime-scale arrival time is indicated in units of TCSPC channel number j. The resolution of the lifetime-scale, for instance, is 50 ps when a 50 ns gap exists between two successive excitation pulses and is digitized into 1000 channels. The timing t on the FCS-scale is commonly expressed in terms of excitation cycles; for instance, the resolution is 1/20 MHz = 50 ns for a 20 MHz excitation repetition rate.[298]

Using FLCS, one can purify parasitic contribution from conventional FCS data such as dark counts and afterpulsing of the detector or photons of elastic and Raman scattering. Useful applications such as quick and easy removal of the distorting effect of detector afterpulsing, can be achieved using FLCS. Other advantages of using FLCS is the ability to acquire ACFs for fluorophores in varied environments or molecular states (e.g., conformational or protonation states).[233] A representative example of conventional FCS and FLCS data obtained from a DOPC lipid bilayer is shown in Figure 1.23.[235]
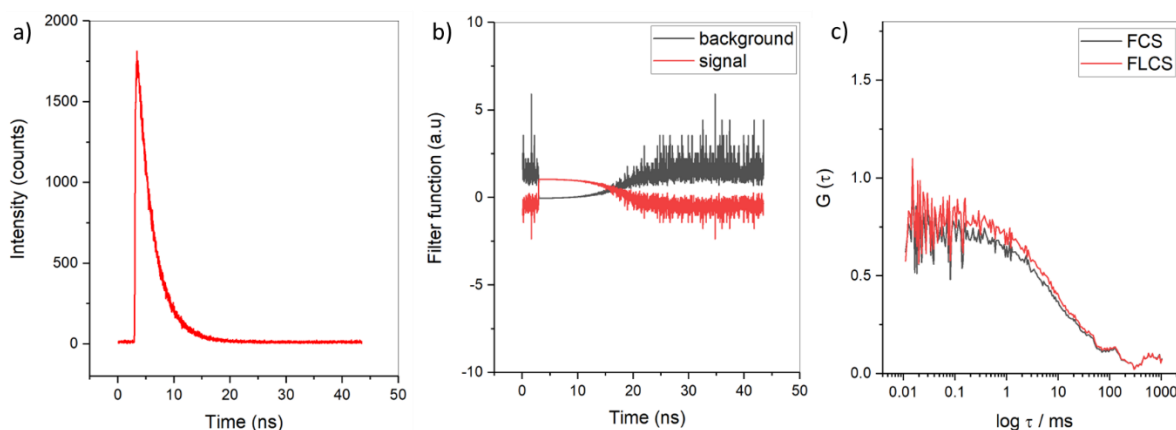
Figure 1.24 FLCS is used to remove background related artefacts from ACF. a) A histogram of photon detection periods (each channel corresponds to 16 ps); equally distributed background induced by detector afterpulsing, thermal noise, or stray light photons adds over 100 counts to each channel. b) FLCS filters for the fluorescence signal (red) and the uniform background (black). c) ACF estimated without (black) and with FLCS filtering (blue); the decay in μs time scale is produced by detector afterpulsing, whereas the decrease in autocorrelation amplitude is driven by uncorrelated background (thermal noise, stray light). The results were collected in our laboratory in a supported lipid bilayer on glass that contained fluorescently labelled lipid (DOPE-ATTO655, 0.01 mol%) as a diffusion tracer. The bilayer was prepared by using LB-VF method where the labelled lipid was doped in the outer leaflet during the vesicle fusion process.

1.11 Conclusions and scope of the thesis

Triplet-triplet annihilation upconversion (TTA-UC) is a photophysical process where higher energy photons are produced from low energy photons. Triplet photosensitizers which acts as donor molecules in TTA-UC should have desirable photophysical properties to qualify as a triplet photosensitizer. BODIPY molecules are a useful prospect as photosensitizers, with excellent photostability and photophysical properties. While their triplet yields are low they can be functionalised in to promote ISC through spin-orbital coupling and/or heavy atom substitution to improve their prospects as photosensitizer for TTA-UC. Liposomal inclusion of functional TTA-UC machinery can pave a path for various biological applications translation of the machinery to membrane or as a mechanism for red excited drug delivery.

Biophysical models of cell membranes are a useful way to understand at a simple level the unit functions of the complex cell membrane and they are also an excellent way to understand membrane function generally. In this chapter different types of cell membrane models including LUV, GUV, SLB, and pore suspended bilayer are overviewed. The interaction of

embedded molecules within the lipid bilayer of the membrane and their dynamics can be investigated by making use of a number of photophysical and biophysical techniques including basic fluorescence spectroscopy to single molecule detection techniques like FLCS.

In this thesis, the TTA-UC mechanism and fundamental process has been covered in detail. TTA-UC in solution was initially realized using some newly synthesized BODIPY-based and Ru-based photosensitizers and the study is extended to liposomal model membranes. The steady state photophysical properties like absorption, emission and lifetime of the photosensitizers were evaluated and TTA-UC was demonstrated in solution with suitable annihilator. The influence of different physico-chemical properties of the lipids on the efficiency of TTA-UC was also evaluated. Further studies on the effect of enzyme catalysed membrane hydrolysis on TTA-UC was investigated. The lateral diffusion of the photosensitizer within the membrane was measured by FLCS at a highly fluidic, and stable MSLB platform, as the efficiency of TTA-UC highly depends on the photosensitizer's collisional frequency. The MSLB platform was validated by studying the interaction of biomembrane with small molecule drugs and photosensitizers.

Chapter 2

BODIPY Charge Transfer Dyad Sensitized Triplet-Triplet Annihilation Upconversion in Solution and Model Membranes

2.1 Introduction

Triplet-triplet annihilation upconversion (TTA-UC) is an anti-Stokes photophysical process in which two low energy photons combine leading to emission of a high energy photon.[5,20,72] The process has come into focus in recent years because of its capacity to overcome limitations in UV and visible light penetrability of tissue. TTA-UC, in theory, can enable local generation of high energy photons inside biological tissues; hence it can initiate a variety of useful processes through highly penetrative red or NIR excitation, and unlike other upconversion processes, it can be initiated using relatively low intensity and incoherent excitation light. TTA-UC is thus muted for application in biological imaging, sensing, photoinduced drug release, and non-biological applications such as photocatalysis, photovoltaics, and photoswitching, as well as organic synthesis.[299–301]

In conventional TTA-UC systems, the photosensitizer and the acceptor/annihilator are the two central molecular components. First, when the photosensitizer molecule absorbs a low energy photon, it is excited to the first excited singlet state ($^1S^*$) (cf. Figure 2.1a). It then undergoes intersystem crossing (ISC) forming the first excited triplet state ($^3S^*$). From the triplet state, the triplet excitons give away its energy to the annihilators or acceptors via intermolecular Dexter-type triplet-triplet energy transfer (TTET). Dexter energy transfer is the mechanism by which electrons are transferred symmetrically between two molecules (intermolecularly) or between two subunits of a molecule (intramolecularly). In contrast to the sixth-power reliance of Förster energy transfer, the reaction rate constant of Dexter energy transfer exponentially decreases with increasing distance. The exchange mechanism usually takes place within 10 Angstroms because the distance has an exponential relationship to the rate of exchange. Consequently, the process of exchange is also known as the short-range transfer of energy. To a large extent, collisions can cause donor and acceptor to collide into each other if they are distinct molecules. The collisional diameter is almost equal to the small distance responsible for energy transmission.[302,303] For this reason, the word "collision" is always used to describe the process of energy transmission between objects. Two annihilator molecule generated in this way, in the triplet state ($^3A^*$) on mutual collision undergo bimolecular TTA, forming singlet excitons of higher energy which emit fluorescence anti-Stokes to the excitation light (Figure 2.1a).[304,305] TTA is an important case of exchange energy transfer in which two triplet chemical groups, react to create two singlet states. In most cases, the difference in energy level between S_0 and T_1 is larger than that between T_1 and S_1 (Figure 2.1b). Accordingly, fluorescence can occur in this system if two molecules in the triplet excited state collide, as this process may

have enough energy to stimulate one of the molecules to the higher singlet states. Following annihilation, the electron will have an energy level that is twice as great as the difference between the lowest possible triplet energies. After TTA process, the molecule which lost its energy is relaxed to the ground state and the other annihilator molecule forms an excited singlet state (^{1}A*). The energy of ^{1}A* is greater than the energy of ^{1}S* and hence when the annihilator molecule goes to the ground state, it emits photons of higher energy photons than that absorbed by the photosensitizer. This delayed fluorescence with higher energy emission is coined as TTA-UC.

Because it controls photon harvesting, ISC, and TTET to the acceptors/annihilators, a highly proficient triplet photosensitizer is critical for achieving high efficiency in TTA-UC. Another critical objective in TTA-UC is to optimise the efficiency of the contributing TTA and UC processes by ensuring maximum quantum efficiency of the underlying elementary photophysical steps whilst minimizing competing paths, as shown schematically in Figure 2.1a.[13,40,306,307]
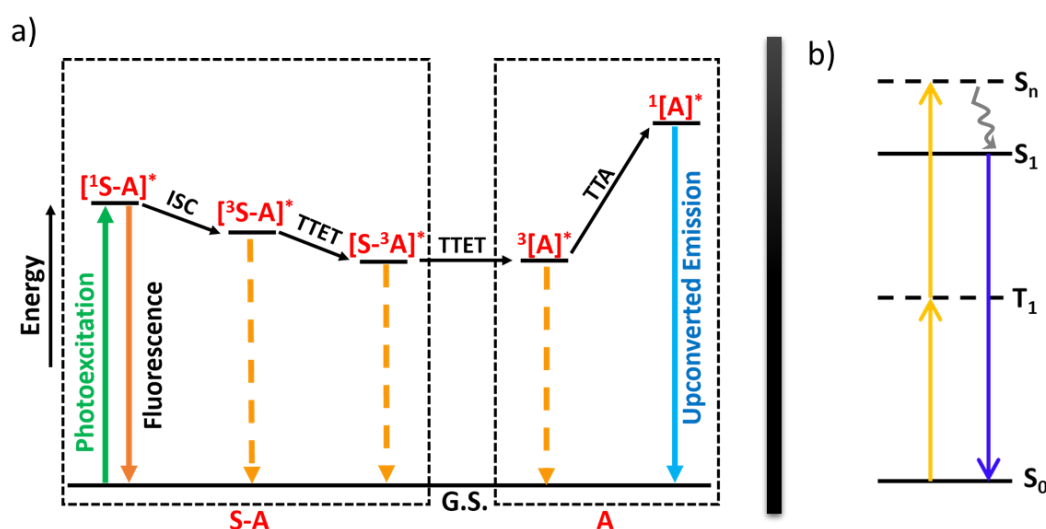
Figure 2.1 a) Jablonski diagram of TTA-UC mechanism. b) Schematic diagram for triplet-triplet annihilation.

Furthermore, it is also important to tune the absorption and emission wavelengths of photosensitizer and annihilator to match for efficient TTA-UC. From the perspective of the triplet photosensitizer, it should ideally have high extinction coefficient, a high quantum yield of intersystem crossing Φ_{ISC}, and a long-lived triplet excited state.[308] This is because the ISC occurs in the same time scale as fluorescence, which is on the order of several nanoseconds. An electron would fluoresce before entering a triplet state via thermal relaxation, but in general

fluorescence occurs quicker than the intersystem crossing. To ensure that TTA-UC is thermodynamically feasible, especially for upward TTA step, the relative energetics of photosensitizer and annihilator singlet (S_1) and triplet (T_1) states are critical, which depends on with the energy gap between the singlet state ($E(S_1)$) and twice that of the triplet state ($2 \times E(T_1)$), i.e., $\Delta E_{TTA} = 2 \times E(T_1) - E(S_1)$ for efficient annihilation process. Metal complex luminophores have been widely studied as photosensitizers, due to their efficient intersystem crossing, promoted by spin orbit coupling caused by the heavy metal ion.[7,27,309,310] However, there are advantages to using metal-free photosensitizer systems, and a useful way to emulate the impact of the metal on ISC efficiency is either by introducing a heavy non-metal element into the system or by implementing charge transfer states.[311,312] 4,4-Difluoro-4-bora-3a,4a-diaza-s-indacene (BODIPY) has been evaluated in a number of TTA-UC systems as a metal free photosensitizer.[313,314] It possesses excellent photophysical properties including high molecular brightness. It is also a versatile structure that can be readily modified to tune its photophysical properties. While BODIPY does not exhibit efficient intersystem crossing (ISC), introduction of heavy atoms, iodo derivatives of -BODIPYs have been shown to efficiently form triplet state and undergo TTA-UC with appropriate annihilators.[77,315] Conversely, Wang et al. reported a higher lifetime for heavy atom-free BODIPY-perylene dyad (436 µs) than conventional iodinated BODIPY photosensitizers (62 µs). In such heavy atom-free photosensitizers, the intersystem crossing is happening because of spin-orbit charge transfer intersystem crossing (SOCT-ISC) and hence they also can be used as effective triplet photosensitizers.[86]

Hydrophobic BODIPY derivatives, which are widely used as contrast dyes in cell imaging, have been frequently studied in liposomes for imaging administration or as membrane labels as they are lipophilic and tend to accumulate in membrane or lipid droplet structures in live cells.[316,317] They can also be synthetically tuned for labelling different membrane phases and they have been widely used as probes for biophysical studies on giant unilamellar vesicles (GUVs) structures.[316,318,319] Despite their propensity for membrane labelling, they have not to date been studied as photosensitizers for TTA-UC within lipid membrane environments, despite inclusion in nanoparticle hosted TTA-UC systems.[320,321] Inclusion in liposomes or micelles offers an approach for delivering TTA-UC components for imaging, or it can be used directly for imaging of liposomes or cell membranes. Bonnet et al. for example, reported TTA-UC as a means of imaging the membranes of giant unilamellar vesicles comprised of DOPC or DMPC using palladium tetraphenyltetrabenzoporphyrin as photosensitizer and perylene as

annihilator.[246] Their findings demonstrated one of the early findings on the significant potential of TTA-UC for imaging uses under anoxic conditions, paving the way for cell membrane imaging with upconverted light. Bonnet et al.'s study above shows that upconverting light can be used to successfully image GUVs, but they don't explain how the excited state properties of the photosensitizer and annihilator in solution change when they are incorporated into model membranes, and how other membrane physicochemical properties, such as the role of lipid head group charge, systematic variation of fluidity, and its partition into phase separated lipid compositions, are affected. In the chemotherapeutic window (600-900 nm), photoactivatable chemotherapeutic agents are used, and understanding the efficient TTA-UC in cell-free model membranes and the interplay function of membrane biophysical properties will aid in formulating liposome-based drug delivery to target sites.

Liposomes along with lipid nanoparticles are commonly used drug delivery systems with properties including excellent biocompatibility and safety, protection of the encapsulated substances from physiological degradation[322], increased drug half-life, and regulation of drug molecule release[323]. In addition, liposomes can passively or actively target the diseased site to selectively transport their payload, reducing the systemic side-effect, increasing the maximum-tolerated dose, and maximising therapeutic benefits.[324,325] While cancer treatment takes up the bulk of this field's attention, drug delivery also encompasses fields like infection, anesthesia, vaccine, lung disease, and photodynamic therapy.[249,326–333] Chorilli et al. for example, have studied phthalocyanine-loaded nanostructured lipid carriers functionalized with folic acid for photodynamic therapy.[334] Recently, Oshiro Junior et al. created nanostructured lipid carriers (NLCs) using a combination of thermoresponsive and cationic quaternary ammonium surfactants like pluronic F-127 (PF-127-FA) and cetrimonium bromide (CTAB), functionalized with folic acid, to target breast cancer cells.[335] These studies are demonstrated as alternatives to radiotherapy, chemotherapy, and/or surgery aimed at eliminating the tumour and, as a result, improving the patient's life quality. The utility of TTA-UC in liposomal membrane comprised of phospholipids-as the main building blocks of plasma membrane, is critical for better understanding the aftermath liposome-based drug delivery and, in particular, visualising the target sites without any toxicity effect. Prior to visualising the targeted sites and liposome-based drug delivery, it is critical to understand the reconstitution of TTA-UC pair within liposome, its stability, and providing a means to improve TTA-UC efficacy, and this chapter revolves around these aspects and provides extensive molecular detail for optimising

TTA-UC using metal free photosensitizer which was specifically designed and synthesized in our laboratory and a known conventional annihilator.[336]

Since lipid environments are typically more viscous than most organic solvents, the photosensitizer and annihilator used in reconstituting TTA-UC in liposomal membranes must have long-lived triplet state lifetimes (μs to several ms) while also diffusing freely to promote TTET and TTA yields.[337] Furthermore, as stated earlier, the Φ_{ISC} of the photosensitizer should be high as they have to produce a large number of triplets. Even though the BODIPY-perylene donor-acceptor dyad is lipophilic in nature, doping of the compound into the membrane is limited to μM concentrations as the excess concentration may either precipitate in the buffer media as they are insoluble in water or the elevated concentration of dyad can often change the intrinsic biophysical properties of the membrane. In addition, at the same time, the photosensitizer and acceptor molecules need to have high absorption (extinction) coefficient to yield efficient TTA-UC with low dyad concentrations in the biomembrane. Indeed, because BODIPY-perylene dyads have long triplet state lifetime, high extinction coefficient,[313] lipophilicity,[314,338] they are suitable for incorporation into membranes as photosensitizers for upconversion studies and thus can be used to investigate TTA-UC.

In the present study, a new TTA-UC system is established based on BODIPY photosensitizers, with and without iodine substitution in solution with annihilator, perylene, then transferred this TTA-UC to liposome. The impact of the membrane composition was then investigated, looking at membranes of varying fluidity, lipid's head group charge, and phase separated membrane on the presence and efficiency of TTA-UC. The chemical structures of the photosensitizers and annihilator are given in Figure 2.2. Additionally, the excited state properties of the photosensitizer and annihilator in the membrane have also been investigated and compared with that in solution. To better understand the photophysical behaviour of the photosensitizer in the lipid environment as a function of viscosity, specifically its lateral diffusivity, the diffusion behaviour of the BODIPY in a two-dimensional model lipid membrane was investigated. Our results showed on iodination of the BODIPY-perylene dyad, heavy atom improves ISC efficiency in solution and membranes, boosting TTA-UC efficiency.
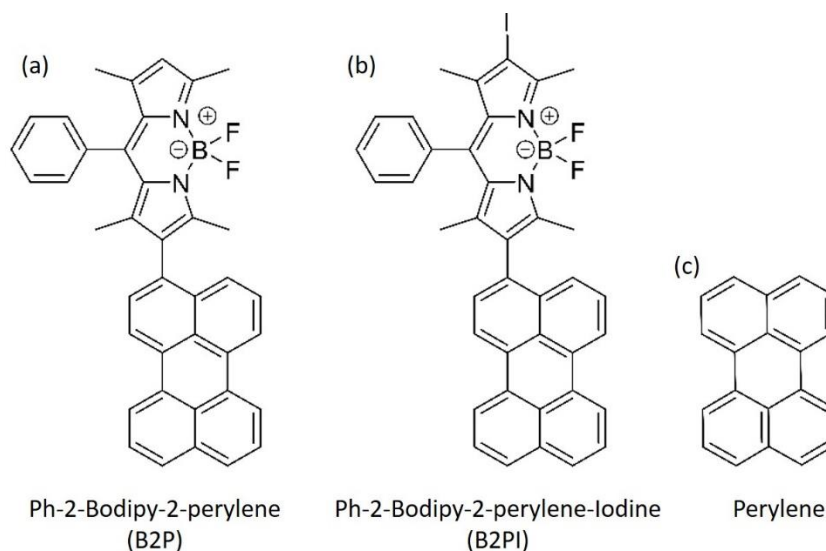
Figure 2.2 Chemical structure of a) Ph-2-perylene (B2P), b) Ph-2-perylene-iodine (B2PI), and c) perylene. Molecules (a) and (b) are synthesized by Ruben Arturo Arellano Reyes (DCU).

2.2 Aims and objective

TTA-UC provides exciting prospects for medical applications such as photoactivatable drug delivery and biological imaging because it does not necessitate high energy or coherent excitation sources, unlike other UC phenomena. However, because of the thermodynamic demands of the process it requires careful tuning of photosensitizer optical properties to optimise process efficiency. Designing effective organic photosensitizers for TTA-UC is difficult because of the need for a triplet multiplicity of reactants. BODIPY derivatives, due to their attractive tuneable photophysical characteristics and versatile, synthetic chemistry are proving useful as TTA-UC sensitizers. BODIPY-based photosensitizers have been used fairly widely as metal free photosensitizers for TTA-UC process in solution.

This chapter aims to compare two BODIPY-perylene based photosensitizers in terms of their efficiency towards TTA-UC and then to evaluate their ability toward TTA-UC in both solution and liposomal biomembrane when combined with annihilator, perylene. The first photosensitizer is functionalised with a heavy Iodine atom (B2PI), to promote intersystem crossing (ISC) through spin orbit coupling, and the second molecule is a heavy-atom-free photosensitizer (B2P). Intense oxygen sensitive upconversion emission from B2PI-perylene and B2P-perylene dyad further needs to be supported by threshold power density (I_{th}) measurements which indicates the efficiency towards TTA-UC for each photosensitizer. The presence of an iodine atom on BODIPY-moiety may promote spin-orbital charge transfer intersystem crossing (SOCT-ISC) and provided higher triplet yield. The triplet lifetimes of the

photosensitizers will be examined in dioxane using nanosecond transient absorption spectroscopy.

The lipophilic character of the photosensitizers makes them suitable for liposomal encapsulation using large unilamellar vesicles (LUVs) and giant unilamellar vesicles (GUVs) as cell-free biomimetic model membranes. The comparison of intense oxygen sensitive upconverted emission would be possible for B2PI and B2P with the annihilator under green excitation in both DOPC liposomal (LUV and GUV) models. The bio-delivery of the TTA-UC system will further be investigated at LUVs of varied membrane compositions ranging from different alkyl chain length to different melting transition temperature single component lipids to more complex phase separated membrane composition. This chapter also aims to investigate how TTA-UC intensity correlates with membrane fluidity/viscosity and this would explain in liposomal system, as it is a bimolecular process, whether the collisional frequency of the TTA-UC components is the driving efficiency of the TTA-UC process.

Furthermore, both conjugates will be evaluated towards their suitability for confocal based fluorescence imaging and for their selectivity towards different phases of GUVs. In a pore-suspended biomembrane, which is amenable for fluorescence lifetime imaging and lifetime correlation spectroscopy, the translational diffusion of the photosensitizer will be examined. Overall, this study investigates the choice of TTA-UC pair and its optimal TTA-UC efficiencies within the biomembrane that can be tuned by altering the fluidity of the membrane which may have important implications for TTA-UC triggered liposomal bio-delivery.

2.3 Materials and Methods

2.3.1 Materials

Ph-2-BODIPY-2-Perylene (B2P) and Ph-2-BODIPY-Perylene-Iodine (B2PI) were synthesized by following the procedure reported earlier by Reyes et al.[336] 1,2-Dioleoyl-sn-glycero-3-phosphocholine (DOPC) [purity (>99%)], 1,2-dimyristoyl-sn-glycero-3-phosphocholine (DMPC), 1-palmitoyl-2-oleoyl-glycero-3-phosphocholine (POPC), 1,2-dilauroyl-sn-glycero-3-phosphocholine (DLPC), 1,2-dipalmitoyl-sn-glycero-3-phosphocholine (DPPC), 1,2-dioleoyl-sn-glycero-3-phospho-L-serine (DOPS), 1,2-dioleoyl-3-trimethylammonium-propane (DOTAP), L-α-phosphatidylcholine (Egg PC), and Sphingomyelin (Brain, Porcine) were purchased from Avanti Polar Lipids (Alabama, USA) and used without further purification. 1,2-Dioleoyl-sn-glycero3-phosphoethanolamine-labeled ATTO655 (DOPE-ATTO655) was purchased from ATTO-TEC GmbH (Siegen, Germany). Perylene, sodium

sulfite, cholesterol, D-(+)-Glucose, sucrose, agarose, 1,4-dioxane, chloroform and phosphate buffer saline (PBS) tablets were purchased from Sigma-Aldrich (Wicklow, Ireland). Aqueous solutions were prepared using Milli-Q water (Millipore Corp., Bedford, USA). The polydimethylsiloxane (PDMS) silicon elastomer was purchased from Dow Corning GmbH (Wiesbaden, Germany) and mixed following supplier instructions. Monodisperse polystyrene (PS) latex sphere with a diameter of 4.61±0.4 μm was obtained from Bangs Laboratories Inc. (Fishers, IN, USA).

2.3.2 Photophysical Steady State Studies

Electronic spectra were acquired on a Jasco V670 UV/vis NIR spectrophotometer using a quartz cuvette with 1 cm pathlength. Fluorescence spectra were collected on a Varian Cary Eclipse Fluorescence Spectrophotometer. All photophysical measurements were performed at room temperature (293 K).

2.3.3 Photophysical Time Resolved Studies

Luminescent lifetime data were acquired up to 10000 counts using a Time Correlated Single Photon Counting (TCSPC) system by PicoQuant with a laser excitation source 450 nm. Measurements were performed in triplicate and PicoQuant TimeHarp software was used for data analysis and fitting.

Nanosecond time-resolved absorption (ns-TA) data were collected using a custom-built setup reported by Dura et al. at Friedrich-Schiller University, Jena in collaboration with research group of Prof. Benjamin Dietzek-Ivanšić,[339] The electronics and programming to record the difference absorption signal are developed by Pascher Instruments (Lund, Sweden). All ns-TA spectra were measured by placing the samples in 1 cm pathlength quartz-made inert cuvettes. The pump pulse energy was 0.12±0.01 mJ for all ns-TA measurements.

2.3.4 TTA-UC Measurements

The TTA-UC measurements were carried out in the same fluorescence spectrophotometer using an additional laser purchased from Edmund Optics with 532 nm excitation of 10 mW power with 1 mm beam diameter. The TTA-UC measurements were performed in the fluorescence spectrophotometer by blocking the excitation line in bioluminescence measurement mode. The solution measurements were carried out by deaerating the sample through N_2 purging for 30 min in a quartz cuvette of 1 cm pathlength. The upconverted emission in vesicles was recorded in the presence of 20 mM sodium sulfite as an oxygen

scavenger. The upconverted emission was recorded across the range 400 to 500 nm to avoid the interference from the excitation source.

Threshold power density measurements: 1 cm Schlenk cuvettes were used to keep solutions under inert atmosphere. The emission spectra were recorded using an FLS980 emission spectrophotometer (Edinburgh Instruments) with a 532 nm (CW532-100, Roithner LaserTechnik GmbH) laser diode. A combination of neutral density filters (OD = 1 and/or 2) was used to record emissions at higher excitation powers.

2.3.5 Reconstitution of photosensitizers and annihilator into Large Unilamellar Vesicles (LUVs)

Reconstitution of molecular sensors into LUVs was carried out using a hydration extrusion method. The photosensitizers were mixed with lipid in 5088:10:1 molar ratio of lipid:annihilator:photosensitizer in chloroform in 1.5 mL glass vial and the mixture was dried under nitrogen flow leading to the formation of a lipid film along the sides of the glass vial. Complete evaporation of the solvent was ensured by keeping it under vacuum for 60 min. The film was then hydrated with 1 mL phosphate buffer saline (PBS) at pH 7.4 and the film was suspended into the buffer by vortexing for 60 s. This solution was extruded through a 100 nm polycarbonate membrane typically 11 times to achieve uniform large unilamellar vesicles of around 100 nm diameter. The diameter and homogeneity of the resulting liposomes was confirmed using dynamic light scattering (DLS).

2.3.6 Preparation of Giant Unilamellar Vesicles (GUVs)

Both single and ternary phase GUVs were prepared by electroformation using the Vesicle Prep Pro (VPP) (Nanion Technologies, Munich, Germany). Single phase GUVs were comprised of DOPC lipid and the ternary phase GUVs were prepared using DOPC, brain sphingomyelin, and cholesterol in 4:4:2 molar ratios to a final concentration of 5 mM, this ratio forms phase-separated domains in the GUV.[316,340–342] The photosensitizer and annihilator molecules were mixed with the lipid stock with 5088:10:1 lipid:annihilator:photosensitizer ratio. To identify phase selectivity of the photosensitizer in the vesicle, the lipophilic tracer dye DiD was used to co-label the vesicle at a concentration of 0.1 mol% to lipid along with the photosensitizer. The lipid-dye stock solution was drop casted as several droplets of 1 μL onto a pair of conductive ITO slides and the solvent was evaporated by purging with N_2 then stored in vacuum for 45 min. ITO slides were carefully introduced into the chamber along with 0.23 mM of warm sucrose solution and the slides were placed one above the other separated by an O-ring of 0.7

mm thickness greased on the conductive side of the ITO sides. The electroformation was initiated by applying an alternating voltage of 0 to 3 V at 55 °C temperature raised for 5 min, and then 3 V was continuously applied at 10 Hz frequency for 170 min at 55 °C followed by fall time of 5 min. The vesicle solution was collected from the slides using a 1 mL pipette and to that 230 mM glucose solution was added to maintain the osmolarity.

2.3.7 Confocal microscopy of giant unilamellar vesicles (GUVs)

Confocal fluorescence images of the GUVs were collected using a Leica TSP inverted (DMi8) confocal microscope. The excitation line was selected from a white light laser used as an excitation source for B2P, B2PI and DiD labelled GUVs and a pulsed 405 nm diode laser was used to excite perylene. A 40x-oil immersion objective was used. B2P was excited at 514 nm and the emission was collected at 630–640 nm. Similarly, the excitation and emission wavelengths ($\lambda_{ex}/\lambda_{em}$) for other dyes were as follows: 514/650–660 nm for B2PI, 405/441-520 nm for perylene and 633/665–700 nm for DiD. The GUVs were mixed with 0.5% agarose for imaging to impede movement of the vesicles and images collected after 10 min following agarose addition.

2.3.8 PDMS Microcavity Array preparation

20 µL of 0.1% of 4.61 µm PS spheres dispersed in ethanol was drop cast over 1 cm × 1 cm pieces hand cleaved mica. After the evaporation of ethanol, PDMS was mixed with curing agent in 10:1 ratio and was poured over the PS sphere arrays and dried at 90 °C for 60 min. The PS spheres were then removed from the PDMS substrate by sonicating in THF for 15 min and the microcavity arrays of approximately 2 µm diameter were thus obtained. Complete evaporation of THF was ensured by drying the substrate overnight. Critically, before lipid bilayer formation, the substrates were rendered hydrophilic by treatment with oxygen plasma treatment for 5 min prior to aqueous filling, this ensured complete aqueous filling of the pores and a sufficiently hydrophilic interface to support the bilayers. Without this step the bilayers are not stable. Following this, the microcavities were filled by buffer by sonication for 15 min in PBS.

2.3.9 Preparation of Microcavity Array Supported Lipid Bilayers (MSLBs)

Lipid bilayer was spanned cross the aqueous filled microcavities in order to form the microcavity supported lipid bilayer. Initially the lipid monolayer was transferred using Langmuir-Blodgett (LB) technique at the air-water interface as reported earlier.[197,199] 1 mg/mL

lipid solution in chloroform was added to the water subphase of LB trough (NIMA 102D) and allowed the solvent to evaporate for about 10 min. The lipid monolayer was transferred to the PDMS microcavities array at 33 mN/m surface pressure. The liposome solution containing the photosensitizer molecule was introduced to the microfluidic sealed chamber of the PDMS substrate and incubated in the dark for about 90 min for the vesicle fusion to occur. Any residual liposomes were removed by washing with excess PBS and this MSLB was then used for FLCS studies.

2.3.10 Fluorescence lifetime imaging (FLIM) and fluorescence lifetime correlation spectroscopy (FLCS)

FLIM and FLCS studies of lipid as well as B2P in MSLB was accomplished using a MicroTime 200 system (PicoQuant GmbH, Berlin, Germany) consisting of an inverted Olympus X1-71 microscope with an Olympus UPlanSApo 60x/1.2 water immersion objective, a time correlated single photon counting (TCSPC) unit, and a dual single photo avalanche diode (SPAD). A 532 nm laser PicoTA from Toptica (PicoQuant) with a pulse repetition rate of 20 MHz was used to excite B2P probe and a 640 nm laser to excite the DOPE-ATTO655 probe embedded within the microcavity supported lipid bilayer. The excitation light was directed to the sample through the objective lens by a 532/640rpc dichroic mirror. The fluorescence emission was also collected through the same objective and filtered through the same dichroic mirror and by a suitable interference filter. The detection volume in the axial direction was confined onto the SPAD using a 50 µm pinhole.

In FLCS, the diffusing fluorophore emission through the detection volume is analysed by calculating the autocorrelation curve which measures the self-similarity of the signal as a function of time as defined below:

$$G(\tau) = \frac{(\langle \partial I(t) \rangle \langle \partial I(t + \tau) \rangle)}{\langle I(t) \rangle^2}$$

where $\langle \rangle$ denotes the time average, and $\langle \partial I(t) \rangle$ and $\langle \partial I(t+\tau) \rangle$ are the fluorescent intensity fluctuations around the mean value at time, t and t+τ respectively, where τ is the lag time. The FLCS autocorrelation data were fitted to a 2D diffusion model using Equation 2.1:

$$G(\tau) = \left[\frac{1}{N} \right] \left[\frac{1}{1 + \left(\frac{\tau}{\tau_D} \right)^{\alpha}} \right] \tag{2.1}$$

where G(τ) is the autocorrelation function (ACF) of fluorescence fluctuations, N is the average number of diffusing fluorophores in the effective volume, τ is the delay time, τ_D is the diffusion time of the molecules across the confocal volume, α is the anomalous parameter, and c is the contribution of the diffusing species. ACFs were fitted using the two-dimensional model of diffusion to determine the diffusion time and the diffusion coefficient was calculated using Equation 2.2:

$$D = \frac{\omega^2}{4\tau_D} \tag{2.2}$$

where D is the diffusion coefficient and ω is the $1/e^2$ radius of the confocal volume. ω was calibrated using aqueous ATTO-532/ATTO-655 (ATTO TEC, GmbH) dye solution (5 nM) of known diffusion coefficient at 20 °C in water.

The fluorescence lifetime images were acquired for 360 s with a 512 x 512 resolution. Data were analysed using PicoQuant SymPhoTime software.

2.4 Results and Discussion

2.4.1 Steady State Absorption and Emission Spectroscopy in Solution

Prior to applying them in liposome, the photophysical studies (UV-Vis and fluorescence) of Ph-BODIPY-2-perylene (B2P), Ph-BODIPY-2-perylene-iodine (B2PI), and perylene were studied initially in chloroform solution. To try to match the dielectric to a lipid environment, chloroform was used in this study as the solvent. However, in our recent work, it shown that, while the absorbance is largely solvent independent, the emission intensity and wavelength of these compounds are strongly solvent dependent. This is because the emission originates from fluorescence from a charge transfer S_1 state.[336]
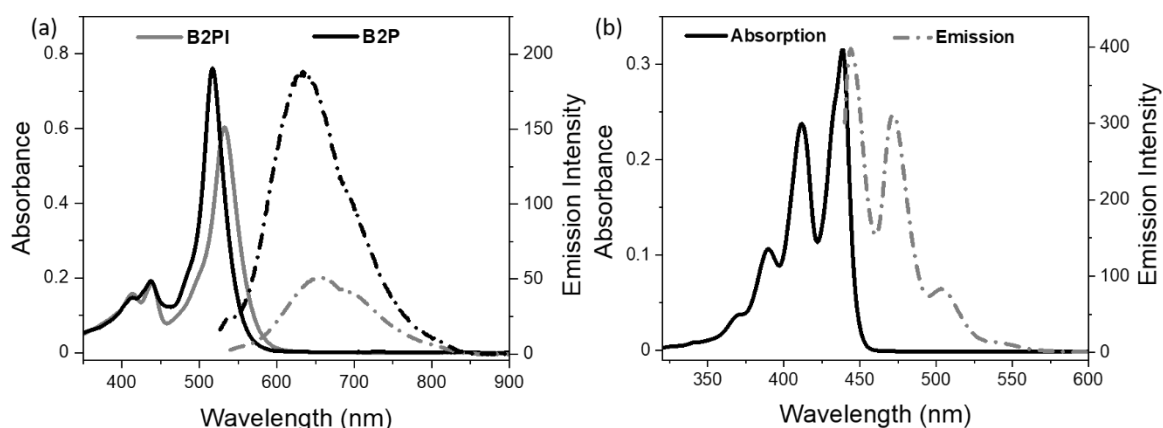
Figure 2.3 Absorption (solid line) and emission spectra (dash dotted line) of (a) 10 µM B2P (black) and B2PI (grey) and (b) 5 µM perylene in chloroform. Emission spectra of B2P, B2PI and perylene were collected by exciting at 517, 532, and 438 nm respectively with 5 nm excitation and emission slit widths.

Figure 2.3a shows the absorption (solid lines) and emission (dotted line) spectra of 10 µM B2P (black), and µM B2PI (grey) in chloroform. Similarly Figure 2.3b shows the perylene's absorption and emission spectra in chloroform at a concentration of 5 µM. The UV-Vis spectra of B2P and B2PI showed absorption bands in the range of 500-560 nm, the molar absorption coefficient of B2PI was 6×10^6 m^2/mol which is lower than that of B2P's molar absorption coefficient 7.5 10^6 m^2/mol obtained from Beer-Lambert equation. The absorption maxima of B2P are centred at 517 nm, but the absorption maxima of B2PI are bathochromically shifted to 532 nm due to the incorporation of an iodine atom to the BODIPY core.[315] Both compounds emit intensely with a broad spectra ranging from 600-800 nm. Quantitatively, iodination causes a red shift in emission maximum for B2PI with fluorescence maxima at 635 for B2P and 655 nm for B2PI. Comparable bathochromic shifts have been reported previously on iodination of charge transfer compounds of BODIPY at the 2 and 6 position.[72,315]

B2P and B2PI have absolute fluorescence quantum yield of 11.80±0.5% and 2.5±0.1% respectively in dioxane when measured using integrating sphere. The decrease in fluorescence quantum yield in the iodinated compound, is attributable to increased efficiency of intersystem crossing (ISC) from the heavy atom effect/spin-orbital coupling which was the anticipated advantage preparing an iodination version of the BODIPY derivatives in TTA-UC.[343]

2.4.2 Triplet-Triplet Annihilation Upconversion in Solution

Initially, the TTA-UC was established in solution prior to the incorporation to the lipid bilayer membrane. Keyes group has recently reported on a work on efficient upconversion but

significant solvent dependence using the TTA-UC pair B2P-perylene and B2PI-perylene .[336] Also observed that TTA-UC is more efficient for B2PI because iodination facilitates ISC from single excited state to the triplet excited state via spin-orbit coupling, a well-known heavy atom effect.[83,344,345]

Previous work of ours found that 5 µM B2P and 100 µM perylene, as well as 2.5 µM B2PI and 25 µM perylene, in deaerated dioxane at 10 nm slit widths under 532 nm illumination, resulted in effective TTA-UC.[336] In contrast, in this work, a different concentration scheme is employed, where the photosensitizer and annihilator concentrations are both held constant at 1 and 10 µM respectively. This concentration allowed for effective TTA-UC in solution. To prevent any unintended consequence, such as precipitation problems or changes to the intrinsic biophysical characteristics of the liposome membrane, the concentrations in liposomes was further decreased by a factor of four. Although other concentration and solvent variables were used, the above concentration was used because it is central to this chapter's goal of understanding how TTA-UC works effectively in the liposomal model. As can be seen in Figure 2.4a, when N_2 is used to deaerate dioxane, the strength of the B2PI-perylene pair is up to roughly nine times (9x) more intense (black, Figure 2.4a) than that of the B2P-perylene pair (red, Figure 2.4a).
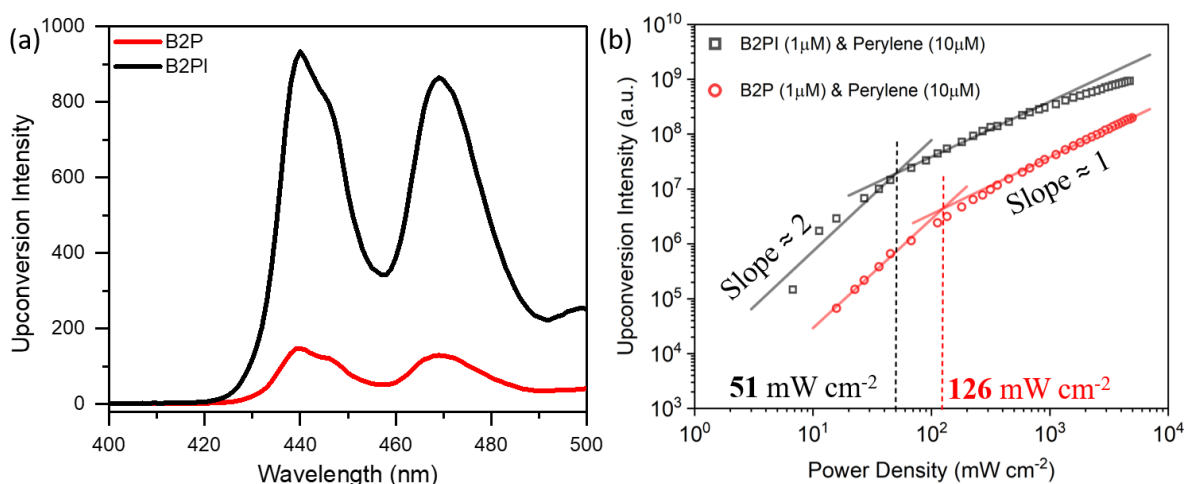
Figure 2.4 TTA-UC from (a) 1 µM B2P with 10 µM perylene (red) and 1 µM B2PI with 10 µM perylene (black) in deaerated dioxane at 10 nm slit widths, (b) log (power density) vs log (upconversion emission intensity at 443 nm) of B2P & B2PI (1 µM) with perylene (10 µM) in dioxane at 532 nm excitation.

A 532 nm laser was used to irradiate both B2P- and B2PI-perylene samples dissolved in dioxane under deaerated conditions for the experiment. Two prominent anti-Stokes emission peaks were evident at 443 nm and 473 nm, consistent with perylene emission, and thus is

ascribed to the upconverted emission through triplet-triplet annihilation. As noted earlier, the observed enhanced TTA-UC efficiency for B2PI with perylene is due to the enhanced ISC from the heavy atom effect.

Further validation of efficient TTA-UC can be obtained from threshold power density measurement. Since its discovery, the quadratic incident light power dependence of the anti-Stokes fluorescence has been widely used as a convenient measure to mechanistically support sensitised photochemical upconversion through TTA.[20] Typically, this power dependence is measured in steady-state photoluminescence studies with a wide range of irradiance from both coherent (laser) and non-coherent (lamp) excitation sources. Here, it is shown experimentally that photochemical upconversion from B2PI-perylene and B2P-perylene dioxane solutions under 532 nm filtered laser excitation has a power dependence somewhere between quadratic and linear. Each sample was subjected to a systematically changing power density that was applied via neutral density filters and measured with a power metre. In the threshold power density measurements, the upconversion intensity was considered directly as a function of excitation power density. As shown in Figure 2.4b, when the photosensitizer in N_2 saturated dioxane is selectively excited with 532 nm output from a CW laser, the intensity of the singlet fluorescence emanating from perylene at 443 nm is a linear function of incident power density. Figure 2.4b shows that the slope has considerably decreased at higher excitation power densities. As expected, the slope of B2PI-perylene plot (black, Figure 2.4b) is 2.0, indicating quadratic dependence, at low incident powers. As the incident photon flux is increased, the slope of the plot shifts away from its starting value and continues to do so until the sample reaches a slope of 1.0 at the highest incident power densities. The B2P-perylene system (red, Figure 2.4b) exhibited a comparable slope deviation to the B2PI-perylene system, albeit with a relatively weaker UC intensity. This finding is consistent with what has been seen in similar studies on various sensitised TTA compositions[346–348], and it shows clearly that a wide range of power-dependent responses can be measured in a single sample, depending on the initial and final photon flux used in the experiment. The slope transition point is the spot at which the process transitions from low annihilation to high annihilation region occurs.[346] In the case of B2PI, the threshold power density (I_{th}) at which the strong upconversion region has reached is 51 mW cm^{-2} compared with 126 mW cm^{-2} for B2P. The lower I_{th} value of B2PI indicates higher efficiency towards TTA-UC.

2.4.3 Time-Resolved Absorption and Emission Spectroscopy in Solution

The photophysical processes underlying the TTA-UC were studied at the microsecond time scale using the photosensitizers B2P and B2PI in the presence and absence of perylene by nanosecond transient absorption (ns-TA). The ns-TA of the above-mentioned samples was determined in 1,4-dioxane, and the concentrations of B2P and B2PI were 5 µM, while perylene was 100 µM.
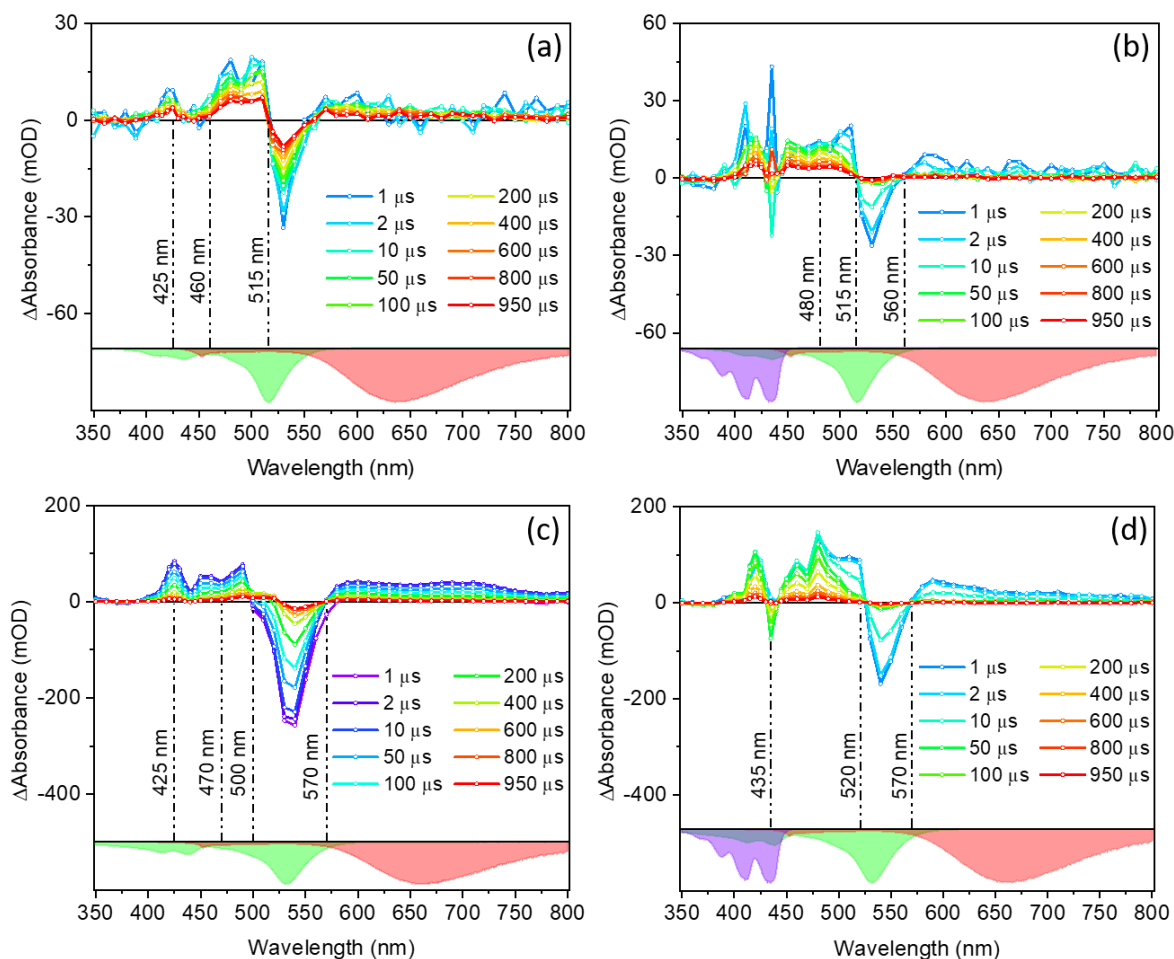
Figure 2.5 Nanosecond transient absorption spectra of (a) B2P - 5 µM, (b) B2P - 5 µM & perylene 100 µM, (c) B2PI - 5 µM, (d) B2PI - 5 µM & perylene 100 µM. In the bottom- inverted absorbance of photosensitizer is in green and inverted emission of photosensitizer is in red, inverted absorbance of perylene is in violet of the respective sample. Legend remains same for all figures. Arrows in (b) and (d) show changes in the spectra with respect to (a) and (c) respectively upon addition of 100 µM perylene. Data courtesy of Keshav Kumar Jha (Friedrich Schiller University Jena).

The ns-TA spectra of B2P is shown in Figure 2.5a and B2P with perylene in Figure 2.5b. The ground state bleach (GSB) extending from 515 nm to 560 nm dominates in both figures. A broad excited state absorption (ESA) was observed and they are present across the visible region except the dominant GSB region. Figure 2.5a & 2.5b show dominant ESA in B2P from 460 nm to 515 nm and this matches closely with the ESA of triplet perylene. The ESA band

from 560 nm to 800 nm is expected to have contributions from the triplet states of both BODIPY and perylene. In Figure 2.5b, when 100 µM of perylene was added to 5 µM B2P, some of the differential absorption signatures increased in intensity between 420 nm and 455 nm. This may be because of triplet-triplet energy transfer (TTET) from the BODIPY-dyads to the additional perylene, whereas the lack of intensity increases between 480 and 515 nm suggests that the contribution from triplet perylene in this region can arise from CRT (charge recombination??) (intramolecular process) rather than TTET process.[92,349]

Similarly, Figure 2.5c & 2.5d shows the ns-TA of B2PI with and without the addition of perylene. Figure 2.5c shows the dominant GSB in B2PI from 500 nm to 570 nm and the ESA dominates everywhere in the visible region in between 350nm to 800 nm except for the whole GSB region. Two ESA peaks are present at 425 nm and 490 nm. Whereas the addition of 100 µM of perylene caused a rise in the ESA intensity at 425 nm and from 480 nm to 520 nm. The GSB peak has decreased and narrowed in 520 nm to 570 nm range due to the rise of ESA in 480 nm-520 nm region.

While comparing Figures 2.5a and 2.5c of B2P and B2PI respectively, a red shift is observed in the negative peak of GSB similar to the spectral shift already occurred in the steady state absorption spectra due to the presence of additional iodine atom in B2PI. The ESA of B2PI is more intense than that of B2P due to the higher number of triplet state formation caused by the presence of iodine; for instance, ESA at 480 nm for B2P is 5 mOD and for B2PI is 70 mOD. Moreover, the addition of perylene did not result significant increase in the intensity of ESA between 480 and520 nm for B2P, whereas in the instance of B2PI, the ESA signal has increased in the aforementioned wavelength range. It is clear that the inclusion of perylene, which populates the triplet states by TTET in the 480-520 nm region, is responsible for the improvement in ESA.
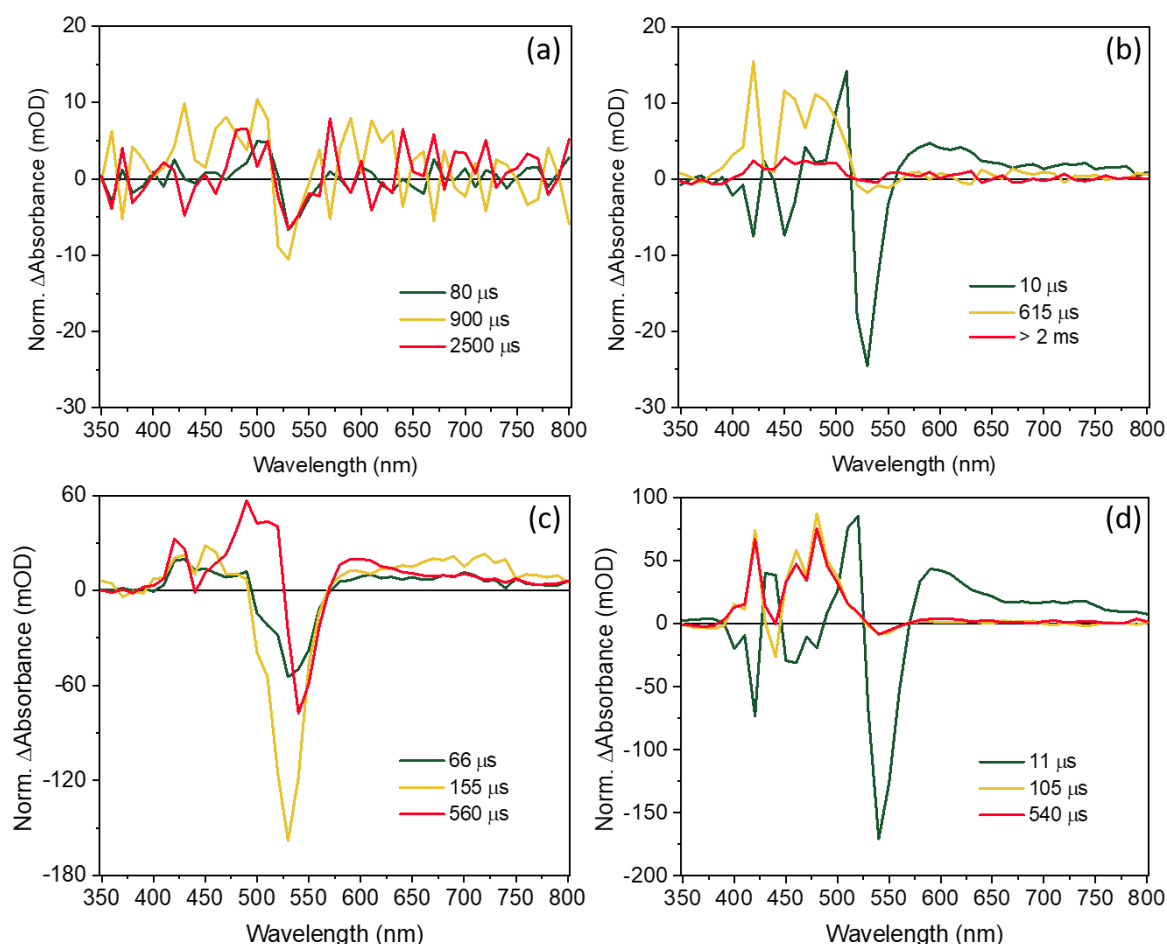
Figure 2.6 Decay associated spectrum (DAS) of the global fit of the kinetics of (a) B2P - 5 µM, $\tau_1 = 80$ µs, $\tau_2 = 900$ µs, $\tau_3 = 2500$ µs (b) B2P - 5 µM & perylene 100 µM, $\tau_1 = 10$ µs, $\tau_2 = 615$ µs, $\tau_3 = >2$ ms (c) B2PI - 5 µM, $\tau_1 = 66$ µs, $\tau_2 = 155$ µs, $\tau_3 = 560$ µs (d) B2PI - 5 µM & perylene 100 µM, $\tau_1 = 11$ µs, $\tau_2 = 105$ µs, $\tau_3 = 540$ µs. Data courtesy of Keshav Kumar Jha (Friedrich Schiller University Jena).

TTET occurs when external perylene is added to B2P and B2PI solution as evident from the changes in spectra of Figure 2.5. Upon addition of 100 µM perylene to 5 µM B2P the lifetimes of the B2P sample changes to 10 µs, 615 µs, and >2 ms from 80 µs, 900 µs, and 2500 µs as shown in Figure 2.6a & 2.6b. In the case of B2PI, after the addition of 100 µM perylene, the lifetimes of the sample are 11 µs, 105 µs, and 540 µs as given in Figure 2.6c & 2.6d. These three lifetimes are quenched lifetimes of ^{3}CT (11 µs), BODIPY-centred triplet (107 µs) and perylene-centred triplet (512 µs). This observation clearly shows the TTET process is quenching the photosensitizer. The associated kinetics (symbols) and corresponding global fits (dotted line) for B2P, and B2PI are shown in Figures S2.3 and S2.4 in the absence and presence of perylene. These triplet state lifetimes are comparable to those of orthogonally aligned cyclic BODIPY derivatives synthesized by Zhao et al.[350] (hundreds of microseconds) but significantly longer than those of typical heavy atom-containing triplet photosensitizers with comparable

long-wavelength absorption ($\tau_T = 1.7\,\mu s$ for 2,6-diiodo-bisstyrylBODIPY).[351,352] However, this high triplet state lifetime is crucial for their applications in photocatalysis and photodynamic therapy (PDT), as the triplet state lifetimes of photosensitizers would significantly influence the efficiency with which triplet energy is transferred across molecules via intermolecular diffusion.[47,75,353,354]

2.4.4 Reconstitution of photosensitizers to lipid bilayer for FLCS and FLIM studies

As mentioned in the previous section, the optimal diffusion of photosensitizer within a dielectric environment in general, and a biomembrane in particular, necessitates collision with annihilator, which can yield efficient TTA-UC. As a result, initially both B2P-perylene and B2PI-perylene pair were reconstituted in the highly fluidic DOPC large unilamellar vesicles (LUVs). The LUVs were prepared using extrusion method as detailed in experimental section. The B2P- and B2PI-perylene doped DOPC liposomes are 140±5 nm (Figure 2.7) in diameter, as measured by dynamic light scattering (DLS).
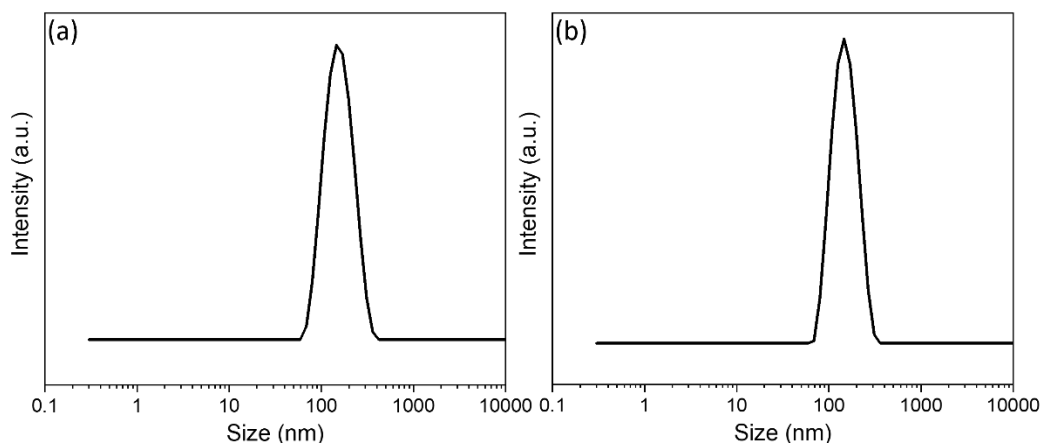
Figure 2.7 Dynamic light scattering spectra of DOPC liposomes containing 0.25 μM of each (a) B2P and (b) B2PI with 2.5 μM perylene in PBS of pH 7.4. Average hydrodynamic radius is 140 nm.
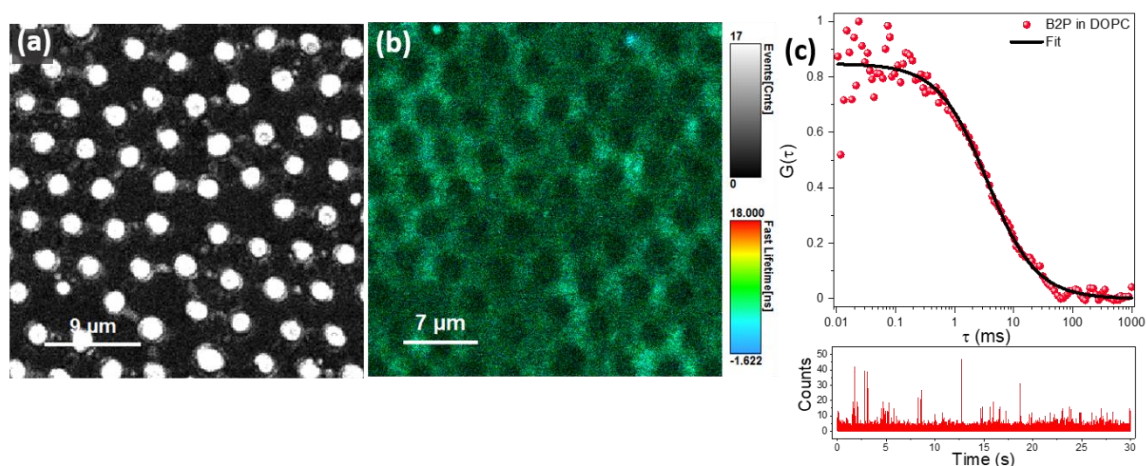
Figure 2.8 (a) reflectance and (b) fluorescence lifetime images of microcavity supported lipid bilayer of DOPC labelled with 5 nM B2P (upper leaflet). (c) Representative normalised FLCS autocorrelation function measured over a single cavity and the corresponding intensity-time trace (bottom panel). FLCS data were collected from 40-50 cavities and the average is shown. The solid lines are the 2D diffusion fit using equation 2.1. All measurements were carried out at RT in PBS at pH 7.4.

Table 2.1 Diffusion coefficient and other parameters of B2P photosensitizer calculated from the FLCS data.

Sample	Diffusion coefficient, D ($\mu m^2 s^{-1}$)	Anomaly coefficient, α	Transit time (ms)
B2P in DOPC bilayer	8.6	1.01	3.26

Due to diffraction limit of optical microscope, visualizing the LUVs individually in a confocal microscope and thus reliably determining their diffusion coefficient by FLCS is not possible. Herein, a previously established PDMS microcavity 2D array platform which is suitable for studying lipid-protein and lipid-drug interactions using confocal microscopy has been employed.[187,194,355,356] The rationale behind using a pore suspended bilayer over PDMS microcavity array is to render a highly fluidic bilayer where diffusivity has been shown to be akin to GUV.[187,193,196] Furthermore, in comparison to GUV, PDMS based suspended planar lipid bilayer system are highly amenable to optical imaging methods including fluorescence lifetime imaging and correlation spectroscopy. They can be used for protein reconstitution and have the synthetic versatility of SLBs with control over its asymmetry across the leaflet. They also require minimum sample volume in the microfluidic chamber.[187,196] The PDMS based microcavity array was prepared by soft lithographic technique as detailed in experimental

methods, which can give a close packed ordered array with dimensions ranging from micrometres to millimetre.[357] Herein, to visualize the photosensitizer containing bilayer using FLIM, B2P photosensitizer (0.01 mol%) was doped only to the upper leaflet of DOPC bilayer during the preparation step of LUVs and fused over the Langmuir-Blodgett (LB) transferred DOPC monolayer spanning the aqueous filled PDMS microcavity array. Figure 2.8a shows a representative white light reflectance image of the buffer filled cavity arrays, where the white circular regions are indicative of the reflectance from the filled buffer originated from the refractive index mismatch between the PDMS and buffer. Typically, a reflectance image was acquired first in order to assess whether or not the cavities are buffer filled. At instances, where the cavities are not occasionally buffer filled, the bilayer did not form due to the lack of lipid monolayer support and these regions are then excluded from diffusion study. Occasional unfilled pores are evident in PDMS arrays because of the larger size of these pores (2 µm diameter) and the hydrophobicity of the substrate that can sometimes mitigate against aqueous filling. The corresponding fluorescence lifetime image (FLIM) is shown in Figure 2.8b in the identical regimes as that of Figure 2.8a. When combined both reflectance and FLIM image, it can be concluded that the bilayer is successfully spanned over the buffer filled cavity array. The image acquisition was carried out each time by Z-scanning to identify the maximum brightness of the fluorophore (B2P) doped in the outer membrane leaflet, and selectively positioning the confocal plane just over the bilayer plane. Due to the large cavity size, it is possible to carry out point fluorescence correlation spectroscopy in lifetime mode with the observation/detection volume at the centre of the cavities with spanned bilayer. At least 40-50 independent FLCS point measurements were typically acquired for each measurement and averaged. Figure 2.8c bottom panel shows a typical intensity-time trace for B2P as it diffuses in and out of the confocal volume. The fluorescence spikes are consistent with single B2P molecule diffusing translationally across the DOPC membrane in 2D. The ACF from FLCS was shown in the upper panel of Figure 2.8c as $G(\tau)$ versus lag time (τ) (open symbol). The solid line represents the fit using 2D diffusion model equation defined in equation (2.1). From the fit, the transit time (τ_D) was evaluated and the diffusion coefficient was determined as 8.6 $\mu m^2 s^{-1}$, according to the equation (2.2). The observed D value is comparable to the commercial ATTO based lipidic tracer DOPE-ATTO655 as determined in a control experiment of DOPC MSLB as shown in Figure 2.9, where the lipid diffusivity was 9 ± 1 $\mu m^2 s^{-1}$. This indicates that B2P is fully inserted into the bilayer and remain diffusive translationally across 2D plane of DOPC. Additionally, the anomaly coefficient (α) was found to be 1.01 indicating B2P diffusion is Brownian (Table 2.1).
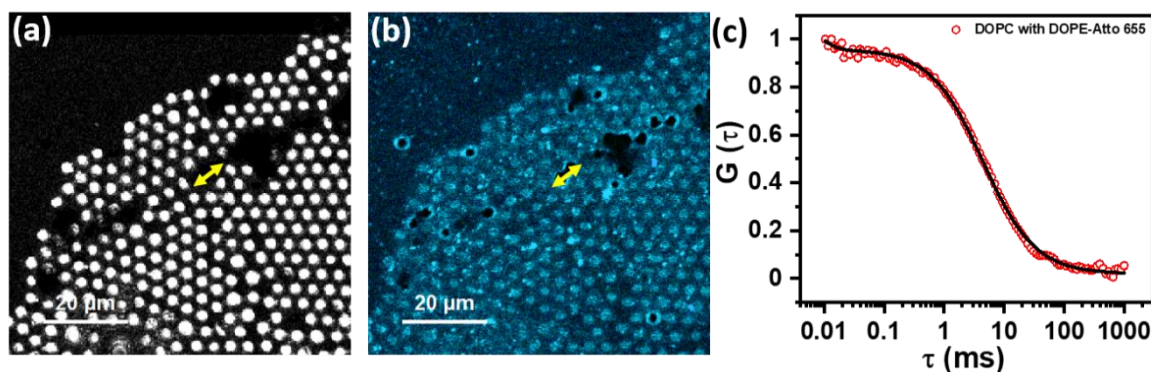
Figure 2.9 (a) Reflectance image and (b) fluorescence lifetime image of DOPC lipid spanning cavities labelled with 0.01 mol% DOPE-ATTO655. (c) Representative normalized FLCS autocorrelation curve measured over a single cavity spanned with DOPC bilayer labelled with DOPE-ATTO655. FLCS data were collected from 40-50 cavities and the average is shown. The solid lines are the 2D diffusion fit using equation 2.1. All measurements were carried out in PBS at pH 7.4.

The fluorescence lifetime of B2P from the MSLB and in solution are provided in Table 2.2 and the analysis of decay from MSLB is shown in Figure S2.5. The overall result from both FLIM and FLCS measurements shows that B2P is properly inserted into the lipid membrane and diffuses according to Brownian motion, within this environment indicating it is likely suitable for TTA-UC studies.

Table 2.2 Comparison of lifetime and corresponding amplitude of B2P in DOPC MSLB, dioxane and chloroform.

Sample	T_1 (ns)	T_2 (ns)	A_1 (kCnts)	A_2 (kCnts)
B2P in DOPC	2.81±0.046	6.8±0.25	11.9±0.058	7.9±0.12
B2P in Dioxane	1.79		6235.6	
B2P in Chloroform	2.76	1.24	855.1	5271

2.4.5 Triplet-Triplet Annihilation Upconversion in liposomes

Having observed and optimised TTA-UC in dioxane solution with a dielectric constant (ε_r) of 2.25 in section 2.4.1, the TTA-UC study of B2P- and B2PI-perylene pairs was extended in a lipidic environment noting that the dielectric constant is similar in DOPC (ε_r = 2-3) to that of dioxane (ε_r =2.25). As mentioned before in the introduction section, one of the reasons for investigating TTA-UC in a model lipidic environment is to establish a route for upconversion that can be applied to cell imaging by shifting the activation wavelength of photoactivatable prodrugs nearer to the phototherapeutic window. Since cell membranes are complex biological systems made up of tens of thousands of lipids and proteins, often they are difficult to isolate

and study directly using biophysical approaches. However, characterization of simpler biomimetic lipid membrane as models, offer a valuable means to study the physicochemical properties of the most abundant lipid species in cells. Indeed, biomimetic lipid membranes are easier to make in the laboratory with control over its size, phase, fluidity/viscosity, and stability. Because the photosensitizers B2P and B2PI are molecular rotors, it is interesting to see how the varying membrane physicochemical properties such as fluidity/viscosity, vesicle size, hydrophobic core chain length and head group charge etc. modulate TTA-UC efficiency of the B2P/B2PI photosensitizer with perylene annihilator system.[343] Importantly, for UC to be carried out efficiently within target sites, TTA-UC supramolecular assemblies necessitate co-localization of photosensitizer and annihilator, and the cell membrane model can be an appropriate delivery vehicle that can confine the photosensitizer and annihilator to direct to the target sites.

Initially, DOPC large unilamellar vesicles (LUVs) were prepared with hydrodynamic diameter $\sim140\pm5$ nm, as well as two distinct giant unilamellar vesicles (GUVs) comprising of pristine DOPC and ternary phase separated DOPC:SM:Chol (2:2:1) GUVs of dimension ~10-30 µm and embedded with B2P- and B2PI-perylene pairs. LUVs of such dimensions are capable of permeating the cell membrane and have been used as cargo carriers in drug delivery because of their biocompatibility, ability for improved permeability, low toxicity, and high retention effect.[279,358,359] GUVs on the other hand are suitable for imaging due to its comparable size to that of cell.[360]

In the solution-based study, N_2 was used to remove oxygen for effective UC, but in the liposome-based study, 20 mM sodium sulfite was added exogenously as oxygen scavenger. Photosensitizers were used at a concentration of 0.25 µM of either B2P or B2PI mixed with 2.5 µM perylene, which is fourfold lower than that of solution based study and was chosen to prevent any unintended effects, such as precipitation or modulating any physicochemical properties of the lipid membrane. Both pairs showed substantial anti-Stokes shifted emission, as shown in Figure 2.10a attributed to TTA-UC. The upconverted emission was observed only after the addition of sodium sulfite as oxygen scavenger and the perylene-reconstituted liposomes under same experimental conditions did not give TTA-UC, which confirms that the emission signal obtained is due to TTA-UC. When TTA-UC emission amplitude of B2PI-perylene was compared to that of the B2P-perylene pair, under identical excitation conditions, B2PI showed a much more intense up to five-fold increase emission peak than B2P consistent with solution studies and ascribed to heavy atom promotion of ISC by iodination. Even after

diluting the dyad concentration four times in DOPC liposomes, the intensity of the B2PI-perylene pair was reduced by approximately 50% in liposomes compared to solution. This is most likely due to the TTA-UC pair being confined to the same 2D region within the liposomes. Overall, it indicates B2PI-perylene as a promising pair for TTA-UC in liposome formulations and may have the potential to be used for targeted therapies, since liposomes are widely used to deliver drugs to cells.
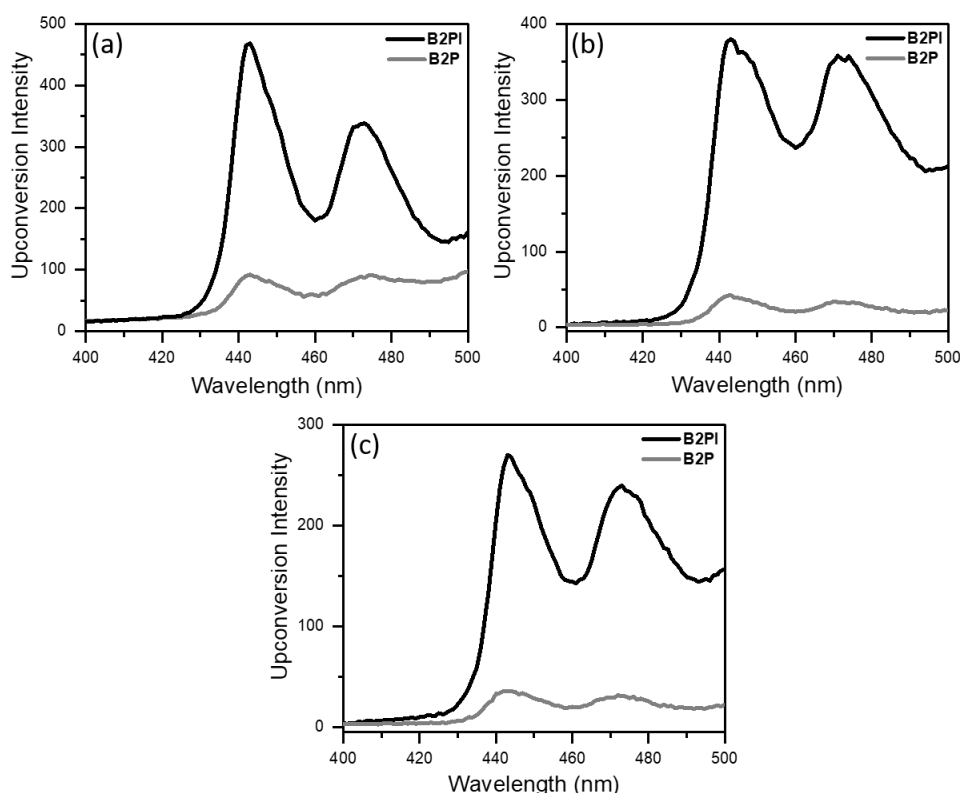
Figure 2.10 TTA-UC in a) DOPC LUV with 0.25 µM B2PI(black)/B2P(grey) and 2.5 µM perylene, (b) DOPC GUV, and (c) GUV of DOPC:SM:Chol (2:2:1) reconstituted with ~0.32 µM B2PI/B2P with ~3.2 µM perylene. All measurements are recorded with 2.5 nm emission slit width at 532 nm excitation in presence of 20 mM sodium sulfite.

Although LUVs clearly facilitate TTA-UC, it is difficult to visualize them using confocal microscopy due to its small size. In order to facilitate imaging of the BODIPY doped liposomes, GUVs of 10-30 µm in size were prepared. GUVs are considered to be useful cell membrane models because of their similar dimensions and low curvature which bears analogy to the cell membrane.[361,362] First to confirm that the photosensitizers were reconstituted into GUVs and to understand their location and observe TTA-UC phenomena in the membrane, confocal based fluorescence imaging of GUVs was carried out. For visualization, 0.38 µM of either B2P or B2PI mixed with 3.8 µM perylene was embedded in both single-component

DOPC and three-component DOPC:SM:Chol (2:2:1) GUVs. From the confocal fluorescence images shown in Figure 2.11, it is clear that both B2P and B2PI are integrated into the membrane leaflet and there is no emission from the background solution. Notably, in the ternary composition of GUVs, the photosensitizer probe partitions to the liquid disordered (L_d) phase, which was independently confirmed by co-labelling with a known L_d partitioning lipidic probe[316] (DiD) which will be discussed in preceding section. After microscopy characterization, GUVs of both DOPC and DOPC:SM:Chol doped with B2P-perylene and B2PI-perylene were then studied for TTA-UC. Figure 2.10b and 2.10c shows representative plots for both B2P-perylene and B2PI-perylene in DOPC and DOPC:SM:Chol GUVs. Although the trend of B2PI-perylene emission is higher than that of B2P-perylene in both the GUVs, when compared, the overall intensities of both B2PI-perylene and B2P-peryleneare modestly decreased (25%) for DOPC:SM:Chol than that of DOPC. This decrease is likely to be due to the higher viscosity of DOPC:SM:Chol membrane than that of DOPC, where it is widely believed that cholesterol and SM are tightly packed making the membrane more ordered (cf. Figure 2.11). As shown in Figure 2.12d, however, perylene does not show phase selectivity and emits from both L_d and L_o phases thus the local concentration of perylene within L_d phase where the photosensitizer resides is reduced, reducing collision probability leading to this observed decrease in TTA-UC.
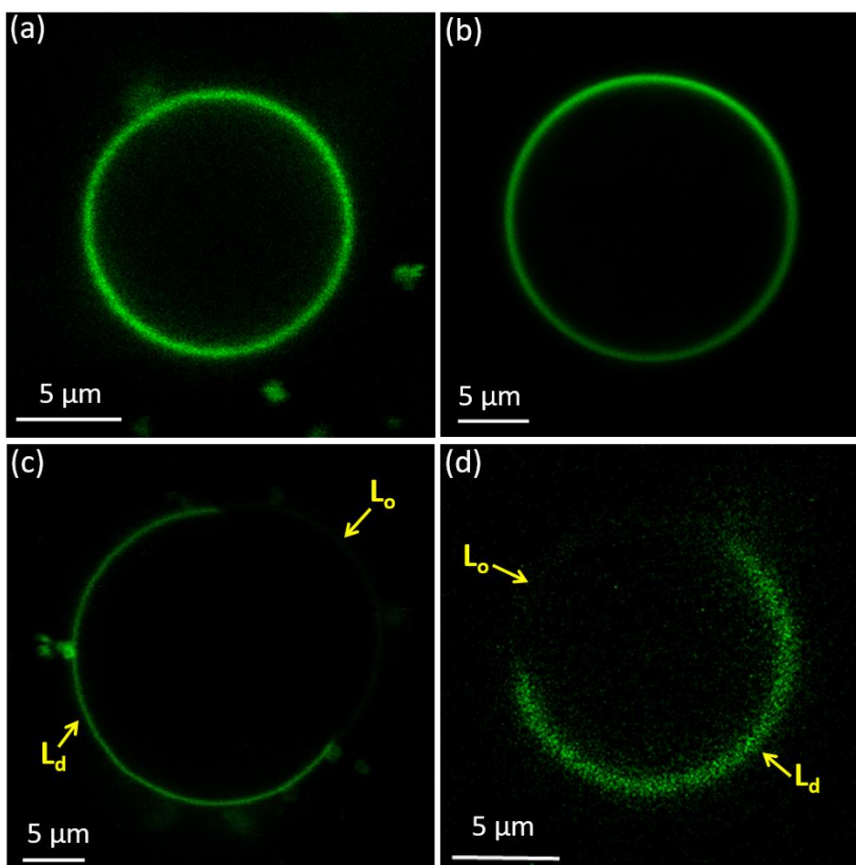
Figure 2.11 Confocal microscopy images of DOPC (a and b) and DOPC:SM:Chol (c and d) GUVs showing the membrane doped with B2P (a and c) and B2PI (b and d). The scale bar in panel a-d is 5 µm. $\lambda_{ex}/\lambda_{em}$=514/600-700 nm. Liquid ordered (L_o) and liquid disordered (L_d) phases are marked in yellow.

To better understand the distribution of the phase separated liposome, the liposomes were co-labelled with B2P and DiD in GUVs composed of DOPC:SM:Chol. DiD, a probe that associates selectively with liquid disordered phase (L_d). Figure 2.12 shows the fluorescence images of the GUVs where it can be seen that the B2P is distributed inhomogeneously throughout the GUV and has clear co-localisation with the DiD tracer.[316] This clearly confirms that the B2P photosensitizer shows selectivity for the L_d phase. Similarly, B2PI was also found to be mainly localise in the L_d phase. Because the heavy iodine substituent in the photosensitizer reduces the fluorescence quantum yield, they are not effective probes for confocal fluorescence imaging. However, it was sufficiently luminescent to confirm, from imaging, that it is incorporated into the same L_d phase as B2P.
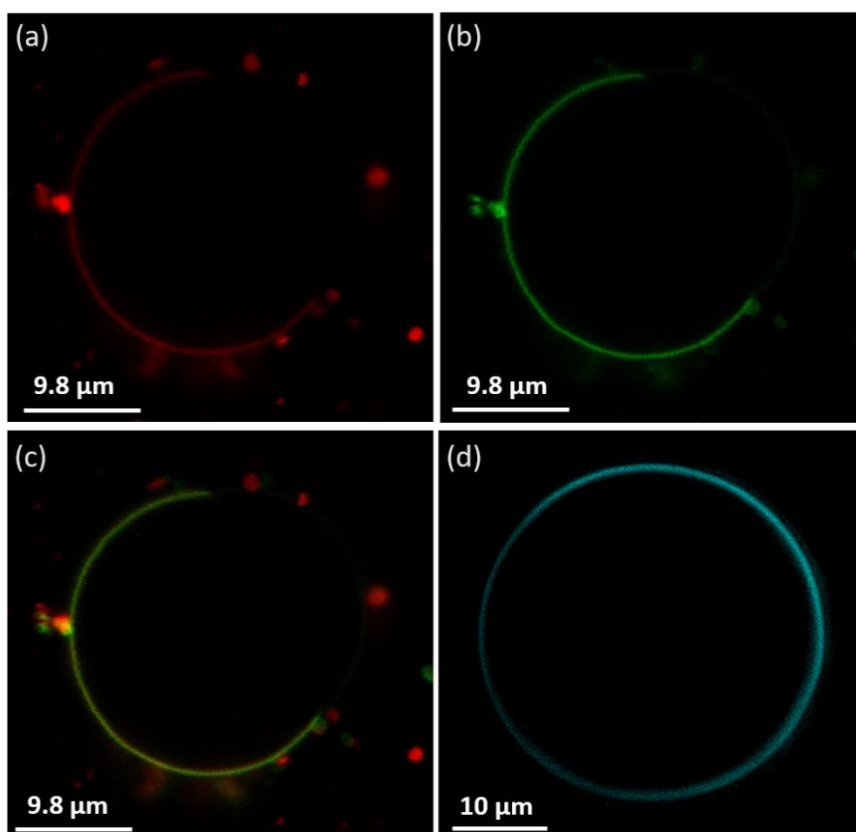
Figure 2.12 Confocal fluorescent images of phase separated GUVs DOPC/BSM/Chol (2:2:1) mol%. GUV labelled with (a) DiD (red), (b) B2P (green), (c) overlay image of B2P and DiD emission, and (d) perylene (blue). For B2P, $\lambda_{ex}/\lambda_{em}$=514/600-650 nm for DiD, $\lambda_{ex}/\lambda_{em}$=633/665-700 nm and for perylene, $\lambda_{ex}/\lambda_{em}$=405/440-500 nm.

2.4.6 The impact of membrane physicochemical properties on TTA-UC

As TTA-UC requires a collision between photosensitizer and annihilator, next attempt was to examine the impact of liposomes' physicochemical properties, particularly their fluidity behaviour, on TTA-UC by comparing its emission intensities across different membrane compositions. Next, the TTA-UC efficiency was compared as a function of varied alkyl chain length, degree of saturation/unsaturation, lipid phase transition temperature and varied lipid head group and charge chemistry. The zwitterionic DOPC is di-unsaturated, with a phase transition temperature (melting transition temperature), T_m of approximately -17 °C, whereas POPC is monounsaturated, with a T_m of approximately 2 °C. The zwitterionic DMPC and DLPC lipids have saturated alkyl chain lengths of C14 and C12, respectively, and T_m values of 23 and 2 °C.[363–365] The chemical structure of individual lipids are provided in Figure 1.6 (chapter 1) and the T_m along with the head group/alkyl chain configuration are shown in Table 2.3. The lipid diffusivity of various membranes was assessed first before comparing TTA-UC

efficiency across different membranes. To obtain the lipid diffusivity in the above membrane compositions, the diffusion coefficient values of different membranes were measured at MSLB using FLCS (cf. Table 2.3). While comparing the diffusivity values of membranes, it was observed that highly unsaturated phospholipids are typically more fluidic (higher diffusivity value) than their saturated counterparts. The TTA-UC efficiency in liposomes of different lipids were compared by incorporating B2P and B2PI along with perylene into the membrane bilayer which are shown in Figure 2.13.
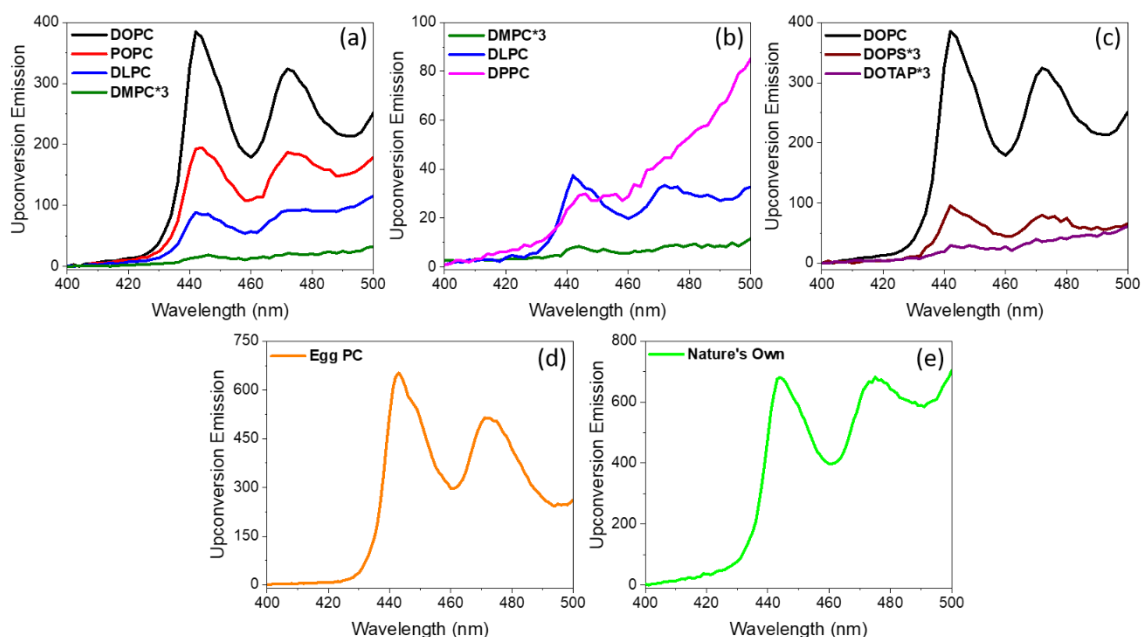
Figure 2.13 TTA-UC from liposomes of different lipids with different (a) fluidity and number of double bonds, (b) alkyl chain length, (c) charge. TTA-UC in (d) egg PC, and (e) nature's own liposomes. All samples contain 0.25 µM of B2PI and 2.5 µM of perylene and the measurements were recorded at 2.5 nm emission slit width under 532 nm excitation in presence of 20 mM sodium sulfite.

Role of membrane fluidity: Figure 2.13a shows the upconverted emission observed from the B2PI-perylene pair in DOPC, POPC, DMPC and DLPC liposomes under identical experimental conditions. A trend of DOPC>POPC>DLPC>>DMPC was observed towards the efficiency/intensity of TTA-UC. Table 2.3 provides the measured diffusion coefficients (D), obtained from MLSBs of the same composition. And clearly the fluidity of the membrane tracks the TTA-UC intensity. As expected, the TTA-UC pair in DOPC liposomes showed the highest intensity upconverted signal (Figure 2.13a black), owing to the high fluidity (low viscosity) of this membrane. Considering that the diffusion coefficient of B2P was 8.6 $\mu m^2 s^{-1}$, and the DOPE-ATTO655 lipid label for DOPC had a D value of 9.6 $\mu m^2 s^{-1}$, it follows that the photosensitizer-annihilator collision frequency in DOPC's 2D membrane should be relatively

high. While both POPC and DLPC have the same T_m, the fluidity of POPC is higher (D= 8.7 $\mu m^2 s^{-1}$) than that of DLPC (D=7.4 $\mu m^2 s^{-1}$), so that TTA-UC is still higher in POPC. The difference in upconversion intensity/fluidity could also be attributed to the fact that POPC has one unsaturated double bond, resulting in a higher TTA-UC than DLPC, which lacks any double bond. DMPC, on the other hand, has elicited the least TTA-UC emission due to its high T_m of 23 °C and associated diffusivity value of 3.5 $\mu m^2 s^{-1}$. The integrated area under the peak centred at 443 nm was assessed for quantitative purposes and shown as a bar plot in Figure 2.14.
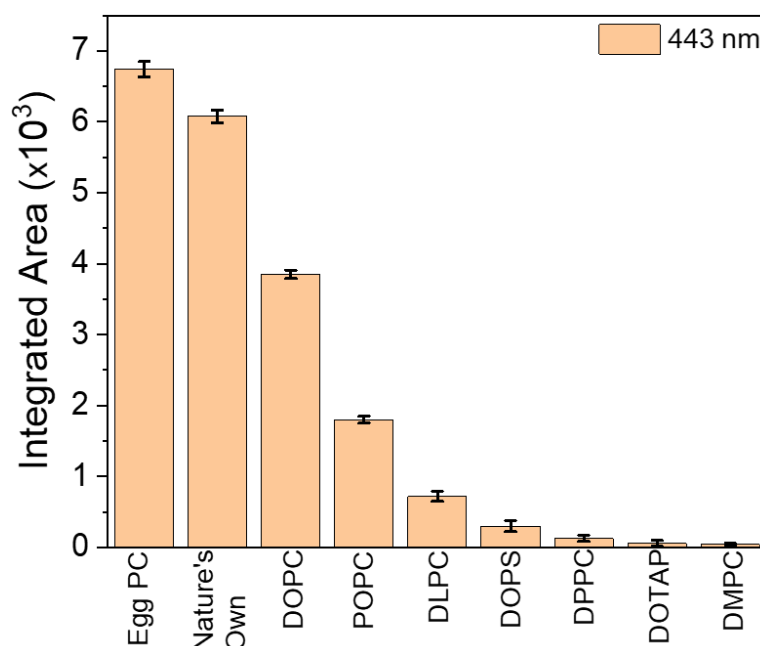
Figure 2.14 Comparison bar diagram of integrated mathematical area of 443 nm peak in different liposomes containing 0.25 µM B2PI and 2.5 µM perylene (n=3).

Role of alkyl chain length: To assess the effect of alkyl chain length on TTA-UC intensities, three membrane compositions, DLPC (C12), DMPC (C14), and DPPC (C16) liposomes, were compared. The TTA-UC of the B2PI-perylene combination of these three compositions is depicted in Figure 2.13b. It was observed that DLPC had the highest TTA-UC signal of the three, but when compared to DLPC, the signal in DMPC was decreased by 90%. Although DPPC produced a reasonably good signal at 443 nm, the peak at 473 nm was broadened and no quantification could be performed. At ambient temperature (22±1 °C), the difference in intensity observed is due to DLPC (C12) being more fluidic than DMPC and DPPC (cf. Table 2.3). Given the gel like behaviour of DPPC (C16), the UC intensity should be substantially lower than the DMPC intensity, but this does not appear to be the case, as higher UC emission

intensity was detected for DPPC. This behaviour was found to be even more surprising when the relative intensity of DLPC and DPPC was compared at 443 nm and found that they are nearly similar to one another. The broadening of the red shift band at 473 nm may be due to gel-like phases formed by higher alkyl chain length failing that render the optimal spacing between the TTA-UC pair. To understand this unexpected behaviour DLS was carried out to see if aggregation is occurring and the results shown in Figure 2.15 indicate that DPPC liposomes have a very big hydrodynamic diameter compared to other liposomes. So, the anomalous behaviour of DPPC in the TTA-UC emission could also be due this large size, which may be due to aggregation of the liposomes or simply that large LUVs are formed. Figure 2.16 shows that DPPC has high scattering in absorption spectra and the emission is very poor in B2PI loaded DPPC liposomes which may be due to Mie scattering due to their large size. Why this impedes TTA-UC is unclear, but it may be that the scattering obscures the emission or that the gel phase which promotes aggregation is not fluid enough to support collision.
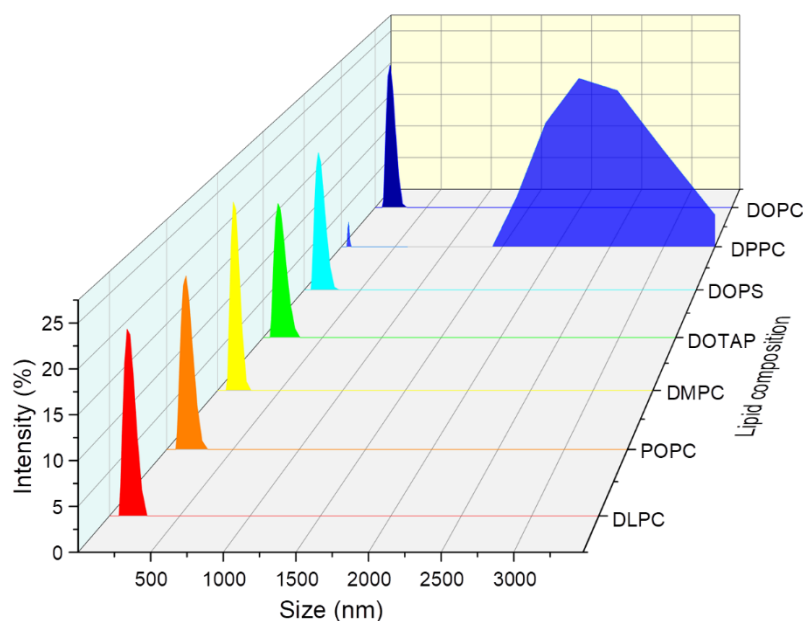
Figure 2.15 Dynamic light scattering data of different liposomes containing 0.25 µM B2PI and 2.5 µM perylene.
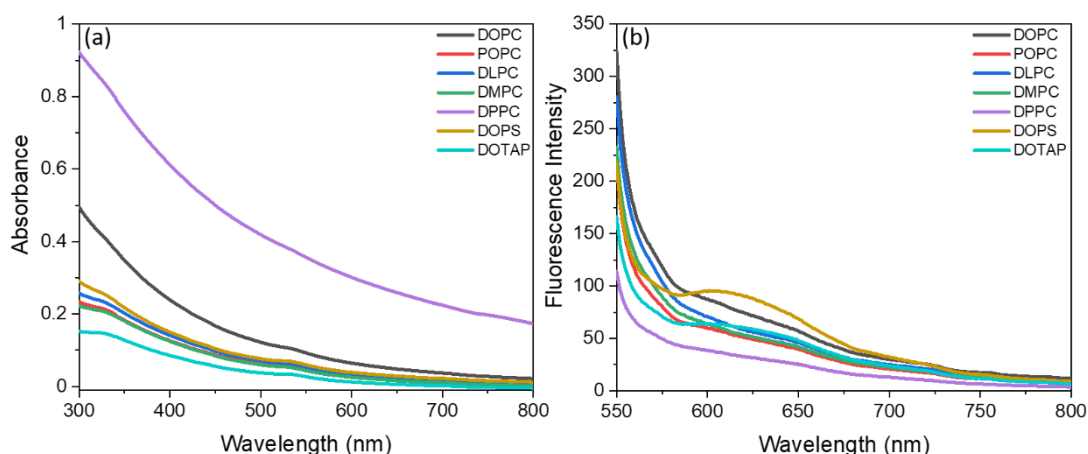
Figure 2.16 (a) Absorption and (b) emission spectra of 0.25 µM B2PI in different liposomes.

Role of membrane charge: Figure 2.13c illustrates the impact of membrane charge on TTA-UC. In this context, three different sets of liposomes were prepared comprising the neutral (DOPC), negatively charged (DOPS), and positively charged (DOTAP) lipid membranes. As expected DOPC, the neutral lipid has the highest UC intensity when compared to DOPS, whereas DOTAP has the lowest UC intensity. At physiological pH of 7.4, B2PI and perylene are neutral, however, the electrostatic interaction between COO^- of DOPS and N^+ of B2PI contributes to the modest UC signal. The electrostatic repulsion between the $(CH_3)_3N^+$ of DOTAP and N^+ of B2PI could explain the low UC intensity in the instance of DOTAP.

Table 2.3 Different parameters of lipids used in this work along with phase transition temperature, mathematical area of the integration of 443 nm peak, and diffusion coefficient measured using FLCS.

Lipid	Lipid Conc (mM)	Phase Transition Temp (^{0}C) ^aT_m	Alkyl Chain Length & double bond	Diffusion co-efficient, D ($\mu m^2 s^{-1}$) DOPE-Atto655	Integrated area of 443 nm peak
DOPC	1.272	-17	18:1	9.6	3848
POPC	1.272	-2	16:0-18:1	8.7	1802
DLPC	1.272	-2	12:0	7.4	719.47
DMPC	1.272	24	14:0	3.5	43.06
DPPC	1.272	41	16:0	NA	127.60
DOPS	1.272	-11	18:1	9.5	302.841
DOTAP	1.272	<5	18:1	7.2	57.27

Egg PC	1.272	8.2	6742
Nature's own	1.272	7.8	6076

2.4.7 TTA-UC at highly plasma membrane mimetic biomembranes

In considering the prospect of TTA-UC at biological membranes, it was finally examined whether TTA-UC could be observed at more typically biomimetic membranes. It is difficult to exactly mimic the enormous complexity of the eukaryotic cell membrane and its asymmetry in liposomes. Nonetheless TTA-UC was investigated using phosphatidylcholine total extract that is expected to partially mimic the eukaryotic membrane, as it is comprised of a biomimetic mixture of different alkyl chain lengths of different unsaturated and saturated alkyl chains.[366] This lipid extract is expected to contain some of the nanoscale phase domains in the membrane.[367] As can be seen in Figure 2.13d, remarkably intense TTA-UC was observed from egg PC liposomes with more than 60% increase from the TTA-UC intensity of DOPC liposomes. Further extending to the higher mammalian plasma membrane (MPM) mimetic lipid compositions for TTA-UC study, a membrane composition containing 32% DOPC, 25% DOPE, 20% cholesterol, 15% SM, and 8% DOPS which was coined 'Nature's Own' by Lentz– et al. was chosen. Since MPM composition is highly fluidic in nature, high UC intensity was observed (Figure 2.13e).[368,369] One of the reasons that speculate the efficiency remains high in such complex membranes is the propensity for the photosensitizer to localise in the L_d phase. This phase is expected to be the most fluid and so it will promote diffusional collision required for TTA-UC as well as condense the concentration of the photosensitizer and annihilator into the L_d domains promoting their collision probability.

2.5 Conclusions

Novel pairs of photosensitizers and annihilator for efficient triplet-triplet annihilation upconversion (TTA-UC) was established. BODIPY-2-Peylene-Iodine (B2PI) shows a good efficiency towards TTA-UC and BODIPY-2-Perylene (B2P) also exhibits good performance as a photosensitizer for a heavy atom free photosensitizer. Initially, the photophysical properties of both photosensitizers, B2P and B2PI and annihilator were studied in solution and observed that these pairs have the propensity to yield efficient upconversion due to their spectral overlap. The threshold power density (I_{th}) measurement further supported this where a deviation of slopes from quadratic behaviour to linear regime (slope 2.0 to slope 1.0) occurred at different points with lower value for B2PI which occurred at 51 mW cm^{-2} compared with

126 mW cm^{-2} for B2P. The lower I_{th} value of B2PI indicated that it has higher efficiency towards TTA-UC. Nanosecond transient absorption spectroscopic studies were performed on B2P and B2PI to investigate the triplet lifetimes and three different lifetimes were observed for both B2P and B2PI which corresponds to triplet charge transfer state (^{3}CT), BODIPY-centred triplet and perylene centred triplet. For B2PI those three lifetimes are 60 µs, 525 µs and 1500 µs and for B2P, they are 80 µs, 900 µs, and 2500 µs. The reduction in triplet lifetimes after the addition of perylene confirms the quenching by triplet energy transfer and annihilation processes. TTA-UC experiments were carried out in dioxane solution followed by reconstitution of upconversion pair in different membrane models such as LUV, GUV and the study shows that both B2P and B2PI are good photosensitizers with more efficiency from B2PI. The dependence of TTA-UC on viscosity was studied for the first time in liposomes by reconstituting the photosensitizer-annihilator pair into liposomes of different composition across a range of measured (by FLCS) diffusivities and the results shows that TTA-UC decreased on increase of viscosity. Among the liposomes studied, the highly fluidic zwitterionic DOPC membrane elicited most efficient TTA-UC intensity.

Finally, the study was extended into more complex biomembrane compositions that mimic the mammalian plasma membrane compositions to understand, notwithstanding much greater complexity in the mammalian membrane, if we might expect that if the pairs could be reconstituted together into cell membranes, might we expect to see TTA-UC, and indeed efficient TTA-UC was observed. The overall study suggests that the TTA-UC may be possible in the real cell membrane by liposome formulation with the newly developed photosensitizers.

Chapter 3

Role of phospholipase A$_2$ modulating Triplet-Triplet Annihilation Upconversion of B2PI-perylene pair within Model Biomembrane

3.1 Introduction

Phospholipid metabolism is an essential metabolic activity in all living organisms that occurs through specific signalling pathways.[370,371] Due to their strong catalytic ability to hydrolyse, one of the lipid-associated enzymes, phospholipases, play an important physiological and pathological role. Based on the phospholipid substrate hydrolytic sites (scheme 3.1), the enzymes phospholipases A_1, A_2, C, and D produce small molecules from phospholipid cleavage that play crucial functions as mediators in cellular metabolism.
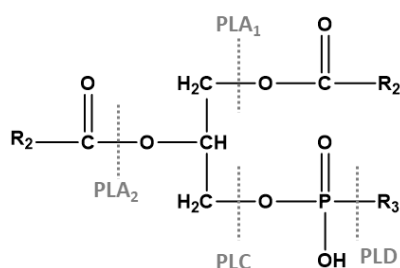
Scheme 3.1 The cleavage sites of phospholipases (A_1, A_2, C and D) acting on phospholipids ($R_3=$ choline, serine, ethanolamine, inositol etc; R_1 and R_2 are the acyl chains and can be varied in terms of its saturation or chain length. Depending on the phospholipase types its action on phospholipids can result in free fatty acids and lysophospholipids (PLA_1 and PLA_2), diacylglycerol (PLC) and phosphatidic acids (PLD).

Acyl groups at the sn-2 position of glycerophospholipids are largely polyunsaturated and serve as substrates for oxygenases that form eicosanoids and docosanoids, lipid mediators that play important roles in regulating cell immune functions and inflammatory response, and thus PLA_2s have garnered considerable attention over the years. PLA_2 enzymes are divided into four classes based on molecular mechanisms that differ on the basis of factors including, cellular localization, substrate selectivity, and calcium dependence. Cytosolic PLA_2 ($cPLA_2$), calcium independent PLA_2 ($iPLA_2$), secreted PLA_2 ($sPLA_2$), and platelet activating factor acetyl hydrolases are the four types. Each variety of PLA_2 has distinct molecular structures and mechanisms of action, and they have varied calcium demands and associations with different receptor-mediated signalling pathways depending on the cell type.[372] Phospholipase A_2 (PLA_2) overexpression has been linked to the development and spread of cancers including notably gastrointenstinal, colon, breast and prostate cancers.[373–375]

PLA_2 is water soluble and catalyze the deacylation of glycerophospholipids at the sn-2 position, resulting in the formation of two lipid mediators—fatty acid derivatives and lysophospholipids—that function as signalling molecules in a wide range of cancers.[376] Several

studies indicate that PLA_2 is interfacially activated, meaning that its activity increases when the substrate is presented in an aggregated form (vesicles, bilayer, etc.) rather than in its monomeric form.[377] Additionally, lipid domains and defects in the bilayer significantly impact the hydrolysis activity on vesicular substrates. Atomic force microscopy (AFM) analysis has revealed that these defects often take the shape of holes in the bilayer.[378] It is anticipated that the development of enzyme-sensitive amphiphilic prodrugs and their nanoassemblies might be useful as a novel approach towards effective delivery of anticancer drugs.[379]

However, despite many studies linking PLA_2s to immune cells and inflammatory diseases in the peripheral lymphoid tissues,[380] studies on specific PLA_2 in the CNS are relatively limited due to the complex makeup of different cell types in different brain regions. It is still difficult to decipher the chemical mechanisms underlying PLA_2 action in the intricate cellular setting in which it operates. Furthermore, no findings on liposomal based drug delivery mediated by PLA_2 to various target sites have been found in the setting of targeted therapeutics. This is because the fluorophores used in conventional fluorescence-based imaging/spectroscopy approaches are easily photobleached during high power radiation approaches like those used in photodynamic therapy (PDT) or chemotherapy, making it difficult to gain useful information using these methods. To circumvent this issue, as discussed earlier in chapter 2, although TTA-UC based approaches are promising in this context, prior to optimising a condition where the drug is delivered to the target site via liposomal based drug delivery vehicle mediated by PLA_2 with an incorporated TTA-UC pair, it is critical to understand the molecular basis of PLA_2 action and its impact on TTA-UC efficiencies at simplified biomimetic model liposomal membrane. To date, most PLA_2 binding, and kinetics research has been done in simpler bulk phospholipid dispersions[381] or in Langmuir monolayers at the air-water interface[382–385] or in supported lipid bilayer (SLB)[386–390] systems. In addition, while the rate of product generation can be tracked in a vesicle or micelle dispersion,[391] the position of the enzyme or the distribution of reaction products between the surface and bulk phases are difficult to predict. Whilst monolayer based studies at the air/water interface however only mimic half of the membrane, supported lipid bilayers though a better mimic and accessible to various surface sensitive interrogation, experience friction due to the underlying substrate that impede the lateral movement of lipids or reconstituted species. In contrast, free-standing giant unilamellar vesicles (GUV) offer a useful model membrane due to lack of any substrate effects and due to their large size, they are suitable for (bio)imaging. Although studying the lateral diffusion of membrane lipids, proteins, photosensitizer, annihilator etc. within the GUVs are indeed

possible, they are challenging for example in fluorescence lifetime correlation spectroscopy (FLCS) studies, because of difficulty in maintaining the focus of the confocal volume on a single bilayer due to the movement of the vesicles.[392] Spatially resolved FLCS studies are beneficial in resolving the dynamics of analytes such as TTA-UC pairs, membranes, and drugs in particular locations. Previously, for example, exploiting palladium tetraphenyltetrabenzoporphyrin complex as photosensitizer and perylene as the annihilator reconstituted within GUVs composed of either DOPC or DMPC, Askes et al. were able to image the membrane under red-to-blue light upconversion.[246] In another report, exploiting large unilamellar vesicles (100 nm size) of DOPC, DMPC, and DSPC etc. Poznik et al. have studied TTA-UC upon reconstituting platinum porphyrin PtOEP and an amphiphilic derivative of tris-(bipyridine) ruthenium(II) as photosensitizers and lipophilic diphenylanthracene as annihilator.[393] The above studies not only provided a means for successful membrane reconstitution, but also shed light on how to design suitable chelating ligands and/or select metal complex centre as a lipophilic photosensitizer for efficient TTA-UC in presence of an annihilator. The reconstitution and selection of membrane composition and its intrinsic fluidity are just as important for efficient TTA-UC as the latter component. This was confirmed in chapter 2, showing that a more fluidic membrane (low viscosity environment) lead to more efficient TTA-UC than a less fluidic membrane (high viscosity environment), which is crucial when designing a model for bioimaging and finding a suitable nanocarrier that can reach the target site. Although, from the above study one could easily select out a highly fluidic membrane nanocarriers based on its low melting transition temperature (e.g., DOPC, $T_m = -17$ °C), however, under cellular environment at the target site, the influence of external bioagents such as proteins, enzymes, metal salts can alter the fluidity of such membrane. To date, however, no studies have been performed exploring how PLA_2 modulates the fluidity of a single-component membrane or its impact on TTA-UC. Since the lipid fluidity is the main modulator for efficient TTA-UC, understanding the change in fluidity pertaining to PLA_2 action and its hydrolytic product organization could provide an experimental testbed for optimizing efficient liposomal nanocarriers for targeted therapy and in vivo or in cells alteration to TTA-UC might be an interesting way to understand changes to the fluidity of a liposome or its disruption.

In chapter 2 it was demonstrated that a combination of a new iodinated BODIPY derivative (B2PI), which was synthesized in our laboratory and a known perylene annihilator results in considerable TTA-UC in solution and in the membrane of a liposome. In addition, its TTA-UC

efficiency was measured in a range of model liposomal membranes of variable viscosity in Chapter 2 and found that it maintains its greatest level in low-viscosity (highly fluidic membrane composition) environments. In principle, in applying liposomal drug delivery vehicles it is expected that at the tumour site, the liposome would undergo hydrolysis catalysed by PLA_2 to form sn-1-ether lysophospholipid, a powerful membrane disruptor that itself can be employed to destroy cancer cells. But the key principle is that as the liposome disrupts under the enzymolysis, the cancer medicines are released. As a result, the lysophospholipids and the medicines launched a combined assault on the cancer cells. Indeed, liposomal drug delivery methods that exploits the PLA_2-induced release of encapsulated medicines have been reported.[394–397] Hence in order to quantify the efficient TTA-UC in presence of PLA_2 in the liposomal membrane, it is also equally important to unravel the PLA_2 mediated membrane organization, underlying phospholipase kinetics, role of Ca^{2+} and inhibition etc. at a more biomimetic model membrane which is free of any substrate effect. In this context, microcavity based pore-suspended lipid bilayer (MSLB) which is amenable to various surface sensitive techniques such as single molecule-based fluorescence lifetime correlation spectroscopy, fluorescence lifetime imaging, and label-free electrochemical impedance spectroscopy etc. will provide valuable insight underlying the membrane reorganization before and after PLA_2.

3.2 Aims and objective

The normal function of lysosomes in lipid metabolism is critical for understanding phospholipidosis (PLD). Lipids enter lysosomes through a variety of mechanisms, including autophagy of organelles such as the endoplasmic reticulum and mitochondria, and endocytic routes such as receptor-mediated endocytosis of lipoproteins. The most important function of lysosomes in lipid metabolism appears to be lipid degradation, which is carried out by various enzymes, one example being glycerophospholipid ester hydrolysis by phospholipase A_2 (PLA_2). Understanding PLD and its inherent biophysical role of fluidity in efficient triplet-triplet annihilation upconversion (TTA-UC) is important for targeted therapeutic purposes.

This work presents a robust technique for demonstrating efficient TTA-UC using B2PI-perylene at a liposomal model membrane without and with the presence of PLA_2. The study will focus on whether the presence of PLA_2 and Ca^{2+}, the phospholipid's metabolite, lysophopholipid causes a change in packing of the overall bilayer; and if this change in membrane packing modulates the TTA-UC efficiency in single component DOPC liposomes.

In the presence of imipramine, a competitive inhibitor of PLA$_2$, or in the absence of Ca^{2+}, the change in enzymatic action will be studied.

Further characterization of Ca^{2+} dependent enzymatic activity and drug-based inhibition studies needs to be performed using confocal-based fluorescence lifetime imaging (FLIM), fluorescence lifetime correlation spectroscopy (FLCS), and electrochemical impedance spectroscopy (EIS) to investigate the role of Ca^{2+}, effect of inhibitor, and to see how PLA$_2$ modulates the lipid packing. The EIS study can reveal about the change in thickness of the bilayer. Nanoscale imaging using atomic force microscopy (AFM) in liquid mode at a mica-supported lipid bilayer is used to further confirm the PLA$_2$ caused lipidosis in presence of Ca^{2+}, and to observe any change in membrane morphology due to PLA$_2$ induced lipid hydrolysis. Overall, this chapter aims to provide a molecular basis for enzymatic action at a true biomimetic pore-suspended bilayer model membrane and how the resulting hydrolytic product influenced TTA-UC efficiencies. Understanding the aforementioned element will provide a better understanding of the targeted therapeutics during liposomal mediated drug delivery and may even indicate TTA-UC as a useful means of monitoring liposome properties and integrity in cellulo and in-vivo.

3.3. Materials and methods

3.3.1 Materials

B2PI was synthesized according to the protocol mentioned in Reyes et al.[336] Perylene was purchased from Sigma Aldrich. PLA$_2$ was from Sigma. 1,2-dioleyl-*sn*-glycerophosphocholine (DOPC) in powder form were purchased from Avanti polar lipids (Instruchemie, The Netherlands). 1,2-dioleoyl-*sn*-glycero-3-phosphoethanolamine labeled ATTO655 (DOPE-ATTO655) and ATTO532 (DOPE-ATTO532) was purchase from ATTO-TEC GmbH (Siegen, Germany). Polydimethylsiloxane silicon elastomer (PDMS) was purchased from Dow Corning GmbH (Wiesbaden, Germany). Gold disk electrodes consisting of silicon wafers coated with a 100 nm layer of gold on a 50 Å layer of titanium adhesive were obtained from AMS Biotechnology Inc. Monodisperse polystyrene latex spheres of different sizes were obtained from Bangs Laboratories Inc. The commercial cyanide free gold plating solution (TG-25 RTU) was obtained from Technic Inc. All other HPLC grade reagents were obtained from Sigma-Aldrich and used as obtained. Ultra-pure water with a resistivity 18.2 MΩcm was produced by a Milli-Q (Millipore Academic) system and used for buffer preparation. Tris-HCl buffer was prepared using trisaminomethane, purchased from Sigma Aldrich to a final concentration of

0.1 M and the pH was adjusted to 7.4 using HCl. 0.1 M NaCl was also added and the buffer was stored in refrigerated conditions.

3.3.2 Fabrication of gold and PDMS microcavity array

Polystyrene (PS) microsphere lithographic techniques were used to fabricate both gold and PDMS microcavity array electrodes, as reported previously.[193,355] In brief, gold coated silicon wafer electrodes were initially cut into ~1 cm ×1.5 cm and cleaned by washing with tetrahydrofuran (THF), ethanol and drying under mild stream of high pure N_2. After that, the electrodes were plasma treated for 5 min to make the gold surface hydrophilic. Following plasma treatment, the gold substrate was placed over chamber in a slanted manner and calculated amount of 1% (v/v) of PS spheres (1 μm diameter) aqueous solution were drop cast over the gold chip. Then, a coverslip was placed over it in such a way that the PS sphere uniformly covers across the whole gold surface area and sandwiched within gold and coverslip. The substrate was left unshaken overnight to evaporate the aqueous solvent in a sealed box with dry silica in it and this generates a hexagonally close packed self-assembled microsphere array as shown in Figure 3.7a. Next, controlled potential (-0.6 V vs. Ag/AgCl (1 M KCl)) electrochemical deposition of gold was carried out over a ~1 cm×1 cm area until when gold deposited from cyanide free gold solution and deposited surrounding each 1 μm sized PS sphere that reached precisely 0.5 μm thickness. The thickness was controlled using the shape of a well characterised amperometric I-t curve (Figure 3.7c). After gold deposition, the substrate was rinsed with Milli-Q water and subsequently electrochemically cleaned by sweeping the potential from -0.2 to 1.6 V (3 cycles) in 0.05 M H_2SO_4 using cyclic voltammetry. This step results removal of the top oxide layers and helps self-assembled monolayer formation. The substrate was then rinsed with milli-Q water, dried under N_2, and soaked for at least 48 hrs in an ethanolic solution of 1 mM 6-Mercapto-1-hexanol (MH) to form self-assembled monolayer (SAM). During these steps, the PS spheres template remained in place hexagonally ordered throughout and allowed MH SAM formation exclusively to the interstitial planar top gold regions (Figure 3.7a, step iv, vide infra). The chemical modification of the substrate renders top gold surface hydrophilic due to the terminal -OH group of MH. After SAM formation, the substrates were washed with copious amount of ethanol to remove any unbound thiols and further washed multiple times with THF. The THF wash step results in the complete removal of PS spheres leaving periodic micropore arrays with pore diameters of 1 μm and 0.5 μm depth with SAM at the interstitial planar regions. Before and after PS removal

steps were confirmed using cyclic voltammetry. The cavities were then PBS buffer filled and used for bilayer formation for electrochemical impedance study.

For fluorescence lifetime imaging (FLIM) and fluorescence lifetime correlation spectroscopy (FLCS) studies, the arrays were prepared using optically transparent PDMS substrate. Freshly cleaved mica sheets of a few micrometres in thicknesses (height, h) were cut to ~1 cm (length, l)×1 cm (breadth, b) dimension and glued to glass cover slides. 20 µL of ethanolic 4.61 µm PS solution (0.1% v/v) was drop cast onto the mica surface. The hexagonally packed array was formed spontaneously after ethanol evaporation and behaved as master mould. Next, PDMS casting over this mica supported PS array mould was performed and cured at 90 °C for 1 hour. After the curing process was completed, the PDMS was gently peeled off the mica-containing glass cover slip holding the PS array. The thin chamber created at the PDMS has identical dimensions given by the mica sheet thickness, making it ideal for confocal imaging and spectroscopy. The microcavity array was then formed by dissolving the PS sphere template from the PDMS substrate in tetrahydrofuran (THF) for 15 min via sonication. During the THF treatment, PDMS substrate was swollen a bit and upon drying overnight in vacuum, it regained its usual size with the resulting micropore cavity hexagonal array with a pore diameter of ~2 µm and pore depth of ~0.5 µm confirmed by AFM. The PDMS substrates were plasma cleaned for 5 min to make the surface hydrophilic and the microcavities were buffer filled by sonication and stored inside buffer for further use.

3.3.3 Liposome preparation

Large unilamellar vesicles (LUV) or liposomes were prepared by the hydration extrusion method. The DOPC lipid dissolved in chloroform was mixed with desirable concentration of photosensitizer and annihilator or with 0.01% DOPE-ATTO655 into a 1.5 mL vial. The solvent was evaporated under N_2 flow and complete evaporated completely by putting the reaction vial in vacuum for 30-60 min. A thin lipid film was obtained along the sides of the vial and it was hydrated with 1 mL Tris-HCl buffer followed by 60 s of vortexing to mix the solution thoroughly. The solution was extruded through a polycarbonate membrane of 100 nm pore size at least 11 times or more as required. The hydrodynamic diameter the liposomes were measured by dynamic light scattering in a Malvern Zetasizer Ultra instrument. The vesicle solutions are stored at 2 °C and used within 3 weeks of preparation.

3.3.4 Fabrication of microcavity suspended lipid bilayers

The assembly of lipid bilayer spanned across the aqueous filled microcavity array, both gold and PDMS array substrates were achieved by using a combination of Langmuir-Blodgett transfer followed by vesicle fusion (LB-VF) method, as shown schematically in Figure 3.8a. Briefly, in order for a Langmuir-Blodgett transfer, 50 μL of 1 mg/mL of DOPC dissolved in chloroform was added dropwise to the Langmuir trough (KN2006, KSV-NIMA technology). A lag time of 10 min was set before compressing and decompressing the lipid monolayers (two times each) below the collapse surface pressure. Next, the monolayer is compressed until the surface pressure is reached 33 mN/m and allowed to equilibrate for at least 5 min at the designated surface pressure. Then, the buffer filled gold and/or PDMS which was submerged in the LB trough using a clip holder was vertically pulled from the water surface at a speed of 5 mm/min resulting a transfer of a single layer of lipid as proximal leaflet. For distal leaflet, vesicle fusion (VF) method was carried out. The fusion process on gold was carried out immediately by submerging the LB transferred monolayer spanned array into the LUV solution (0.2 mg/mL) and allowing it to fuse for at least one hour. For PDMS substrate, the monolayer spanning PDMS substrate was sealed within a microfluidic chamber and subjected for vesicle fusion. For fluorescence-based imaging and spectroscopy, the liposomes are doped with 0.01 mol% of DOPE-ATTO655. After VF processes completed, the substrates were washed with Tris-HCl buffer gently to remove any unfused vesicles and at no scenario, the membranes are exposed to air.

3.3.5 TTA-UC Measurements

The TTA-UC measurements were carried out on the same fluorescence spectrophotometer using an additional laser purchased from Edmund Optics with 532 nm excitation of 10 mW power with 1 mm diameter beam with 1.27 Wcm^{-2} power density. The TTA-UC measurements were performed in the fluorescence spectrophotometer by blocking the excitation line in bioluminescence measurement mode. The upconverted emission measurements in liposomes was carried out by deaerating the sample by purging N_2 in a quartz cuvette of 1 cm pathlength. For the activation of enzyme, calcium chloride dihydrate was added to the liposome solution and incubated for 15 min. The upconverted emission was recorded across the range 400 to 500 nm to avoid the interference from the excitation source.

3.3.6 Electrochemical Impedance Spectroscopy

Electrochemical measurements were performed with a CH760A potentiostat (CH Instruments, USA). A standard 3-electrode cell comprised of gold microcavity suspended bilayer as working electrode, an Ag/AgCl (1 M KCl) reference electrode and a platinum wire auxiliary electrode. The EIS data were measured over a frequency range of 0.05 to 10^5 Hz with an AC modulation amplitude of 0.01 V at a potential DC bias of 0 V (vs Ag/AgCl). All measurements were carried out in a glass cell (approximate volume of 4 mL) in contact with Tris-HCl buffer maintained at pH 7.4. The EIS of the aqueous filled microcavity array coated with the lipid bilayer was measured initially prior to the addition of PLA_2 to ensure signal stability. The non-Faradaic EIS signal from the MSLBs was evaluated for stability and it was found that when initially placed in contact with the Tris-HCl buffer at 0 V an initial fluctuation of resistance is seen that stabilizes within an hour and then remains unchanged over a prolonged window (24 h). A time lag of 60-90 min was allowed for bilayer to equilibrate and following which additional 30 min was allowed for incubation of Ca^{2+} prior to the addition of PLA_2. Each EIS measurement takes approximately 4 min and was carried out at room temperature (22±1 °C). The measured data were analysed using Z-View software applying the equivalent circuit fitting model (ECM) (Figure 3.9a, inset) that was established and tested previously as a good model for the MSLB[152] Using this approach, membrane resistivity and capacitance values before and after PLA_2 binding can be estimated. The circuit consists of a parallel combination of solution resistance (R_s) and capacitor in series with a parallel combination of constant phase element, CPE (C_{array}) and a cavity resistive element (R_{array}) of the microcavity array, and the membrane is approximated by a resistive element (R_M) in parallel with a CPE (Q_M). A Constant Phase Element (CPE) is used in the equivalent circuit instead of pure capacitors as the impedance of solid electrodes usually deviates from pure capacitor due to microscopic chemical inhomogeneity on both the electrode surface and in the lipid bilayer. Depending on the composition, as described below, from EIS, the bilayer resistance for an intact bilayer range from 2 to 10 MΩ (compared to kΩ resistance of SAM modified cavity array prior to bilayer deposition). It is previously shown that this resistance range corresponds to an intact SLB and so used the resistance values to validate the bilayer prior to measurement.[195]

3.3.7 Fluorescence lifetime imaging and fluorescence lifetime correlation spectroscopy

Fluorescence lifetime imaging (FLIM) and fluorescence lifetime correlation spectroscopy (FLCS) experiments were performed using a MicroTime 200 system (PicoQuant GmbH,

Germany) consisting of FCS module, dual SPD detection unit, time-correlated single photon counting (TCSPC), and inverted microscope model Olympus X1-71 with an Olympus UPlan SApo 60×/1.2 water immersion objective. Before FLIM, reflectance images were collected using an optical density (OD3) filter which assesses the buffer filled cavities. The fluorescently labelled lipid probe DOPE-ATTO655 was excited using pulsed picosecond lasers at 640 nm LDH-P-C-640B. A single mode optical fibre guides the laser to the main unit and provides a homogeneous Gaussian profile. The laser was pulsed at 20 MHz, corresponding to an interval of 50 ns. The emitted fluorescence was collected through the same microscope objective and dichroic mirror z532/635rpc blocked the back scattered light and HQ670lp AHF/Chroma filter for 640 nm was used to clean up the signal. Fluorescence was detected using a single photon avalanche diode from MPD (PicoQuant). The TCSPC system (PicoHarp 300 from PicoQuant) enabled simultaneous assessment of the lifetime in a nanosecond range along with the time of diffusion in the millisecond range. A 50 μm pinhole was used to confine the volume of detection in the axial direction whilst blocking all off-focal-plane light. Leaflet by leaflet characterization of MSLB over gold and PDMS substrate was achieved by doping the leaflets individually with two different fluorescently labelled lipids that are not spectrally overlapped. The proximal leaflet was doped with 0.05 mol% of DOPE-ATTO532 during LB transfer step, and the outer leaflet of the bilayer was doped with 0.05 mol% DOPE-ATTO655 during the LUV preparation step. FLIM image from proximal leaflet was excited using 532 nm laser, PicoTA from Toptica (PicoQuant) and the fluorescence signals filtered through HQ550lp AHF/Chroma. A representative FLIM images of proximal and distal leaflet of DOPC MSLBs that spanned over gold and PDMS array are shown in Figures 3.8c and 3.8d respectively.

Spatially resolved point fluorescence lifetime correlation spectroscopy measurements were carried out from the centre of PDMS based MSLB cavity array, where the upper leaflet of bilayer was doped with 0.01 mol% of DOPE-ATTO655. Point FLCS measurements were then recorded for 30 s per cavity, with an average of 40-50 cavities were studied for every bilayer and enzyme type. All measurements were recorded at room temperature 20±0.4 °C. The fluorescence fluctuation intensity is multiplied by a time shifted replica of varying values (lag time, τ) and the temporal averages yields autocorrelation function (ACF), G (τ) for the respective lag time. The ACF obtained from the bilayer spanned over 2D PDMS array is fitted using eq. (3.1).

$$G_{2D}(\tau) = \frac{1}{N}\sum_{i=1}^{m} \left(1 + \left(\frac{\tau}{\tau_{Di}}\right)^{\alpha}\right)^{-1}$$ (3.1)

where, τ_{Di} is the translational transit time of the ith fluorescently diffusing species during in and out from the confocal volume, α is anomaly coefficient typically indicates when the diffusion is Brownian ($\alpha=1$) or not ($\alpha \neq 1$). After knowing, the transit time, the diffusion coefficient (D) was determined using eq. (3.2),

$$D = \frac{\omega_0^2}{4\tau_D}$$ (3.2)

where, ω_0 is the waist diameter of the confocal beam determined as $1/e^2$ of 0.135 and obtained by calibrating the microscope system with an aqueous solution of ATTO655 with known diffusion coefficient value diffusing freely in 3D.

3.4 Results and discussion

3.4.1 TTA-UC Results

To understand if TTA-UC efficiency is influenced by enzymatic hydrolysis of DOPC phospholipid by phospholipase A$_2$ (PLA$_2$), both 0.5 μM B2PI and 5 μM perylene were embedded as TTA-UC pair within the DOPC liposome. Upon 532 nm laser excitation, an anti-Stokes emission peak centred at 444 nm and 474 nm (Figure 3.1a) was observed. Unlike in chapter 2, where TTA-UC on DOPC liposomal membranes was studied, the current experimental setup uses Tris-HCl (pH 7.4) instead of PBS, because enzymatic activity is highly dependent on the presence of Ca^{2+}, and in PBS Ca^{2+} forms complex with phosphate ions, causing it to precipitate, whereas Ca^{2+} is completely soluble in Tris-HCl.

Before studying Ca^{2+} dependent phospholipase A$_2$ hydrolysis and its role in TTA-UC, control experiments are performed to see if Ca^{2+} ion has any impact on TTA-UC. When 5 mM Ca^{2+} was added to the DOPC liposome containing TTA-UC pair, the upconversion intensity is modestly increased (red, Figure 3.1a) compared to the liposome without Ca^{2+} (black, Figure 3.1a). Next, 5 μM PLA$_2$ was added to the liposome and monitored the upconversion at time intervals of 10, 30 and 60 min. As shown in Figure 3.1a, the upconversion emission signal gradually decreases with respect to time. To express the changes quantitatively, the extent of decrease in upconversion emission intensity was shown in bar plot in Figure 3.1b. As discussed in chapter 2, a correlation between membrane fluidity and upconversion efficiency is expected, for example a decrease in upconversion emission for B2PI-perylene pair was observed at highly saturated phospholipids such as DMPC or DPPC liposomes due to their saturation /gel phase. DOPC was observed to promote highest TTA-UC efficiency attributed to its high fluidity. Here, the decrease in upconversion emission in presence of PLA$_2$ may be due to greater packing

of lysophospholipids and fatty acid in the liposome as the catalytic product of DOPC. Further confirmation of PLA2-mediated increase in lipid packing is provided by FLCS studies, which are covered in the next section (*vide infra*).
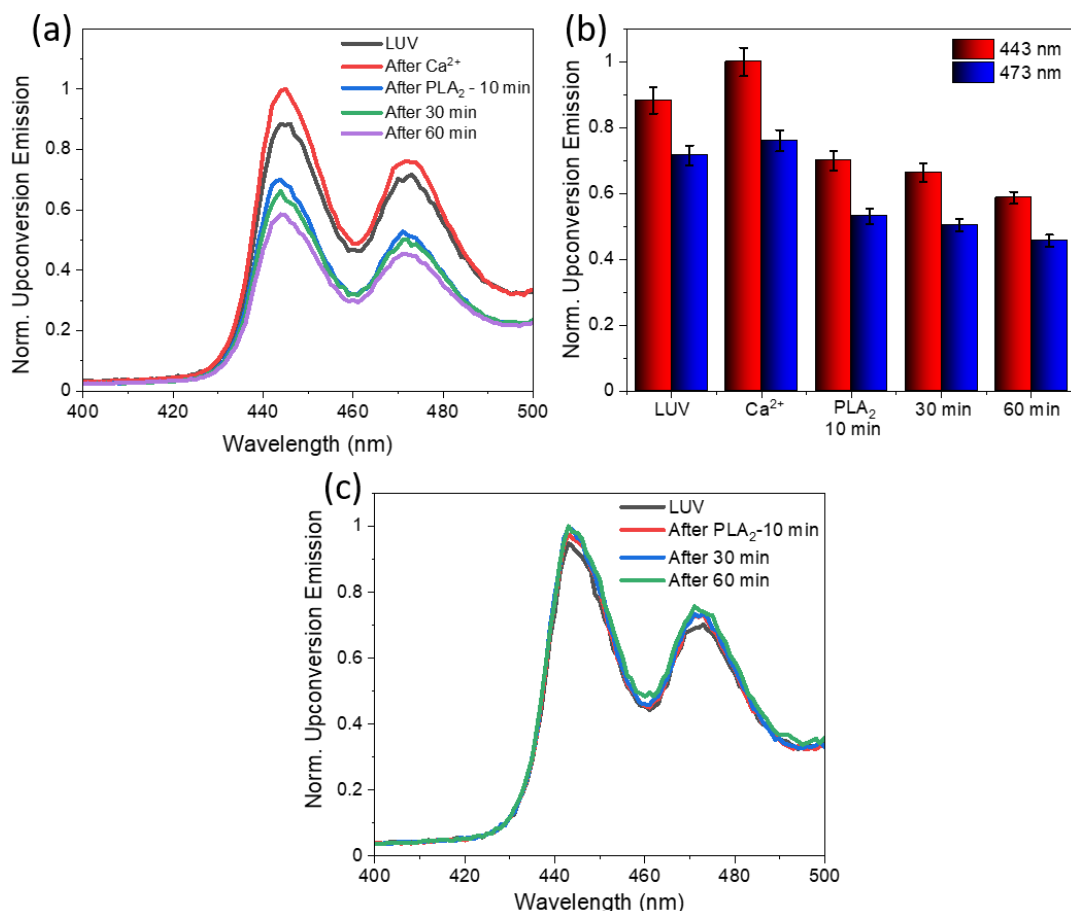
Figure 3.1 (a) Normalised TTA-UC emission spectra from DOPC liposomes incorporated with 0.5 µM B2PI and 5 µM perylene before (black) and after (red) the addition of 5 mM Ca^{2+} and after the addition of 5 µM PLA2 measured at 10, 30 and 60 min. (b) Corresponding intensity histogram of each spectra in panel (a) and (c) control measurement of DOPC liposomes incorporated with 0.5 µM B2PI and 5 µM perylene with the addition of 5 µM PLA2 in the absence of Ca^{2+}. All liposomes are in deaerated Tris-HCl buffer of pH 7.4. All samples were excited with a 532 nm laser and the upconverted emission was collected with 5 nm slit width.

As a control, to confirm that the changes to TTA-UC are not indirect effects due to impact of PLA2 on membrane fluidity, in the absence of Ca^{2+} in the liposomal contact solution, upon addition of PLA2 (5 µM) the upconversion emission remain indistinguishable to that of pristine bilayer's upconversion emission intensity as shown in Figure 3.1c. This observation adds to the growing body of evidence suggesting that Ca^{2+} is needed for PLA2 catalytic action. It also further indicates that the reorganization of the hydrolytic product resulted in better packing of

the membrane thereby lowering the TTA-UC modestly. This result also indicates that the PLA$_2$ incubation time window and the working concentration of the TTA-UC pair are congruous to hydrolyse the DOPC and concurrently observe a detectable TTA-UC signal during low energy radiation. Although, the overall reduction of UC intensity is 30% when compared to bare liposomal membrane (in the absence of either Ca^{2+} and/or PLA$_2$), exceeding the incubation window beyond 1 h did not reduce any intensity, suggesting that the incubation window of 1h is adequate for complete hydrolysis. Next, control experiments are performed to verify that the decrease in upconversion emission intensity shown in Figure 3.1a is indeed caused by hydrolysis of DOPC by PLA$_2$, resulting in greater packing of alkyl chain, and not simply due to physisorption of PLA$_2$ at the liposomal membrane surface, which would have resulted in increased overall packing (or increase in viscosity) of the DOPC membrane. If the latter case is true, then the use of a small molecule inhibitor, imipramine toward PLA$_2$ catalytic activity should not prevent the decrease in upconversion emission to an extent similar in magnitude to that shown in Figure 3.1a. To test this above hypothesis, PLA$_2$ was pre-incubated with 20 μM of imipramine and added this solution to the liposomal solution in presence of Ca^{2+}. The TTA-UC was monitored at different time intervals. Figure 3.2a shows representative data, revealing that overall, upconversion emission did not diminish when catalytic activity of PLA$_2$ is blocked. This indicates that it is likely enzymatically induced fluidity changes that are responsible for TTA-UC modification, supporting the notion that the hydrolytic product, lysophospholipids and free fatty acids pack more tightly increases the overall viscosity of membrane.
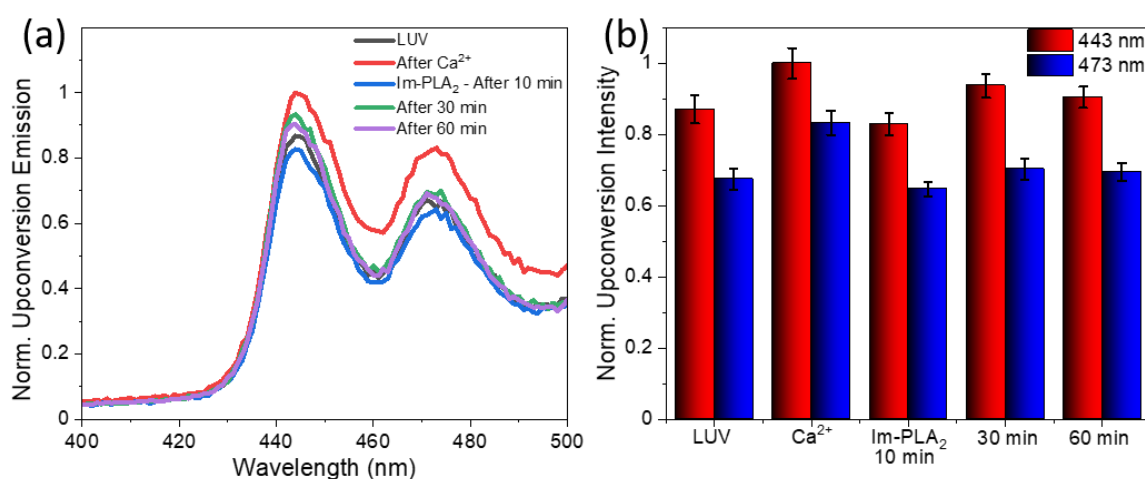
Figure 3.2 (a) Normalised TTA-UC emission spectra from DOPC liposomes incorporated with 0.5 μM B2PI and 5 μM perylene before (black) and after (red) the addition of 5 mM Ca^{2+} and after the addition

of 5 μM PLA$_2$ pre-incubated with 20 μM imipramine measured at 10, 30 and 60 min. (b) Corresponding intensity histogram of each spectrum in panel (a). All liposomes are in Tris-HCl buffer of pH 7.4.

Modest, but non-systematic changes to upconversion emission intensities at different time intervals (as shown in Figure 3.2b), are observed. Within 10 min, the emission is 5% decreased but upon further incubation, emission intensities increase. Such variation could be due to the presence of excess imipramine in the contact solution that has a propensity to passively permeate across the DOPC liposome bilayer membrane thereby increasing the fluidity (decreasing the viscosity) of membrane. This aspect of imipramine induced increase in DOPC fluidity will be addressed in chapter 5.

3.4.2 Dynamic light scattering (DLS)

Dynamic light scattering is typically used to determine the particle size. Here, DLS was conducted to determine the effect, if any, that the interaction between PLA$_2$ and liposomes has on the liposomes' size and integrity. In the absence of PLA$_2$, the average particle size of DOPC liposome containing B2PI and perylene was 120±5 nm in Tris-HCl buffer, pH 7.4 (Figure 3.3a). In the presence of only PLA$_2$ without Ca^{2+}, the liposome solution appeared homogeneous to the naked eye, and the resulting size distribution is unimodal (Figure 3.3b). After PLA$_2$ treatment in presence of Ca^{2+}, the particle size distribution become bimodal. In Figure 3.3c, liposomes of 120±5 nm diameter remain but in addition, a new species with average diameter of 760 nm appears, and the PLA$_2$ treated liposomal solution looked hazy to pristine eye. In contrast, the particle size distribution in the absence of Ca^{2+} (Figure 3.3c) but in presence of PLA$_2$ and for liposomes incubated with imipramine treated PLA$_2$ in presence of Ca^{2+} (Figure 3.3d) remain unchanged with a diameter of 120±5 nm.
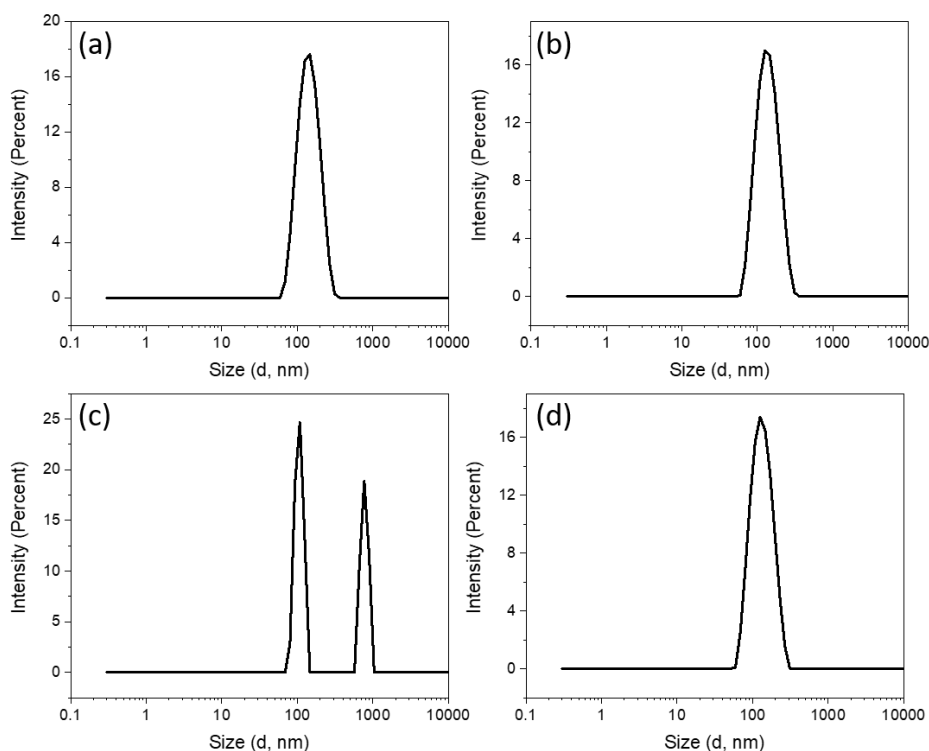
Figure 3.3 Dynamic light scattering (DLS) spectra showing the hydrodynamic radius of DOPC liposomes incorporated with 0.5 µM B2PI and 5 µM perylene a) without and b) with the presence of 5 µM PLA$_2$ in the absence of Ca^{2+}, (c) in presence of 5 mM Ca^{2+} after incubation with PLA$_2$ and (d) after incubation of imipramine treated PLA$_2$ in presence of Ca^{2+}. All liposomes are in Tris-HCl buffer of pH 7.4.

In addition, the full width half maximum (FWHM) of the size distribution becomes narrower due to the PLA$_2$ activity as compared to when there is no activity of PLA$_2$. Typically, PLA$_2$ enzymatic activity is manifested by two sites: the catalytic site, which is responsible for substrate binding and fatty acid cleavage from the sn-2 position of a glycerophospholipid, and the interface binding site (IBS), which is responsible for protein attachment to the lipid membrane. IBS is created by positively charged and hydrophobic amino acids on the protein molecule's outer surface. A plausible explanation for the biomodal particle size distribution could be some absorption of PLA$_2$ on the bilayer surface without changing the integrity of the membrane or any bilayer disruption. The increase in size distribution of liposome in presence of Ca^{2+} and PLA$_2$ is also observed in a prior research for a different lipid, POPC.[398] Overall the study reveal that the decrease in TTA-UC intensity as demonstrated earlier was caused exclusively due to B2PI-perylene distribution within the bilayer.

3.4.3 Fluorescence lifetime imaging (FLIM) and fluorescence lifetime correlation spectroscopy (FLCS) studies on PLA₂ catalysed hydrolysis of DOPC membrane

The PLA₂ induced lipid hydrolysis and the observed decrease in TTA-UC intensity of B2PI-perylene pair as demonstrated in previous section was possibly due to increase in packing order of membrane without any membrane disruption. To confirm this hypothesis, independent measurements using fluorescence-based lifetime imaging (FLIM) and fluorescence lifetime correlation spectroscopy (FLCS) were carried out. Liposomes are so small, using confocal methods to image or interrogate their fluidity by FLCS is impossible. Therefore, the PDMS based pore-suspended lipid bilayers was used, as a versatile biomimetic but true model bilayer system, amenable to FLIM and FLCS to interrogate directly the impact of PLA₂ and its catalytic effect on membrane organization and its fluidity.

Figure 3.4a shows representative FLIM images of DOPC MSLB over a PDMS based microcavity array that filled with Tris-HCl buffer. To visualize the bilayer, the upper leaflet of DOPC bilayer was fluorescently doped with 0.01 mol% DOPE-ATTO655. The membrane was prepared via the LB-VF method detailed in experimental section and the MSLB was sealed within a microfluidic chamber. Upon addition of 5 mM Ca²⁺, the FLIM image shows evidence of modest reorganization of membrane (Figure 3.4b), noting the diffraction limit of the method, any nanoscale reorganisation can be seen. However, upon addition of PLA₂, the overall molecular brightness has increased (Figure 3.4c). Figure 3.4d shows representative auto correlation function (ACF) traces obtained from the centre of the micropore of DOPC bilayer (open black), in presence of 5 mM Ca²⁺ (open red) and in presence of both Ca²⁺ and PLA₂ (open blue). The solid lines in the panel 3.4d show the fit to the 2D diffusion model, equation 3.1. All FLCS measurements were performed at the bilayer plane by positioning the observation FLCS volume at the centre of the cavity that spanned bilayer. The diffusivity obtained from the bilayer was determined as 10.1±0.2 μm²s⁻¹ and upon Ca²⁺ addition, the lipid diffusivity reduced modestly to 9.3±0.17 μm²s⁻¹. Upon further addition of 5 μM PLA₂, on 30 min of incubation, the lipid diffusivity reduced significantly to 1.4±0.3 μm²s⁻¹ i.e., there is a marked increase in the packing of membrane (or increase in viscosity) of the membrane, according to the inverse relationship between diffusion coefficient and viscosity defined by Stokes-Einstein relation, $D = k_B T/6\pi\eta r$; where k_B is the Boltzmann constant; T is the absolute temperature; η is the dynamic viscosity; and r is the radius of fluorescent particle. In all FLCS before, after Ca²⁺ and PLA₂, the anomaly coefficient was 1, indicating the diffusion

was Brownian. This results further support the notion, discussed above, that the reduction in upconversion emission is due to increase in viscosity of the membrane caused by PLA$_2$ activity.
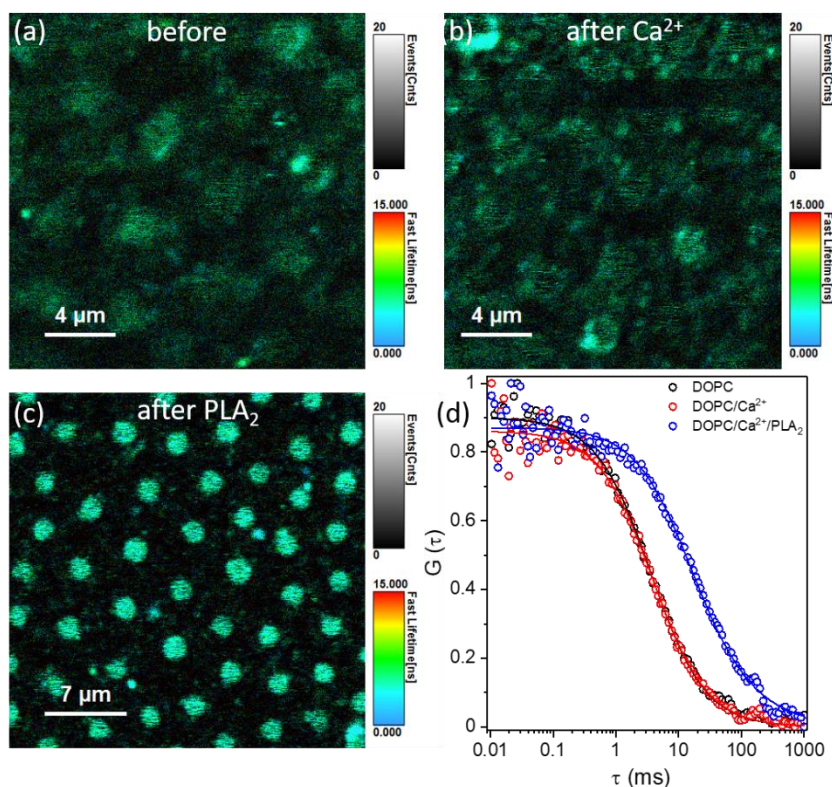
Figure 3.4 Fluorescence lifetime images (FLIM) of DOPC MSLBs labelled with 0.01 mol% DOPE-ATTO655 (upper leaflet) (a) before, (b) after the addition of 5 mM Ca^{2+}, and (c) after the addition of 5 µM PLA$_2$ in presence of Ca^{2+}. (d) Representative FLCS autocorrelation functions of DOPC MSLB labelled with 0.01 mol% DOPE-ATTO655 (upper leaflet) before (open black), after 5 mM Ca^{2+} addition (open red) and after the addition of 5 µM PLA$_2$ in presence of Ca^{2+} (open blue). FLCS data were collected from 40-50 cavities and the average is shown. The solid lines are the 2D diffusion fit using equation 3.1. The scale bar in each panel is 4 µm. All measurements were carried out in Tris-HCl buffer at pH 7.4.

As a control, FLIM and FLCS studies were carried out in the absence of Ca^{2+} in the contact solution of DOPC MSLB. Figure 3.5a shows a representative reflectance image showing the buffer filled cavities and Figure 3.5b shows the corresponding FLIM image, that confirm that the bilayer is spanned across the buffer filled cavities. Upon addition of PLA$_2$, the molecular brightness in FLIM was largely unchanged (Figure 3.5c) compared to that of FLIM image when Ca^{2+} was present (Figure 3.4c). Unlike behaviour in the presence of Ca^{2+}, lipid diffusivity after PLA$_2$ incubation $^+$ is modestly reduced to 8.5 ±0.22 µm^{2}s^{-1} as shown in Figure 3.5d (red). The lifetime value obtained from the pore-spanning membrane (number of pores analysed = 8) was only modestly increased from 3.11±0.05 ns to 3.2±0.03 ns. This may indicate some

physisorption of PLA$_2$ at the bilayer surface. This observation further confirms that Ca^{2+} is necessary in order for the hydrolysis of DOPC to occur.
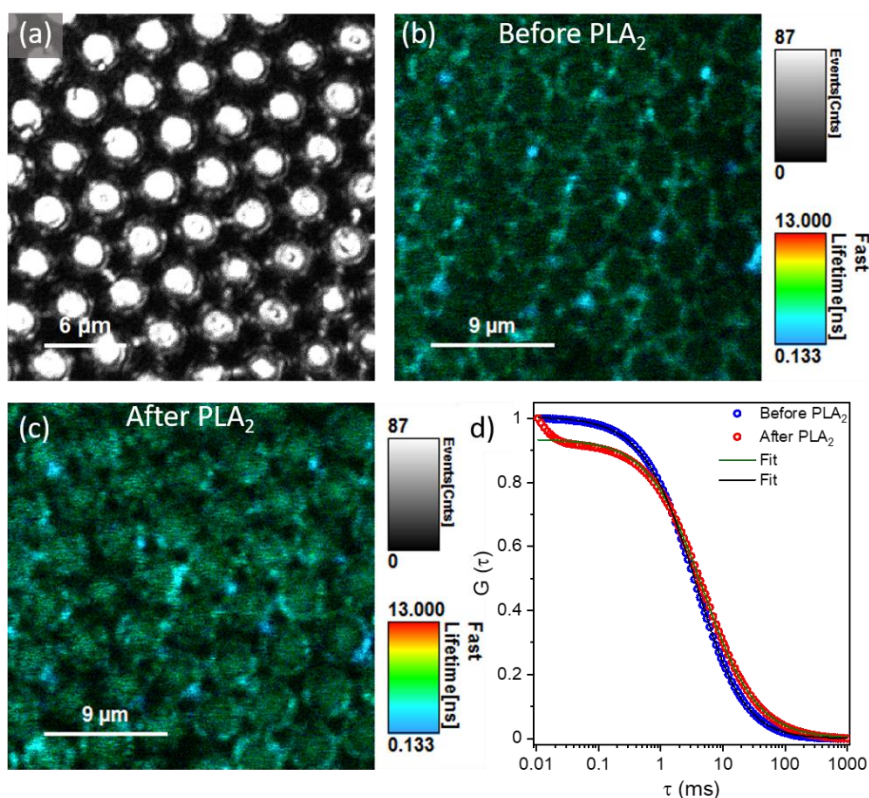
Figure 3.5 Representative reflectance image of DOPC MSLBs with scale bar 6 µm and fluorescence lifetime images (FLIM) of the same DOPC MSLB labelled with 0.01 mol% DOPE-ATTO655 (upper leaflet) (b) before, (c) after the addition of 5 µM PLA$_2$ in the absence of Ca^{2+} with 9 µm scale bar. (d) Representative FLCS autocorrelation functions of DOPC MSLB labelled with 0.01 mol% DOPE-ATTO655 (upper leaflet) before (open blue), and after the addition of 5 µM PLA$_2$ (open red) in the absence of Ca^{2+}. FLCS was measured over 40-50 cavities and the average is shown. The solid lines are the 2D diffusion fit using equation 3.1. All measurements were carried out under Tris-HCl buffer of pH 7.4.

When PLA$_2$ is pre-treated with imipramine as an inhibitor and then incubated with DOPC MSLB in presence of Ca^{2+}, the FLIM image (Figure 3.6c) remain indistinguishable from that of the pristine DOPC MSLB without (Figure 3.6a) and with presence of Ca^{2+} (Figure 3.6b). Figure 3.6d shows the comparison of ACF traces before (black), after Ca^{2+} (red) and after imipramine treated PLA$_2$ (green) incubation. The lipid diffusivity after 30 min of PLA$_2$ treated imipramine incubation is reduced to 4.1±0.3 µm^{2}s^{-1}, and this value is higher than that of drug untreated PLA$_2$ incubation value (1.4±0.3 µm^{2}s^{-1}). This suggests that although imipramine behaves as inhibitor for the hydrolytic action of PLA$_2$, the resultant lipid mobility though

reduced due to weak adsorption of imipramine-PLA$_2$ to the membrane surface, but remain fluidic, which is again consistent with our upconversion emission data. The FLIM signal in the other hand, after the addition of imipramine incubated PLA$_2$ remain largely unchanged as shown in Figure 3.6c.
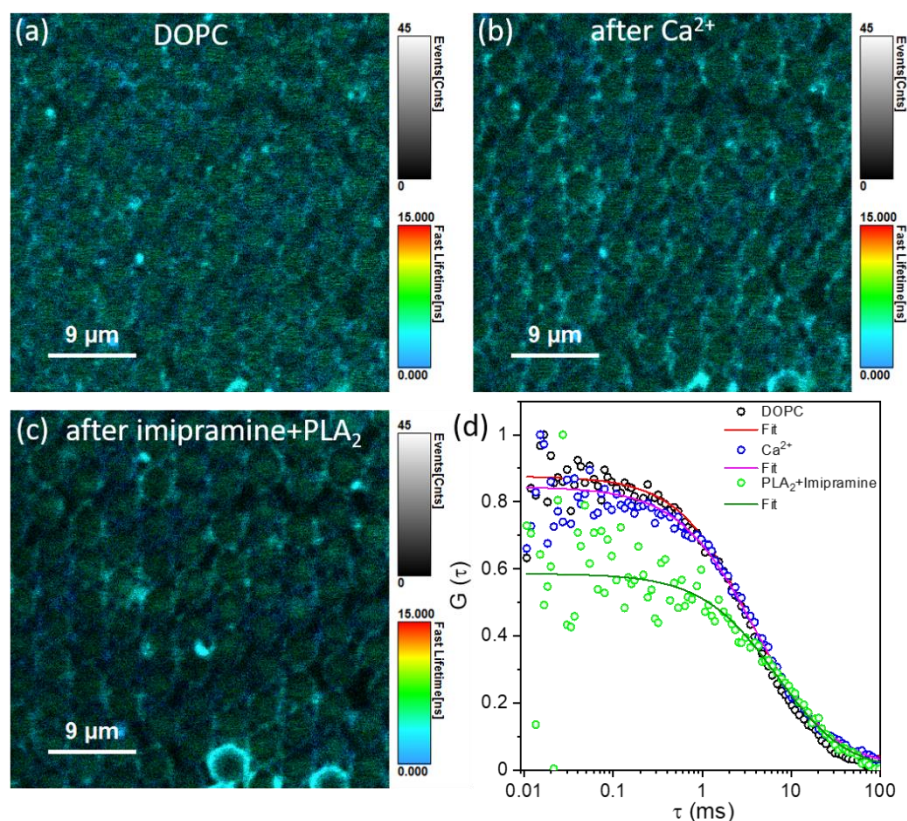
Figure 3.6 Fluorescence lifetime images (FLIM) of pristine DOPC MSLB (a) before, and after addition of (b) 5 mM Ca^{2+}, and (c) PLA$_2$ pre-incubated with imipramine in presence of Ca^{2+} taken at the identical regime. The concentration of imipramine and PLA$_2$ were 20 μM and 5 μM respectively. In each case in panel b and c, the images were acquired following 30 min of incubation. (d) ACF traces obtained from pristine bilayer (open black) before, after Ca^{2+} (open blue) and after PLA$_2$ treated imipramine (open green) further spanned over PDMS microcavity array filled with Tris-HCl buffer. The scale bar in each panel is 9 μm. The solid lines are the 2D diffusion fit using equation 3.1.

3.4.4 Electrochemical impedance studies of lipid hydrolysis using PLA$_2$

Binding of Ca^{2+} to phospholipase A$_2$ (PLA$_2$) alters the conformation of PLA$_2$ and triggers its catalytic activity upon binding to phospholipid. Due to the exposure of the catalytic triad and an increased hydrophobic surface are upon Ca^{2+} binding, the affinity of the enzyme increases and this facilitates hydrolysis of phospholipid.[399–402] To test this assumption, the binding of PLA$_2$ to native phosphatidylcholine, DOPC bilayer suspended over gold microcavity imprinted array was first assessed using label free highly sensitive electrochemical impedance

spectroscopy (EIS). Hexagonally packed microcavity array (1cm×1cm), with each pore diameter 1 μm and pore depth 0.5 μm imprinted array was fabricated over gold coated silicon chips by soft-lithography method using 1 μm polystyrene sphere, according to our established protocols and further briefly presented in Figure 3.7.[184,197,199]
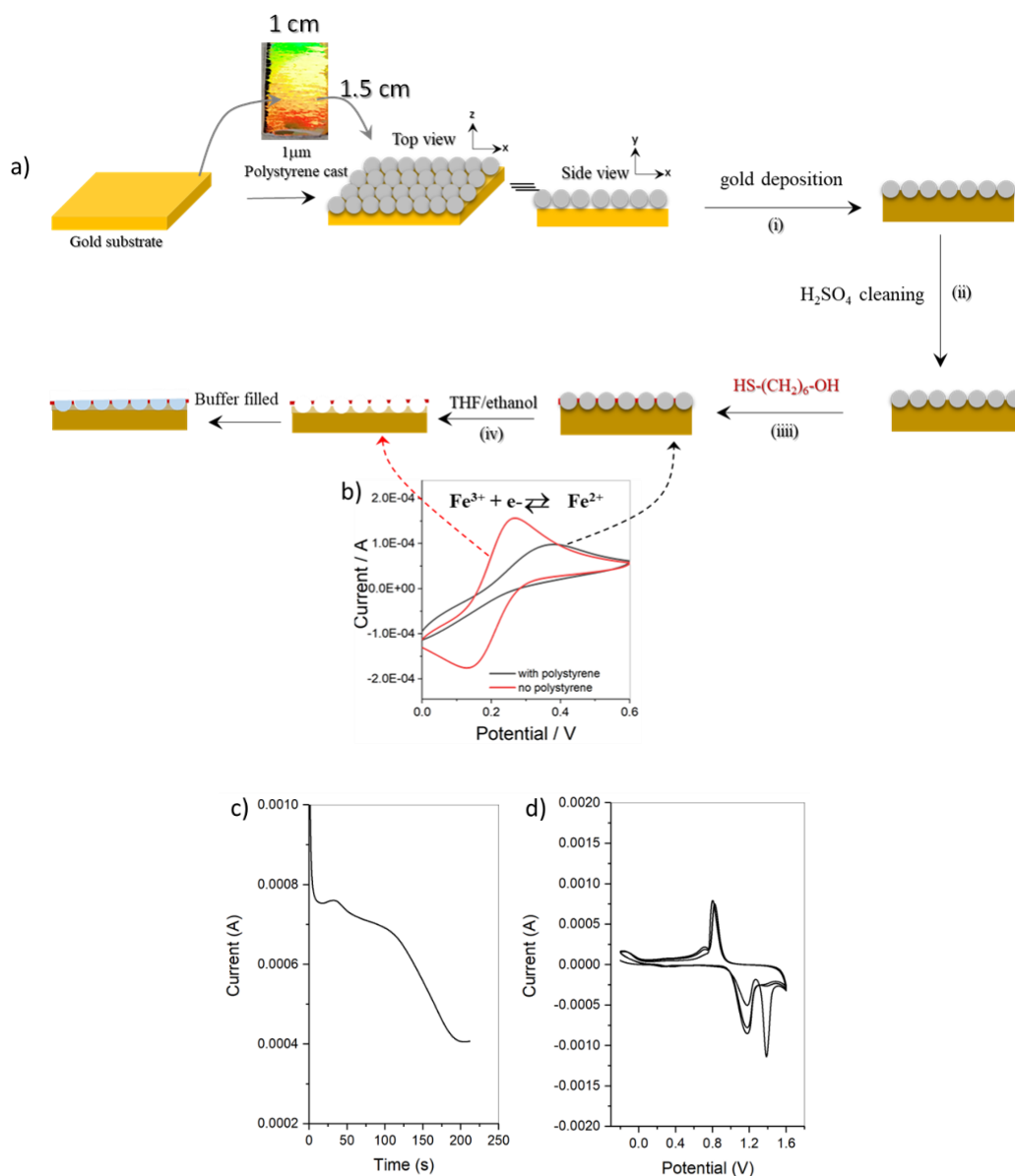
Figure 3.7 Schematic illustration of hemisphere gold microcavity array fabrication step using soft lithography. Initially, gold substrate cut into ~1 cm×1.5 cm on to which aqueous solution of 1 μm sized PS sphere (1% v/v) was drop cast and following solvent removal well packed hexagonally monolayer PS array formed as shown in curved arrow in panel a. *step (i)* Controlled potential gold deposition was carried out using amperometric I-t curve and the growth was monitored using the shape of the curve until gold deposited to the equator of PS sphere as shown in panel c. In *step ii* the gold oxide layers are removed by repetitive scanning (3 cycles) the substrate in a 0.05 M H_2SO_4. In *step iii* the substrate was

immersed in ethanolic solution of 1 mM 6-mercapto hexanol for at least 48 hours. The excess thiol and polystyrene were removed in *step iv* by washing step using ethanol and THF, resulting hemisphere microcavity array. Cyclic voltammograms confirm the PS removal step, where the electron transfer process of Fe^{2+}/Fe^{3+} is restored (red) upon PS removal in an otherwise was blocked by insulating PS sphere (black). All the cyclic voltammetry and amperometry measurements were carried out using three-electrode conventional system where the gold electrode employed as working, Ag/AgCl (1 M KCl) as reference and platinum wire as counter electrodes. Data courtesy of Dr. Nirod Kumar Sarangi (DCU).

Microcavity suspended lipid bilayers (MSLBs) over gold microcavity imprinted array were prepared via LB-VF method as shown schematically in Figure 3.8a. The successful formation of bilayers that spanned over gold microcavity array was further confirmed via FLIM imaging. Leaflet by leaflet assembly of MSLB over gold substrate was achieved by doping each leaflets independently by two different fluorescently labelled lipids that are not spectrally overlapped. The proximal leaflet was doped with 0.05 mol% of DOPE-ATTO532 during LB transfer step, and the outer leaflet of the bilayer was doped with 0.05 mol% DOPE-ATTO655 during the LUV preparation step. FLIM image from proximal leaflet was excited using 532 nm laser, PicoTA from Toptica (PicoQuant) and the fluorescence signals filtered through HQ550lp AHF/Chroma. A representative FLIM image of proximal (Figure 3.8c) and distal (Figure 3.8d) leaflet of DOPC MSLBs along with reflectance image (Figure 3.8b) are shown, indicating successful bilayer formation. Note that, since EIS is a label-free technique, fluorescent labelling is not necessary. Nonetheless, the circular fluorescent feature confirms that bilayer indeed formed above the imprinted cavity array covering the whole cavity area.
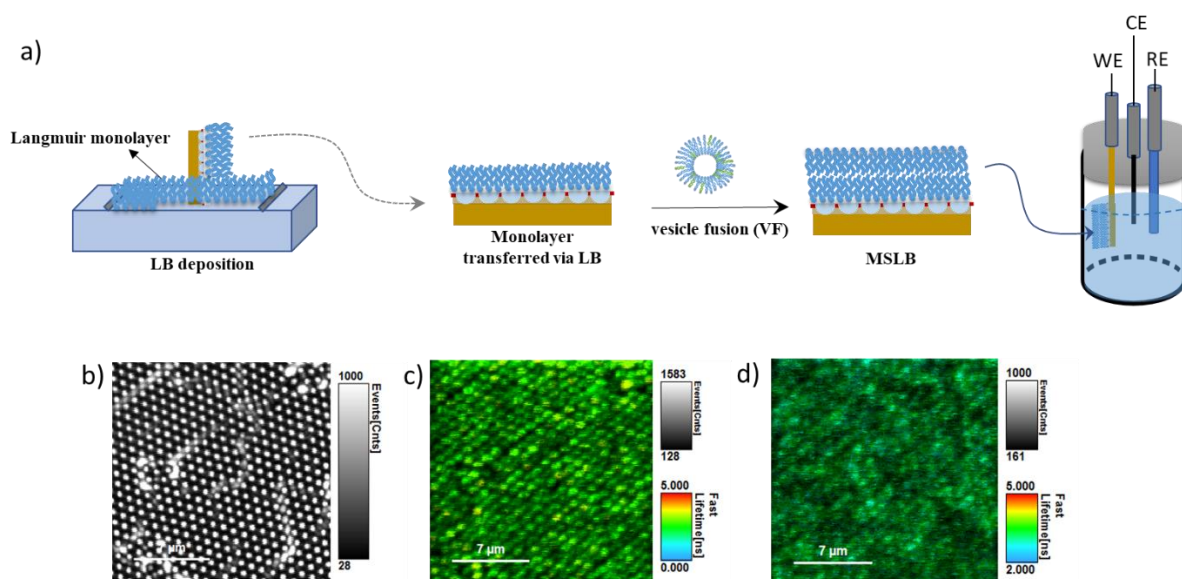
Figure 3.8 (a) Schematic illustration of MSLB fabrication using Langmuir-Blodgett (LB) transfer followed by vesicle fusion (VF) step along with the EIS cell setup. Characterization of DOPC MSLB spanned over buffer filled gold microcavity array substrate. (b) Reflectance image shows that each cavity (white circular regions) is buffer filled and the corresponding FLIM images obtained from the (c) proximal leaflet doped with 0.05 mol% DOPE-ATTO532 and (d) distal leaflet doped with 0.05 mol% DOPE-ATTO655. The scale bar in each panel is 7 µm.

Following MSLB preparation, the gold chip was introduced to the electrochemical cell (schematically shown in Figure 3.8a) placed in contact with 3 to 4 mL of Tris-buffer, pH 7.4 and non-Faradaic EIS measurements were carried out. A typical non-Faradaic Nyquist and angular frequency normalized complex capacitance plot of bare cavity (black square) and DOPC MSLB EIS data at different time intervals are shown in Figure 3.9 a and b respectively. The data reveals that the bilayer is electrically stable as reflected in stable signals from the equilibrated Nyquist and complex capacitance plots. The Nyquist traces as semicircle arcs represents the real (Z') and imaginary (Z'') parts of the complex impedance, which originate from the resistance and capacitance of the electrochemical cell. When compared to the bare cavity or bilayer-free electrodes (black square, Figure 3.9a), the non-Faradaic Nyquist trace of a DOPC spanned MSLB shifts more towards $-Z''$ (y-axis), indicating an increase in impedance or decrease in admittance of the membrane due to the presence of dielectrics (here lipid bilayer membrane). It is worth noting that the presence of mercaptohexanethiol SAM only slightly increases the impedance compared to the bare cavity array, because thiol molecules self-assemble spatially only to the intestinal region of the imprinted array, and thus the corresponding Nyquist trace is similar to that of the bare cavity array. Furthermore, the

membrane stability can be visualized as stable/equilibrated signal plots from the complex capacitance plots (Figure 3.9b), Y''/ω vs Y''/ω, where Y is the electrode admittance and ω is the angular frequency. In part, the plot shown in Figure 3.9b are semi-circular and indicate near-ideal behaviour for DOPC MSLB over time. The diameter of the semicircle is proportional to the magnitude of the capacitance. As seen from Figure 3.9b, the capacitance of a bare gold array electrode (black square) decreases by one-fold from 4.2×10^{-5} F to 4×10^{-6} F upon bilayer assembly. The EIS signal of MSLB remains unchanged over 10h time as shown below, indicating that the membrane is electrochemically stable. For quantitative analysis, the best fits to the experimental curves are obtained using the equivalent circuit model (ECM) shown in the inset of Figure 3.9a. A representative fitted data to Nyquist and complex capacitance plot corresponding to 10h stability is shown in solid wine lines in both panels of Figure 3.9 a and b.
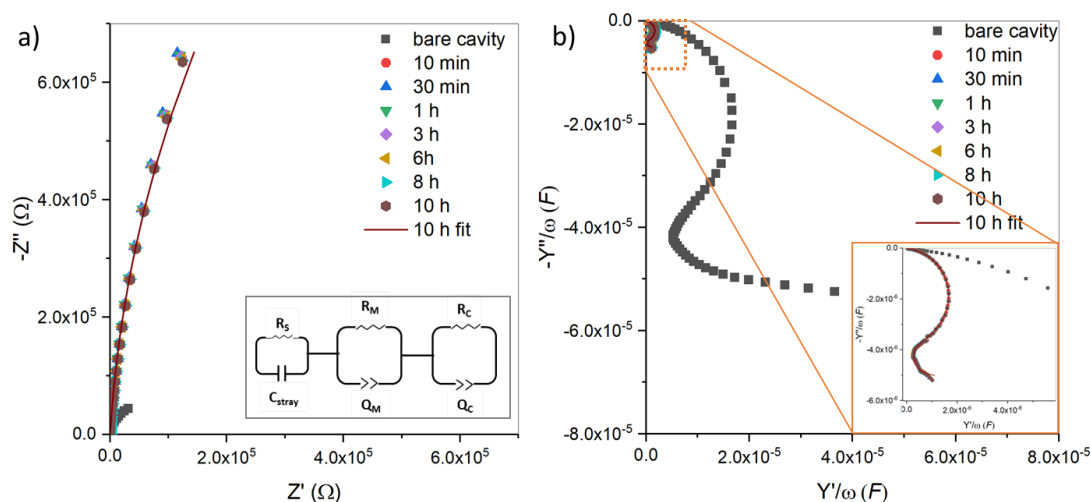
Figure 3.9 Representative time-dependent non-Faradaic (a) Nyquist (Z'' vs Z') and (b) angular frequency normalized complex capacitance (Y''/ω vs Y'/ω) plot of DOPC MSLB spanned over 1 μm diameter cavity imprinted gold electrode. The bilayer was prepared using LB-VF method. Prior to bilayer formation, the EIS response of bare cavity array electrode (black square) is included in both panels. Inset in panel a show the equivalent circuit model used to fit the EIS data. Solid wine lines in panel a,b are the corresponding fit to 10h data. In panel b, inset shows the expanded view highlighted in dotted square box. All EIS measurements are performed in Tris-HCl of pH 7.4 buffer at 0 V bias potential with an A.C amplitude of 10 mV within a frequency range of 0.05 Hz and 10^5 Hz. EIS was recorded in conventional 3-electrode system where MSLB over gold behave as working electrode, Ag/AgCl (1 M KCl) as reference electrode and Pt wire as counter electrode. Data courtesy of Dr. Nirod Kumar Sarangi (DCU).

The absolute magnitude of DOPC membrane resistance (R_M) and capacitance (Q_M) are found to be 4.7 MΩ and 4.8 µFs^{m-1} respectively. Note that these values are not normalized to electroactive area of the working electrode. Also, in the ECM circuit, the introduction of a constant phase element ($CPE = 1/Q(j\omega)^m$) rather than a pure capacitor element yielded a better fit; where Q is analogous to the magnitude of the capacitance (C), ω is the angular frequency expressed in rad/s, and m is a CPE exponent real number (~0.94±0.01). While the expression $C_M(\omega) = Q_M\,\omega^{m-1}$ can be used to estimate true membrane capacitance (C_M) from the Q_M value, it only holds true for a specific ω, limited to the specific ECM, and thus not used in this work. Nonetheless, when normalized to the actual electroactive surface area, the absolute membrane resistance (R_M) and capacitance (C_M) were found to be in the ranges of 15-40 MΩcm^2 and 0.7-0.9 µFcm^{-2}, respectively. These values are expected for a highly insulating defect free bilayer and ranges within the previously reported values.[144,199,403–406] The relative change in membrane resistance (ΔR) and membrane capacitance (ΔQ) values induced by PLA$_2$ binding to the membrane is employed here as the absolute values vary depending on electrode area and uniformity of pore packing. ΔR is defined as $R_M^{PLA2} - R_M^0$, where R_M^{PLA2} and R_M^0 are the membrane resistances in the presence and absence of PLA$_2$. Likewise, ΔQ is defined as $Q_M^{PLA2} - Q_M^0$.

Figure 3.10 a and b shows representative temporal evolution of relative change in resistance and capacitance of DOPC MSLB induced by PLA$_2$ without and with the presence of 5 mM Ca^{2+}. Prior to PLA$_2$, the relative change in membrane resistance and capacitance over a 20 h experimental window remains unchanged, indicated by a horizontal dotted line near to the origin of Y-axes of Figure 3.10. In the absence of Ca^{2+} in the contact buffer, upon addition of PLA$_2$, the membrane resistance increases and stabilizes within 4-6 hours as seen in (red filled circle) in Figure 3.10a. Accordingly, the relative change in capacitance decreased and saturates out within the same time window, as shown in Figure 3.10b. Since capacitance (C) is inversely related to the thickness (d) of bilayer membrane ($C = \epsilon\varepsilon_0 A/d$), where ϵ is vacuum permittivity, ε_0 is dielectric constant and A is the electrode area over which bilayer is spanned, an overall decrease in capacitance suggests that the membrane is thickening, which is consistent withPLA$_2$ adsorption to the bilayer. The addition of 5 mM Ca^{2+} to the contact buffer of DOPC membrane resulted only modest decrease in resistance (ΔR = -0.08 MΩ) without any accompanying changes to capacitance due to the electrostatic interaction of Ca^{2+} with the phosphate group of DOPC. In contrast, when 5 mM Ca^{2+} was present in the DOPC MSLB contact buffer, PLA$_2$ elicited a rapid drop in resistance completed within 1h a stable signal for

1-5r and beyond 5h, a modest but systematic decrease in resistance was evident (black filled square, Figure 3.10a). This is consistent with the findings of Bilewicz et al. who have observed a decrease in charge transfer resistance of a hybrid tethered dodecanethiol-DPPC:cholesterol bilayer during PLA_2 binding.[407] The corresponding capacitance data showed no change up to 5 h whereafter the capacitance increased modestly with time. A decrease in resistance without accompanying any changes to capacitance suggests nanopore-formation and the subsequent increase in capacitance is taken to be due to membrane thinning. Our results indicate that under Ca^{2+} mediated action of PLA_2, DOPC membrane undergoes enzymatic degradation of DOPC, as the resulting lysophospholipid and fatty acid undergo extensive rearrangement making the overall membrane more porous and tightly packed, and the latter is consistent with our FLCS study. Given no change in capacitance at least in the early stage of incubation resulting nanopore formation supports this argument, however membrane thinning at prolong incubation (beyond 5h) is likely lipid exclusion from the bilayer. Another plausible explanation for this behaviour is that when the enzyme and bilayer come into contact, they create a network of hydrogen bonds and salt bridges that allow lipid polar heads to move towards corresponding amino acids in interface binding sites (IBS), thereby bending the outer leaflet (a dint formation). At this intermediate stage, hydrophobic interactions with acyl chains of lipids are predicted to be outcompeted by the creation of hydrogen bonds and salt bridges. This is consistent with a model of membrane binding proposed by Stahelin and Cho (ref) for peripheral proteins, in which electrostatic interactions initially bring the protein molecules to the membrane surface, and subsequent membrane penetration by aliphatic and aromatic residues results in the formation of strong protein-membrane complex.[408] This complex are stabilized primarily by hydrophobic interactions and could be further stabilized by hydrogen bonds and electrostatic interactions. When a dint forms in a lipid bilayer, the resulting hydrophobic mismatch causes additional changes to the bilayer's structure. In fluidic membranes like DOPC, where lipid lateral mobility is high, enzyme-induced hydrophobic mismatch causes lipids to move outside the contact area. Some lipids leave the contact area entirely, while others have only the polar head group outside and the tails inside. This strengthens hydrophobic contacts. Loss of hydrophobic volume due to lipid exclusion is compensated by hydrophobic tails of lipids from the opposite leaflet of the bilayer, creating another dint on the opposite side, making the overall membrane packed strongly. This argument is also well supported by molecular dynamic simulation.[398]
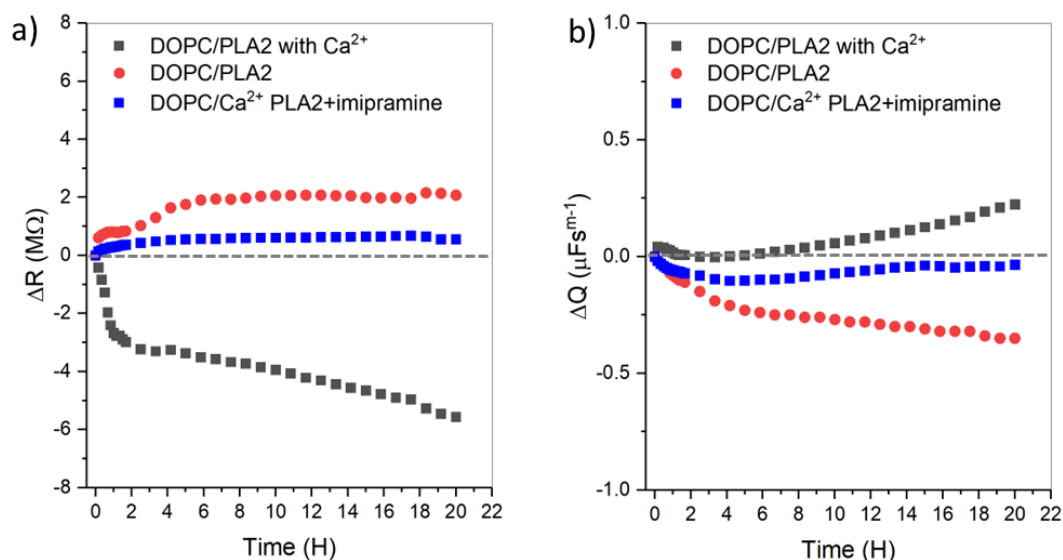
Figure 3.10 PLA$_2$ induced relative change in membrane (a) resistance and (b) capacitance of DOPC MSLB in the absence (red) and presence (black) of 5 mM Ca^{2+} in the contact Tris-HCl buffer. The Blue data in both panels are the trend of resistance and capacitance change of DOPC MSLB induced by pre-incubated 5 μM PLA$_2$ with 20 μM imipramine. All data points are the average of triplicates under identical experimental conditions. Data courtesy of Dr. Nirod Kumar Sarangi (DCU).

The enzymatic effect of PLA$_2$ is eliminated, as reflected in a modest overall increase in resistance (blue filled square, Figure 3.10a) and decrease in capacitance (blue, Figure 3.10b) when PLA$_2$ is pre-incubated with 20 μM imipramine drug and allowed to interact to the DOPC MSLB in Ca^{2+} containing buffer. The pre-incubation with imipramine could either change the PLA$_2$ conformation and/or could block the catalytic active sites of the PLA$_2$ enzyme. The overall contrast of EIS data nonetheless reveals a weak physisorption of PLA$_2$ to the membrane's surface when PLA$_2$ is pre-incubated with the imipramine drug which support the modest decrease in lipid diffusivity as discussed earlier.

To understand any topographic changes to the membrane on PLA$_2$ interaction, e.g. pore formation, atomic force microscopy imaging was carried out on DOPC planar supported lipid bilayer (SLB) membrane, in this case over freshly cleaved mica substrate under buffer. SLB was selected for the AFM research rather than MSLB because the membrane in MSLB is partially undulated, as discovered in a recent study from Keyes laboratory, making it difficult to detect any nanoscale changes caused by protein binding.[199] The DOPC membrane as formed is homogeneous as shown in Figure 3.11a and the corresponding line profile analysis in panel 3.11e (black). Upon addition of PLA$_2$ following 1 h of incubation, the overall membrane remains homogeneous but occasional features attributed to nanoclusters of PLA$_2$ island of

height 2-3 nm (cf. Panel 3.11e, blue) are evident protruding at the membrane surface. These results are consistent with the decrease in admittance of the bilayer as reflected in the EIS data in the absence of Ca^{2+}. In the presence of Ca^{2+} in the buffer, PLA_2 induced significant membrane heterogeneity with extensive changes to packing evident and pore-like features reflected in Figure 3.11c and the corresponding line profile (red) in Figure 3e. These results again support the overall increase in admittance of the membrane from EIS and further supports Ca^{2+} mediated effect of enzymatic action of PLA_2. When PLA_2 is pre-incubated with imipramine for 30 min and allowed to interact, the membrane topography remains homogeneous (Figure 3.11d) consistent with the studies above that enzymatic activity of PLA_2 at the membrane is inhibited by imipramine.
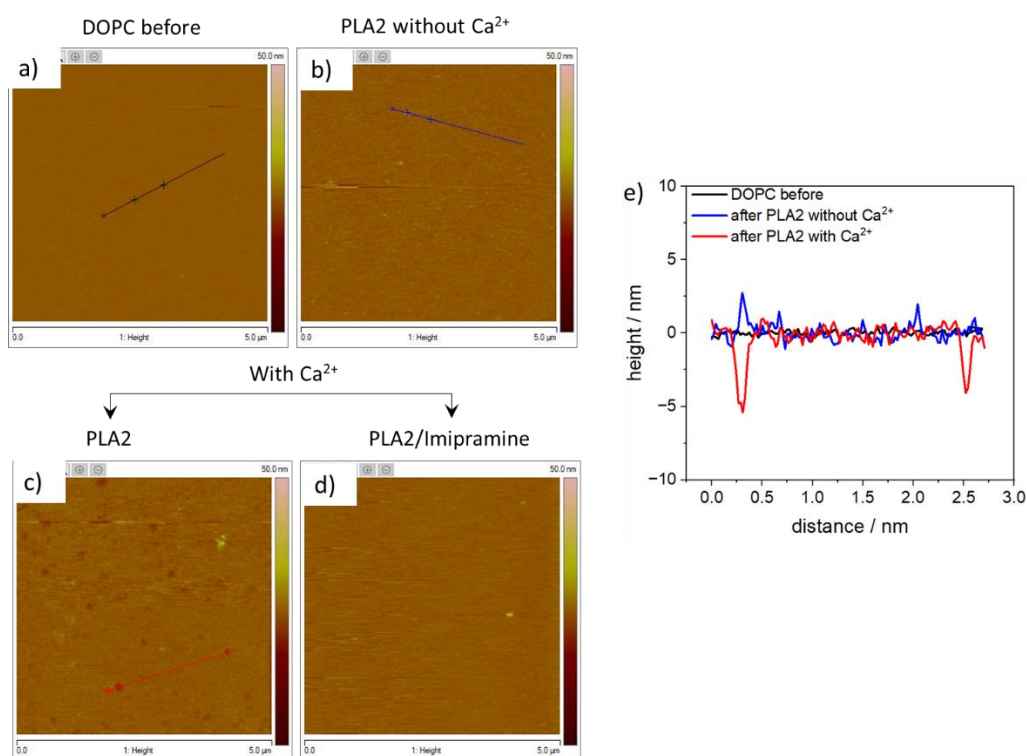
Figure 3.11 Topographic AFM images of DOPC lipid bilayer (a) without and (b) with presence of PLA_2 in the absence of Ca^{2+} supported over mica substrate. Panel (c) represents the AFM image of DOPC bilayer in presence of 5 mM Ca^{2+} after incubation with PLA_2. Panel (d) represents the AFM image of DOPC MSLB after incubation of imipramine treated PLA_2 in presence of Ca^{2+}. Panel e illustrate the line profile analyses obtained from the region of interest as indicated by line in panel a-c. All imaging was carried out under Tris-HCl buffer of pH 7.4. The image size was 5μm×5μm. Data courtesy of Dr. Nirod Kumar Sarangi (DCU).
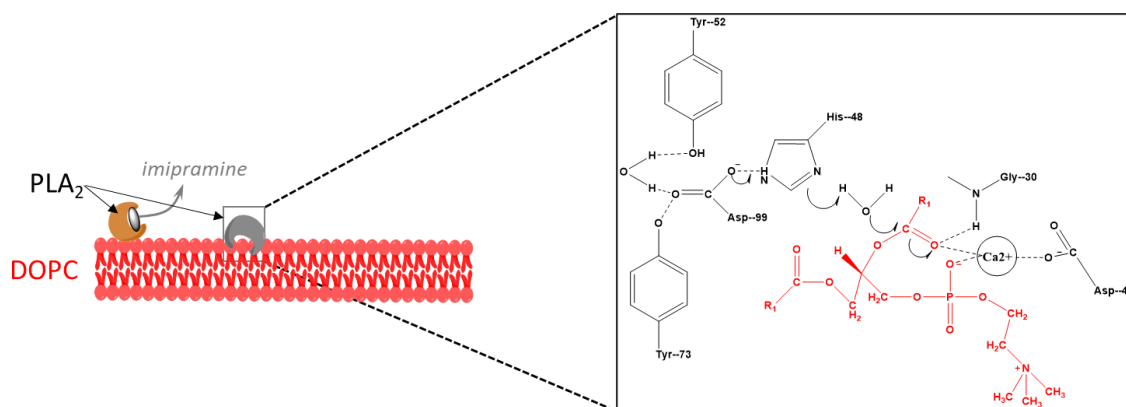
Scheme 3.2 (*left*) Schematic illustration of PLA$_2$ binding to DOPC bilayer and its inhibition using imipramine). (*right*) The chemical structure showing the catalytic triad of PLA$_2$ and its interaction with lipid head group in presence of Ca^{2+}.

3.5 Conclusions

In conclusion, the TTA-UC of B2PI-perylene reconstitute in DOPC liposome was compared in the lack of enzyme and with the presence of activated enzyme phospholipase PLA$_2$ and found that the TTA-UC in the presence of PLA$_2$ is lower than that of the pristine liposome. The observed decline in intensity is more pronounced when Ca^{2+} is present in the contact solution in the presence of PLA$_2$, implying that Ca^{2+} activates the catalytic activity. Although the intensity of TTA-UC is lower in the presence of PLA$_2$ than in the absence of PLA$_2$, the intensity of TTA-UC is significant enough to identify upconverted light as a result of TTA. This decrease in intensity is mainly the result of hydrolytic products lipid packing of lysophospholipids and fatty acid. As a control, it was observed that either Ca^{2+} was missing but PLA$_2$ was present, or imipramine treated PLA$_2$ in the presence of Ca^{2+} did not reduce TTA-UC intensity, confirming that enzymatic activity caused a decrease in TTA-UC intensity due to an increase in packing order. Figure 3.12 depicts the molecular level mechanism of PLA$_2$ in the presence of Ca^{2+} and imipramine's function as a PLA$_2$ inhibitor. The increased lipid packing was further confirmed using fluorescence lifetime correlation spectroscopy (FLCS), as the lipid diffusivity obtained from pore suspended DOPC bilayer is significantly reduced from 10.1±0.2 µm^{2}s^{-1} to 1.4±0.3 µm^{2}s^{-1} due to hydrolysis. The PLA$_2$ association to the membrane surface did not disintegrate or lose bilayer properties, as verified by FLIM and DLS analysis, which revealed that after enzymatic activity, PLA$_2$ remained associated with the membrane, causing liposome size to increase. The enzymatic activity was further confirmed using a label-free EIS analysis, which found that Ca^{2+}-mediated PLA$_2$ activity increases membrane admittance, whereas in the absence of Ca^{2+} or imipramine-treated PLA$_2$ in the presence of Ca^{2+}, membrane admittance

decreases. The decrease in membrane admittance resulted from PLA_2's weak association with the membrane surface in the absence of hydrolysis, whereas the increase in membrane admittance resulted from widespread membrane reorganisation as nanoscale pore formation, allowing for easier ion transfer across MSLB. This finding is backed further by molecular level topographic imaging with AFM.

Overall, this study shows that TTA-UC is efficient during enzymatic action, which has the potential for targeted therapy in terms of drug release to target sites as well as imaging using TTA-UC modalities. Deciphering enzymatic hydrolysis and changes in biophysical properties using MSLB as a true biomimetic membrane system amenable to multimodal surface sensitive interrogation provides molecular level insights not only to the specific enzyme used here but also to other enzymes.

Chapter 4

Ruthenium(II)   Polypyridyl   Complex   Sensitized   Triplet-Triplet
Annihilation Upconversion

4.1 Introduction

In the previous chapters, BODIPY based photosensitizers have been utilized for TTA-UC. Metal complexes like Ru(II) complexes can also be used as efficient triplet photosensitizers. The d^6 transition metal complexes have excellent luminescent properties, which has attracted a great amount of attention because these complexes exhibit various tunable palate of emission colours.[409–412] Among all the luminescent transition metal complexes, ruthenium(II) polypyridyl complexes have a rich history of synthetic chemistry as they have been studied extensively.[70,413] Moreover, depending on the ligand attached to the ruthenium(II) polypyridyl complexes, they have tuneable photophysical and photochemical properties, as well as the ability to have multiple heteroligands.[414,415] Because of these properties, ruthenium(II) polypyridyl complexes are being extensively used for various biological applications including many diagnostic and therapeutic applications.[409,416–421]

Due to their metal-to-ligand charge transfer triplet excited state (^{3}MLCT), Ru(II) polypyridyl complexes, such as [Ru(bpy)$_3$][PF$_6$]$_2$, have excellent photophysics, with long phosphorescence lifetimes (from a few hundred ns to µs). They also have large Stokes shifts of about 150 nm with long emission wavelengths beyond 600 nm. Usually these complexes have UV/Vis absorption below 450 nm with moderate molar absorption coefficient (ε) values. Many synthetic modifications have been reported to tune them for visible light absorption and to efficiently transfer the excitation energy to the coordination centre in order to initiate photophysical processes involving triplet excited states.[422] The reports on femtosecond transient absorption experiments of well-known [Ru(bpy)$_3$]$^{2+}$ (bpy=bipyridine) complex show that intersystem crossing (ISC) is ultrafast and happens in less than 100 fs when the compound is excited to the first singlet excited states (absorption maximum around 450 nm).[423,424] Thus, the spin-allowed fluorescence from the excited singlet states is overruled by ISC triplets, leading to the formation of triplet states with near unity quantum yields.[425]

Ru(II) complexes have been previously used as photosensitizers for TTA-UC. Castellano *et al.* used [Ru(dmb)$_3$][PF$_6$]$_2$ as photosensitizer for TTA-UC with 9,10-diphenylanthracene (DPA) as annihilator.[426] The absorption maxima of the complex is at 450 nm and the triplet excited state energy level was derived from phosphorescence wavelength, 600 nm (2.07 eV), hence DPA was used as annihilator which has T$_1$ excited state energy level of 1.77 eV (700 nm). The upconverted emission of DPA was observed at 430 nm (λ_{ex} = 514.5 nm, 24 mW or λ_{ex} = 532 nm, <5 mW) and TTA-UC using low-power density was

demonstrated.[309] Zhao and co-workers synthesized a series of four of Ru(II) polyimine photosensitizers conjugated to chromophoric moieties such as coumarin, BODIPY, or pyrene and studied them for upconversion with annihilator (DPA or perylene).[422,427,428] The excited state lifetime of the Ru(II) complexes containing chromophore was extended by switching the ^{3}MLCT for the emissive state to the intraligand excited state (^{3}IL) or by balancing both ^{3}MLCT and ^{3}IL excited states and the upconversion emission has improved.[429] A qualitative Jablonski diagram of TTA-UC process between Ru(II) photosensitizer and annihilator is shown in Scheme 4.1.[309]
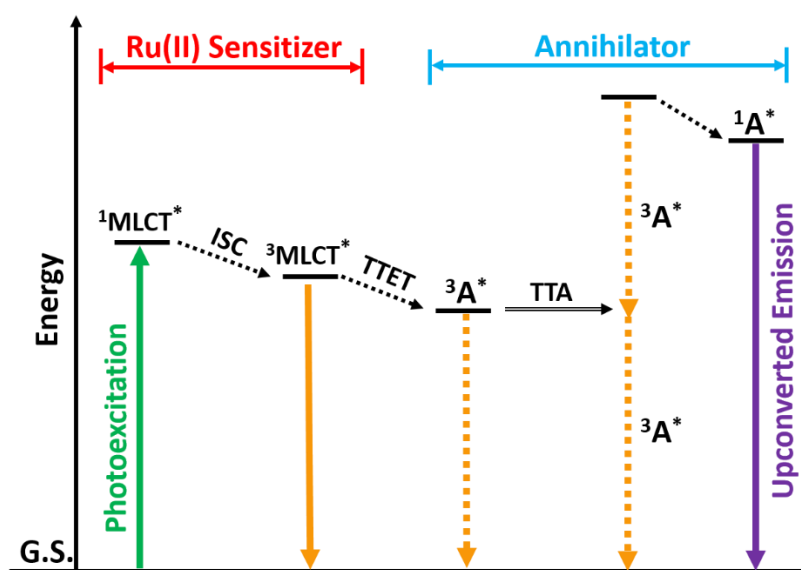
Scheme 4.1 Qualitative Jablonski diagram displaying TTA-UC process between Ru(II) photosensitizer and annihilator. GS:ground state (S_0) ^{3}MLCT*:Metal-to-ligand-charge-transfer triplet excited state, TTET:Triplet–triplet energy transfer, ^{3}A*:Triplet excited state of annihilator, TTA:Triplet–triplet annihilation, ^{1}A*:Singlet excited state of annihilator. The emission band observed for the photosensitizers alone is the ^{3}MLCT emissive excited state. The emission bands observed in the TTA process are the simultaneous ^{3}MLCT* phosphorescence emission and the ^{1}A* fluorescence emission.

Photoactivated chemotherapy, also known as PACT, has recently emerged as an approach that provides the prospect of spatial and temporal control over (when and where) the drug activation. PACT is a method in which a biologically active compound with a light-cleavable protecting group that restricts the interaction with the cell-environment with spatiotemporal control and it gets unprotected by suitable light irradiation.[430] PACT includes photodynamic therapy (PDT), a method of treatment that is currently being researched. The photosensitizer (PS) and its ability to produce free radicals of type I or reactive singlet oxygen ($^1O_2$; type II) is the primary factor that determines how well PDT works. Photosensitizers are photoactive

molecules that, when activated by light, can generate (or catalyse the formation of) reactive oxygen species (ROS). These ROS have the potential to cause cell death by causing damage to the various cell structures of microorganisms and diseased mammalian cells. Traditional photosensitizers are natural molecules or their derivatives, which are known astetrapyrrolic compounds. When compared to these traditional photosensitizers, Ru(II) compounds have excellent photophysical properties, such as absorption in the visible range, one- and two-photon absorption in the biological therapeutic window. Additionally, some ruthenium photosensitizers have the ability to possess a good PDT even when exposed to conditions with low oxygen levels or under hypoxic conditions.

Liposomes are useful carriers for anticancer drugs, helping them reach tumour tissues. Due to their longer lifespan in the blood, liposomes, in particular those with polyethylene glycol chains, have been identified as versatile and biocompatible drug carriers. Shen et al. developed a liposome based theranostic nanodelivery system for ruthenium complex and in their study, liposome based ruthenium treatment induces double strand DNA breaks and induces apoptosis in MDA-MB-231 breast cancer cells.[431] Researchers have circumvented the low solubility issue by encapsulating the Ru in temperature sensitive liposomes and modify the liposomes with gold nanorods that permit precise Ru release into tumours.[432] Bonnet et al. used a clinical grade PDT laser source to trigger the activation of the ruthenium(II) polypyridyl complex which is functionalised in liposomes via the in situ red to blue light generated through TTA-UC. Through this process they were able to trigger the hydrolysis of the Ru-S bond using radiative energy transfer and to release Ru(II) complex upon excitation with a 630 nm laser.[93] According to these results, liposomal delivery of Ru(II) complexes to the target site and their activation is of value in anti-tumour activity research.

In this work, a bis-tridentate Ru(II) complex, based on the bqp-ligand (bqp = 2,6-di(quinolin-8-yl)pyridyl) complex has been studied as a potential photosensitizer for TTA-UC in solution and liposomes. These type of complexes have been reported earlier by Abrahamsson et al.[433] Many bis-tridentate complexes have a problem of very short excited state lifetimes (e.g. $\tau \approx$ 0.25 ns for $[Ru(tpy)_2]^{2+}$, tpy is 2,2′:6′,2″-terpyridine) and this does not allow them to be used as photosensitizers. Therefore, many attempts have been made to extend the excited state lifetime of the ^{3}MLCT state in bis-tridentate Ru(II) complexes.[434–436] In the case of Ru-bqp-oct ($[Ru(bqp)(bqpCOOC_8H_{17}](PF_6)_2$), the photosensitizer used in this work, the triplet character of the excited state is improved through mixing ^{3}LC states which can happen in tridentate ligand coordinated ruthenium polypyridyl complexes by expanding the N-Ru-N angles of the

coordination cage. As a result, the excited state lifetime of this complex is several microseconds long at room temperature for ^{3}MLCT. Therefore, this complex can be used as a triplet photosensitizer for TTA-UC. The complex is also conjugated with an octyl chain to increase the lipophilicity which will allow the complex to get embedded into the lipid bilayer.

Ru-bqp-oct
[Ru(bqp)(bqpCOOC$_8$H$_{17}$)](PF$_6$)$_2$
Where bqp = 2,6-di(quinolin-8-yl)pyridyl
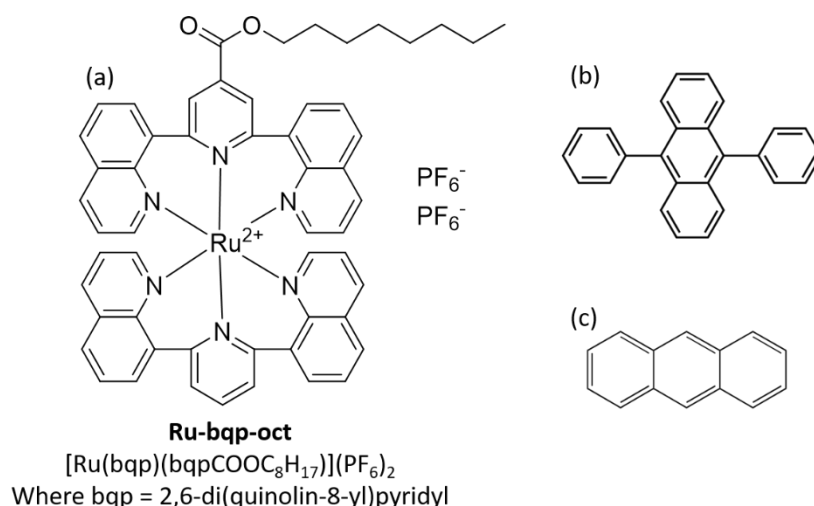
Figure 4.1 Chemical structure of (a) triplet photosensitizer Ru-bqp-oct, and annihilators (b) 9,10-diphenylanthracene, and (c) anthracene. Molecule (a) is synthesized by Christopher S. Burke (DCU).

In order to perform TTA-UC, one needs both a reliable photosensitizer and an efficient annihilator or acceptor. A good photosensitizer has a low fluorescence quantum yield, whereas a good annihilator should have high fluorescence quantum yield. At the same time, the annihilator should have a slightly lower triplet state energy than the photosensitizer with which it is paired. Unsubstituted anthracene has a fluorescence quantum yield of about 30%, and it has high intersystem crossing efficiency and triplet yield. The transition probabilities can vary significantly when the 9- and 10-positions of anthracene is substituted with some functional groups, e.g., the fluorescence quantum yield of 9,10-dimethylanthracene is about 70%. When bulky phenyl groups are substituted to anthracene, the [4+4] photocycloaddition is hampered which they can undergo at high concentrations under irradiation.[437] Diphenylanthracene has been successfully used as annihilator for TTA-UC and it has shown green-to-blue upconversion quantum yield (Φ_{UC}) ranging from 36 to 52% with the benchmark photosensitizer platinum(II) octaethylporphyrin.[438] Therefore 9,10-diphenylanthracene and anthracene can be used as annihilators with Ru(II) polypyridyl complexes.

Herein, the TTA-UC behaviour of Ru-bqp-oct and anthracene derivative pair was exploited initially at solution phase and found that at 1:20 micromolar ratio concentration, it gives

efficient TTA-UC. This concentration was later used to reconstitute within LUV, GUV and PDMS to obtain insight on TTA-UC, its localization and corresponding fluidity respectively.

4.2 Aims and objective

The field of TTA-UC is still emerging and although a number of triplet photosensitizers has been reported, there is still room for improvement in both photosensitizer and annihilator properties. Ruthenium(II) polypyridyl complexes are advantageous as triplet photosensitizers due to their unity triplet quantum yields and tuneable photophysical properties through structural modifications of their ligands.

This chapter aims to introduce Ru(II) polypyridyl complex with a long alkyl chain as a potential photosensitizer with triplet ligand centred character for TTA-UC. The TTA-UC has to be investigated in several solvents along with different annihilators to obtain the parameters for better efficiency. All annihilators may not be suitable with the photosensitizer to give UC and hence the performance of the annihilators towards TTA-UC and the reason for their ability to produce, or not, upconversion can be evaluated in terms of their quenching efficiency. A long-term objective of this work is to use this sensitizer in liposomal delivery vehicles; thus, the photosensitizer is modified with a long alkyl chain, and to compare the photophysics in solution and liposomes. The efficiency of incorporation of the photosensitizer into the lipid bilayer will be investigated with fluorescence spectroscopic and microscopic techniques to confirm the effective doping of liposome with the complex.

4.3 Materials and Methods

4.3.1 Materials

$[Ru(bqp)(bqpCOOC_8H_{17})](PF_6)_2$, also called Ru-bqp-oct where bqp = 2,6-di(quinolin-8-yl)pyridyl was synthesized by Christopher Burke, by following the procedure reported by Keyes et al. and Abrahamsson et al.[310,439] 1,2-Dioleoyl-sn-glycero-3-phosphocholine (DOPC) [purity (>99%)], and 1,2-dimyristoyl-sn-glycero-3-phosphocholine (DMPC) were purchased from Avanti Polar Lipids (Alabama, USA) and used without further purification. 1,2-distearoyl-sn-glycero-3-phosphoethanolamine-N-[amino(polyethylene glycol)-2000] (DSPE-MPEG(2000) sodium salt) was purchased from Cayman chemical. 1,2-Dioleoyl-sn-glycero3-phosphoethanolamine-labeled ATTO655 (DOPE-ATTO655) was purchased from ATTO-TEC GmbH (Siegen, Germany). 9,10-diphenylanthracene, anthracene, 9-anthracenecarboxylic acid, perylene, pyrene, phenanthrene, fluorine, rubrene, sodium sulfite, D-(+)-Glucose, sucrose, agarose, 1,4-dioxane, and phosphate buffer saline (PBS) tablets were purchased from Sigma-

Aldrich (Wicklow, Ireland). Aqueous solutions were prepared using Milli-Q water (Millipore Corp., Bedford, USA). The polydimethylsiloxane (PDMS) silicon elastomer was purchased from Dow Corning GmbH (Wiesbaden, Germany) and mixed following supplier instructions. Monodisperse polystyrene (PS) latex sphere with a diameter of 4.61 ± 0.4 μm was obtained from Bangs Laboratories Inc. (Fishers, IN, USA).

4.3.2 Photophysical Measurements

Absorbance spectra were measured using a Jasco V670 Spectrophotometer and data analysis was performed using Jasco Spectra Manager v2 software and Origin Pro 2020b. Fluorescence and upconverted emission measurements were acquired using a Varian Cary Eclipse Fluorescence Spectrophotometer (Varian Cary Eclipse Software v1.1). Fluorescence lifetime measurements were accomplished on a PicoQuant FluoTime 100 Compact FLS TCSPC system using a 450 nm pulsed laser from PicoQuant PDL800-B source and an external Thurlby Thandar Instruments TGP110 10 MHz pulse generator to enable acquisition of long lifetime data. Data was collected up to 10,000 counts and decay curves were achieved using PicoQuant Fluofit software and tail-fit statistical modelling. Fitting was evaluated with the tailfit criteria; $0.9 < \chi^2 < 1.1$ and by analysis of the residuals.

4.3.3 Triplet–triplet annihilation upconversion (TTA-UC)

10 mW fixed focus 532 nm Laser (Edmund Optics) was used as the excitation source. Upconverted emission spectra were recorded in biochemiluminescence mode and by blocking the excitation source from the fluorescence spectrophotometer. The laser power was measured using a power meter (Edmund Optics) and the diameter of the laser spot at 532 nm was 1 mm. Measurements were performed after deaeration by bubbling nitrogen through the samples for 30 min. All measurements were carried out in a quartz cuvette of 10 mm pathlength.

Threshold power density measurements: The solutions were prepared and transferred to a 1 cm Schlenk cuvettes under inert atmosphere for measurements. The emission spectra were recorded using an FLS980 emission spectrophotometer (Edinburgh Instruments) with a 532 nm (CW532-100, Roithner LaserTechnik GmbH) laser diode. A combination of neutral density filters (OD = 1 and/or 2) was used to record emissions at higher excitation powers.

4.3.4 Stern-Volmer Quenching Studies

Emission quenching studies were performed against 20 μM Ru-bqp-oct in acetonitrile which was titrated with increasing concentrations of quencher. Fluorescence emission spectra,

excitation spectra and lifetime decay were measured for each quencher concentration. The Stern-Volmer quenching constant (Ksv) and the bimolecular quenching constant (k_q) were obtained by fitting the data according to the Stern-Volmer equation;

$$\frac{I_o}{I} = \frac{\tau_0}{\tau} = 1 + K_{SV}[Q] \tag{4.1}$$

Where I_0 and I are the fluorescence emission intensities of Ru-bqp-oct photosensitizer in the absence and presence of quencher respectively. τ_0 and τ are the lifetimes of Ru-bqp-oct in the absence and presence of the quencher respectively. K_{SV} is the Stern-Volmer constant, $K_{SV} = k_q\tau_0$. $[Q]$ is the molar concentration of the quencher. The lifetime of the Ru-bqp-oct photosensitizer was obtained by fitting the luminescence intensity decays using a single exponential model for each concentration of the quencher separately. The slopes of the Stern-Volmer plots were obtained by fitting the plots to the linear equation in each case to obtain K_{SV} from which k_q was extracted for the entire range of quencher concentrations measured in every instances.

4.3.5 Photophysical Time Resolved Studies

Nanosecond time-resolved absorption (ns-TA) spectra was measured at Friedrich-Schiller University, Jena in collaboration with research group of Prof Benjamin Dietzek-Ivanšić, using a custom-built setup reported by Dura et al.[339] The electronics and programming to record the difference absorption signal are developed by Pascher Instruments (Lund, Sweden). All ns-TA spectra were measured by placing the samples in quartz-made inert cuvettes of 1 cm pathlength. The pump pulse energy was 0.12 ± 0.01 mJ for all ns-TA measurements.

4.3.6 Preparation of Large Unilamellar Vesicles (LUV)

The large unilamellar vesicles (LUV) (or liposomes) were prepared by hydration extrusion method. The lipid dissolved in chloroform was mixed with desirable concentration of photosensitizer and annihilator together or separately into a 1.5 mL vial. The solvent was evaporated by purging nitrogen and complete evaporation of the solvent was ensured by putting the reaction vial in vacuum for 30-60 min. A thin lipid film was formed along the walls of the vial and this was hydrated with 1 mL phosphate buffer saline (PBS) and the lipid-dye mixture was thoroughly mixed using vortex for 60 s. The resultant solution was taken in a 1 mL Hamiltonian syringe and extruded through a polycarbonate membrane of 100 nm pore size. The solution was passed through the membrane for at least 11 times or more as required. For DMPC lipid, the extrusion was performed at 30°C, which is above the melting transition

temperature of DMPC. The hydrodynamic radius of the resulting liposomes was measured using dynamic light scattering (DLS), Melvern Zetasizer Ultra.

4.3.7 Preparation of Giant Unilamellar Vesicles (GUV)

The GUVs were prepared by electroformation method using a Nanion Vesicle Pro instrument. DOPC lipid was mixed together with Ru-bqp-oct and the mixed solution was drop cast over the conductive side of indium-tin oxide (ITO) slides inside of an O-ring of 0.7 mm thickness that had been greased to the surface. The sample was dried in a nitrogen flow, and the complete evaporation was ensured by placing the slides in vacuum for 45 min. Then the one slide was introduced to the Nanion instrument chamber and warm 230 mM sucrose solution was then added inside the O-ring. On top of that slide, another slide was placed with the electric coils contacting the conductive side of both slides. Alternating current voltage of 0 to 3 V was applied at a temperature of 37 °C raised for 5 min and the applied voltage 3 V was applied continuously at a frequency of 10 Hz for electroformation to take place. This process was continued for 170 min at the same temperature with falling time of 5 min at the end. After the completion of electroformation, the top slide was removed the vesicle solution was collected with a pipette tip of large size by cutting the edge. The vesicle solution was added to 230 mM glucose solution to uphold the osmolarity inside and outside the vesicles.

4.3.8 Confocal Microscopy of Giant Unilamellar Vesicles (GUVs)

The fluorescence images of the GUVs were taken using a Leica TSP inverted (DMi8) confocal microscope. A 40x-oil immersion objective was used with the excitation line chosen from a white light laser as an excitation source. The Ru-bqp-oct within the GUV was excited at 496 nm and the emission was collected within 620-800 nm. Since the GUVs are highly mobile and difficult focus during the imaging process, the sample was mixed with 0.5% agarose to restrict the movement of the vesicles and the images were taken after 10 min of agarose addition.

4.3.9 PDMS Microcavity Array Preparation

Hand cleaved mica sheet pieces of 1 cm x 1 cm sized was glued onto a glass slide and then 20 µL of 0.1% solution of 4.61 µm sized polystyrene (PS) spheres in ethanol was drop cast over the mica sheets. The PS spheres self-assembled over the mica surface during the evaporation of ethanol. Once all of the ethanol gets evaporated, a desirable hexagonal assembly of PS spheres were obtained. Polydimethylsiloxane (PDMS) mixed with curing agent in 10:1 ratio was then added to the top of the glass slide without any air bubbles and this was dried at 90 °C

for about 60 min. The dried PDMS was removed from the glass slide, then sonicated for 15 min in THF in order to remove the PS spheres and this resulted in the formation of microcavity arrays of approximately 2 µm diameter on PDMS substrate. THF was evaporated by drying the substrate overnight. Since the PDMS substrate is hydrophobic in nature, it was oxygen plasma treated for 5 min to make it hydrophilic prior to lipid bilayer formation. The oxygen plasma treatment ensured aqueous filling inside the cavities and provided a sufficiently hydrophilic interface to support the lipid bilayers as the bilayers are unstable without this step. Prior to lipid monolayer transfer, the PDMS substrate was sonicated in PBS for 15 min to ensure the aqueous filling inside the cavities.

4.3.10 Preparation of Microcavity Supported Lipid Bilayers (MSLBs)

The DOPC lipid bilayer was prepared over the aqueous filled microcavities and this is called as microcavity supported lipid bilayer (MSLB). The lipid monolayer was transferred onto the PDMS substrate using the Langmuir-Blodgett (LB) technique from air-water interface.[187,195,199,357] The lipid solution in chloroform of 1 mg/mL concentration was added dropwise to the water subphase of LB trough and the solvent was allowed to evaporate for 10 min. The lipid monolayer was transferred to the PDMS substrate with microcavities at a surface pressure of 33 mN/m. Later the substrate was enclosed within a microfluidic chamber and liposomes doped with Ru-bqp-oct was introduced into the chamber. The sample was allowed to incubate for 90 min for lipid bilayer fusion and any residual liposomes within the chamber was washed away by flushing with excess amount of PBS. The resultant MSLB was used for FLCS and FLIM studies.

4.3.11 Fluorescence Lifetime Imaging (FLIM) and Fluorescence Correlation Spectroscopy (FCS)

Fluorescence lifetime imaging (FLIM) and fluorescence correlation spectroscopy (FCS) measurements on MSLB were performed using a MicroTime 200 system (PicoQuant GmbH, Germany) integrated with FCS module, dual SPAD detection unit, time-correlated single photon counting (TCSPC), and inverted microscope model Olympus X1-71 with an Olympus UPlan SApo 60x/1.2 water immersion objective. Further details are given in chapter 2 and 3 along with the equations used for data analysis and fitting.

4.4 Results and Discussion

4.4.1 Photophysical studies
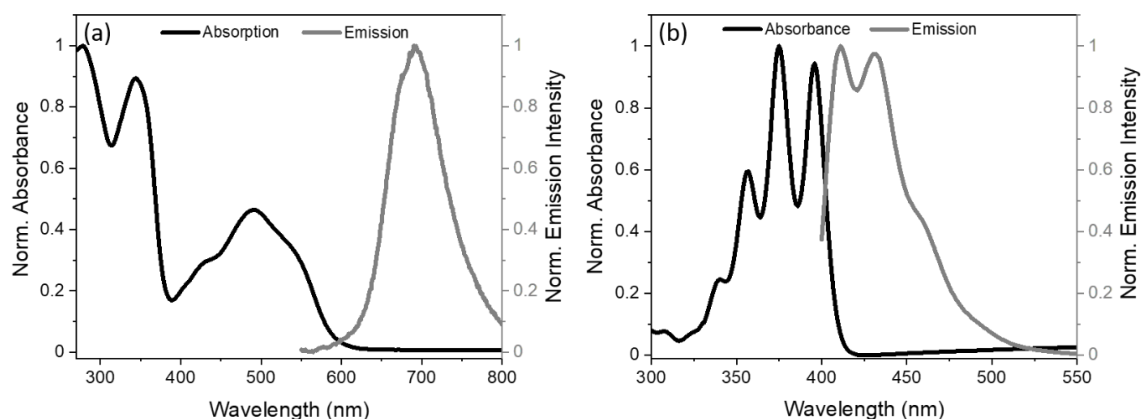
Figure 4.2 Normalised absorption and emission spectra of (a) 10 µM Ru-bqp-oct in acetonitrile, and (b) 20 µM 9,10-diphenylanthracene (DPA) in chloroform. The emission spectra of Ru-bqp-oct and DPA were collected by exciting at 490 nm and 395 nm respectively. Excitation and emission slit width of 5 nm was used.

Figure 4.2a shows the absorption (black) and emission (grey) spectra of the photosensitizer Ru-bqp-oct obtained from acetonitrile at a concentration of 10 µM. The observed absorption maxima and peak position of Ru-bqp-oct are consistent with that reported for $[Ru(dqp)_2]^{2+}$, the analogous complex reported previously without the Oct tail.[440–442] The absorption band centred at 343 nm is assigned to ligand centred transitions whereas the broad absorption band ranging from 400 to 600 nm with a maxima at 490 nm originated due to dπ-π* singlet metal-to-ligand charge transfer (^{1}MLCT) transition.[433] The π-π* transitions in the ligand moieties contribute to the absorption band in the UVB region.[443,444]
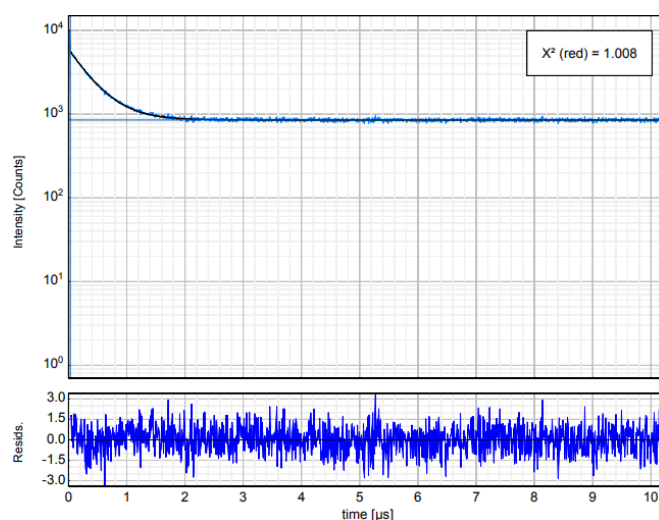
Figure 4.3 Lifetime decay curves and fit of 10 µM Ru-bqp-oct in acetonitrile under 450 nm excitation.

The emission spectrum of Ru-bqp-oct in acetonitrile on excitation to the lowest energy absorption band maxima at 490 nm shows an intense emission centred at 690 nm, and its emission band is relatively broad when compared to conventional metal-free fluorophores, ranging from 600 to 800 nm in wavelength. In addition, the Stokes shift (emission wavelength-excitation wavelength), which equals to ~200 nm is typical of a triplet charge transfer transition but very high compared to organic based fluorophores (<80 nm), this can be a key advantage in imaging or in TTA-UC where high concentrations of luminophore may accumulate but will not self-quench. The typical absorption and emission spectra of the potential annihilator DPA in chloroform is given in figure 4.2b.[445] When compared, the emission profile of both Ru-bqp-oct and DPA did not overlap suggesting that this can potentially be used for TTA-UC studies as well as simultaneous detection using fluorescence based imaging tools. The emission lifetime of the Ru-bqp-oct complex in solution (acetonitrile). As expected, the complex shows a single exponential emission decay with a lifetime of 384 ns in presence of air and 2.51 µs in deaerated conditions.[446,447] The emission lifetime decay curve and the corresponding fit is shown in Figure 4.3.

4.4.2 Triplet-Triplet Annihilation Upconversion (TTA-UC)

This Ru-bqp-oct complex exhibits strong and broad absorption as well as long-lived triplet excited states, making it potentially useful as a triplet photosensitizer.[448–450] Consequently, Ru-bqp-oct can thus be used as a photosensitizer for TTA-UC. Since this complex has a broad absorption, extending over to nearly 600 nm, the 532 nm is close to but on the red edge of the MLCT band (green laser) and can be used to excite TTA-UC.
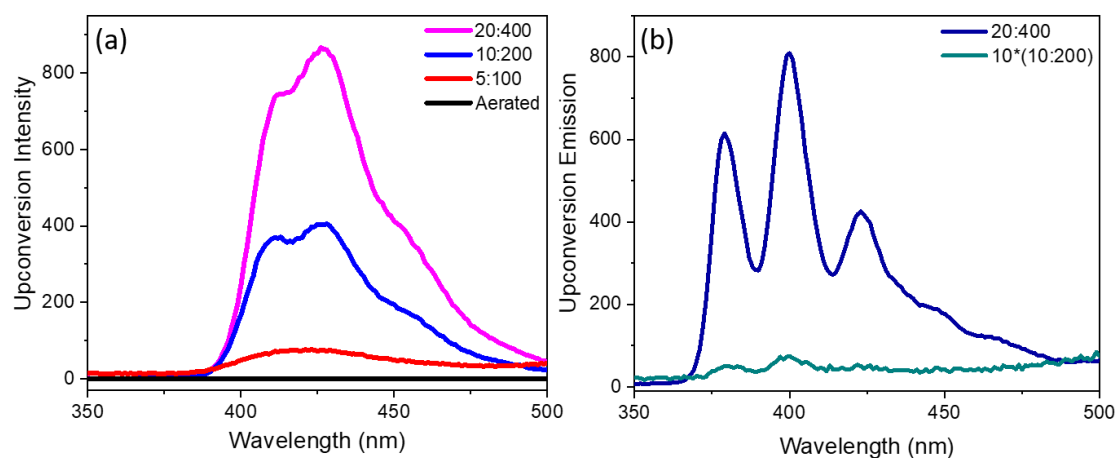
Figure 4.4 Upconverted emission from deaerated acetonitrile containing (a) Ru-bqp-oct and DPA at 1: 20 ratio with three different concentrations of 5 µM:100 µM, 10 µM:200 µM, and 20 µM:400 µM photosensitizer:annihilator concentrations including one sample before deaeration showing the absence

of TTA-UC and (b) 20 μM Ru-bqp-oct and 400 μM anthracene at 5 nm slit width under 532 nm excitation.

Firstly, to identify the best annihilator, the triplet photosensitizer Ru-bqp-oct was tested for TTA-UC with a number of different annihilators, including DPA, anthracene, 9-anthracenecarboxylic acid, phenanthrene, pyrene, perylene, fluorine, and rubrene in deaerated acetonitrile upon excitation with a 532 nm laser. Upconversion was only observed with DPA or anthracene annihilator. Figure 4.4a shows representative upconverted emission from deaerated acetonitrile that contains Ru-bqp-oct as photosensitizer and DPA as annihilator. This photosensitizer-annihilator pair was optimised by examining two different ratios, 1:10 and 1:20, with 1:20 showing the best upconversion efficiency. In addition to DPA, anthracene annihilator also provides comparable TTA-UC efficiencies, however, at low concentrations of Ru-bqp-oct (10 μM) and anthracene (200 μM), the efficiency of anthracene was found to be lower than DPA. Figure 4.4b shows that the TTA-UC signal for an anthracene-based system is 5-6 times smaller than that for DPA at same lower concentrations. Nonetheless the anthracene pair may offer a useful TTA-UC system as the upconverted signal extends to the UV. The distinction in efficiency likely originates from thermodynamic effects.

Focusing on the first pair, a strong oxygen sensitive violet emission was observed with the addition of DPA to the triplet photosensitizer Ru-bqp-oct. Controls confirmed that the anti-Stokes emission from the Ru-bqp-oct:DPA system is due to TTA-UC because the upconverted emission bands were absent for samples with DPA alone and Ru-bqp-oct alone under the same experimental conditions. Furthermore, it is evident from the absence of upconverted emission band in presence of oxygen as shown in Figure 4.4a (black). Also, the upconverted emission band was disappeared when oxygen was admitted to the solution which was showing TTA-UC in the deaerated conditions.

Figure 4.5 Digital photograph showing the intense upconverted violet emission from deaerated acetonitrile containing 20 µM Ru-bqp-oct and 400 µM DPA upon excitation with a 532 nm green laser of 10 mW power.

The upconverted emission from the deaerated acetonitrile solution containing Ru-bqp-oct and DPA is clearly visible by eye as shown in the digital photograph in Figure 4.5.

The persistence of TTA-UC across solvents; 1,4-dioxane, ethyl acetate, toluene, hexane and acetonitrile-water mixture, was then explored on the Ru-bqp-oct and DPA pair at 1:20 ratio with 20:400 µM photosensitizer to annihilator concentration. Interestingly, the process showed significant solvent dependence, and only 1,4-dioxane and acetonitrile exhibited significant upconversion emission intensity as shown in Figure 4.6a. To explore if a more polar, and potentially anionic annihilator is effective with Ru-bqp-oct, 9-anthracenecarboxylic acid (9-ACA) was also investigated as a potential annihilator. The rational for using 9-ACA, a derivative of anthracene, is that the availability of free carboxylic acid not only can aid solubility in protic solvents, but also, if combined with Ru-bqp-oct, can provide efficient TTA-UC, and later, 9-ACA can be further be modified with suitable other ligand/functional group for specific application. Interestingly, when combined with Ru-bqp-oct, the 9-ACA showed TTA-UC only in ethyl acetate and a weak process in acetonitrile. Since the normal broad emission band of 9-ACA is around 465 nm, the upconverted emission was also observed in the same region as it is given in Figure 4.6b.
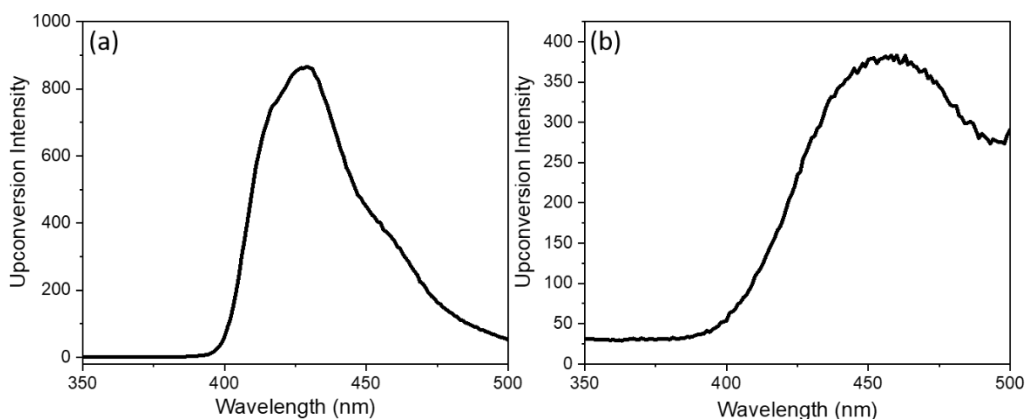
Figure 4.6 Upconverted emission from the deaerated solution containing 20 µM Ru-bqp-oct photosensitizer with annihilators (a) DPA in 1,4-dioxane and (b) 9-anthracenecarboxylic acid in ethyl acetate at 5 nm slit width under 532 nm excitation.

4.4.3 Threshold Power Density Measurements

Threshold power density measurements provides important validation of efficient TTA-UC. It has been widely used to support sensitized photochemical upconversion through TTA due to the quadratic incident light power dependence of the anti-Stokes fluorescence.[20] In steady-state photoluminescence experiments, the power dependence is usually measured with both coherent (laser) and non-coherent (lamp) sources of excitation. In the present study, it is experimentally shown that Ru-bqp-oct and DPA in deaerated acetonitrile solution undergo photochemical upconversion under 532 nm laser excitation with power dependence that lies somewhere between quadratic and linear. Through the use of neutral density filters, the power density was systematically changed and measured with a power meter. During the threshold power density measurements, the upconversion intensity was examined directly as a function of excitation power density. As shown in Figure 4.7, when the photosensitizer is selectively excited with the 532 nm output from a CW laser in N_2-saturated acetonitrile, the intensity of the singlet fluorescence emanating from DPA at 426 nm is a linear function of incident power density. Figure 4.7 shows that the slope has decreased considerably at higher excitation power densities. With increasing incident photon flux, the slope of the plot, progressively shifts away from the starting value and at high incident power densities, the slope reaches 1.0. According to this study, a wide range of power-dependent responses can be measured in a single sample for various sensitized TTA compositions. This finding also concurs with data from similar studies on different sensitized TTA compositions. At the slope transition point, the process transitions from the low annihilation region (quadratic) to the high annihilation region (linear) is called threshold power density (I_{th}).[346] In the linear regime, for a particular concentration, the

maximum quantum efficiency is achieved, and beyond this point, the intensity of the upconverted emission is directly proportional to the number of triplet excited states sensitized.[451,452]
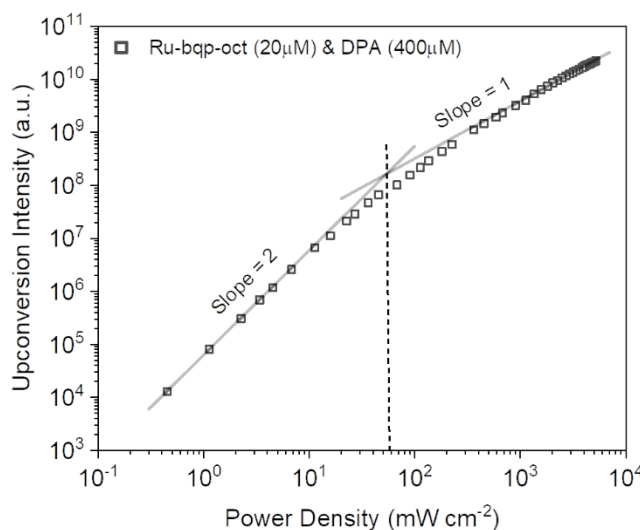
Figure 4.7 Double logarithmic plot of upconversion emission signal at 426 nm measured as a function of the power of incident laser of 532 nm in a mixture of 20 µM Ru-bqp-oct and 400 µM DPA in deaerated acetonitrile. The linear fits with slopes 1 and 2 at high and low power regimes are included.

The I_{th} value of 20 µM Ru-bqp-oct and 400 µM DPA is 54 mW cm^{-2}. A low I_{th} value is an indication of high TTA-UC efficiency. There are some reports on even lower Ith value, for example, Liang et al. has reported 3.63 mW cm^{-2} for an upconversion system containing Ru(II) phenanthroline complex and 2-substituted anthracene named DTACI.[453]

4.4.4 Stern-Volmer analysis with Annihilators as Quencher

Given thermodyanamic properties it was surprising that some of the annihilators explored with Ru-bqp-oct, did not show TTA- UC, one prospect, is that they quench emission from Ru through for example electron transfer proceses. To examine this, it was evaluated if quenching is observed by Stern-Volmer analysis, equation 4.1.[454–456]

Ideally, lifetime measurements are used to distinguish static quenching from dynamic quenching and they can also be distinguished by their dependence on temperature and viscosity. When temperature is higher, diffusion will be faster, resulting in higher collisional quenching, and weakly bound complexes will typically dissociate, resulting in lower static quenching. Quenching increases the rate at which the excited state depopulates, resulting in a decrease in lifetime and quenching also depopulates the excited state without fluorescence

126

emission, resulting in a decrease in yield. Since only fluorescence molecules are observed, static quenching does not decrease lifetime, as uncomplex fluorophores are unquenched.[457]

Finally, fluorescence lifetime measurements are essential to discriminating static from dynamic quenching. Indirect methods can sometimes be used in place of direct measurements of dynamic quenching, such as fluorescence lifetime anisotropy, which is in fact dependent on fluorescence lifetime and has no other direct method to establish dynamic quenching. The differences between lifetime- and intensity-derived quenching efficiencies or Stern-Volmer plots are characteristics of static mechanisms of quenching, or mixed static and dynamic mechanisms of quenching or an inner-filter effect parallel to quenching.[458]

If the annihilator is also an electron transfer quencher, TTA-UC will not take place. Emission spectra of 20 µM Ru-bqp-oct were collected in presence of increasing concentrations of DPA and perylene and the corresponding Stern-Volmer plot is given in Figure 4.8. The data do not fit to Stern-Volmer equation (green dotted line) and hence a linear fit (red line) is also used.
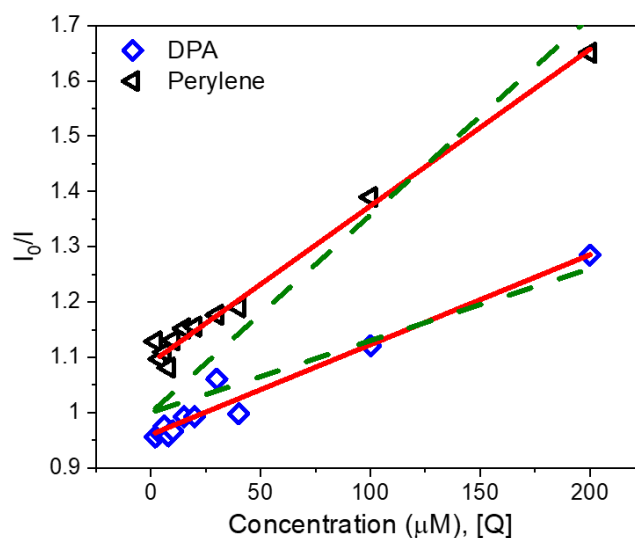
Figure 4.8 Stern-Volmer plot obtained from the emission spectra of 20 µM Ru-bqp-oct titrated against increasing concentrations of DPA (blue open square) and perylene (black open triangle) as quenchers in acetonitrile upon 532 nm excitation. Red line is the linear fit and green dotted line is the Stern-Volmer fit.

Interestingly from Figure 4.8, DPA is observed to quench emission from Ru but the effect is very weak and unlikely to compete significantly compete with TTA-UC mechhanism.[459] The Stern-Volmer quenching constant (K_{sv}) can be calculated from the Stern-Volmer and since the data points are not fitting to Stern-Volmer equation, the K_{SV} can be considered as affinity constant in static system. So, the affinity constant value for Ru-bqp-oct/DPA pair is $0.00136\pm1.09 \times 10^{-4}$ M^{-1}. Notably there is no impact on lifetime data of Ru, thus any quenching

occurring is static, again, making it unlikely to compete with TTA-UC. Perylene is a commonly used annihilator because of the suitable photophysical properties such as high fluorescence quantum yield, long lived triplet state etc. Therefore, perylene was used as a quencher to study its efficiency towards TTA-UC along with Ru-bqp-oct as photosensitizer. Interestingly perylene was a modestly effective quencher of Ru-bqp-oct. The affinity constant for Ru-bqp-oct/perylene pair is $0.00283 \pm 8.67 \times 10^{-5}$ M^{-1}. Quenching has affected the emission lifetimes of the triplet photosensitizer. Longer lifetimes after the addition of perylene roots for more efficient quenching of the luminescence emission. The quenching plot of perylene shows a larger slope than that of DPA.[460,461]

4.4.5 Nanosecond Transient Absorption Measurements

Nanosecond transient absorption (nsTA) spectroscopy was used to study the dynamics of the photophysical processes underlying Ru-bqp-oct/DPA TTA-UC. The photosensitizer Ru-bqp-oct (20 µM) was studied with and without 400 µM DPA as annihilator to explore the processes occurring at picosecond to microsecond timescale. The measurements were performed in acetonitrile under inert conditions.
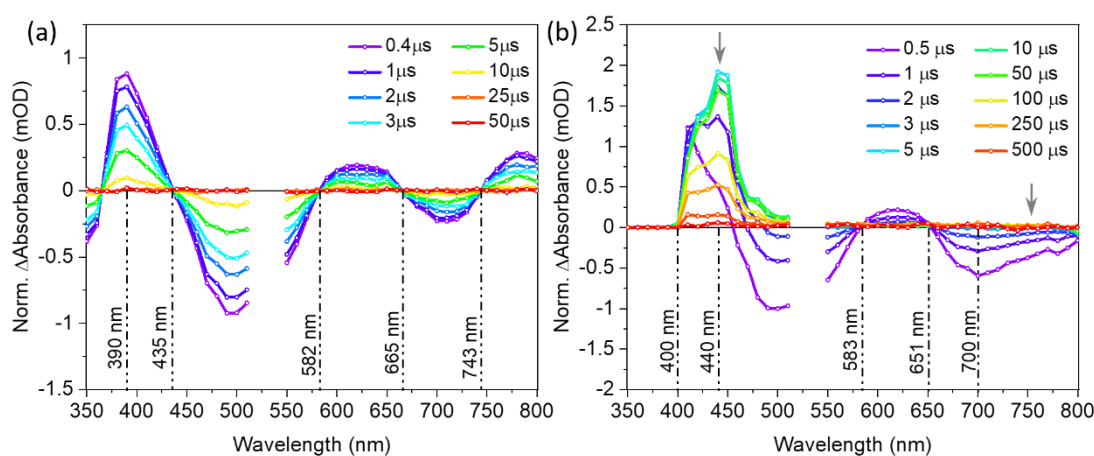
Figure 4.9 Nanosecond transient absorption spectra of (a) Ru-bqp-oct - 20 µM, and (b) Ru-bqp-oct - 20 µM & DPA 400 µM in deaerated acetonitrile. Arrows in (b) show the changes in the spectra with respect to (a) upon addition of 400 µM perylene.

The ns-TA spectra of Ru-bqp-oct without DPA is shown in Figure ns-TA spectra of B2P is given in Figure 4.9a and Figure 4.9b shows the same with DPA. As shown in Figure 4.9a, the stimulated emission for Ru-bqp-oct is centred on 700 nm, while ground state bleach (GSB) is at 500 nm, and excited-state absorption (ESA) is near 400 nm. Using monoexponential global fit to the data, it was found that the photosensitizer has a characteristic decay time of 4.3 µs,

which can be ascribed to the triplet state lifetime of the photosensitizer. Abrahamsson et al. has previously reported on $[Ru(dqp)_2]^{2+}$ and the decay time is consistent with their observations.[439,441] The excited state lifetime of 50 µM DPA under identical experimental conditions are reported in the literature to be 3.1 ms.[462,463]

The differential absorption features of the photosensitizer remain visible even after the addition of 400 µM DPA to the solution (Figure 4.9b). However, an additional ESA band appears as indication of the triplet state of DPA.[464] Due to triplet-triplet energy transfer (TTET) in presence of DPA, the ^3S lifetime of the photosensitizer has reduced to <100 ns (almost got quenched). The triplet lifetime of annihilator is biexponential with τ_{dec1}=25 µs and τ_{dec2}=110 µs. In the absence of DPA, the ground state bleach (GSB) dominates over the spectral range from 435 nm to 582 nm. Another GSB is seen in Figure 4.9a between 665 nm and 743 nm which is similar to the emission band of the photosensitizer and attributed to stimulated emission. When DPA was added, the second GSB shifts to the blue and broadens. As shown in Figure 4.9a, a intense ESA is observed from 365 nm to 435 nm with a peak maximum at 390 nm. A tail end of GSB corresponding to the absorption band of ligand centred transition is visible which ends at 365 nm. In Figure 4.9b, the dominant ESA centred at 440 nm and the changes in the ESA from Figure 4.9a is indicated by an arrow which matches with the emission characteristics of DPA (cf. Figure 4.2b) and the differential absorption signature has increased here. The intensity of GSB centred on 700 nm has increased with the presence of DPA.

4.4.6 Reconstitution of Ru-bqp-oct into lipid bilayer

In order to examine if the TTA-UC process observed in solution occurs in lipsoome, Ru-bqp-oct was reconstituted into DOPC liposomes prepared through hydration extrusion method. Figure 4.10a shows the dynamic light scattering (DLS) result of large unilamellar vesicles (LUV) reconstituted with Ru-bqp-oct and the hydrodynamic radius of the vesicles obtained are around 145±5 nm.
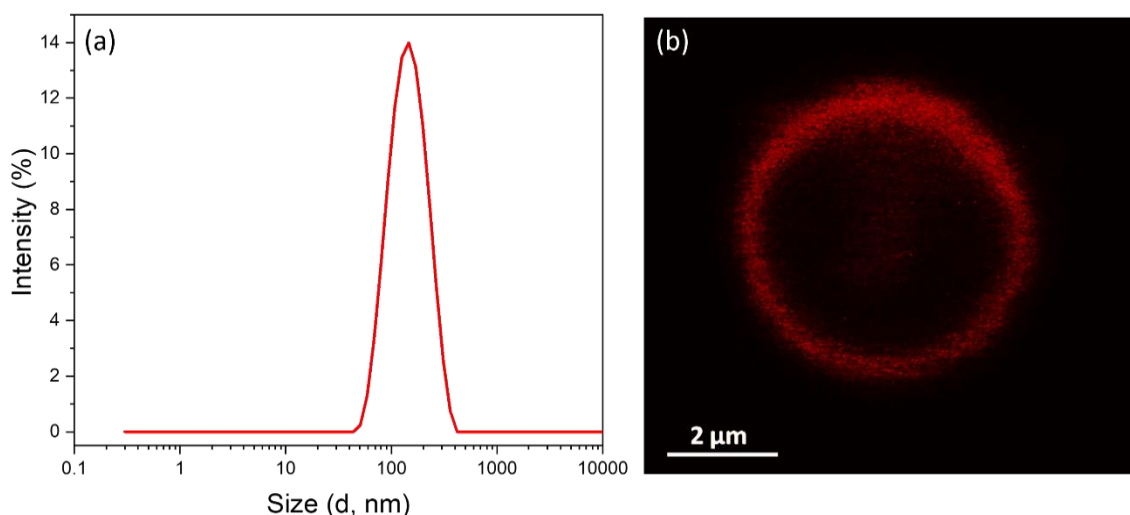
Figure 4.10 (a) DLS spectra of DOPC large unilamellar vesicles labelled with Ru-bqp-oct and (b) confocal image of GUV of DOPC lipid labelled with Ru-bqp-oct. λ_{ex} = 496 nm. The emission was collected within 620-800 nm.

LUVs cannot be visualized individually in a confocal microscope because of the diffraction limit of the optical microscope. In order to confirm the reconstitution of Ru-bqp-oct within the bilayer, giant unilamellar vesicles of 5-10 µm size were prepared. These GUVs can facilitate the imaging of Ru-bqp-oct doped vesicles. A GUV is considered to be a useful cell membrane model due to its similar dimensions and low curvature, which has analogous characteristics to the real cell membrane. For visualization, 5 µm of Ru-bqp-oct was reconstituted into the GUV and the confocal image was taken by exciting the sample at 496 nm and the emission was collected from 620 to 800 nm. Figure 4.10b shows the confocal image of DOPC GUV labelled with Ru-bqp-oct where it is clear that the photosensitizer is confined to the lipid bilayer of the membrane with no emisson from background solution. The lifetime of the photosensitizer within the lipid bilayer of liposomes was measured to be 643±8 ns. The lifetime of the photosensitizer has increased almost 2 times from solution to the introduction into the membrane both under aerated conditions. This may be due to restricted oxygen quenching or due to the more rigid environment of the liposomal membrane.

4.4.7 FCS and FLIM studies of Ru-bqp-oct in Microcavity Supported Lipid Bilayer

Due to the smaller size of LUVs and the diffraction limit of the confocal microscope, the diffusion coefficient (D) of the photosensitizer cannot be determined reliably from them. On the other hand, the measurement of D is a good way to confirm the reconstitution of the photosensitizer within the lipid bilayer. There are many reports on fluorescence lifetime correlation spectroscopy (FLCS) measurements on GUVs to find out the D value.[465] As

mentioned in previous chapters, measuring the translational diffusion using GUVs while feasible, is difficult due to their high mobility, they tend to diffuse in and out of the confocal focus. And while addition of agarose gel to restrict the movement can help it may affect the accuracy of diffusivity calculations and the lifetime of the probe. This work utilizes the previously established PDMS microcavity 2D array platform which is suitable for studying lipid-protein, lipid-drug and lipid-photosensitizer interactions using FLCS as seen in previous chapters.[187,194,355,356] PDMS microcavity array with pore suspended bilayer were used as they can render a highly fluidic bilayer where diffusivity has been shown to be akin to GUV. In this regard, the MSLB platform is very useful to understand diffusivity of luminophore in membrane due to its high stability and highly addressable nature.

After the transfer of DOPC lipid monolayer over the aqueous filled micron-sized cavities by Langmuir-Blodgett technique, the bilayer was produced by vesicle fusion using the Ru-bqp-oct reconstituted LUVs inside the microfluidic chamber.
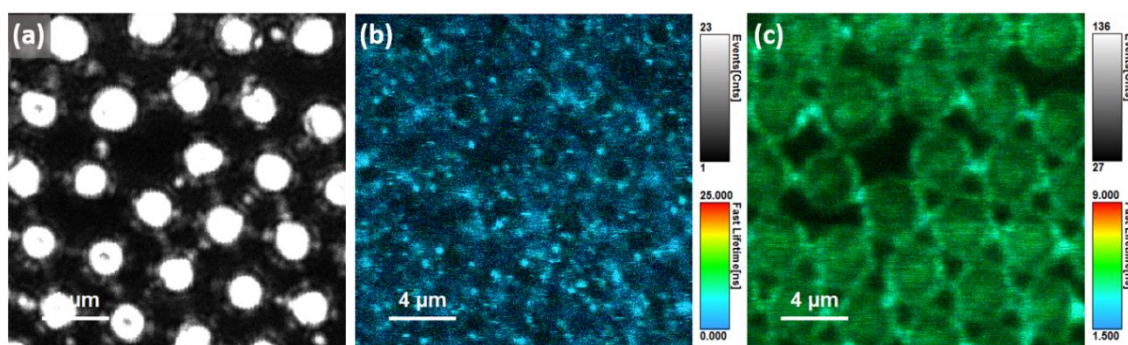
Figure 4.11 (a) Reflectance image of microcavity supported lipid bilayer showing the aqueous filled cavities, fluorescence lifetime images of DOPC bilayer labelled with (b) Ru-bqp-oct at 532 nm excitation and (c) DOPE-Atto655 at 640 nm excitation. Scale bar indicated 4 µm.

The reflectance image shown in Figure 4.11a which is generated due to the back scattering of light from the aqueous filled cavities and as described earlier, serves to identify the buffer filled cavities since some cavities may remain unfilled where they appear dark. Figure 4.14b shows fluorescence lifetime image (FLIM) at the same area as that of Figure 4.11a taken by exciting Ru-bqp-oct selectively after z-scanning to find the membrane. When combined both reflectance and FLIM image, it can be concluded that the bilayer is successfully spanned over the buffer filled cavity array. The lipid bilayer was co-labelled with DOPE-ATTO655 in order to have a better understanding about the focus, bilayer position and diffusion of the membrane. Figure 4.11c shows the FLIM taken by exciting the DOPE-ATTO655 dye with a 640 nm laser and the formation of bilayer was confirmed. FLIM of Ru-bqp-oct within the bilayer was

captured by exciting the sample with a 532 nm laser and the image shows a uniform labelling of the photosensitizer over the span of the membrane.
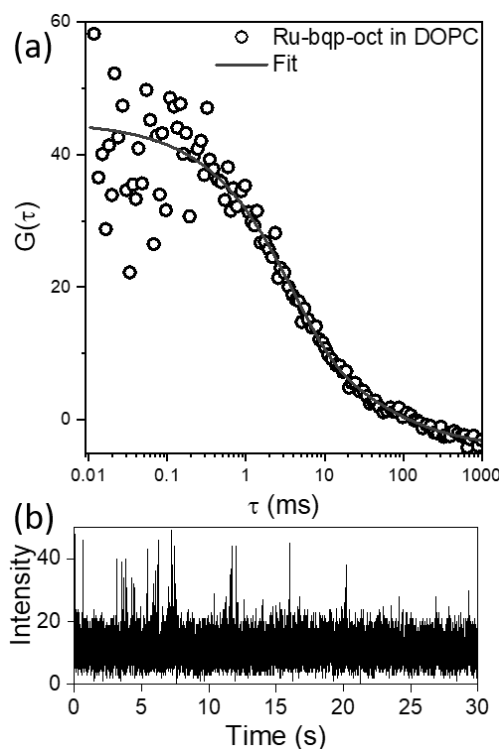
Figure 4.12 (a) Representative fluorescence lifetime correlation spectroscopic (FLCS) autocorrelation function (ACF) of DOPC MSLB labelled with 10 nM Ru-bqp-oct (upper leaflet) and the (a) corresponding intensity-time trace. FLCS was measured over 40-50 cavities and the average is shown. The solid lines are the 2D diffusion fit using equation 2.1. All measurements were carried out under PBS of pH 7.4.

Fluorescence lifetime correlation spectroscopy (FLCS) was used to determine the translational diffusion coefficient of the photosensitizer in the membrane. Due to the large cavity size, it is possible to carry out point FLCS measurements with the observation/detection volume at the centre of the cavities with spanned bilayer. FLCS experiment was performed on the MSLB and the measurements were carried out over many cavities (atleast 40-50 cavities each time). A representative autocorrelation function (ACF) from FLCS is given in Figure 4.12a as $G(\tau)$ versus lag time (τ). The solid line is the fit using 2D diffusion model equation defined in equation 2.1. The transit time was extracted after the fit and the average diffusion coefficient was determined as 5.7±2.2 $\mu m^2 s^{-1}$, according to equation 2.2. At the same time, a reduction was observed in the lipid diffusivity value as 7.4±1.4 $\mu m^2 s^{-1}$ with α value of 0.871. The photosensitizer has a good diffusivity value, but interestingly, it does not follow Brownian motion as the α value (0.65) is not close to 1. Such sub diffusion is surprising in DOPC and the

spikes in the intensity-time trace shown in Figure 4.12b may indicate that there is aggregation of the complex possibly through the Oct tails.

4.4.8 TTA-UC in Model Membranes
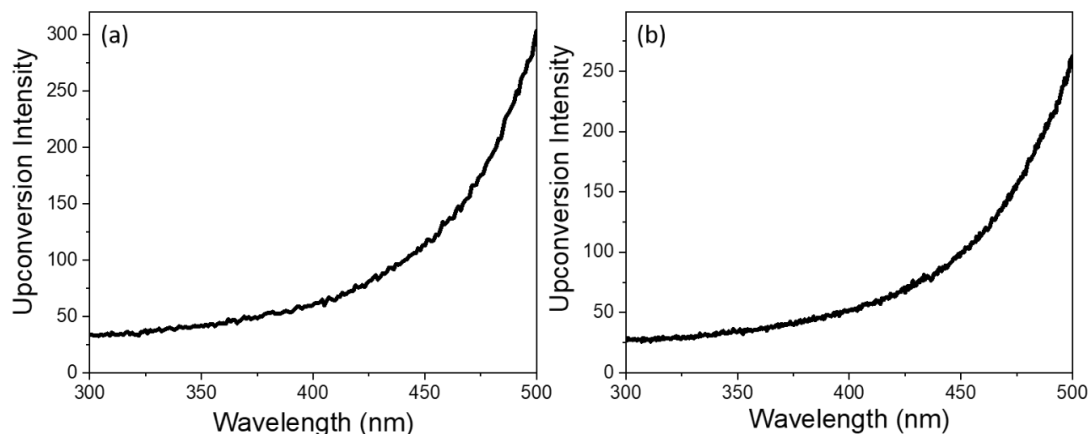
Figure 4.13 (a) DOPC and (b) DMPC+DSPE-MPEG(2000) liposomes of 140 nm diameter containing 5 µM Ru-bqp-oct and 100 µM DPA in deaerated PBS at 532 nm excitation.

After reconstitution was verified, it was evaluated if TTA-UC could be observed in the lipid bilayer when Ru is combined with the annihilator. Initially, the studies were carried out using DOPC liposomes containing 0.5 µM Ru-bqp-oct and 10 µM DPA, but upon excitation with 532 nm under deaerated conditions in phosphate buffered saline (PBS) no upconverted signal was found. As upconversion was not occurring, the concentration was progressively increased to ten times (10x). Further increase in concentration was also attempted, but the encapsulating efficiency within the liposomes was limited as the photosensitizer formed a red-coloured precipitation from the solution. In a subsequent attempt, the photosensitizer to annihilator ratio was varied from 1:20 to 1:5, 1:10, 1:30. As an alternative to deaeration by purging inert gas, sodium sulfite was used as oxygen scavenger to remove molecular oxygen from the liposomes. The study was carried out also on with different lipid compositions, including as DMPC, DMPC+DSPE-PEG(2000), and DMPC+DMPE-PEG(2000), as polyethylene glycol (PEG) has been shown to be the optimal choice for obtaining sterically-stabilized liposomes.[249,255] Also, alternative approaches were tried with anthracene as annihilator, but none of these attempts were successful. Two representative spectra of such results are given in Figure 4.13 a, and b.

The reason for the absence of anti-Stokes emission in the liposomes with the Ru-bqp-oct could be due to the orientation of the photosensitizer within the liposomes. The TTET is a Dexter energy transfer and requires collision between donor and acceptor. The annihilator molecule is more likely to be deeply embedded within the membrane and if the photosensitizer is oriented

at the interface (due to its charge) with the tails anchored in the bilayer at the interface, the collision of the chromophore parts of the molecule will not take place preventing energy transfer. Another possible explanation could be the aggregation of the photosensitizer within the bilayer resulting in no energy transfer with the annihilator molecule and rather the interactions between the photosensitizer molecules. The former is more likely to be the explanation and computational simulations are ongoing that may provide better insight into the orientation and triplet energy transfer.

4.5 Conclusions

In this chapter, a different photosensitizer was used as a photosensitizer for TTA-UC other than the BODIPY-derived compounds which was already been studied in earlier chapters. Ru-bqp-oct complex with high triplet ligand centred character was investigated as a photosensitizer for TTA-UC. Given the excellent photophysical properties, this photosensitizer shows good efficiency towards TTA-UC when combined in deaerated acetonitrile with suitable annihilator. For better upconversion results, the experimental conditions were tested with a series of annihilators and solvents, among which anthracene derivatives and acetonitrile found to give good TTA-UC. An investigative study on the fixed concentration of photosensitizer with increasing concentrations of annihilators as quencher revealed that perylene is quenching the emission of the photosensitizer and that could be the reason why it is not acting as an annihilator for this particular photosensitizer. The Stern-Volmer plot also shows that even though DPA exhibits quenching behaviour, it is very weak and unlikely to compete with TTA. A detailed evaluation of different concentrations and ratios of photosensitizer and annihilator resulted in fixing 1:20 better. The measurement of TTA-UC as a function of power density shows that, 54 mW cm^{-2} is the threshold power density (I_{th}) at which the transition from low annihilation regime to high annihilation occurs, indicating good efficiency. The nanosecond transient absorption results show that the triplet state lifetime of the photosensitizer is 4.3 µs, which is getting quenched upon addition of the annihilator to <100 ns. The lifetime of TTET process is 0.6 µs and the annihilator in presence of photosensitizer has a bi-exponential decay with 25 µs and 110 µs triplet state lifetimes. Prior to studying the TTA-UC process in biomembranes, the reconstitution of the photosensitizer within the bilayer was confirmed with the help of GUVs and its confocal image. Fluorescence lifetime correlation spectroscopy (FLCS) was employed to study the diffusion of the photosensitizer across the bilayer using Ru-bqp-oct doped microcavity supported lipid bilayer (MSLB). The translational diffusion coefficient of the photosensitizer was calculated to be 5.7 µms^{-1}, which is not as fast as the diffusion of the

membrane label with an anomalous coefficient showing non-Brownian behaviour. This feature along with prominent spikes in the intensity-time trace may be due to aggregation of the photosensitizer. The photosensitizer and annihilator were incorporated into DOPC liposomes and there was no indication of TTA-UC signal from the system. More attempts with different experimental parameters and lipid compositions also resulted in the absence of anti-Stokes emission. The reason for this observation is likely to originate from the differential orientation of the photosensitizer and annihilator in the membrane that prohibits effective collision leading to Dexter energy transfer required for TTA and the computational studies on the orientation of the molecules within the lipid bilayer are under process.

Chapter 5

Microcavity Supported Lipid Bilayers: Versatile tools for understanding membrane fluidity responses to drug and fluorophores

5.1 Introduction

Biomimetic cell membrane models have been studied and developed for decades in part because of its traffic behaviour in controlling analyte movement in and out across the cell membrane as well as the outer natural photosynthesis's massive size, ultimate efficiency, and sustainability.[466,467] An integrated image of operation rich in spatiotemporal details has emerged after decades of study of the molecular organization and photodynamics of various natural systems. We are already familiar with lipids and their most common aggregate formation, bilayers, in chapter 1 which serve essential structural functions such as cellular compartmentalization and hosting membrane proteins from basic cell biology. Lipid bilayers, as a molecular scaffold, provide appropriate sites for photosynthetic protein fragments to anchor, and their well-defined aqueous/lipid interfaces and hydrophobic interior further direct protein folding and assembly.[468] In terms of drug development, the lipid bilayer forecasts the passive permeation of small molecule drugs.[469,470] In this chapter, the reason why pore-suspended lipid bilayers are a true biomimetic model membrane is explained and how they can be used to investigate drug-membrane interactions as well as translational lipid and metal-complex based photosensitizer diffusivity.

In the early phases of drug development, artificial membranes provide a useful tool for studying drug interactions with the membrane and can be used to predict both passive membrane permeability and membrane-associated toxicological problems without the complexity of the living cell.[471] Molecular insights into -membrane-molecular interactions are also crucial when the molecular target is a membrane protein or when permeation is facilitated by protein interaction. To investigate the behaviour of membrane lipids with small compounds, many researchers turn to biomimetic models like liposomes and supported lipid bilayers (SLB) techniques. But unilamellar vesicles have some disadvantages, like membrane undulation and restricted stability, compositional versatility, and interrogation methods. However, these techniques cannot be used to investigate lateral diffusion of proteins and lipids in the membrane because of interference from the interfacial support on the fluidity and functionality of the bilayer and associated proteins in SLBs.[472] While modifications such as tethered lipid bilayer membranes and cushioned bilayer membranes[473] have been introduced to supported membrane models in an effort to increase fluidity, the lateral mobility of lipids and reconstituted proteins still does not reach the levels seen in giant unilamellar vesicles (GUVs).[392] When comparing the lateral lipid diffusion in the inner and outer leaflets of planar-supported lipid bilayers, Zhang and Granick found that the component in the inner leaflet usually diffused slowly.[474]

Thus, it is advantageous to study suitable biomimetic platform that is lack of any frictional interaction of substrate and at the same time it should provide the associated optimal fluidity in the context of small molecule analyte binding studies or the development of suitable model fluorescent probes for targeted therapeutics and imaging applications.

5.1.1 Small molecule drug interaction with lipid bilayer

On administration, most drugs must pass through cellular membranes before reaching their intended intracellular target. Predicting membrane permeability or membrane-associated toxicity during the design of drugs with intracellular targets requires an understanding of the interaction of pharmaceuticals with the lipid membrane.[475–477] The phospholipid bilayer, sterols, and membrane proteins form the complex semipermeable matrix that make up the cellular membranes. Thickening, curvature, permeability, and fluidity of a membrane are all characteristics that can be affected by the particular or non-specific interactions of small molecules like drugs with the bilayer.[478,479] Anaesthetic molecules like chloroform, halothane, and diethyl ether, for instance, have been shown to increase local disorder in lipid tails close to the intercalating anaesthetic molecule, causing the membrane to expand laterally.[480] To kill off the fungi, the antifungal drug amphotericin B creates holes in the membrane of the cell wall.[481–483] Some antibiotics, like valinomycin and gramicidin, porate or create ion channels, that damage the membrane reflected in their changes to the membrane's electrochemical impedance.[186,484,485] The integrity of the barrier effect, cell signalling, and adhesion are just a few of the biological functions of membranes that can be profoundly influenced by the modifications imposed on them by many drug molecules as they associate with and permeate these dynamic structures, contributing to the drug's toxicity.[486–489]

5.1.2 Role of tricyclic antidepressant drugs (TCAs) on membrane fluidity

Imipramine (Figure 5.1a) and its metabolites, desipramine (Figure 5.1b) are the tricyclic antidepressant drugs (TCAs) and often linked to fatal overdoses.[490] Since the emergence of serotonin reuptake inhibitors (SSRIs)[491], TCAs uses to treat depression are considerably declined[492], as the former has lesser side effect. Despite not being utilized in psychiatric pharmacotherapy, the TCAs, however, are still a viable treatment choice for severe depression with melancholic symptoms, post-stroke depression, fibromyalgia, migraine prevention as well as neuropathic pain.[493–497] In particular, use of desipramine seems to benefit adolescent and adult attention deficit/hyperactivity disorder.[498] Very recently, the use of antidepressant as

repurposed medication for the improvement of Alzheimer's diseases (AD) cognition has been reported.[499]
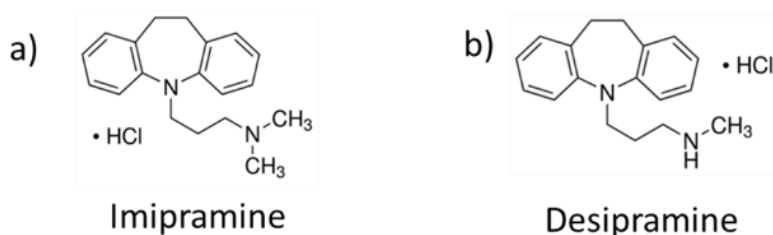
Figure 5.1. Chemical structure of a) imipramine, and b) desipramine.

Because of their lipophilic properties, tertiary amines imipramine and desipramine are extensively distributed in plasma albumin and extravascular tissue.[491] From 0.5 to 26 μg/mL (μM), the blood levels can cause varying degrees of toxicity. N-demethylation of tertiary amines, such as imipramine, is linked to cytochrome P450 2C19 action.[500] In terms of CYP2D6 inhibition, desipramine is not a potent inhibitor, while imipramine is a potent inhibitor of both CYP2C19 and CYP1A2.[501] According to the 'amine theory,' at a concentration of 100 μM in C6 glioma cells, these drugs prevent re-uptake of neurotransmitters at synapses by stereospecifically binding to opiate receptors and thereby altering lipid concentrations and reorganization.[502,503] The incorporation of these cationic amphiphilic medicines (CADs) into lipid bilayers is known to result in lipidosis, the accumulation of various phospholipids in the cell, by inhibiting phospholipase.[502–505] New in vivo evidence suggests that imipramine, a drug being considered for repurposing, can modulate lipid-protein interactions, making it potentially useful in the therapy of Kala-azar or visceral leishmaniasis.[506,507] Antidepressants have been shown to affect membrane protein activity by partitioning into cell membranes and altering the bilayer input to conformational changes in membrane proteins, as shown by Kapoor et al.[508]

Even while such drugs bind to proteins/enzymes and influence their activity, it is unclear how the physicochemical properties of lipid membranes, particularly headgroup charge affect small molecule drug binding. Changes in lipid membranes can have indirect effects on membrane protein function, membrane integrity and on the overall efficiency of solute/drug transport within the cell because they serve as the concentrating platform for receptor proteins/lipids and act as the traffic for various analytes movement in and out across them.[509] The drug's capacity to partition between the membrane and the solution is a crucial factor in determining its pharmacological action.[510] Drug concentrations in brain homogenate have been found to correlate with the RBC plasma membrane partitioning values for TCAs. TCA levels in brain

tissue and its membrane are greater than ten times higher than those in RBCs and their membrane.[511] Antidepressant partitioning to brain cell membrane via electrostatic contact between cationic TCA and anionic phosphotidylglycerol (PG) is proposed. It's important to remember that antidepressants can alter membrane lipid content, and that lipid composition has been shown to play a vital role in mental disorders.[512] Anionic lipids in particular are required for increased TCA affinity for lipid membranes, highlighting the importance of studying the effect of TCAs on a variety of lipid compositions in order to deduce their biological functions.[513] Therefore, gaining a molecular understanding of drug-membrane interaction[514] in general and TCAs-lipid bilayer interactions in particular will provide in-depth information of antidepressant mode of action.[515] However, studying such an interaction at the molecular level is often challenging because of the intricacy of the cell membrane. Here, the first move toward improved molecular understanding is the provision of a system for investigating the binding selectivity of various medications for different membranes and quantifying their interaction at artificial cell surface mimics.

Previously, multilamellar vesicle bilayer of phosphatidylcholine-phosphatidylglycerol in combination with solid state NMR study has indicated that desipramine and imipramine elicit distinct changes of the membrane surface, particularly on the headgroup order of phospholipids, their conformation and dynamic properties.[516] Using radioligand binding assay, TCA interaction with various neutral and negatively charged liposomes have been reported, where interaction between them was predominated by noncovalent interactions.[517] Antidepressant clomipramine has more of an effect on saturated phospholipid bilayers than on unsaturated phospholipid membranes, according to electron paramagnetic resonance results from liposome models.[518] Using isothermal titration calorimetry, the binding constant of imipramine and desipramine with L-α-lecithin liposomes were found to be 4.21 and 7.45 μM respectively.[519] Using optical trapping confocal Raman spectroscopy, Harris et al.[513] observed changes in acyl chain conformation of phospholipid vesicle membranes and their intra- and intermolecular order related to the antidepressant's effect. Although these studies were useful for understanding the mode of action of TCAs with liposomal membrane, the studies often require elevated concentrations of analyte beyond the physiological level to detect the impact of drug-membrane interaction. For instance, classic approaches for examining lipid phase transitions, such as differential scanning calorimetry and nuclear magnetic resonance spectroscopy, are not amenable to physiologically relevant (μM) drug concentrations because substantial (mM) concentrations are necessary to observe a response from these methods.

Furthermore, liposome models are not so amenable for surface sensitive spectroscopy approaches, single molecule based FLIM and FCS methods.

5.1.3 Role of antimalarial drug quinacrine on membrane fluidity

The drug quinacrine (Figure 5.2a) has a wide range of potential medical applications. It has been used as an antimalarial medication for nearly a century, and now it is also being studied as a potential cancer treatment.[520] The increased amounts of free hemin caused by its action as a beta-hematin inhibitor cause oxidative stress via peroxidase reactions, which in turn inhibits proteolysis and damages the parasite's membrane, explaining its antimalarial efficacy. The anticancer effects of quinacrine have only lately been discovered, but they are promising .[521,522] It inhibits tumorigenesis in endometrial cancer (EC)[523], acts as a potent Ca^{2+} channel blocker[524,525], induces p53, a tumour suppressor protein[523,526], and downregulates NFκB signalling, all of which contribute to its antitumor action.[527] In addition, new research shows that quinacrine attaches to and intercalates with DNA.[520,528] Consequently, it has been repurposed as a chemotherapeutic drug, specifically for gynaecological malignancies[524], lung cancer[529], and is presently undergoing phase 2 clinical trial in the treatment of prostate, lung, and colorectal cancer.
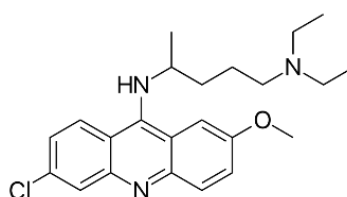
Figure 5.2 Chemical structure of quinacrine.

A decrease in membrane order due to the effect of drug may affect membrane protein activity and protein-mediated resistance to multiple drugs. This makes the study of drug effects on membrane packing and passive permeability of particular interest.

5.1.4 MSLB-a robust platform for studying artificial photosensitizer lateral diffusion

Researchers into biomimetic light energy utilization have been greatly influenced by natural photosynthesis because of its enormous scope, final efficiency, and long-term viability. Lipids and their assemblies have long been known as potent molecular scaffolds in the construction of artificial photosynthetic systems due to their important and ubiquitous role in all photosynthetic machinery. Key photosynthetic processes, including energy transfer and photoinduced electron transfer, can be studied in well-defined, natural-like membrane settings thanks to the extensive use of model lipid bilayers, such as black lipid membranes and

liposomes (vesicles), solid supported lipid bilayers to host natural and synthetic photo- and redox-active species.[530–533]

Lipid bilayers serve as a molecular scaffold, offering photosystem I and II protein fragments stable anchoring sites, and guiding the folding and assembly of these proteins with their well-defined aqueous/lipid interfaces and hydrophobic core.[534] Small amphiphilic species like plastoquinone are held in close proximity to their protein electron-transfer partners by the lipid bilayers that serve as the shared host for these processes.[535] Due to their low dielectric constant, lipid bilayers aid in directing photogenerated charges along predetermined pathways. This same property enables biomembranes to sustain a pH gradient, which in turn drives the ATP-generating enzyme ATP synthase that is embedded in the bilayer.[536] Because of the mechanical strength of lipid bilayers and their robust association with the anchored proteins, many photosynthetic protein complexes, such as ATP synthase and cytochrome bc1, experience substantial motions or conformational changes while carrying out their functions. The oxygen evolving complex, photosystems I and II, and natural electron relays are all embedded in the lipid bilayer of the thylakoid membrane to maximize the efficacy and directionality of electron transfer during natural photosynthesis. The use of artificial mimics of thylakoid membranes, such as lipid-based supramolecular assemblies like liposomes, is a promising strategy for artificial photosynthesis. To co-embed catalysts and photosensitizers, photocatalytic liposomes are a useful platform because they are simple to prepare, can solubilize apolar compounds in water, and can even enable charge separation.[537–539] Furthermore, they provide a novel approach to the separation of molecular catalysts and photosensitizers in water, with the former group being kept close to the water-bilayer contact and the latter group being kept close to each other to increase electron transfer rates.

The above lipid models have been around for a long time, but that hasn't stopped them from being useful. Nevertheless, as discussed earlier, there is always scope in improving the biomimicry in terms of its optimal fluidity and amenable to surface sensitive techniques to better understand the photosynthesis system at single molecule level. Pore-suspended lipid structures typically exhibit superior stability, robustness, and precise control in composition and architecture in comparison to earlier lipid models used in artificial photosynthesis study.[540] Herein, PDMS based pore-suspended lipid bilayer has been utilized to reconstitute ruthenium-based photosensitisers [Ru(bpy)$_2$(bpy-(4,4'-C$_n$)$_2$)](PF$_6$)$_2$ (RuC$_n$; n= 9 and 19). These ruthenium photosensitizers were chosen because they are known to be effective at fueling rhenium-catalysed CO$_2$ reduction. This is true both in terms of their ground-state redox potential and

their excited-state energy.[541] Furthermore, immobilizing metal compounds with photochemical or catalytic activity on the lipid bilayer of liposomes typically involves functionalizing them with alkyl tails (C_n) to increase their lipophilicity. Self-assembly within the liposome bilayer is enabled when a metal-containing complex is hydrophilic enough to produce an alkyl-functionalized molecule that superficially mimics an amphiphile. To accept electrons and protons from the bulk aqueous environment, the catalytically active centre of such amphiphiles must be located in the metal head group, which must be near enough to the bulk water phase. Understanding the lateral diffusion of amphiphilic metal complex and its headgroup orientation within a true biomimetic model membrane is of value in terms of its catalytic performance.

These studies paved a path for establishing and validating the MSLB platform for lateral diffusion studies using FLIM and FLCS for the other chapter works of this thesis. The drug-based studies helped in understanding how a drug interacts with artificial membrane can determine its use in liposome delivery agent, for example the facts like whether the drug can escape the liposome without disruption can be evaluated. The photosensitizer-based study helped to establish a route for evaluating the lateral diffusion of photosensitizers used for triplet-triplet annihilation upconversion.

5.2 Aims and Objective

Cell membranes are complex dynamic systems that can be altered by drug molecules, affecting their physicochemical properties. Model membranes offer a way to study membrane behaviour isolated from the complexity of the cell that can provide insight into how drugs alter the membrane's biophysical properties. When compared with other model membrane systems, solid supported lipid bilayer (sSLB) excels in terms of their practical utility, though they have drawbacks in terms of their fluidity, and protein reconstitution. However, microcavity pore spanning lipid bilayers, in which the proximal leaflet of a bilayer spans across a micron scale deep aqueous/buffer reservoir and the distal leaflet exposing towards bulk, are promising alternatives that can show good stability without the sSLB's drawbacks. Our laboratory (Keyes' Lab) invented microcavity supported lipid bilayers (MSLBs) for studying protein-lipid and peptide-lipid interactions at the single molecular level using optical microscopy and spectroscopy.

Chapter 5 aims to discuss the versatility of MSLB platform used in the preceding chapters in detail and its application for investigating how small molecule drugs interact and thus modulate the fluidity of different membranes using fluorescence lifetime imaging (FLIM) and

fluorescence lifetime correlation spectroscopy (FLCS). This chapter discusses MSLB platform in four sections and initially targets to do a comparison of leaflet-by-leaflet diffusivity of sSLB and MSLB to validate the use of MSLB as a better biomimetic bilayer versus conventional glass supported lipid bilayer (SLB). The next section intent to investigate how different charged MSLBs, such as zwitterionic, negatively and positively charged membranes, respond to imipramine, a cationic antidepressant drug, and its metabolite, desipramine. Then this chapter also aims to examine how more complex membranes single component DOPC bilayer to binary DOPC:Cholesterol (3:1) and ternary DOPC:SM:Cholesterol (2:2:1) responds to antimalarial quinacrine drug. Finally, the lateral diffusion of a metal complex photosensitizer in MSLB platform will be interrogated. A thorough examination of the aforementioned studies using FLIM and FLCS provides insight into the interaction of cell membrane models with small molecule drugs and photosensitizers in the context of drug discovery applications.

5.3 Materials and Methods

5.3.1 Materials

1,2-Dioleoyl-sn-glycero-3-phosphocholine (DOPC) [purity (>99%)], 1,2-dioleoyl-sn-glycero-3-phospho-(1'-rac-glycerol) (sodium salt) (DOPG), 1,2-dipalmitoyl-sn-glycero-3-phosphocholine (DPPC), 1,2-dioleoyl-3-trimethylammonium-propane (DOTAP), and Sphingomyelin (Brain, Porcine) were purchased from Avanti Polar Lipids (Alabama, USA) and used without further purification. Sodium 1,2-distearoyl-sn-glycero-3-phosphoethanolamine N-(carbonyl-methoxypolyethylene glycol-2000) (NaDSPE-PEG2000) was purchased from Lipoid. 1,2-Dioleoyl-sn-glycero3-phosphoethanolamine-labeled ATTO655 and ATTO532 (DOPE-ATTO655 and DOPE-ATTO532) were purchased from ATTO-TEC GmbH (Siegen, Germany). Cholesterol, and phosphate buffer saline (PBS) tablets were purchased from Sigma-Aldrich (Wicklow, Ireland). Aqueous solutions were prepared using Milli-Q water (Millipore Corp., Bedford, USA). The polydimethylsiloxane (PDMS) silicon elastomer was purchased from Dow Corning GmbH (Wiesbaden, Germany) and mixed following supplier instructions. Monodisperse polystyrene (PS) latex sphere with a diameter of 4.61 ± 0.4 μm was obtained from Bangs Laboratories Inc. (Fishers, IN, USA).

5.3.2 Reconstitution of Fluorophores into Large Unilamellar Vesicles (LUVs)

The fluorophores were incorporated into LUVs using hydration extrusion method. For drug interaction studies, the selected lipid mixture was mixed with DOPE-ATTO655 in 50000:1 lipid:dye (mol/mol) ratio. The same ratio was used for lipid:DOPE-ATTO532 composition as

well for leaflet by leaflet studies. For anti-depressant drugs study apart from DOPC, DOPC:DOPG and DOPC:DOTAP compositions were used in 3:1 molar ratio. For quinacrine work, DOPC:Cholesterol was taken in 3:1 molar ratio and DOPC:SM:Chol was taken in 2:2:1 ratio and DOPC was taken as such as another lipid composition. For photosensitizer's diffusion studies, DPPC:DSPE-MPEG2000:RuCn was taken in $100:1:10^{-4}$ molar ratio. For LUV preparation the corresponding lipid was mixed with fluorophore in chloroform in a 1.5 mL glass vial and the mixture was dried with N_2 after which a thin lipid film has formed along the sides of the glass vial. Then the vial was stored in vacuum for 60 min to ensure the complete evaporation of the solvent. The film of lipid-fluorophore mixture was hydrated with 1 mL PBS of pH 7.4 and vortexed for 1 min to mix the film fully into the buffer. The resulting solution was extruded through a polycarbonate membrane of 100 nm pore size a minimum of 11 times to yield LUVs of uniform size, doped with fluorophore. The extrusion process was always carried out above the phase transition temperature of the membrane for each given composition, so for DPPC:DSPE-MPEG2000 and DOPC:SM:Chol, the extrusion process was carried out at 45 °C (above the phase transition temperature of DPPC and SM) and for the remaining lipid mixtures, the extrusion was performed at room temperature. The resulting LUV suspension was then diluted to a final volume of 0.2 mg/mL, and LUV size was measured to be ~120 nm by dynamic light scattering (Malvern zetasizer Ultra). The vesicle solutions are stored at 2 °C and used within 3 weeks.

5.3.3 PDMS Microcavity Array preparation

The method of preparation of PDMS based microcavity arrays is given in chapter 2, section 2.3.8.

5.3.4 Preparation of Microcavity Array Supported Lipid Bilayers (MSLBs)

The microcavity supported lipid bilayer was prepared by spanning the desirable lipid bilayer across the aqueous filled microcavities. The lipid monolayer was prepared by transferring lipid or lipid mixture by using the Langmuir-Blodgett technique at the air-water interface. 50 µL of the lipid or lipid mixture dissolved in chloroform was added to the water subphase of LB trough (NIMA 102D) at 1 mg/mL concentration and the chloroform was allowed to evaporate for 10 min. Later the lipids were compressed and decompressed within the tough for 2 times each below the collapse surface pressure. The resultant monolayer was compressed until the surface pressure reached 33 mN/m (40 mN/m for DPPC:DSPE-MPEG2000) and allowed to equilibrate for at least 5 min at the designated surface pressure. Then, the buffer filled PDMS which was

submerged in the LB trough using a clip holder was vertically pulled from the water surface at a speed of 5 mm/min resulting a transfer of a single layer of lipid as proximal leaflet. For distal leaflet, vesicle fusion (VF) method was carried out. The monolayer covered PDMS substrate was sealed within a microfluidic chamber and subjected for vesicle fusion for 90 min. After VF processes completed, the substrates were washed with PBS buffer gently to remove any unfused vesicles and at no scenario, the membranes are exposed to air.[198]

5.3.5 Atomic Force Microscopy (AFM)

Atomic force microscopy (AFM) image of PDMS microcavity substrate was taken using the Veeco Bioscope II system (Nanotec House, Cambridge) coupled with a Zeiss Axiovert inverted optical microscope IX70. Topographic AFM images were acquired in liquid mode in PBS, using silicon nitride cantilevers PNP-TR-20 (NANO WORLD) with a nominal force constant of 0.32 N m^{-1} and a tip radius of 20 nm. The resonance frequency was kept as low as possible during image acquisition, and the scan rate was maintained at 0.5 Hz. All AFM images were analyzed using Nanoscope 7.30 software, and the whole images were plane fitted with a 1st order polynomial.

5.3.6 Electrochemical Impedance Spectroscopy (EIS)

A detailed EIS experimental procedure is given in chapter 3, section 3.3.6. The EIS measurements and AFM were performed by Dr. Nirod Kumar Sarangi.

5.3.7 Fluorescence Lifetime Imaging (FLIM) and Fluorescence Lifetime Correlation Spectroscopy (FLCS)

A detailed description of FLIM and FLCS experimental setup is given in chapter 2 and 3. The equations used for fitting the autocorrelation function (ACF) with a 2D diffusion model is also given in chapter 2 and 3. The equations used in finding the diffusion coefficient of photosensitizer in the lipid bilayer and solution are given in equation 5.1 and 5.2 respectively.

5.4 Results and Discussion

5.4.1 Lateral diffusion of lipids in proximal and distal leaflets and a comparison of SLB and MSLB

Even though SLB is widely studied and a versatile model with reliable results, frictional interactions with the surface and leaflet registry seem to be a hindrance to lateral diffusion. The DOPC lipid diffusion values on SLB based measurements are usually 2 to 4 µm^{2}s^{-1} and they are low compared to free standing membranes.[236,542] To evaluate the comparative fluidity of SLB with MSLB, leaflet by leaflet evaluation can provide better insights. Prior to small-

molecule drug binding studies, especially in the context of fluorescence lifetime imaging and single molecule-based fluorescence lifetime correlation spectroscopy, the lipid diffusivity at both inner (proximal) and outer (distal) leaflet of a model DOPC based SLB as well as microcavity array supported lipid bilayers (MSLB) are compared. A representative FLIM image of DOPC SLB and MSLB prepared over planar glass and buffer filled PDMS microcavity array substrate are shown in Figure 5.3a and b respectively, where the upper leaflet was fluorescently doped with lipid tracer DOPE-ATTO655 (0.01 mol%). The inner leaflet of the lipid bilayer was prepared via Langmuir-Blodgett (LB) method and the outer leaflet was prepared by vesicle fusion method, as detailed in previous chapter (s). To accrue lipid diffusivity from the individual leaflet, the lipid tracer was specifically doped to the designated leaflet. A representative autocorrelation function (ACF) trace obtained from proximal (black open square) and distal leaflet (red open circle) of a DOPC lipid bilayer supported over planar glass substrate is shown in Figure 5.3c. The corresponding lipid diffusivity value of proximal and distal leaflet after fitting to a 2D diffusion model equation was found to be 3.8 ± 0.2 $\mu m^2 s^{-1}$ and 5.5 ± 0.3 $\mu m^2 s^{-1}$ respectively, suggesting that the lower leaflet diffusivity is hindered possibly due to frictional interaction with the underlying glass substrate. In contrast, when the lipid diffusivity obtained from the proximal and distal leaflet of the DOPC MSLB suspended over PDMS substrate, the respective diffusivity values from proximal and distal leaflet are 10.2 ± 0.12 $\mu m^2 s^{-1}$ and 10.3 ± 0.14 $\mu m^2 s^{-1}$ respectively, and within the experimental error, these values are indistinguishable, indicating that, the lipid diffusivity from both the leaflets are same. Furthermore, when compared the magnitude of diffusivity values of SLB and MSLB, the diffusivity remains is nearly 50% lower for SLB based bilayer which indicated that the frictional interaction of the underlying substrate to the lower leaflet can also reduce the upper leaflet diffusion. However, this is not the case for MSLB system, unlike the aqueous environment at the distal site of the bilayer, the deep aqueous micron scale reservoir underneath the proximal leaflet ensures the membrane is in contact with water rather than solid substrate and so the lipids retain liposome-like fluidity in these regions without hindrance caused by frictional interaction with the substrate.
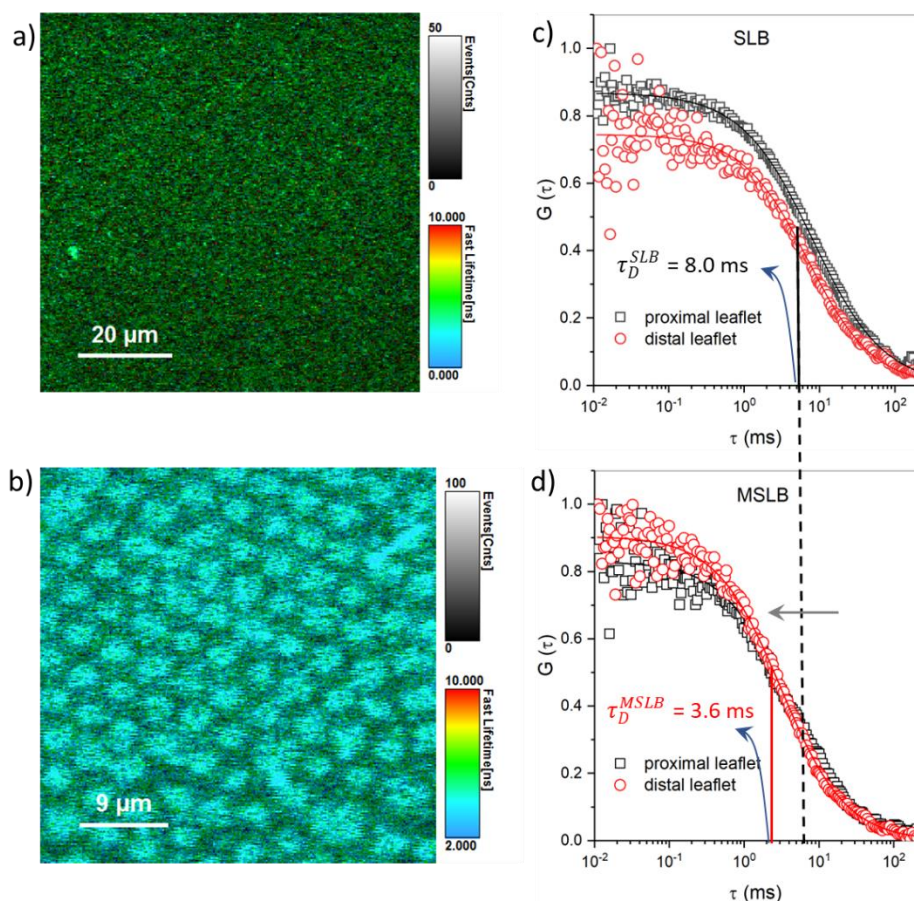
Figure 5.3 FLIM images of DOPC bilayer supported over a) planar glass substrate and b) PDMS microcavity array. In both the FLIM images, the upper leaflet is doped with 0.01 mol% DOPE-ATTO655. c) ACF obtained from the proximal leaflet (open square black) and distal leaflet (red circle) of a DOPC bilayer from c) glass SLB, and d) PDMS MSLB. The ACFs are fitted using 2D diffusion model equation. The vertical solid black and red lines (panel c and d) demarcate the respective transit time obtained from the fit for SLB and MSLB. The left arrow mark in panel d indicates the transit time shift from higher (SLB) to lower (MSLB) value.

Doping two separate lipidic labels to each leaflet of a bilayer that do not spectrally overlap allows for independent FLIM imaging of each leaflet, which is a useful way of confirming successful bilayer over PDMS substrate. To achieve this, DOPE-ATTO532 (0.01 mol%) was incorporated into the proximal leaflet of DOPC before being transferred to the buffer-filled PDMS cavity array via the LB technique. Next, DOPE-ATTO655 (0.01 mol%) was combined with the LUV preparation step and allowed to fuse with the DOPC to create the lipid bilayer. In Figure 5.4a, a reflectance image of the PDMS microcavity array reveals the circular white structures that as described, are the buffer filled cavities underneath the bilayer, the bright image is due to the refractive index mismatch between PDMS and water. Figure 5.4b shows the FLIM image of the bottom DOPC leaflet labelled with DOPE-ATTO532, and Figure 5.4c

shows the FLIM image of the upper DOPC MSLB leaflet doped with DOPE-ATTO655, both at the same regime. For both, continuous homogenous fluorescence is observed, with no discontinuities or breaks, confirming the successful formation of lipid bilayer. In an independent experiment using AFM, the pore diameter of PDMS cavity array (without lipid bilayer) was verified to be ~2 μm and the pore depth was ~0.5 μm (Figure 5.4d). This individual pore diameter is sufficient for easy focusing of the confocal observation volume at the centre of any designated pore. This enables FCS based single molecule detection or for averaging a large number of data sets by sampling pore-by-pore across substrate and the pore-depth is sufficient for reconstitution of any membrane spanning proteins/peptides. Figure 5.4e shows a representative snapshot showing the spatial points (marked in '+' for 1 to 7 in cavities) at the centre of pores considered for FLCS acquisition (Figure 5.4e). More importantly, as mentioned earlier in the chapter, the MSLB array, which for fluorescence studies is sealed within a microfluidic array, needs only a 50-150 μL analyte volume, which is significant in terms of the cost-effectiveness of the analytes.
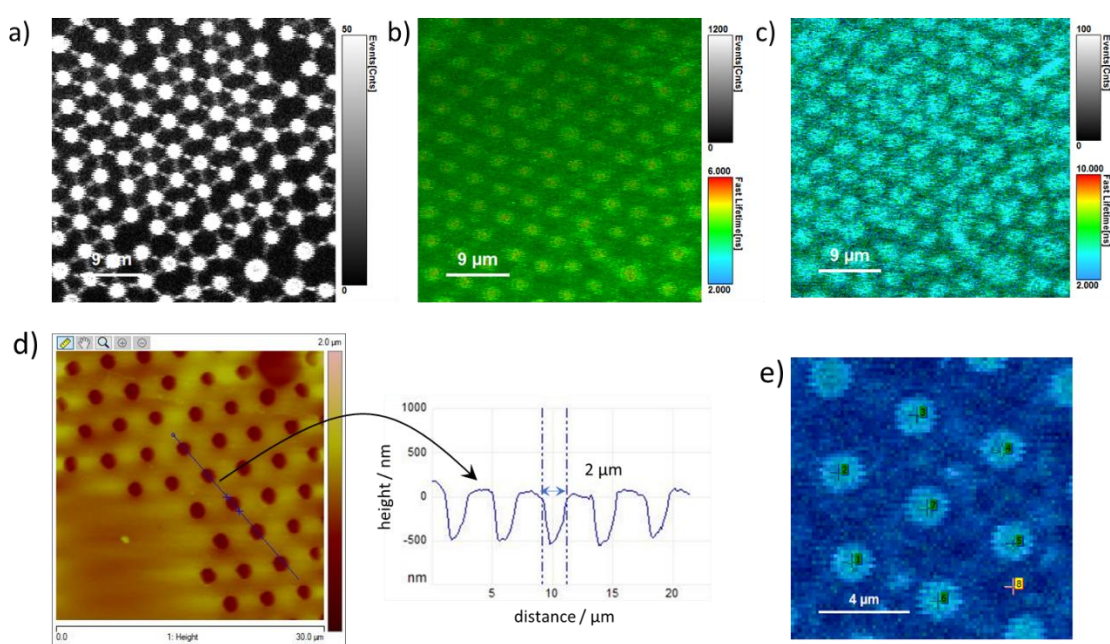
Figure 5.4 Characterization of DOPC MSLB spanned over buffer filled PDMS microcavity array substrate. a) Reflectance image shows that each cavity (white circular regions) is buffer filled and the corresponding FLIM images obtained from the b) proximal leaflet doped with 0.01 mol% DOPE-ATTO532 and c) distal leaflet doped with 0.01 mol% DOPE-ATTO655. d) atomic force microscopy image of PDMS based microcavity array (left) without lipid bilayer taken in liquid mode and the corresponding line profile analysis (right) obtained from the line section indicated by curved arrow. e) A zoomed-in image of DOPC MSLB over PDMS indicating the spatial point (numbered 1-7), typically

from the centre of pore array where FLCS measurements are taken. AFM image courtesy of Dr. Nirod Kumar Sarangi (DCU).

These above characterisation results, leaflet by leaflet study, and the experimental testbed (a PDMS-based MSLB) are relevant for gauging the changes in lipid diffusivity caused by analyte binding, and MSLB's optimum fluidity can enable the analysis of any synthetic novel fluorescent tracer.

5.4.2 Role of tricyclic antidepressant drugs (TCAs) on membrane fluidity
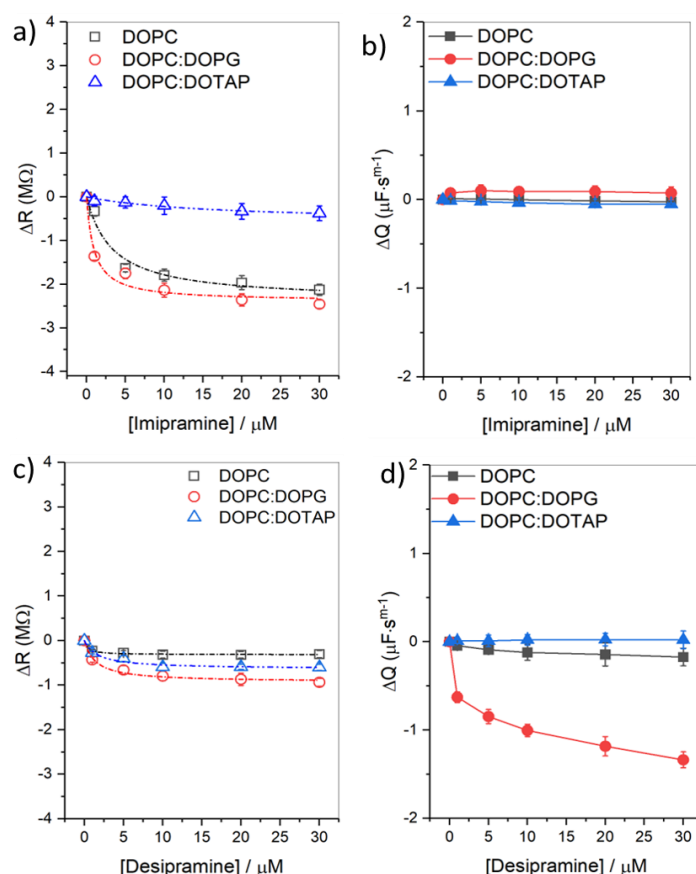
Figure 5.5 Imipramine concentration-dependent relative change in membrane (a) resistance and (b) capacitance. Panel c and d show desipramine induced relative membrane resistance and capacitance changes respectively. The raw data for DOPC, DOPC:DOPG, and DOPC:DOTAP MSLBs are represented in each panel by open (resistance) and filled (capacitance) symbols such as square, circle, and triangle. In each panel, each data point represents a mean value of SD and was assessed in triplicate for each bilayer type. Data courtesy of Dr. Nirod Kumar Sarangi (DCU).

Figure 5.5a shows the drug concentration dependent resistance data and it was observed that imipramine significantly increase the drug permeability to negatively charged DOPC:DOPG membrane, an intermediate permeability for DOPC membrane while for DOPC:DOTAP, imipramine have a modest impact. From the capacitance data given in Figure 5.5b and d, a

150

modest membrane thinning was observed and significant thickening to the negatively charged membrane caused by imipramine and desipramine respectively. The capacitance remain largely unchanged to positively charged DOPC:DOTAP membrane in presence of both imipramine and desipramine. The passive permeation of imipramine to neutral DOPC membrane did not change the capacitance to large extent whereas desipramine modestly thickened the membrane and accordingly reflected with high association constant (Ka) value.

To bridge the above gap, in this section, FLIM and FLCS were exploited at PDMS based MSLB comprised of varied surface charge to examine the impact of two antidepressants, imipramine and desipramine (cf. chemical structure Figure 5.1a and b) on the fluidity of membrane. Figure 5.4a shows representative reflectance (top panel) and FLIM (bottom panel) images of pristine DOPC MSLB with the fluorescent lipid marker DOPE-ATTO655 (0.01 mol%) present in the membrane's outer leaflet. Reflectance pictures were used to determine the ideal X-Y plane for membrane acquisition by first analysing the distinct individually buffer-filled pores that resulted from the refractive index mismatch between the PDMS and buffer (displayed in each top panel of Figure 5.6a-c). There are times when the cavities are not being filled by buffer, and such cavities are clearly visible as dark circles on the reflectance and FLIM images (cf. arrow in panel 5.6a), and these regions are avoided in imaging studies. Figures 5.6b and c shows representative FLIM images (bottom panel) obtained after 30 min of incubation with 10 μM imipramine and 10 μM desipramine, respectively and the corresponding reflectance images are shown in the upper panel. Similarly, Figures 5.6d and e show exemplary FLIM images before and after imipramine and desipramine incubation with DOPC:DOPG and DOPC:DOTAP, respectively. When all of the FLIM images were evaluated, considerable membrane reorganization was found in the DOPC:DOPG membrane as shown in Figure 5.6d, a minor influence on the DOPC membrane, and very little impact on the DOPC:DOTAP membrane, with no considerable membrane damage.
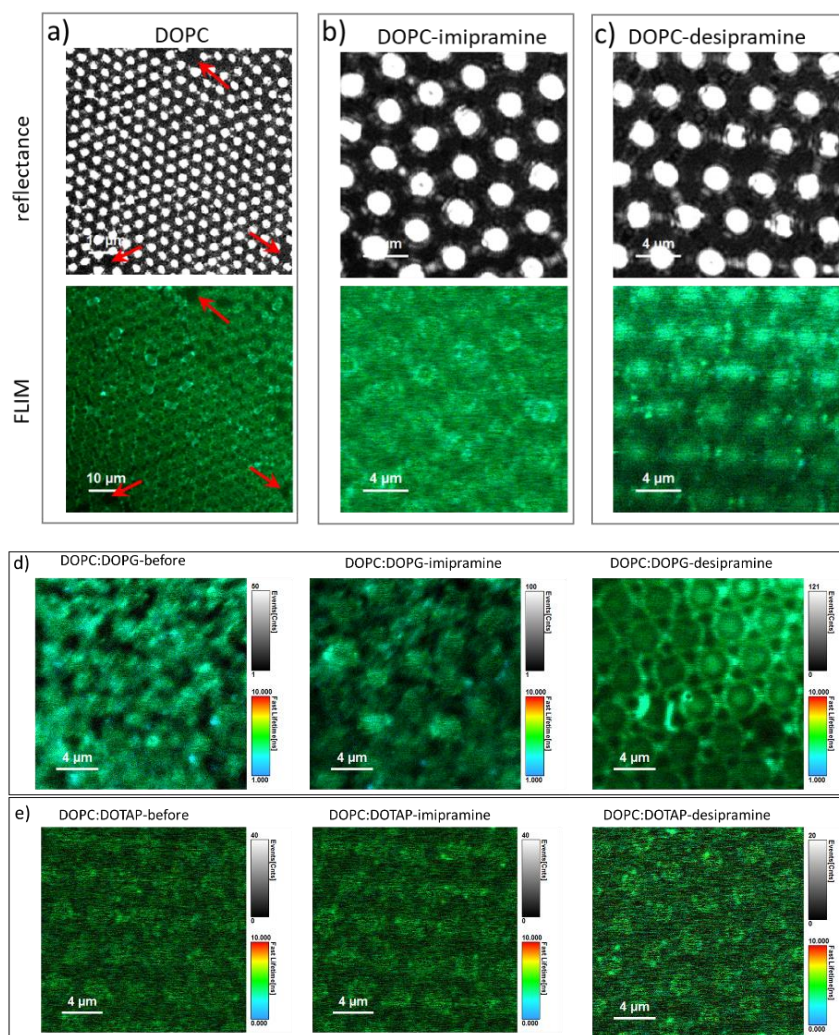
Figure 5.6 Representative reflectance (top) and fluorescence lifetime (bottom) images of DOPC MSLBs assembled over a PDMS cavity array substrate in the a) absence, and presence of b) imipramine and c) desipramine. In the reflectance images, the white circular features represent the cavities that are buffer filled. FLIM images of d) DOPC:DOPG (3:1) and e) DOPC:DOTAP (3:1) before and after imipramine and desipramine binding. The FLIM image of bilayers are obtained from a fluorescently labelled lipid probe, DOPE-ATTO655 (0.01 mol%) present at the upper leaflet of the bilayer. The drug concentration was 10 μM.

For better insights into the antidepressant induced change in membrane fluidity, fluorescence lifetime correlation spectroscopy (FLCS) measurements were carried out.
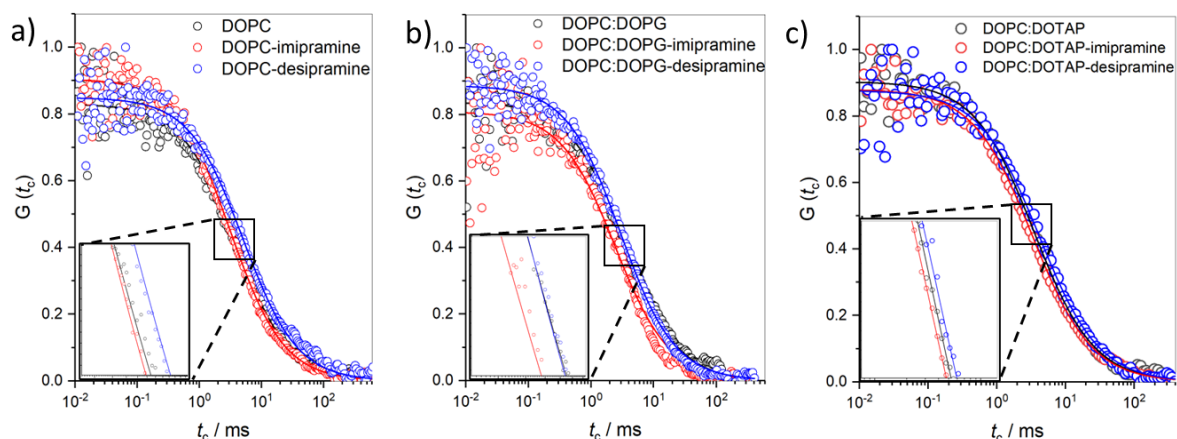
Figure 5.7 Representative FLCS autocorrelation function data obtained from the centre of the pore spanning different membranes such as (a) DOPC, (b) DOPC:DOPG (3:1) and (c) DOPC:DOTAP (3:1) before (black open symbol) and after imipramine (red open symbol), desipramine (open blue symbol). The drug concentration was 10 μM. At least 40-50 ACFs are acquired from spatially distinct membrane spanning pores across 3 independent bilayers without and with the presence of drugs. The solid lines in panel a-b are the representative fit using the 2D diffusion model equation. Inset in panel a-b are the expanded view highlighted in square box.

Figures 5.7a-c shows the representative FLCS autocorrelation function (ACF) traces of pristine DOPC membrane without (open black) and in presence of 10 μM imipramine (open red) and 10 μM desipramine (open blue). The corresponding solid lines are the fit using 2D diffusion model equation as defined in chapter 2 (equation 2.1). The drug incubation time of 30 min (confirmed from EIS) was set before the FLCS measurements. Each ACF was acquired by spatially positioning the confocal observation spot at the centre of a filled, bilayer spanned cavity and are averaged of at least 40-50 cavities across triplicates. Before drug addition, the diffusivities of DOPE-ATTO655 obtained from DOPC, DOPC:DOPG and DOPC:DOTAP MSLBs are 9.9±0.12, 10.79±0.11 and 10.24±0.11 $μm^2s^{-1}$ respectively. In the presence of 10 μM imipramine, the diffusivity of DOPC increased to 11.54±0.07 $μm^2s^{-1}$ whereas in presence of desipramine, the diffusivity decreased to 7.07±0.15 $μm^2s^{-1}$. This suggests, interestingly, that imipramine and desipramine induces respectively lipid disordering and ordering of zwitterionic DOPC membrane respectively. The respective lipid diffusivity in presence of imipramine and desipramine at DOPC:DOPG membrane was found to be 14.78±0.15 and 12.07±0.07 $μm^2s^{-1}$ indicating that both the drugs reduced lipid order at the negatively charged DOPC:DOPG membrane, and the extent of lipid alkyl chain disordering is more prominent for imipramine than desipramine. In contrast, the imipramine causes the lipid diffusivity at DOPC:DOTAP

membrane to modestly increase only by 10.86 ± 0.33 $\mu m^2 s^{-1}$, and is within the experimental error, suggesting that the drug has a modest impact. Similarly, desipramine induces a modest lipid ordering effect to the DOPC:DOTAP membrane. Although, the above studies are in line with the EIS data (Figure 5.5), where the resistance decrease caused by imipramine are linked to lipid disordering effect irrespective of any types of membrane, however, the impact of desipramine only caused negatively charged membrane to fluidize and negatively affect to neutral and positively charged membrane. The alternation of local bilayer properties due to amphiphilic molecules in general is linked to diverse functions such as signalling, initiation of protein sorting etc., and antidepressant small molecules in particular, is linked to redistribution of the drugs in the vicinity of membrane spanning proteins. With the exception of some modest reorganization caused by the drug-membrane interaction, which results in a change in the lipid diffusivity, the above FLIM image observations indicate that the integrity of the bilayer was maintained upon interaction with the drug. The resulting diffusion coefficients for each membrane composition before and after the drugs are tabulated in Table 5.1.

Table 5.1 Diffusion coefficient values of three different membranes obtained before and after the addition of imipramine and desipramine obtained using fluorescence lifetime correlation spectroscopy.

Lipid composition	Diffusion coefficient, D ($\mu m^2 s^{-1}$)		
	Before drug	After drug	
		imipramine	desipramine
DOPC	9.9 ± 0.12	11.54 ± 0.07	7.07 ± 0.15
DOPC:DOPG	10.79 ± 0.11	14.78 ± 0.15	12.07 ± 0.07
DOPC:DOTAP	10.24 ± 0.11	10.86 ± 0.33	10.02 ± 0.24

5.4.3 Role of antimalarial drug quinacrine on membrane fluidity

EIS data given in Figure 5.8 shows the EIS data of quinacrine added to DOPC and ternary DOPC:SM:Chol membranes. The drug reduces membrane resistance and increases impedance in both membranes. For the ternary membrane the impact is greatest indicating possible reorganisation of lipid domains as reflected by decrease in admittance of membrane. Conversely permeation is arrested at the cholesterol/DOPC membrane, but the drug binds/intercalates at membrane interface making it more resistant to ion permeation as reflected in non-Faradaic impedance in an increase in admittance of the membrane. Overall the EIS data shows that the is permeable toward DOPC and the ternary DOPC:SM:Chol compositions.
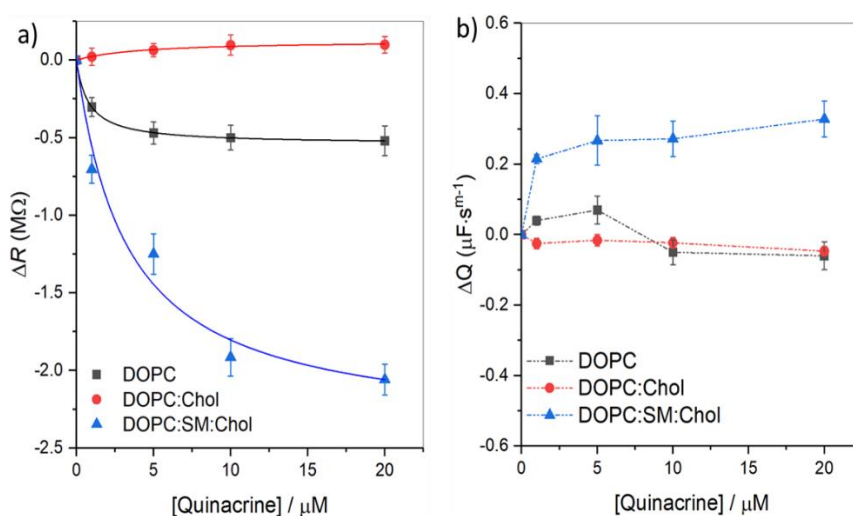
Figure 5.8 The plot represents the relative change in membrane (a) resistance and (b) capacitance for a designated lipid composition versus quinacrine concentrations. In each panel, the symbols ■, ● and ▲ represent DOPC, DOPC:Chol and DOPC:SM:Chol membrane compositions. In panel (a), solid lines are the best-fit curves to the Langmuir isotherm model. Each data point given is a mean value ±SD and was assessed in triplicate for each bilayer type. Data courtesy of Dr. Nirod Kumar Sarangi (DCU).

The effect of drugs on membrane packing and passive permeability is of particular interest since it has been proposed that a decrease in membrane order may affect membrane protein activity and protein-mediated multi drug resistance.[543,544] To gain a better understanding of these effects, confocal fluorescence lifetime imaging and fluorescence lifetime correlation spectroscopy has been used to probe the influence of quinacrine on the fluidity of the DOPC, DOPC:Chol (3:1), and DOPC:SM:Chol (2:2:1) membranes in an analogous pore-suspended membrane at an optically transparent PDMS substrate. Figure 5.9 shows representative reflectance and fluorescence lifetime images of the three different MSLBs comprised of DOPC, DOPC:Chol (3:1) and DOPC:SM:Chol (2:2:1) before and after quinacrine incubation. For

FLIM and FLCS measurements, fluorescent lipid marker DOPE-ATTO655 (0.01 mol%) labels the outer leaflet of the MSLBs. Before quinacrine addition, the fluorescence marker distributes equally over the pore array giving homogenous FLIM images of DOPC (Figure 5.9b) and DOPC:Chol (Figure 5.9e). In contrast, the FLIM image of DOPC:SM:Chol MSLB appears heterogeneous (Figure 5.9h, inset), this is attributed to the expected phase separation of high melting SM and low melting DOPC lipid, and DOPE is known to show preference for liquid disordered, (L_d) phases.[545]
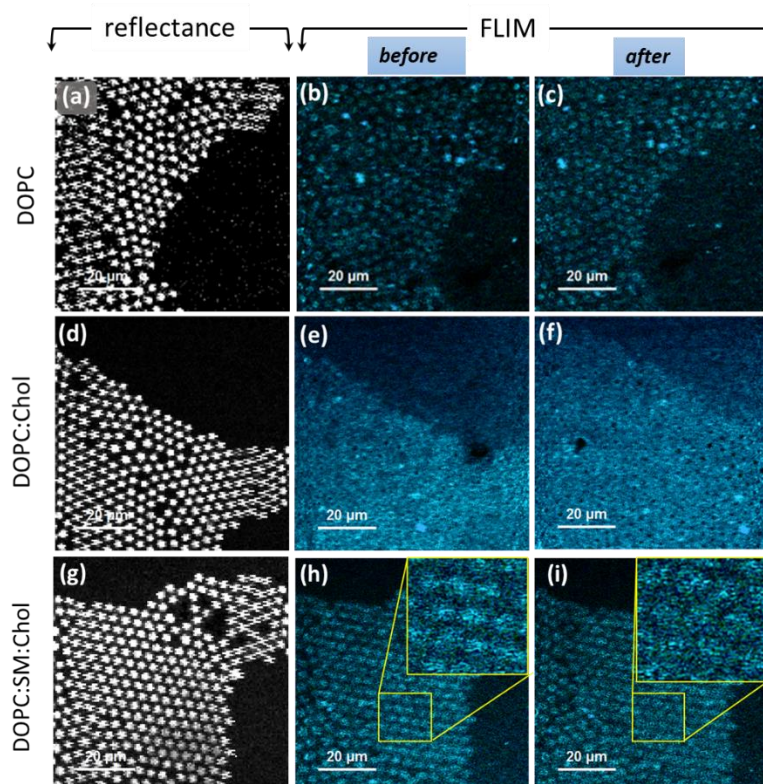
Figure 5.9 Representative reflectance and fluorescent lifetime images of MSLBs formed on a PDMS substrate. Panel a, d and g are the reflectance images of DOPC, DOPC:Chol and DOPC:SM:Chol MSLBs obtained from confocal microscopy, where the white circular spot represents an aqueous filled cavity and the black area corresponds to planar and/or unfilled cavities. Panels b, e, and h show the corresponding fluorescence lifetime images of the respective bilayers before drug addition. The fluorescence lifetime images of bilayers are obtained from a fluorescently labeled lipid probe, DOPE-ATTO655 (0.01 mol%) present at the upper leaflet of bilayer on PDMS microcavity array. Panels c, f and i shows the respective fluorescence lifetime images obtained after 30 min of incubation with quinacrine (~10 µM). The scale bar at each panel is 20 µm. Inset in panel (h) and (i) are the expanded regions showing a modest membrane homogenization caused by quinacrine, which is highlighted in yellow square box.

The addition of quinacrine (10 μM) had no discernible effect on the FLIM images of DOPC (Figure 5.9c) and DOPC:Chol (Figure 5.9f) membranes. In contrast, some modest membrane homogenization seems to occur after quinacrine incubation with DOPC:SM:Chol membrane (Figure 5.9i, inset). Crucially, FLIM imaging confirms that the membranes remain intact throughout drug treatment in all instances, precluding membrane disruption as a contributor to the observed decrease in electrochemical resistance for DOPC and DOPC:SM:Chol.[144]

Next, to evaluate the impact of quinacrine interaction on membrane order, point fluorescence lifetime correlation spectroscopy (FLCS) measurements were carried out before and after quinacrine binding at these different MSLBs. Figure 5.10 shows representative FLCS data acquired from the different membrane compositions; DOPC (black, Figure 5.10a), DOPC:Chol (black, Figure 5.10b) and DOPC:SM:Chol (black, Figure 5.10c) prior to drug incubation at MSLBs.
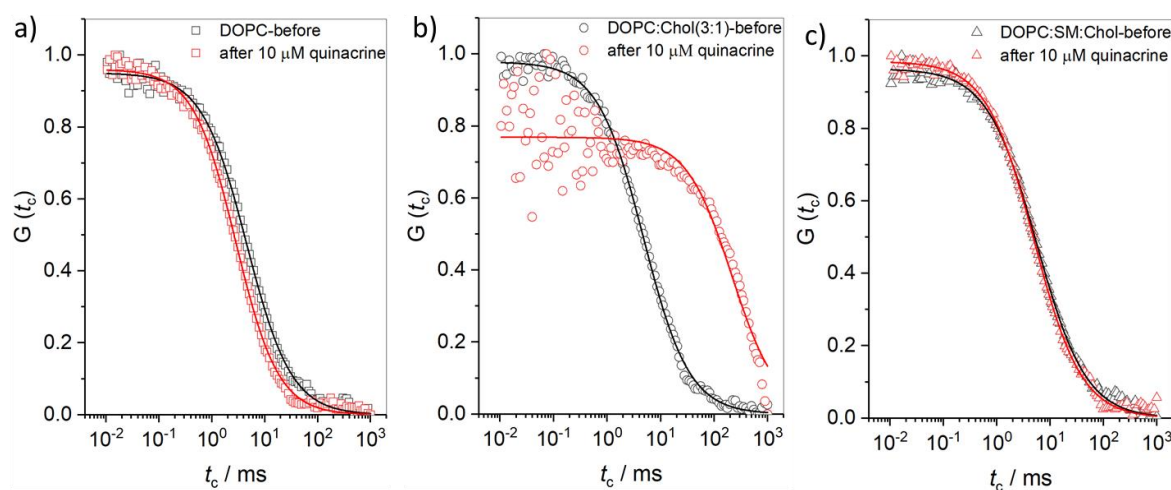
Figure 5.10 Representative FLCS autocorrelation function data obtained from different membranes such as (a) DOPC, (b) DOPC:Chol (3:1) and (c) DOPC:SM:Chol (2:2:1) before (black open symbol) and after incubation with 10 μM quinacrine (red open symbol). The distal leaflet of all the membranes are doped with 0.01 mol% DOPE-ATTO655. The lipid membrane spanned across the ~ 2 μm cavity PDMS array filled with the PBS buffer, pH 7.4. In each panel, solid lines are the representative fit using the 2D diffusion model equation. At the centre of pore spanning membranes of various bilayer types, at least 40-50 FLCS measurements are performed before and after drug incubation.

The lipid diffusivity was determined by fitting the ACF data to the 2D model equation. Before drug addition, the diffusivity values for DOPC, DOPC:Chol (3:1), and DOPC:SM:Chol (2:2:1) were calculated as 9.3±0.6 μm^{2}s^{-1}, 7.8±0.3 μm^{2}s^{-1}, and 6.2±0.4 μm^{2}s^{-1}, respectively. The data is compiled from around 40–50 measurements taken before and after drug binding for each

membrane type and averaged. The trend, as expected, reflects the membrane ordering effect of cholesterol in DOPC, and the DOPC:SM:Chol (2:2:1) composition, the former is expected to contain L_d phase at room temperature and the latter contain both L_o and L_d phase. When DOPC membrane is treated with 10 μM quinacrine, the lipid diffusivity increased from 9.3±0.6 to 13.03±0.4 μm^{2}s^{-1} (Figure 5.10a), indicating that the drug reduced the DOPC membrane packing. Remarkably, in contrast, the lipid diffusivity of the DOPC:Chol (3:1) membrane decreased dramatically from 7.8±0.3 μm^{2}s^{-1} to 0.19±0.7 μm^{2}s^{-1} (Figure 5.10b) on exposure to quinacrine. The magnitude of reduced diffusivity at DOPC:Chol membrane could be due to the intercalation effect of quinacrine to the aromatic backbone of cholesterol resulting gel-like behaviour of membrane. For the DOPC:SM:Chol membrane, on the other hand, consistent with DOPC data, drug induced only a modest increase in lipid mobility from 6.2±0.4 μm^{2}s^{-1} to 7.41±0.25 μm^{2}s^{-1} (Figure 5.10c), again associated with reduced lateral order. The resulting diffusion coefficients for each membrane composition before and after quinacrine are tabulated in Table 5.2.

Table 5.2 Diffusion coefficient values of three different membranes obtained before and after the addition of quinacrine obtained using fluorescence lifetime correlation spectroscopy.

Membrane composition	Diffusion coefficient, D (μm^{2}s^{-1})	
	Before quinacrine	After quinacrine
DOPC	9.3±0.6	13.03±0.4
DOPC:Chol	7.8±0.3	0.19±0.7
DOPC:SM:Chol	6.2±0.4	7.41±0.25

5.4.4 MSLB-a robust platform for studying artificial photosensitizer lateral diffusion
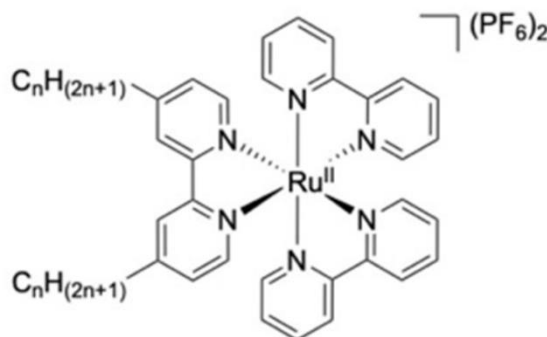
Figure 5.11 Structure of RuCn where n=9 or 19.[185]

Although series of amphiphilic RuC_n of varying alkyl chain length have been synthesized in our collaborator's laboratory[185], herein, only two of the RuC_n complexes (Figure 5.11) shall be discussed of varied alkyl chain length (n = 9, and 19) diffusion studies using FCS. Prior to FCS study at MSLB, the 3-dimensional bulk diffusion of $RuC_{n=19}$ was initially carried out at a concentration of 10 nM in acetonitrile. Figure 5.12a illustrates fluorescence intensity-time trace originated due to freely single molecule diffusion of $RuC_{n=19}$ across the observed confocal volume without any aggregation. The ACF trace is shown in Figure 5.12b (open black circle) and the corresponding fit data using 3D diffusion model equation is shown in red solid line. The diffusion coefficient was evaluated by fitting the ACF using 3D diffusion model (solid red line, Figure 5.12b) and found to be 199 $\pm$14 $\mu m^2 s^{-1}$. The lipid composition used in the present study was DPPC:NaDSPE-PEG2K (100:1 mol%) for lower and upper leaflet, however additional 4×10^{-4} mol% of RuC_n was doped only to the upper leaflet of MSLB. Since at such a low concentration of RuC_n and with intrinsic low quantum yield, reasonable FLIM signal was not obtained, however, as a control the formation of MSLB was independently verified by co-labelling the outer leaflet of bilayer using a red lipid fluorophore, DOPE-ATTO655. A typical FLIM image obtained for DOPE-ATTO655 channel is shown in Figure 5.12c indicating the successful formation of bilayer. Nonetheless, the above concentration of RuC_n complex is sufficient to yield single molecule diffusion using FCS modality across the bilayer.
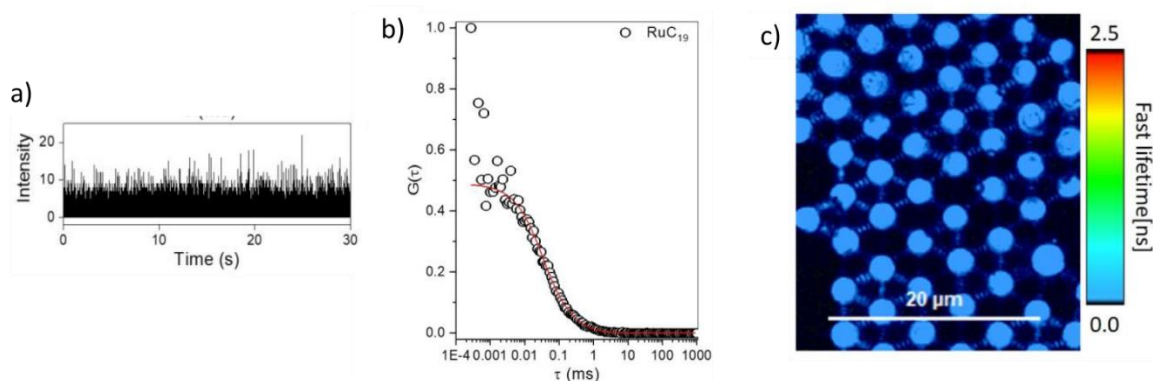
Figure 5.12 a) Intensity-time trace and b) the corresponding ACF originated due to the diffusion of $RuC_{n=19}$ in acetonitrile. c) Fluorescence lifetime image of MSLBs comprised of DPPC:NaDSPE-PEG2K:RuC_{19}. The membrane is co-labelled with 10 nM DOPE-ATTO655 and the image shows the fluorescence from the ATTO probe above the pores of the arrays confirming that the bilayer has formed.

Figure 5.13 displays representative fluorescence lifetime ACF graphs for RuC_n in MSLBs consisting of DPPC:NaDSPE-PEG2K:RuC_n. Intriguingly, the ACFs in both instances demonstrated the presence of two diffusing components originating from membrane bound

RuC$_n$. The diffusion coefficients of the RuC$_n$ molecules were determined by fitting the ACF with the two-component model equation 5.1 as defined below:

$$G(\tau) = \left[\frac{1}{N}\right]\left[\frac{1}{1+\left(\frac{\tau}{\tau_{D1}}\right)^{\alpha_1}}\right] + \left[\frac{1}{1+\left(\frac{\tau}{\tau_{D2}}\right)^{\alpha_2}}\right] \qquad (5.1)$$

where G(τ) is the autocorrelation function of fluorescence fluctuations, N is the average number of diffusing fluorophores in the effective volume, τ is the delay time, τ_{D_1} and τ_{D_2} are the diffusion time of the molecules across the confocal volume of the 1st component and 2nd component respectively, α_1 and α_2 are the anomalous parameters of the 1st and 2nd components, respectively, and c is the contribution of the diffusing species.

The diffusion coefficient of RuC$_{19}$ in acetonitrile was determined by fitting the ACF with 3D diffusion model equation given below:

$$G(\tau) = \left[\frac{1}{N}\right]\left[\frac{1}{1+\left(\frac{\tau}{\tau_D}\right)^{\alpha}}\right]\left[\frac{1}{\sqrt{1+\left(\frac{\tau}{\tau_D}\right)^{\alpha}K^2}}\right] \qquad (5.2)$$

where K is the length to diameter ratio of the confocal volume.
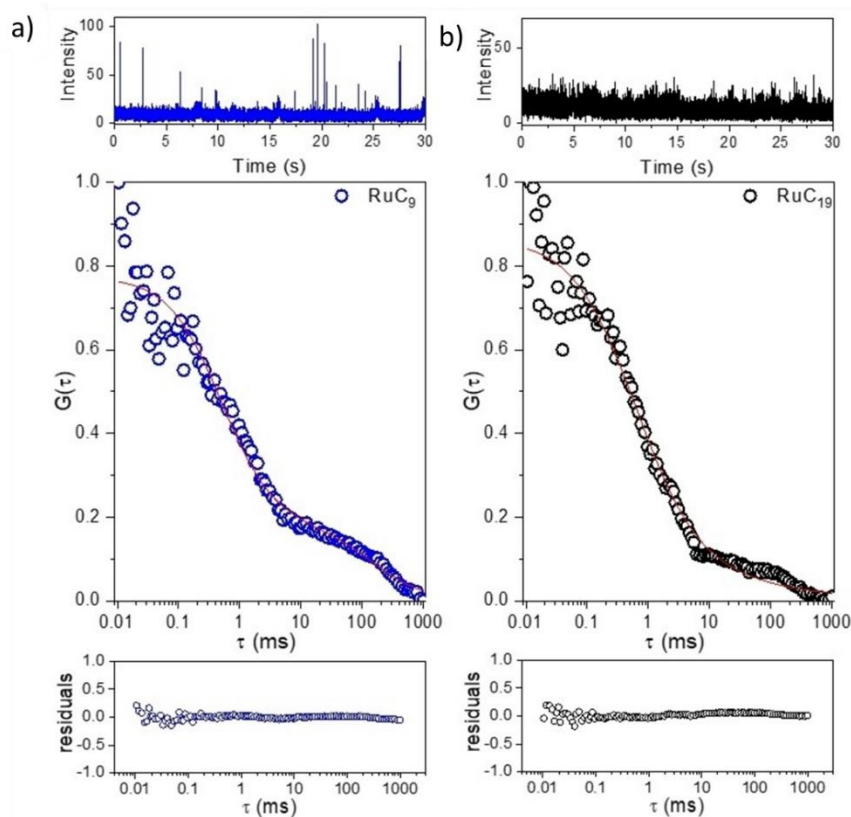
Figure 5.13 Representative intensity-time trace (top) and ACF (middle panel) data measured over a single microcavity of MSLBs comprised of DPPC:NaDSPE-PEG2K:RuC$_n$ in a ratio of $100 : 1 : 4 \times 10^{-4}$ for (a) RuC$_{n=9}$, and (b) RuC$_{n=19}$. The red lines in each panel are the fit using two-component diffusion model given in equation 5.1. In each panel, the residuals plots (bottom) that indicate the quality of the fit to the two-dimensional model of diffusion. Experimental conditions: [DPPC]=1.36 mM, [NaDSPE-PEG2K]=13.6 μM, and [RuC$_n$]=40 nM in phosphate buffer saline (pH=7.7). Bulk concentration [RuC$_n$] indicates theoretical concentration (before extrusion).

The two-dimensional diffusion coefficients of the slow-moving component for RuC$_{n=9}$ and RuC$_{n=19}$ was equal at 0.3 ± 0.9 μm^{2}s^{-1} and 0.4 ± 0.8 μm^{2}s^{-1}, respectively, which are within experimental error are equal. These numbers correspond to the fluidity of a typical DPPC bilayer diffusivity: The presence of 1 mol% NaDSPE-PEG2K at room temperature has been shown to only slightly mitigate the transition temperature of 41 °C for DPPC[546], so that the membrane is in the gel phase at experimental temperature (22 °C), resulting in typical two-dimensional diffusion coefficients below 1 μm^{2}s^{-1}. The fast-moving component's diffusion values were 82 ± 7 μm^{2}s^{-1} for RuC$_{n=9}$ and 49 ± 2 μm^{2}s^{-1} for RuC$_{n=19}$, which is on the one hand much faster than that of lipid probes fully embedded in the hydrophobic core of the membrane but on the other hand much slower than the value measured for diffusion in bulk solution (199 ± 14 μm^{2}s^{-1}). Therefore, RuC$_n$ molecules, which are obviously associated with the bilayer but

not deeply embedded in it, are a likely candidate for the fast-moving components. It is also possible that NaDSPE-PEG2K-derived domains are linked to the fast-diffusing complexes.[547] Super-diffusion at the membrane contact occurs quickly after PEG modification, as was previously mentioned.[548] A value of anomalous factor (α) higher than 1 was observed, which is characteristic of super-diffusion. The α value of slow diffusion component is effectively equal to 1 for $RuC_{n=19}$, showing free Brownian diffusion, but is below 1 for $RuC_{n=9}$, possibly indicating some self-aggregation of the complex in the membrane, which is consistent with the intensity-time trace in Figure 5.13a, which shows some clustered (closely spaced intensity spikes) peaks. The overall resulting diffusivity and other fit parameters for the $RuC_{n=9}$ and $RuC_{n=19}$ complexes are tabulated in Table 5.3.

Table 5.3 Fluorescence correlation spectroscopy data of RuCn in MSLBs of DPPC:NaDSPE-PEG2K.

Metal complex	D_1 ($\mu m^2 s^{-1}$)	D_2 ($\mu m^2 s^{-1}$)	A_1 (%)	A_2 (%)	α_1	α_2
$RuC_{n=9}$	82±7	0.3±0.9	82	18	1.12±0.07	0.64±0.01
$RuC_{n=19}$	49±2	0.4±0.8	56	44	1.20±0.05	0.98±0.02

The relative contribution or amplitude of the fast- and slow-diffusing components was discovered to vary with the length of the alkyl chain. In comparison to RuC_{19}, 82 percent of RuC_9 was the rapid component (D_1). As a result, the diffusion values for the fast component changed with molecule mass, whereas the diffusion values for the slow component did not. The latter finding was consistent with complexes that are well-embedded in the bilayer and basically follow the diffusion rate of other lipids in the membranes; it thus directly represents the typical viscosity of a gel phase membrane at room temperature, as described above. However, the larger amplitude of the fast-diffusing component observed for RuC_9 correlates well with the C_9 liposome system's higher photocatalytic performances and faster electron transfer rate observed by TA spectroscopy when compared to the C_{19} system.[185] To our knowledge, the coexistence of two distinct types of membrane-embedded RuC_n species with different diffusion coefficients is unprecedented. It implies that the fast-diffusing RuC_n molecules at the liposome interface are primarily involved in the photocatalytic process, and that the higher proportion of fully embedded and slowly diffusing molecules obtained with more hydrophobic amphiphiles (here RuC_{19}) is responsible for the lower electron transfer rates and overall lower yields for photocatalytic CO_2 reduction in DPPC liposomes as reported by us. It may even be that RuC_{19} species are just too slow diffusing to have any substantial

collision frequency for efficient electron transfer, i.e., that they are photocatalytically "dead". In other words, when all redox and excited state properties of photosensitisers and catalysts are equal, it is the lateral diffusion of the molecules within the lipid bilayer that decides photocatalytic efficacy, so shorter alkyl chains are actually better than longer ones. As a side note, it is extremely difficult to be certain about the orientation of the fast-diffusing species with respect to the membrane based on the available experimental data. The diffusion coefficient of the slow-diffusing component is very similar to that of a gel phase lipid bilayer, implying that this fraction of the complex is incorporated into the membrane in a manner similar to that of amphiphilic lipids, with the metal head group oriented close to the zwitterionic lipid head group at the aqueous interface and the alkyl tail embedded in the membrane's hydrophobic core. The fast component, on the other hand, may lie along the membrane interface, i.e., be poorly embedded, or may be linked with PEG domains at the membrane interface. At this point, it is also impossible to evaluate the relative orientation vs. the rate of diffusion of RuC_n. More experiments and/or calculations would be required to reach this determination.

5.5 Conclusions

In the study of individual leaflets using FLIM and FLCS, it is evident that MSLB platform gives a highly fluidic base for the proximal leaflet with a higher diffusion coefficient than SLB platform and with a very similar diffusivity for both the leaflets unlike SLBs.

From the interaction study of tricyclic antidepressants, it was observed that imipramine has an increased drug permeability through negatively charged DOPC:DOPG membrane, an intermediate permeability through DOPC membrane and a modest impact on DOPC:DOTAP membrane composition. Despite modest membrane organization, FLIM images showed no damage to the membrane in presence of antidepressant. According to FLCS results, imipramine causes membrane disorder regardless of the type of bilayer, whereas desipramine produces membrane ordering only when the bilayer is negatively charged. FLCS data showed imipramine induces membrane disordering effect irrespective of any bilayer type, whereas desipramine induces membrane ordering effect with exception to the negatively charged membrane. A future version of this MSLB platform will allow researchers to investigate passive and active modes of drug transport as well as their related kinetics on membranes reconstituted with or without receptor proteins, to study a variety of disease model membranes simulated without and with reconstituted receptor proteins.

In quinacrine based work, FLCS technique helped to evaluate the fluidity of the membrane in response to drug. FLIM experiment confirmed that the membranes remained intact during and after drug interaction, and FLCS experiment showed that the DOPC and ternary membrane, DOPC:SM:Chol undergo increased lipid diffusivity upon drug binding, while the DOPC:Chol membrane became significantly more rigid (tightly packed) with drug interaction, which is speculated that, it has to do with lowering of gel phase transition temperature. This study demonstrated that MSLB platforms can be used for screening passive permeability of antimalarial drugs across a range of biomembranes as well as shedding light on the role of physical properties of membranes in antimalarial drug interactions.

In the last part of the chapter, successful application of the MSLB platform to the study of photosensitizer, RuC_n diffusion across a membrane has been demonstrated. RuC_n molecules in lipid bilayers have been found to exhibit two distinct kinds of amphiphilicity: one that diffuses slowly and is located deep within the membrane, and another that diffuses rapidly and is located at the membrane's interface with water. This study also helped to have an insight about the lateral diffusion study of ruthenium complexes using MSLB platform which was utilized in chapter 4.

The interaction of drugs with membranes is critical for the pharmaceutical industry when it comes to the efficacy and safety of their products. Although the receptors and enzymes found within the cell membrane are typically the targets of the drug molecule, the membrane itself is often disregarded during the drug development process. The membrane, however, is not a neutral solvent; it exerts a direct influence on the protein structures and complexes it encloses. As a result, investigating the biophysical characteristics of membranes and the ways in which drugs affect them is of paramount importance. In addition, the structural stability of the cell can be compromised by the interactions between exogenous amphiphilic substances (including the vast majority of drug classes) and the membrane. None of the drugs tested were able to breach the lipid bilayer, but our results indicate that the modulation of membrane properties varies with the type of drug and membrane used. As a result of the findings, biomimetic bilayer systems can now be confidently used rather than simple lipid bilayers (sSLBs) to examine drug-membrane interactions.

Chapter 6: Conclusions and Future Perspectives

Translation of light addressable machinery to lipid membrane structures is highly desirable, across a range of applications including liposome drug or imaging agent delivery, membrane bound photosynthesis analogues etc. However, liposomes are difficult to address. This thesis focusses on two objectives – the translation of TTA-UC to liposomal systems and the application of MSLBs to interrogate as tools to understand the behaviour of the photosensitizers in these systems in the membrane as it is difficulty to interrogate LUVs directly.

A detailed investigation of novel photosensitizer molecules which can give efficient TTA-UC in biomembrane models can be used to develop design principles to understand what kinds of liposomes promote TTA-UC and what inhibit it, this will make it easier to deliver them to the real cells either by direct uptake or by liposomal delivery. Cell membrane models are an efficient way to mimic real cell membrane and they can be utilised to answer different biologically relevant questions such as fluidity/viscosity of the membranes and their interaction with different constituents. In this study, two BODIPY-perylene dyads and a ruthenium(II) complex were used as photosensitizers for TTA-UC in solution and extended the studies into model membranes including LUV, GUV, and MSLB. It was also aimed to study the effect of different physicochemical properties of lipids on TTA-UC and how the efficiency is changing for membrane related processes such as hydrolysis using different spectroscopic and microscopic techniques. The pore suspended membrane model was also applied to understand how tail length affected diffusion of a Ru(II) photosensitizer, used for photocatalysis in a membrane and applied the MSLB to interrogate drug-membrane interactions.

Chapter 1 presented a brief overview of the TTA-UC process's mechanism and fundamental principles, as an aid to understand the study presented in this thesis. This chapter discussed the importance of membrane composition and its impact on the TTA-UC process. The general basic concepts, terms, and definitions related to the presented work, different membrane models, as well as various surface sensitive experimental techniques for taping various intrinsic properties of lipid bilayer membranes, are thoroughly explained. This also presented some few examples of TTA-UC in liposomes and there is not enough information available about the parameters of the membrane that affect TTA-UC efficiency. Membrane models can help to investigate the process of TTA-UC within them, but they have to be fluidic and interrogable.

In chapter 2, two BODIPY-perylene dyads were studied as photosensitizers for efficient TTA-UC; one heavy atom-free charge transfer complex named B2P and another one with a conjugated iodine atom termed as B2PI. They both showed good performance towards TTA-UC when combined in Dioxane with perylene as annihilator. Nanosecond transient absorption spectroscopic studies were performed on B2P and B2PI to investigate the triplet lifetimes and three different lifetimes were observed for both B2P and B2PI which corresponds to triplet charge transfer state (^{3}CT), BODIPY-centred triplet and perylene centred triplet. The reduction in triplet lifetimes after the addition of perylene confirms the quenching by triplet energy transfer and annihilation processes. Later, B2P- and B2PI-perylene pairs were reconstituted into different membrane models like LUV and GUV for membrane-bound studies of upconversion. Good TTA-UC signal was observed from both pairs with B2PI having more efficiency than B2P like in solution due to spin-orbital charge transfer intersystem crossing (SOCT-ISC). The effect of membrane viscosity on TTA-UC was studied by reconstituting B2PI-perylene into liposomes of different composition across a range of measured (by FLCS) diffusivities and the results show that TTA-UC decreased on increase of viscosity. TTA-UC intensity was highest with the zwitterionic DOPC liposomes, which is highly fluidic in nature. Further extension of the TTA-UC study to the more complex biomembrane compositions that mimic mammalian plasma membranes showed that this new photosensitizer-annihilator pair is efficient even towards the complexity of the mammalian membranes.

In chapter 3, the TTA-UC of B2PI-perylene reconstituted in DOPC liposomes was compared in the absence of enzyme to the presence of activated enzyme phospholipase A_2 (PLA$_2$) and ~30% reduction was observed in the presence of PLA$_2$ from pristine liposome. The reduction was observed when Ca^{2+} is present in the contact solution, implying that Ca^{2+} activates the catalytic activity of PLA$_2$. Even though there is a decline in the intensity of TTA-UC in presence of activated PLA$_2$, the signal is still significant enough to identify upconversion. The decrease in TTA-UC signal is caused mainly due to the result of hydrolytic products packing of lysolipids and fatty acid. Since there was no decrease in TTA-UC intensity in the presence of PLA$_2$ without Ca^{2+}, or imipramine treated PLA$_2$ in the presence of Ca^{2+}, confirms that the decrease of TTA-UC signal caused by the enzymatic activity could be due to an increase in the packing order of hydrolytic products in the liposomes. Further confirmation on the increase of lipid packing was done using FLCS. The lipid diffusivity has significantly decreased from 10.1 ± 0.2 $\mu m^2 s^{-1}$ to 1.4 ± 0.3 $\mu m^2 s^{-1}$ due to hydrolysis. The enzymatic activity was further confirmed with label-free EIS analysis, where there is a decrease in membrane admittance in

the presence of non-activated enzyme or with the presence of inhibitor and this decrease is due to the weak association of PLA_2 with the membrane surface in the absence of hydrolysis. The increase in admittance in the presence of activated PLA_2 comes from the membrane reorganization as nanoscale pore formation, allowing for easier ion transfer across MSLB and this finding of membrane reorganization is confirmed by molecular level topographic imaging with AFM.

In chapter 4, an attempt was made to extend the membrane-based study of TTA-UC to an inorganic metal complex photosensitizer with unity triplet yield. Here, the photosensitizer Ru-bqp-oct known to have strongly mixed ligand and metal triplet ligand centred excited state which is expected to promote TTA-UC. And indeed, the process was observed with good efficiency in deaerated acetonitrile with suitable annihilator. A series of annihilators and solvents were evaluated among which anthracene derivatives and acetonitrile found to be best performing in solution. In selecting an annihilator basic quenching studies and Stern-Volmer analysis were carried out and DPA showed limited quenching consistent with a good annihilator. A detailed optimization on photosensitizer: annihilator ratio was performed and best performance achieved at 1:20 ratio. The threshold power density value for this particular ratio was calculated to be 54 mW cm^{-2}, suggesting the conversion to high annihilation regime from low annihilation regime occurred at low excitation power density, consistent with good TTA-UC performance. The photosensitizer and annihilator were then reconstituted into DOPC lipid bilayer and both were confirmed as embedded in the GUV imaging and FLCS measurements. A moderate diffusion coefficient of 5.7 $\mu m^2 s^{-1}$ was observed for the photosensitizer with non-Brownian behaviour. Further investigation within the liposomes showed no evidence for TTA-UC signal. More attempts with different experimental parameters and lipid composition showed no upconversion. This could be due different orientations of photosensitizer and annihilator where no energy transfer happens. If the photosensitizer is staying in the interface and the annihilator is deeply embedded within the bilayer, the TTET may not occur and thereby no TTA-UC.

In chapter 5, a detailed validation of MSLB platform and investigation of its interaction with small molecule drugs and photosensitizer were carried out. The MSLB platform has been used throughout the thesis and chapter 5 gives insights of their performance and versatility. Based on the analysis of individual leaflets with FLIM and FLCS, it is obvious that MSLB platform provides highly fluidic bases for both proximal and distal leaflets with a higher diffusion

coefficient, unlike SLB platform. As a result of the interaction study with tricyclic antidepressants, it was observed that imipramine has increased drug permeability through negatively charged DOPC:DOPG membrane, an intermediate permeability through DOPC membrane and a modest impact on DOPC:DOTAP membrane composition. Desipramine produces membrane ordering only when the bilayer is negatively charged whereas imipramine causes for all three charges of the bilayer. In quinacrine based work, the fluidity of the membrane was evaluated in response to drug using FLCS. When drug binding occurs on the DOPC and ternary membrane, DOPC:SM:Chol, lipid diffusivity increases, and the DOPC:Chol membrane becomes significantly more rigid (closely packed) due to drug interaction, which could be due to the lowering of gel phase transition temperature. MSLB platform has been successfully used to study the diffusion of RuC_n photosensitizer across membrane in the last part of the chapter.

Overall, the study suggests that liposome formulation with newly developed photosensitizers may enable TTA-UC in real cell membranes. Also, TTA-UC with the newly developed photosensitizer is efficient during enzymatic action, which has the potential for targeted therapy in terms of drug release to target sites as well as imaging using TTA-UC modalities. In addition to providing molecular level insights into the specific enzyme used in this work, MSLB can also be used to examine changes in biophysical properties caused by changes in enzymatic hydrolysis. Also, researchers will be able to investigate passive and active modes of drug transport on membranes with or without receptor proteins using this MSLB platform in future. Rather than simple solid supported lipid bilayers, biomimetic MSLB system can now be constantly used to examine membrane-drug interactions and membrane-photosensitizer interactions. By these features, it would be possible to study TTA-UC directly in MSLB platform with desirable optimisation and the effect of different biophysical properties of the membrane and other membrane-bound molecules on TTA-UC could also be studied using MSLB. After detailed investigation, the bio-delivery of TTA-UC for different applications including photoactivated chemotherapeutic drug delivery would also be possible.

References

1   D. Peer, J. M. Karp, S. Hong, O. C. Farokhzad, R. Margalit and R. Langer, *Nat. Nanotechnol.*, 2007, **2**, 751–760.

2   W. Jeong, J. Bu, L. J. Kubiatowicz, S. S. Chen, Y. Kim and S. Hong, *Nano Converg.*, 2018, **5**, 38.

3   N. Aibani, H. Nesbitt, N. Marino, J. Jurek, C. O'Neill, C. Martin, I. Di Bari, Y. Sheng, K. Logan, S. Hawthorne, A. McHale, J. F. Callan and B. Callan, *Acta Biomater.*, 2018, **80**, 327–340.

4   W. F. Graier, B. G. Hoebel, J. Paltauf-Doburzynska and G. M. Kostner, *Arterioscler. Thromb. Vasc. Biol.*, 1998, **18**, 1470–1479.

5   C. Ye, L. Zhou, X. Wang and Z. Liang, *Phys. Chem. Chem. Phys.*, 2016, **18**, 10818–10835.

6   M. Penconi, P. L. Gentili, G. Massaro, F. Elisei and F. Ortica, 2014, 48–61.

7   C. Kerzig and O. S. Wenger, *Chem. Sci.*, 2018, **9**, 6670–6678.

8   M. Alipour and Z. Safari, , DOI:10.1039/c9cp02987g.

9   V. Gray, K. Börjesson, D. Dzebo, M. Abrahamsson, B. Albinsson and K. Moth-Poulsen, *J. Phys. Chem. C*, 2016, **120**, 19018–19026.

10   C. M. Cruz, I. R. Márquez, I. F. A. Mariz, V. Blanco, C. Sánchez-Sánchez, J. M. Sobrado, J. A. Martín-Gago, J. M. Cuerva, E. Maçôas and A. G. Campaña, *Chem. Sci.*, 2018, **9**, 3917–3924.

11   P. J. Walla, J. Yom, B. P. Krueger and G. R. Fleming, *J. Phys. Chem. B*, 2000, **104**, 4782–4790.

12   F. Auzel, *Chem. Rev.*, 2004, **104**, 139–173.

13   V. Gray, K. Moth-Poulsen, B. Albinsson and M. Abrahamsson, *Coord. Chem. Rev.*, 2018, **362**, 54–71.

14   N. Awwad, M. Yang and F. N. Castellano, in *Emerging Strategies to Reduce Transmission and Thermalization Losses in Solar Cells*, Springer International Publishing, Cham, 2022, pp. 9–28.

15   A. Tokunaga, L. M. Uriarte, K. Mutoh, E. Fron, J. Hofkens, M. Sliwa and J. Abe, *J. Am. Chem. Soc.*, 2019, **141**, 17744–17753.

16   P. Duan, N. Yanai, H. Nagatomi and N. Kimizuka, *J. Am. Chem. Soc.*, 2015, **137**, 1887–1894.

17   X. Cui, A. M. El-Zohry, Z. Wang, J. Zhao and O. F. Mohammed, *J. Phys. Chem. C*, 2017, **121**, 16182–16192.

18 Z. A. VanOrman, A. S. Bieber, S. Wieghold and L. Nienhaus, *MRS Commun.*, 2019, **9**, 924–935.

19 X. Guo, Y. Liu, Q. Chen, D. Zhao and Y. Ma, *Adv. Opt. Mater.*, 2018, **6**, 1–16.

20 T. N. Singh-Rachford and F. N. Castellano, *Coord. Chem. Rev.*, 2010, **254**, 2560–2573.

21 Y. Zhou, F. N. Castellano, T. W. Schmidt and K. Hanson, *ACS Energy Lett.*, 2020, **5**, 2322–2326.

22 P. Bharmoria, H. Bildirir and K. Moth-Poulsen, *Chem. Soc. Rev.*, 2020, **49**, 6529–6554.

23 A. Olesund, V. Gray, J. Mårtensson and B. Albinsson, *J. Am. Chem. Soc.*, 2021, **143**, 5745–5754.

24 A. S. Gertsen, M. Koerstz and K. V. Mikkelsen, *Phys. Chem. Chem. Phys.*, 2018, **20**, 12182–12192.

25 A. B. Pun, S. N. Sanders, M. Y. Sfeir, L. M. Campos and D. N. Congreve, *Chem. Sci.*, 2019, **10**, 3969–3975.

26 X. Cui, A. Charaf-Eddin, J. Wang, B. Le Guennic, J. Zhao and D. Jacquemin, *J. Org. Chem.*, 2014, **79**, 2038–2048.

27 K. Fujimoto, K. Kawai, S. Masuda, T. Mori, T. Aizawa, T. Inuzuka, T. Karatsu, M. Sakamoto, S. Yagai, T. Sengoku, M. Takahashi and H. Yoda, *Langmuir*, 2019, **35**, 9740–9746.

28 N. Harada, Y. Sasaki, M. Hosoyamada, N. Kimizuka and N. Yanai, *Angew. Chemie Int. Ed.*, 2021, **60**, 142–147.

29 C. Wohnhaas, V. Mailänder, M. Dröge, M. A. Filatov, D. Busko, Y. Avlasevich, S. Baluschev, T. Miteva, K. Landfester and A. Turshatov, *Macromol. Biosci.*, 2013, **13**, 1422–1430.

30 S. Askes, M. Meijer, T. Bouwens, I. Landman and S. Bonnet, *Molecules*, 2016, **21**, 1460.

31 D. Dzebo, K. Moth-Poulsen and B. Albinsson, *Photochem. Photobiol. Sci.*, 2017, **16**, 1327–1334.

32 N. Yanai and N. Kimizuka, *Angew. Chemie Int. Ed.*, 2020, **59**, 10252–10264.

33 V. Yakutkin, S. Aleshchenkov, S. Chernov, T. Miteva, G. Nelles, A. Cheprakov and S. Baluschev, *Chem. - A Eur. J.*, 2008, **14**, 9846–9850.

34 T. Dilbeck, S. P. Hill and K. Hanson, *J. Mater. Chem. A*, 2017, **5**, 11652–11660.

35 S. P. Hill and K. Hanson, *J. Am. Chem. Soc.*, 2017, **139**, 10988–10991.

36 L. Huang, E. Kakadiaris, T. Vaneckova, K. Huang, M. Vaculovicova and G. Han, *Biomaterials*, 2019, **201**, 77–86.

37 L. Huang, W. Wu, Y. Li, K. Huang, L. Zeng, W. Lin and G. Han, *J. Am. Chem. Soc.*,

2020, **142**, 18460–18470.

38 V. Gray, A. Dreos, P. Erhart, B. Albinsson, K. Moth-Poulsen and M. Abrahamsson, *Phys. Chem. Chem. Phys.*, 2017, **19**, 10931–10939.

39 J. Wang, Y. Lu, W. McCarthy, R. Conway-Kenny, B. Twamley, J. Zhao and S. M. Draper, *Chem. Commun.*, 2018, **54**, 1073–1076.

40 L. Huang, E. Kakadiaris, T. Vaneckova, K. Huang, M. Vaculovicova and G. Han, *Biomaterials*, 2019, **201**, 77–86.

41 von Alfred Treibs and Franz-Heinrich Kreuzer, *Liebigs Ann. Chem.*, 1968, **718**, 208–223.

42 A. Kamkaew, S. H. Lim, H. B. Lee, L. V. Kiew, L. Y. Chung and K. Burgess, *Chem. Soc. Rev.*, 2013, **42**, 77–88.

43 A. Loudet and K. Burgess, *Chem. Rev.*, 2007, **107**, 4891–4932.

44 G. Ulrich, R. Ziessel and A. Harriman, *Angew. Chemie Int. Ed.*, 2008, **47**, 1184–1201.

45 R. Ziessel, G. Ulrich and A. Harriman, *New J. Chem.*, 2007, **31**, 496.

46 M. Liu, S. Ma, M. She, J. Chen, Z. Wang, P. Liu, S. Zhang and J. Li, *Chinese Chem. Lett.*, 2019, **30**, 1815–1824.

47 J. Zhao, K. Xu, W. Yang, Z. Wang and F. Zhong, *Chem. Soc. Rev.*, 2015, **44**, 8904–8939.

48 K. Chen, Y. Dong, X. Zhao, M. Imran, G. Tang, J. Zhao and Q. Liu, *Front. Chem.*, , DOI:10.3389/fchem.2019.00821.

49 S. Wang, H. Liu, J. Mack, J. Tian, B. Zou, H. Lu, Z. Li, J. Jiang and Z. Shen, *Chem. Commun.*, 2015, **51**, 13389–13392.

50 X. Zhang, Y. Xu, P. Guo and X. Qian, *New J. Chem.*, 2012, **36**, 1621.

51 Y. Xiao, D. Zhang, X. Qian, A. Costela, I. Garcia-Moreno, V. Martin, M. E. Perez-Ojeda, J. Bañuelos, L. Gartzia and I. L. Arbeloa, *Chem. Commun.*, 2011, **47**, 11513.

52 B. Sui, S. Tang, T. Liu, B. Kim and K. D. Belfield, *ACS Appl. Mater. Interfaces*, 2014, **6**, 18408–18412.

53 T. Kowada, H. Maeda and K. Kikuchi, *Chem. Soc. Rev.*, 2015, **44**, 4953–4972.

54 O. Altan Bozdemir, S. Erbas-Cakmak, O. O. Ekiz, A. Dana and E. U. Akkaya, *Angew. Chemie Int. Ed.*, 2011, **50**, 10907–10912.

55 R. Ziessel and A. Harriman, *Chem. Commun.*, 2011, **47**, 611–631.

56 A. Coskun, E. Deniz and E. U. Akkaya, *Org. Lett.*, 2005, **7**, 5187–5189.

57 S. Erbas-Cakmak, O. A. Bozdemir, Y. Cakmak and E. U. Akkaya, *Chem. Sci.*, 2013, **4**,

858–862.

58   G. D. Sharma, S. A. Siddiqui, A. Nikiforou, G. E. Zervaki, I. Georgakaki, K. Ladomenou and A. G. Coutsolelos, *J. Mater. Chem. C*, 2015, **3**, 6209–6217.

59   X. Zhang, Y. Zhang, L. Chen and Y. Xiao, *RSC Adv.*, 2015, **5**, 32283–32289.

60   T. Bura, N. Leclerc, S. Fall, P. Lévêque, T. Heiser and R. Ziessel, *Org. Lett.*, 2011, **13**, 6030–6033.

61   A. Sutter, P. Retailleau, W.-C. Huang, H.-W. Lin and R. Ziessel, *New J. Chem.*, 2014, **38**, 1701–1710.

62   S. Kolemen, O. A. Bozdemir, Y. Cakmak, G. Barin, S. Erten-Ela, M. Marszalek, J.-H. Yum, S. M. Zakeeruddin, M. K. Nazeeruddin, M. Grätzel and E. U. Akkaya, *Chem. Sci.*, 2011, **2**, 949.

63   A. C. Benniston and G. Copley, *Phys. Chem. Chem. Phys.*, 2009, **11**, 4124.

64   B. Verbelen, V. Leen, L. Wang, N. Boens and W. Dehaen, *Chem. Commun.*, 2012, **48**, 9129.

65   S. Niu, C. Massif, G. Ulrich, P.-Y. Renard, A. Romieu and R. Ziessel, *Chem. - A Eur. J.*, 2012, **18**, 7229–7242.

66   S. Zhu, J. Zhang, G. Vegesna, F.-T. Luo, S. A. Green and H. Liu, *Org. Lett.*, 2011, **13**, 438–441.

67   N. L. Bill, J. M. Lim, C. M. Davis, S. Bähring, J. O. Jeppesen, D. Kim and J. L. Sessler, *Chem. Commun.*, 2014, **50**, 6758–6761.

68   B. Wang, P. Li, F. Yu, J. Chen, Z. Qu and K. Han, *Chem. Commun.*, 2013, **49**, 5790.

69   J. Zhao, W. Wu, J. Sun and S. Guo, *Chem. Soc. Rev.*, 2013, **42**, 5323–5351.

70   M. Galletta, F. Puntoriero, S. Campagna, C. Chiorboli, M. Quesada, S. Goeb and R. Ziessel, *J. Phys. Chem. A*, 2006, **110**, 4348–4358.

71   A. A. Rachford, R. Ziessel, T. Bura, P. Retailleau and F. N. Castellano, *Inorg. Chem.*, 2010, **49**, 3730–3736.

72   W. Wu, H. Guo, W. Wu, S. Ji and J. Zhao, *J. Org. Chem.*, 2011, **76**, 7056–7064.

73   L. Huang and J. Zhao, *RSC Adv.*, 2013, **3**, 23377.

74   L. Huang, J. Zhao, S. Guo, C. Zhang and J. Ma, *J. Org. Chem.*, 2013, **78**, 5627–5637.

75   T. Yogo, Y. Urano, Y. Ishitsuka, F. Maniwa and T. Nagano, *J. Am. Chem. Soc.*, 2005, **127**, 12162–12163.

76   A. Gorman, J. Killoran, C. O'Shea, T. Kenna, W. M. Gallagher and D. F. O'Shea, *J. Am. Chem. Soc.*, 2004, **126**, 10619–10631.

77   A. Kamkaew, S. H. Lim, H. B. Lee, L. V. Kiew, L. Y. Chung and K. Burgess, *Chem. Soc. Rev.*, 2013, **42**, 77–88.

78   B. P. Wittmershaus, J. J. Skibicki, J. B. McLafferty, Y. Z. Zhang and S. Swan, *J. Fluoresc.*, 2001, **11**, 119–128.

79   S. G. Awuah and Y. You, *RSC Adv.*, 2012, **2**, 11169.

80   R. Sharma, H. B. Gobeze, F. D'Souza and M. Ravikanth, *ChemPhysChem*, 2016, **17**, 2516–2524.

81   D. V. Dorofeev, S. N. Letuta and D. E. Tsyurko, *Russ. Chem. Bull.*, 2021, **70**, 427–432.

82   C. M. Marian, *Wiley Interdiscip. Rev. Comput. Mol. Sci.*, 2012, **2**, 187–203.

83   J. M. Lee, J. M. Park, H. K. Lee, H. M. Kim, J. H. Kim and J. P. Kim, *Dye. Pigment.*, 2021, **196**, 109662.

84   G. J. Kavarnos, 1990, pp. 21–58.

85   L. B. Niu, L. J. Chen, P. Chen, Y. T. Cui, Y. Zhang, M. Shao and Y. X. Guan, *RSC Adv.*, 2016, **6**, 111421–111426.

86   Z. Wang, M. Ivanov, Y. Gao, L. Bussotti, P. Foggi, H. Zhang, N. Russo, B. Dick, J. Zhao, M. Di Donato, G. Mazzone, L. Luo and M. Fedin, *Chem. – A Eur. J.*, 2020, **26**, 1091–1102.

87   G. Tang, A. A. Sukhanov, J. Zhao, W. Yang, Z. Wang, Q. Liu, V. K. Voronkova, M. Di Donato, D. Escudero and D. Jacquemin, *J. Phys. Chem. C*, 2019, **123**, 30171–30186.

88   J. Zhao, K. Chen, Y. Hou, Y. Che, L. Liu and D. Jia, *Org. Biomol. Chem.*, 2018, **16**, 3692–3701.

89   M. Liu, C. Wang and Y. Qian, *New J. Chem.*, 2021, **45**, 18082–18089.

90   Z. Lou, Y. Hou, K. Chen, J. Zhao, S. Ji, F. Zhong, Y. Dede and B. Dick, *J. Phys. Chem. C*, 2018, **122**, 185–193.

91   Z. Wang, A. A. Sukhanov, A. Toffoletti, F. Sadiq, J. Zhao, A. Barbon, V. K. Voronkova and B. Dick, *J. Phys. Chem. C*, 2019, **123**, 265–274.

92   K. Chen, Y. Dong, X. Zhao, M. Imran, G. Tang, J. Zhao and Q. Liu, *Front. Chem.*, 2019, **7**, 1–14.

93   S. H. C. Askes, A. Bahreman and S. Bonnet, *Angew. Chemie*, 2014, **126**, 1047–1051.

94   M. A. Sgambellone, A. David, R. N. Garner, K. R. Dunbar and C. Turro, *J. Am. Chem. Soc.*, 2013, **135**, 11274–11282.

95   N. J. Farrer, L. Salassa and P. J. Sadler, *Dalt. Trans.*, 2009, 10690.

96   S. Bonnet, B. Limburg, J. D. Meeldijk, R. J. M. Klein Gebbink and J. A. Killian, *J. Am. Chem. Soc.*, 2011, **133**, 252–261.

97 S. H. C. Askes, M. Kloz, G. Bruylants, J. T. M. Kennis and S. Bonnet, *Phys. Chem. Chem. Phys.*, 2015, **17**, 27380–27390.

98 J. S. O'Brien, *J. Theor. Biol.*, 1967, **15**, 307–324.

99 R. F. DeGrella and R. D. Simoni, *J. Biol. Chem.*, 1982, **257**, 14256–14262.

100 B. D. Almquist and N. A. Melosh, *Proc. Natl. Acad. Sci.*, 2010, **107**, 5815–5820.

101 J. K. Jaiswal and S. M. Simon, *Nat. Chem. Biol.*, 2007, **3**, 92–98.

102 M. Pulfer and R. C. Murphy, *Mass Spectrom. Rev.*, 2003, **22**, 332–364.

103 J. M. Deeley, M. C. Thomas, R. J. W. Truscott, T. W. Mitchell and S. J. Blanksby, *Anal. Chem.*, 2009, **81**, 1920–1930.

104 C. M. Talbott, I. Vorobyov, D. Borchman, K. G. Taylor, D. B. DuPré and M. C. Yappert, *Biochim. Biophys. Acta - Biomembr.*, 2000, **1467**, 326–337.

105 L. L. M. Van Deenen, *Pure Appl. Chem.*, 1971, **25**, 25–56.

106 D. Hishikawa, T. Hashidate, T. Shimizu and H. Shindou, *J. Lipid Res.*, 2014, **55**, 799–807.

107 L. Salvia-Trujillo, C. Qian, O. Martín-Belloso and D. J. McClements, *Food Chem.*, 2013, **141**, 1472–1480.

108 H. T. Pham, A. T. Maccarone, M. C. Thomas, J. L. Campbell, T. W. Mitchell and S. J. Blanksby, *Analyst*, 2014, **139**, 204–214.

109 C. I. E. von Deuster and V. Knecht, *Biochim. Biophys. Acta - Biomembr.*, 2012, **1818**, 2192–2201.

110 P. Pignatelli, E. Ettorre, D. Menichelli, A. Pani, F. Violi and D. Pastori, *Haematologica*, 2020, **105**, 562–572.

111 G. Caracciolo, F. Cardarelli, D. Pozzi, F. Salomone, G. Maccari, G. Bardi, A. L. Capriotti, C. Cavaliere, M. Papi and A. Laganà, *ACS Appl. Mater. Interfaces*, 2013, **5**, 13171–13179.

112 S. Leekumjorn and A. K. Sum, *Biochim. Biophys. Acta - Biomembr.*, 2007, **1768**, 354–365.

113 M. Yoda, T. Miura and H. Takeuchi, *Biochem. Biophys. Res. Commun.*, 2008, **376**, 56–59.

114 R. Koynova and R. C. MacDonald, *Nano Lett.*, 2004, **4**, 1475–1479.

115 A. Blume, D. M. Rice, R. J. Wittebort and R. G. Griffin, *Biochemistry*, 1982, **21**, 6220–6230.

116 G. Fragneto and M. Rheinstädter, *Comptes Rendus Phys.*, 2007, **8**, 865–883.

117 W. T. Shier and A. C. Shier, *J. Toxicol. Toxin Rev.*, 2000, **19**, 189–246.

118 B. Ramstedt and J. P. Slotte, *Biochim. Biophys. Acta - Biomembr.*, 2006, **1758**, 1945–1956.

119 C. Lopez and O. Ménard, *Colloids Surfaces B Biointerfaces*, 2011, **83**, 29–41.

120 A. H. Merrill Jr., M. C. Sullards, J. C. Allegood, S. Kelly and E. Wang, *Methods*, 2005, **36**, 207–224.

121 J. A. Shayman, *Semin. Nephrol.*, 2018, **38**, 183–192.

122 H. Miller-Podraza, *Chem. Rev.*, 2000, **100**, 4663–4682.

123 M. E. Hemling, R. K. Yu, R. D. Sedgwick and K. L. Rinehart, *Biochemistry*, 1984, **23**, 5706–5713.

124 D. Martin-Creuzburg and E. von Elert, in *Lipids in Aquatic Ecosystems*, Springer New York, New York, NY, 2009, pp. 43–64.

125 C. Bernsdorff and R. Winter, *J. Phys. Chem. B*, 2003, **107**, 10658–10664.

126 J. G. Roddick, *Phytochemistry*, 1979, **18**, 1467–1470.

127 K. Bloch, 1991, pp. 363–381.

128 C. Megías, J. Pedroche, M. del Mar Yust, M. Alaiz, J. Girón-Calle, F. Millán and J. Vioque, *Plant Foods Hum. Nutr.*, 2009, **64**, 86–93.

129 H. Wu, M. Yu, Y. Miao, S. He, Z. Dai, W. Song, Y. Liu, S. Song, E. Ahmad, D. Wang and Y. Gan, *Acta Pharm. Sin. B*, 2019, **9**, 858–870.

130 M. Doxastakis, A. K. Sum and J. J. de Pablo, *J. Phys. Chem. B*, 2005, **109**, 24173–24181.

131 T. Wang, Z. Feng, C. Wang and N. He, *Colloids Surfaces B Biointerfaces*, 2018, **164**, 70–77.

132 A. Luchini and G. Vitiello, *Biomimetics*, 2020, **6**, 3.

133 C.-H. Wu, Y. Chen, K. A. Pyrshev, Y.-T. Chen, Z. Zhang, K.-H. Chang, S. O. Yesylevskyy, A. P. Demchenko and P.-T. Chou, *ACS Chem. Biol.*, 2020, **15**, 1862–1873.

134 A. Mangiarotti, B. Caruso and N. Wilke, *Biochim. Biophys. Acta - Biomembr.*, 2014, **1838**, 1823–1831.

135 Y.-H. M. Chan and S. G. Boxer, *Curr. Opin. Chem. Biol.*, 2007, **11**, 581–587.

136 M. Doktorova, F. A. Heberle, B. Eicher, R. F. Standaert, J. Katsaras, E. London, G. Pabst and D. Marquardt, *Nat. Protoc.*, 2018, **13**, 2086–2101.

137 M. Breton, M. Amirkavei and L. M. Mir, *J. Membr. Biol.*, 2015, **248**, 827–835.

138 K. Nishimura, T. Matsuura, K. Nishimura, T. Sunami, H. Suzuki and T. Yomo, *Langmuir*, 2012, **28**, 8426–8432.

139 M. C. Woodle and D. Papahadjopoulos, 1989, pp. 193–217.

140 M. S. Terakawa, Y. Lin, M. Kinoshita, S. Kanemura, D. Itoh, T. Sugiki, M. Okumura, A. Ramamoorthy and Y.-H. Lee, *Biochim. Biophys. Acta - Biomembr.*, 2018, **1860**, 1741–1764.

141 S. F. Fenz and K. Sengupta, *Integr. Biol.*, 2012, **4**, 982.

142 M. Guéguinou, T. Harnois, D. Crottes, A. Uguen, N. Deliot, A. Gambade, A. Chantôme, J. P. Haelters, P. A. Jaffrès, M. L. Jourdan, G. Weber, O. Soriani, P. Bougnoux, O. Mignen, N. Bourmeyster, B. Constantin, T. Lecomte, C. Vandier and M. Potier-Cartereau, *Oncotarget*, 2016, **7**, 36168–36184.

143 P. F. Devaux, *Biochemistry*, 1991, **30**, 1163–1173.

144 N. K. Sarangi, A. Prabhakaran and T. E. Keyes, *Langmuir*, 2022, **38**, 6411–6424.

145 A. Moschetta, G. P. VanBerge-Henegouwen, P. Portincasa, W. Renooij, A. K. Groen and K. J. van Erpecum, *J. Hepatol.*, 2001, **34**, 492–499.

146 G. Mariño and G. Kroemer, *Cell Res.*, 2013, **23**, 1247–1248.

147 J. Fantini, C. Di Scala, L. S. Evans, P. T. F. Williamson and F. J. Barrantes, *Sci. Rep.*, 2016, **6**, 21907.

148 R. Lasserre, X.-J. Guo, F. Conchonaud, Y. Hamon, O. Hawchar, A.-M. Bernard, S. M. Soudja, P.-F. Lenne, H. Rigneault, D. Olive, G. Bismuth, J. A. Nunès, B. Payrastre, D. Marguet and H.-T. He, *Nat. Chem. Biol.*, 2008, **4**, 538–547.

149 G. W. Feigenson, *Biochim. Biophys. Acta - Biomembr.*, 2009, **1788**, 47–52.

150 R. F. M. de Almeida, A. Fedorov and M. Prieto, *Biophys. J.*, 2003, **85**, 2406–2416.

151 E. Sezgin, *Biochim. Biophys. Acta - Biomembr.*, 2022, **1864**, 183857.

152 N. K. Sarangi, A. Stalcup and T. E. Keyes, *ChemElectroChem*, 2020, **7**, 4535–4542.

153 D. D. Lasic and D. Papahadjopoulos, *Science (80-.).*, 1995, **267**, 1275–1276.

154 J. W. Kuhlmann, M. Junius, U. Diederichsen and C. Steinem, *Biophys. J.*, 2017, **112**, 2348–2356.

155 E. Parigoris, D. L. Dunkelmann, A. Murphy, N. Wili, A. Kaech, C. Dumrese, N. Jimenez-Rojo and U. Silvan, *Sci. Rep.*, 2020, **10**, 4824.

156 M. J. Hope, M. B. Bally, L. D. Mayer, A. S. Janoff and P. R. Cullis, *Chem. Phys. Lipids*, 1986, **40**, 89–107.

157 S. Sun, Y. Xia, J. Liu, Y. Dou, K. Yang, B. Yuan and Z. Kang, *J. Colloid Interface Sci.*, 2022, **609**, 707–717.

158 G. Milcovich, S. Lettieri, F. E. Antunes, B. Medronho, A. C. Fonseca, J. F. J. Coelho, P. Marizza, F. Perrone, R. Farra, B. Dapas, G. Grassi, M. Grassi and S. Giordani, *Adv. Colloid Interface Sci.*, 2017, **249**, 163–180.

159 M. I. Angelova and D. S. Dimitrov, *Faraday Discuss. Chem. Soc.*, 1986, **81**, 303.

160 H. Bi, B. Yang, L. Wang, W. Cao and X. Han, *J. Mater. Chem. A*, 2013, **1**, 7125.

161 F. Olson, C. A. Hunt, F. C. Szoka, W. J. Vail and D. Papahadjopoulos, *Biochim. Biophys. Acta - Biomembr.*, 1979, **557**, 9–23.

162 M. M. Lapinski, A. Castro-Forero, A. J. Greiner, R. Y. Ofoli and G. J. Blanchard, *Langmuir*, 2007, **23**, 11677–11683.

163 T. Bhatia, P. Husen, J. H. Ipsen, L. A. Bagatolli and A. C. Simonsen, *Biochim. Biophys. Acta - Biomembr.*, 2014, **1838**, 2503–2510.

164 M. Shinitzky and P. Henkart, 1979, pp. 121–147.

165 H. Pace, L. Simonsson Nyström, A. Gunnarsson, E. Eck, C. Monson, S. Geschwindner, A. Snijder and F. Höök, *Anal. Chem.*, 2015, **87**, 9194–9203.

166 S. Svedhem, D. Dahlborg, J. Ekeroth, J. Kelly, F. Höök and J. Gold, *Langmuir*, 2003, **19**, 6730–6736.

167 S. Majd and M. Mayer, *Angew. Chemie*, 2005, **117**, 6855–6858.

168 J. A. Maynard, N. C. Lindquist, J. N. Sutherland, A. Lesuffleur, A. E. Warrington, M. Rodriguez and S.-H. Oh, *Biotechnol. J.*, 2009, **4**, 1542–1558.

169 G. Luo, T. Liu, X. S. Zhao, Y. Huang, C. Huang and W. Cao, *Langmuir*, 2001, **17**, 4074–4080.

170 J. Andersson and I. Köper, *Membranes (Basel).*, 2016, **6**, 30.

171 W. Hao, J. Han, Y. Chu, L. Huang, J. Sun, Y. Zhuang, X. Li, H. Ma, Y. Chen and J. Dai, *Biomaterials*, 2018, **161**, 106–116.

172 M. Merzlyakov, E. Li and K. Hristova, *Biointerphases*, 2008, **3**, FA80-FA84.

173 G. J. Hardy, R. Nayak and S. Zauscher, *Curr. Opin. Colloid Interface Sci.*, 2013, **18**, 448–458.

174 E. T. Castellana and P. S. Cremer, *Surf. Sci. Rep.*, 2006, **61**, 429–444.

175 R. Tero, *Materials (Basel).*, 2012, **5**, 2658–2680.

176 R. P. Richter, R. Bérat and A. R. Brisson, *Langmuir*, 2006, **22**, 3497–3505.

177 R. P. Richter and A. R. Brisson, *Biophys. J.*, 2005, **88**, 3422–3433.

178 W. J. Galush, J. A. Nye and J. T. Groves, *Biophys. J.*, 2008, **95**, 2512–2519.

179   I. Zawisza, A. Lachenwitzer, V. Zamlynny, S. L. Horswell, J. D. Goddard and J. Lipkowski, *Biophys. J.*, 2003, **85**, 4055–4075.

180   K. J. Seu, A. P. Pandey, F. Haque, E. A. Proctor, A. E. Ribbe and J. S. Hovis, *Biophys. J.*, 2007, **92**, 2445–2450.

181   Y. Kurihara, T. Sawazumi and T. Takeuchi, *Analyst*, 2014, **139**, 6016–6021.

182   C. M. A. Brett, S. Kresak, T. Hianik and A. M. Oliveira Brett, *Electroanalysis*, 2003, **15**, 557–565.

183   A. Simon, A. Girard-Egrot, F. Sauter, C. Pudda, N. Picollet D'Hahan, L. Blum, F. Chatelain and A. Fuchs, *J. Colloid Interface Sci.*, 2007, **308**, 337–343.

184   J. Robinson, N. K. Sarangi and T. E. Keyes, *Phys. Chem. Chem. Phys.*, 2023, **25**, 7648–7661.

185   D. M. Klein, S. Rodríguez-Jiménez, M. E. Hoefnagel, A. Pannwitz, A. Prabhakaran, M. A. Siegler, T. E. Keyes, E. Reisner, A. M. Brouwer and S. Bonnet, *Chem. - A Eur. J.*, 2021, **27**, 17203–17212.

186   S. Maher, H. Basit, R. J. Forster and T. E. Keyes, *Bioelectrochemistry*, 2016, **112**, 16–23.

187   H. Basit, V. Gaul, S. Maher, R. J. Forster and T. E. Keyes, *Analyst*, 2015, **140**, 3012–3018.

188   S. Steltenkamp, M. M. Müller, M. Deserno, C. Hennesthal, C. Steinem and A. Janshoff, *Biophys. J.*, 2006, **91**, 217–226.

189   J. M. Crane, V. Kiessling and L. K. Tamm, *Langmuir*, 2005, **21**, 1377–1388.

190   V. Kiessling, S.-T. Yang and L. K. Tamm, 2015, pp. 1–23.

191   F. Heinemann and P. Schwille, *ChemPhysChem*, 2011, **12**, 2568–2571.

192   A. Simon, C. Gounou, S. Tan, L. Tiefenauer, M. Di Berardino and A. R. Brisson, *Biochim. Biophys. Acta - Biomembr.*, 2013, **1828**, 2739–2744.

193   G. B. Berselli, N. K. Sarangi, S. Ramadurai, P. V. Murphy and T. E. Keyes, *ACS Appl. Bio Mater.*, 2019, **2**, 3404–3417.

194   S. Ramadurai, N. K. Sarangi, S. Maher, N. MacConnell, A. M. Bond, D. McDaid, D. Flynn and T. E. Keyes, *Langmuir*, 2019, **35**, 8095–8109.

195   N. K. Sarangi, A. Prabhakaran and T. E. Keyes, *Electroanalysis*, , DOI:10.1002/elan.202060424.

196   J. Robinson, G. B. Berselli, M. G. Ryadnov and T. E. Keyes, *Langmuir*, 2020, **36**, 5454–5465.

197   A. Roy, S. Byrne, N. K. Sarangi, P. V. Murphy and T. E. Keyes, *Front. Mol. Biosci.*, ,

DOI:10.3389/fmolb.2022.1017338.

198   N. K. Sarangi, A. Prabhakaran and T. E. Keyes, *Langmuir*, 2022, **38**, 6411–6424.

199   N. K. Sarangi, M. Shafaq-Zadah, G. B. Berselli, J. Robinson, E. Dransart, A. Di Cicco, D. Lévy, L. Johannes and T. E. Keyes, *J. Phys. Chem. B*, 2022, **126**, 10000–10017.

200   A. Sonnleitner, G. J. Schütz and T. Schmidt, *Biophys. J.*, 1999, **77**, 2638–2642.

201   S. J. Singer and G. L. Nicolson, *Science (80-.).*, 1972, **175**, 720–731.

202   G. L. Nicolson, *Biochim. Biophys. Acta - Biomembr.*, 2014, **1838**, 1451–1466.

203   H. Sunshine and M. L. Iruela-Arispe, *Curr. Opin. Lipidol.*, 2017, **28**, 408–413.

204   M. Chachisvilis, Y.-L. Zhang and J. A. Frangos, *Proc. Natl. Acad. Sci.*, 2006, **103**, 15463–15468.

205   A. Lavi, H. Weitman, R. T. Holmes, K. M. Smith and B. Ehrenberg, *Biophys. J.*, 2002, **82**, 2101–2110.

206   F. Ricchelli, G. Jori, G. Moreno, F. Vinzens and C. Salet, *J. Photochem. Photobiol. B Biol.*, 1990, **6**, 69–77.

207   G. Lindblom and G. Orädd, *Biochim. Biophys. Acta - Biomembr.*, 2009, **1788**, 234–244.

208   W. L. C. Vaz, R. M. Clegg and D. Hallmann, *Biochemistry*, 1985, **24**, 781–786.

209   A. Barba-Bon, M. Nilam and A. Hennig, *ChemBioChem*, 2020, **21**, 886–910.

210   N. Bezlyepkina, R. S. Gracià, P. Shchelokovskyy, R. Lipowsky and R. Dimova, *Biophys. J.*, 2013, **104**, 1456–1464.

211   N. Kahya, D. Scherfeld, K. Bacia, B. Poolman and P. Schwille, *J. Biol. Chem.*, 2003, **278**, 28109–28115.

212   F. S. Ariola, Z. Li, C. Cornejo, R. Bittman and A. A. Heikal, *Biophys. J.*, 2009, **96**, 2696–2708.

213   E. Sezgin, I. Levental, M. Grzybek, G. Schwarzmann, V. Mueller, A. Honigmann, V. N. Belov, C. Eggeling, Ü. Coskun, K. Simons and P. Schwille, *Biochim. Biophys. Acta - Biomembr.*, 2012, **1818**, 1777–1784.

214   X. Woodward and C. V. Kelly, *Chem. Phys. Lipids*, 2020, **233**, 104991.

215   R. Reigada and F. Sagués, *J. R. Soc. Interface*, 2015, **12**, 20150197.

216   G. J. Schütz, H. Schindler and T. Schmidt, *Biophys. J.*, 1997, **73**, 1073–1080.

217   L. Guo, J. Y. Har, J. Sankaran, Y. Hong, B. Kannan and T. Wohland, *ChemPhysChem*, 2008, **9**, 721–728.

218   M.-L. I. E. Harwardt, M. S. Dietz, M. Heilemann and T. Wohland, *Biophys. J.*, 2018,

114, 2432–2443.

219   P. Schwille, J. Korlach and W. W. Webb, *Cytometry*, 1999, **36**, 176–182.

220   C. Leduc, S. Si, J. Gautier, M. Soto-Ribeiro, B. Wehrle-Haller, A. Gautreau, G. Giannone, L. Cognet and B. Lounis, *Nano Lett.*, 2013, **13**, 1489–1494.

221   K. Ritchie and A. Kusumi, 2003, pp. 618–634.

222   H. Shen, L. J. Tauzin, R. Baiyasi, W. Wang, N. Moringo, B. Shuang and C. F. Landes, *Chem. Rev.*, 2017, **117**, 7331–7376.

223   M. J. Saxton and K. Jacobson, *Annu. Rev. Biophys. Biomol. Struct.*, 1997, **26**, 373–399.

224   C. Manzo and M. F. Garcia-Parajo, *Reports Prog. Phys.*, 2015, **78**, 124601.

225   T. K. L. Meyvis, S. C. De Smedt, P. Van Oostveldt and J. Demeester, *Pharm. Res.*, 1999, 16, 1153–1162.

226   A. Carisey, M. Stroud, R. Tsang and C. Ballestrem, 2011, pp. 387–402.

227   E. S. Wu, K. Jacobson and D. Papahadjopoulos, *Biochemistry*, 1977, **16**, 3936–3941.

228   J. Yguerabide, J. A. Schmidt and E. E. Yguerabide, *Biophys. J.*, 1982, **40**, 69–75.

229   J. Ries and P. Schwille, *BioEssays*, 2012, **34**, 361–368.

230   O. Krichevsky and G. Bonnet, *Reports Prog. Phys.*, 2002, **65**, 251–297.

231   E. L. Elson, *Biophys. J.*, 2011, **101**, 2855–2870.

232   P. Kapusta, M. Wahl, A. Benda, M. Hof and J. Enderlein, *J. Fluoresc.*, 2006, **17**, 43–48.

233   P. Kapusta, R. Macháň, A. Benda and M. Hof, *Int. J. Mol. Sci.*, 2012, **13**, 12890–12910.

234   A. Ghosh, N. Karedla, J. C. Thiele, I. Gregor and J. Enderlein, *Methods*, 2018, **140–141**, 32–39.

235   H. Basit, S. G. Lopez and T. E. Keyes, *Methods*, 2014, **68**, 286–299.

236   R. Macháň and M. Hof, *Biochim. Biophys. Acta - Biomembr.*, 2010, **1798**, 1377–1391.

237   J. J. García, L. López-Pingarrón, P. Almeida-Souza, A. Tres, P. Escudero, F. A. García-Gil, D.-X. Tan, R. J. Reiter, J. M. Ramírez and M. Bernal-Pérez, *J. Pineal Res.*, 2014, **56**, 225–237.

238   J. H. Hildebrand and R. H. Lamoreaux, *Proc. Natl. Acad. Sci.*, 1972, **69**, 3428–3431.

239   M. E. Nipper, S. Majd, M. Mayer, J. C.-M. Lee, E. A. Theodorakis and M. A. Haidekker, *Biochim. Biophys. Acta - Biomembr.*, 2008, **1778**, 1148–1153.

240   M. A. Haidekker, T. Ling, M. Anglo, H. Y. Stevens, J. A. Frangos and E. A. Theodorakis, *Chem. Biol.*, 2001, **8**, 123–131.

241   A. B. Clement, G. Gimpl and C. Behl, *Free Radic. Biol. Med.*, 2010, **48**, 1236–1241.

242   D. M. Owen, D. Williamson, C. Rentero and K. Gaus, *Traffic*, 2009, **10**, 962–971.

243   S.-C. Lee, J. Heo, H. C. Woo, J.-A. Lee, Y. H. Seo, C.-L. Lee, S. Kim and O.-P. Kwon, *Chem. - A Eur. J.*, 2018, **24**, 13706–13718.

244   M. A. Haidekker and E. A. Theodorakis, *Org. Biomol. Chem.*, 2007, **5**, 1669–1678.

245   S. Howell, M. Dakanali, E. A. Theodorakis and M. A. Haidekker, *J. Fluoresc.*, 2012, **22**, 457–465.

246   S. H. C. Askes, N. L. Mora, R. Harkes, R. I. Koning, B. Koster, T. Schmidt, A. Kros and S. Bonnet, *Chem. Commun.*, 2015, **51**, 9137–9140.

247   S. H. C. Askes, P. Brodie, G. Bruylants and S. Bonnet, *J. Phys. Chem. B*, 2017, **121**, 780–786.

248   S. H. C. Askes, V. C. Leeuwenburgh, W. Pomp, H. Arjmandi-Tash, S. Tanase, T. Schmidt and S. Bonnet, *ACS Biomater. Sci. Eng.*, 2017, **3**, 322–334.

249   J. Gao, H. Nesbitt, K. Logan, K. Burnett, B. White, I. G. Jack, M. A. Taylor, M. Love, B. Callan, A. P. McHale and J. F. Callan, *Eur. J. Pharm. Biopharm.*, 2020, **157**, 233–240.

250   G. Gregoriadis, *Trends Biotechnol.*, 1995, **13**, 527–537.

251   C. Martin, N. Aibani, J. F. Callan and B. Callan, *Ther. Deliv.*, 2016, **7**, 15–31.

252   H. Nsairat, D. Khater, U. Sayed, F. Odeh, A. Al Bawab and W. Alshaer, *Heliyon*, 2022, **8**, e09394.

253   A. S. Ulrich, *Biosci. Rep.*, 2002, **22**, 129–150.

254   D. . Lasic, *J. Colloid Interface Sci.*, 1990, **140**, 302–304.

255   L. Sercombe, T. Veerati, F. Moheimani, S. Y. Wu, A. K. Sood and S. Hua, *Front. Pharmacol.*, , DOI:10.3389/fphar.2015.00286.

256   D. P. D. Lasic, *Elsevier*.

257   D. . Lasic, *J. Control. Release*, 1997, **48**, 203–222.

258   K. S. Konduri, S. Nandedkar, D. A. Rickaby, N. Düzgüneş and P. R. J. Gangadharam, 2005, pp. 413–427.

259   S. C. de Arajo Lopes, C. dos Santos Giuberti, T. G. Ribeiro, D. dos Santos Ferreira, E. Amaral Leite and M. Cristina, in *Cancer Treatment - Conventional and Innovative Approaches*, InTech, 2013.

260   V. P. Torchilin, F. Zhou and L. Huang, *J. Liposome Res.*, 1993, **3**, 201–255.

261   A.-L. Robson, P. C. Dastoor, J. Flynn, W. Palmer, A. Martin, D. W. Smith, A. Woldu

and S. Hua, *Front. Pharmacol.*, , DOI:10.3389/fphar.2018.00080.

262   H. Hotani, *J. Mol. Biol.*, 1984, **178**, 113–120.

263   W. ALJAMAL and K. KOSTARELOS, *Int. J. Pharm.*, 2007, **331**, 182–185.

264   K. Buyens, S. C. De Smedt, K. Braeckmans, J. Demeester, L. Peeters, L. A. van Grunsven, X. de Mollerat du Jeu, R. Sawant, V. Torchilin, K. Farkasova, M. Ogris and N. N. Sanders, *J. Control. Release*, 2012, **158**, 362–370.

265   M. Çağdaş, A. D. Sezer and S. Bucak, in *Application of Nanotechnology in Drug Delivery*, InTech, 2014.

266   S. Ren, M. Wang, C. Wang, Y. Wang, C. Sun, Z. Zeng, H. Cui and X. Zhao, *Polymers (Basel).*, 2021, **13**, 3307.

267   A. Gonzalez Gomez and Z. Hosseinidoust, *ACS Infect. Dis.*, 2020, **6**, 896–908.

268   R. Cortesi, E. Esposito, A. Maietti, E. Menegatti and C. Nastruzzi, *Int. J. Pharm.*, 1997, **159**, 95–103.

269   D. Needham, *MRS Bull.*, 1999, **24**, 32–41.

270   D. Lombardo, P. Calandra, M. Teresa Caccamo, S. Magazù and M. Alekseyevich Kiselev, *AIMS Mater. Sci.*, 2019, **6**, 200–213.

271   B. Kronberg, A. Dahlman, J. Carlfors, J. Karlsson and P. Artursson, *J. Pharm. Sci.*, 1990, **79**, 667–671.

272   B. Zheng and D. J. McClements, *Molecules*, 2020, **25**, 2791.

273   G. Cevc, *Biochemistry*, 1991, **30**, 7186–7193.

274   R. Xiao, R. Wang, Z. Zeng, Lili Xu and J. Wang, *Int. J. Nanomedicine*, 2012, 4185.

275   T. Nii and F. Ishii, *Int. J. Pharm.*, 2005, **298**, 198–205.

276   I. V. Zhigaltsev, N. Maurer, Q.-F. Akhong, R. Leone, E. Leng, J. Wang, S. C. Semple and P. R. Cullis, *J. Control. Release*, 2005, **104**, 103–111.

277   A. Sharma, *Int. J. Pharm.*, 1997, **154**, 123–140.

278   D. Guimarães, A. Cavaco-Paulo and E. Nogueira, *Int. J. Pharm.*, 2021, **601**, 120571.

279   H. Daraee, A. Etemadi, M. Kouhi, S. Alimirzalu and A. Akbarzadeh, *Artif. Cells, Nanomedicine, Biotechnol.*, 2016, **44**, 381–391.

280   I. Langmuir, *J. Am. Chem. Soc.*, 1917, **39**, 1848–1906.

281   K. B. Blodgett, *J. Am. Chem. Soc.*, 1935, **57**, 1007–1022.

282   O. N. Oliveira, L. Caseli and K. Ariga, *Chem. Rev.*, 2022, **122**, 6459–6513.

283   A.-C. Schöne, T. Roch, B. Schulz and A. Lendlein, *J. R. Soc. Interface*, 2017, **14**, 20161028.

284   J. A. Zasadzinski, R. Viswanathan, L. Madsen, J. Garnaes and D. K. Schwartz, *Science (80-.).*, 1994, **263**, 1726–1733.

285   I. R. Peterson, *J. Phys. D. Appl. Phys.*, 1990, **23**, 379–395.

286   E. Labbé and O. Buriez, *Electrochem. Sci. Adv.*, 2021, **2**, e2100170.

287   P. Sondhi, D. Lingden and K. J. Stine, *Coatings*, 2020, **10**, 981.

288   L. XU, Z.-C. WEI, S. ZENG and Z.-L. HUANG, *J. Innov. Opt. Health Sci.*, 2013, **6**, 1350030.

289   L. M. Hirvonen and K. Suhling, *Meas. Sci. Technol.*, 2017, **28**, 12003.

290   R. R. Duncan, *Biochem. Soc. Trans.*, 2006, **34**, 679–682.

291   R. Datta, T. M. Heaster, J. T. Sharick, A. A. Gillette and M. C. Skala, *J. Biomed. Opt.*, 2020, **25**, 1.

292   D. Magde, E. Elson and W. W. Webb, *Phys. Rev. Lett.*, 1972, **29**, 705–708.

293   R. Rigler, *J. Biotechnol.*, 1995, **41**, 177–186.

294   S. Wennmalm, H. Blom, L. Wallerman and R. Rigler, *Biol. Chem.*, , DOI:10.1515/BC.2001.048.

295   P. Schwille, F. J. Meyer-Almes and R. Rigler, *Biophys. J.*, 1997, **72**, 1878–1886.

296   R. Rigler, �. Mets, J. Widengren and P. Kask, *Eur. Biophys. J.*, , DOI:10.1007/BF00185777.

297   K. Starchev, J. Ricka and J. Buffle, *J. Colloid Interface Sci.*, 2001, **233**, 50–55.

298   T. Otosu and S. Yamaguchi, *Molecules*, 2018, **23**, 2972.

299   X. Xiao, W. Tian, M. Imran, H. Cao and J. Zhao, *Chem. Soc. Rev.*, 2021, **50**, 9686–9714.

300   C. Wohnhaas, V. Mailänder, M. Dröge, M. A. Filatov, D. Busko, Y. Avlasevich, S. Baluschev, T. Miteva, K. Landfester and A. Turshatov, *Macromol. Biosci.*, 2013, **13**, 1422–1430.

301   Q. Dou, L. Jiang, D. Kai, C. Owh and X. J. Loh, *Drug Discov. Today*, 2017, **22**, 1400–1411.

302   D. L. Dexter, *J. Chem. Phys.*, 1953, **21**, 836–850.

303   S. Liu, X. Wang, H. Liu, L. Shen, D. Zhao and X. Li, *J. Mater. Chem. C*, 2020, **8**, 3536–3544.

304   Y. Y. Cheng, T. Khoury, R. G. C. R. Clady, M. J. Y. Tayebjee, N. J. Ekins-Daukes, M. J. Crossley and T. W. Schmidt, *Phys. Chem. Chem. Phys.*, 2010, **12**, 66–71.

305   T. W. Schmidt and F. N. Castellano, *J. Phys. Chem. Lett.*, 2014, **5**, 4062–4072.

306   Q. Chen, Y. Liu, X. Guo, J. Peng, S. Garakyaraghi, C. M. Papa, F. N. Castellano, D. Zhao and Y. Ma, *J. Phys. Chem. A*, 2018, **122**, 6673–6682.

307   B. Pfund, D. M. Steffen, M. R. Schreier, M. S. Bertrams, C. Ye, K. Börjesson, O. S. Wenger and C. Kerzig, *J. Am. Chem. Soc.*, 2020, **142**, 10468–10476.

308   X. Guo, Y. Liu, Q. Chen, D. Zhao and Y. Ma, *Adv. Opt. Mater.*, 2018, **6**, 1700981.

309   J. Zhao, S. Ji and H. Guo, *RSC Adv.*, 2011, **1**, 937–950.

310   K. K. Jha, A. Prabhakaran, C. S. Burke, M. Schulze, U. S. Schubert, T. E. Keyes, M. Jäger and B. D. Ivanšić, *J. Phys. Chem. C*, 2022, **126**, 4057–4066.

311   W. Yin, T. Yu, J. Chen, R. Hu, G. Yang, Y. Zeng and Y. Li, *ACS Appl. Mater. Interfaces*, 2021, **13**, 57481–57488.

312   M. Han, Z. Zhu, M. Ouyang, Y. Liu and X. Shu, *Adv. Funct. Mater.*, 2021, **31**, 1–7.

313   N. Kiseleva, M. A. Filatov, J. C. Fischer, M. Kaiser, M. Jakoby, D. Busko, I. A. Howard, B. S. Richards and A. Turshatov, *Phys. Chem. Chem. Phys.*, 2022, **24**, 3568–3578.

314   D. Lin, J. Zhong, S. Ji, Z. Yuan, L. Xing, Q. He, H. Zhang and Y. Huo, *Dye. Pigment.*, 2021, **185**, 108912.

315   J. T. Ly, K. F. Presley, T. M. Cooper, L. A. Baldwin, M. J. Dalton and T. A. Grusenmeyer, *Phys. Chem. Chem. Phys.*, 2021, **23**, 12033–12044.

316   D. O' Connor, A. Byrne and T. E. Keyes, *RSC Adv.*, 2019, **9**, 22805–22816.

317   H. J. Lv, X. T. Zhang, S. Wang and G. W. Xing, *Analyst*, 2017, **142**, 603–607.

318   L. M. Solanko, A. Honigmann, H. S. Midtiby, F. W. Lund, J. R. Brewer, V. Dekaris, R. Bittman, C. Eggeling and D. Wüstner, *Biophys. J.*, 2013, **105**, 2082–2092.

319   M. V. Gudheti, M. Mlodzianoski and S. T. Hess, *Biophys. J.*, 2007, **93**, 2011–2023.

320   Q. Liu, B. Yin, T. Yang, Y. Yang, Z. Shen, P. Yao and F. Li, *J. Am. Chem. Soc.*, 2013, **135**, 5029–5037.

321   L. Huang, Y. Zhao, H. Zhang, K. Huang, J. Yang and G. Han, *Angew. Chemie*, 2017, **129**, 14592–14596.

322   M. Niu, Y. Lu, L. Hovgaard, P. Guan, Y. Tan, R. Lian, J. Qi and W. Wu, *Eur. J. Pharm. Biopharm.*, 2012, **81**, 265–272.

323   N. Wang, T. Wang, T. Li and Y. Deng, *Colloids Surfaces B Biointerfaces*, 2009, **69**, 232–238.

324   C. Li, Y. Zhang, Y. Wan, J. Wang, J. Lin, Z. Li and P. Huang, *Chinese Chem. Lett.*, 2021, **32**, 1615–1625.

325   C. N. Fries, E. J. Curvino, J.-L. Chen, S. R. Permar, G. G. Fouda and J. H. Collier, *Nat. Nanotechnol.*, 2021, **16**, 1–14.

326   J. W. Park, *Breast Cancer Res.*, 2002, **4**, 95.

327   C. Martin, E. Dolmazon, K. Moylan, C. Fowley, A. P. McHale, J. F. Callan and B. Callan, *Int. J. Pharm.*, 2015, **481**, 1–8.

328   J. A. Jackman, B. K. Yoon, L. Ouyang, N. Wang, A. R. Ferhan, J. Kim, T. Majima and N. Cho, *Adv. Funct. Mater.*, 2021, **31**, 2008352.

329   S. Moghassemi, A. Dadashzadeh, R. B. Azevedo, O. Feron and C. A. Amorim, *J. Control. Release*, 2021, **339**, 75–90.

330   S. Ghosh, K. A. Carter and J. F. Lovell, *Biomaterials*, 2019, **218**, 119341.

331   A. Derycke, *Adv. Drug Deliv. Rev.*, 2004, **56**, 17–30.

332   P. Liu, G. Chen and J. Zhang, *Molecules*, 2022, **27**, 1372.

333   N. Aibani, P. F. da Costa, J. Masterson, N. Marino, F. M. Raymo, J. Callan and B. Callan, *J. Control. Release*, 2017, **264**, 136–144.

334   J. A. Oshiro-Junior, M. R. Sato, F. I. Boni, K. L. M. Santos, K. T. de Oliveira, L. M. de Freitas, C. R. Fontana, D. Nicholas, A. McHale, J. F. Callan and M. Chorilli, *Mater. Sci. Eng. C*, 2020, **108**, 110462.

335   K. M. N. Costa, R. M. Barros, E. O. Jorge, M. R. Sato, M. Chorilli, B. P. G. de Lima Damasceno, D. Nicholas, J. F. Callan and J. A. Oshiro Junior, *J. Nanoparticle Res.*, 2023, **25**, 56.

336   R. A. Arellano Reyes, A. Prabhakaran, R. C. E. Sia, J. Guthmuller, K. K. Ja, T. Yang, B. Dietzek-Ivanšić, V. McKee and T. E. Keyes, *Chem. – A Eur. J.*, , DOI:10.1002/chem.202300239.

337   Y. Murakami and K. Kamada, *Phys. Chem. Chem. Phys.*, 2021, **23**, 18268–18282.

338   M. A. Filatov, *Org. Biomol. Chem.*, 2020, **18**, 10–27.

339   L. Dura, M. Wächtler, S. Kupfer, J. Kübel, J. Ahrens, S. Höfler, M. Bröring, B. Dietzek and T. Beweries, *Inorganics*, 2017, **5**, 21.

340   S. L. Veatch and S. L. Keller, *Phys. Rev. Lett.*, 2005, **94**, 148101.

341   V. Betaneli, R. Worch and P. Schwille, *Chem. Phys. Lipids*, 2012, **165**, 630–637.

342   H.-J. Kaiser, D. Lingwood, I. Levental, J. L. Sampaio, L. Kalvodova, L. Rajendran and K. Simons, *Proc. Natl. Acad. Sci.*, 2009, **106**, 16645–16650.

343   Q. Zhou, M. Zhou, Y. Wei, X. Zhou, S. Liu, S. Zhang and B. Zhang, *Phys. Chem. Chem.*

Phys., 2017, **19**, 1516–1525.

344 M. Nakashima, K. Iizuka, M. Karasawa, K. Ishii and Y. Kubo, *J. Mater. Chem. C*, 2018, **6**, 6208–6215.

345 J. T. Ly, K. F. Presley, T. M. Cooper, L. A. Baldwin, M. J. Dalton and T. A. Grusenmeyer, *Phys. Chem. Chem. Phys.*, 2021, **23**, 12033–12044.

346 A. Haefele, J. Blumhoff, R. S. Khnayzer and F. N. Castellano, *J. Phys. Chem. Lett.*, 2012, **3**, 299–303.

347 J. E. Auckett, Y. Y. Chen, T. Khoury, R. G. C. R. Clady, N. J. Ekins-Daukes, M. J. Crossley and T. W. Schmidt, *J. Phys. Conf. Ser.*, 2009, **185**, 12002.

348 A. Monguzzi, J. Mezyk, F. Scotognella, R. Tubino and F. Meinardi, *Phys. Rev. B*, 2008, **78**, 195112.

349 J. T. Buck, A. M. Boudreau, A. DeCarmine, R. W. Wilson, J. Hampsey and T. Mani, *Chem*, 2019, **5**, 138–155.

350 Z. Zhu, X. Zhang, X. Guo, Q. Wu, Z. Li, C. Yu, E. Hao, L. Jiao and J. Zhao, *Chem. Sci.*, 2021, **12**, 14944–14951.

351 S. Wu, F. Zhong, J. Zhao, S. Guo, W. Yang and T. Fyles, *J. Phys. Chem. A*, 2015, **119**, 4787–4799.

352 J. Ma, X. Yuan, B. Küçüköz, S. Li, C. Zhang, P. Majumdar, A. Karatay, X. Li, H. Gul Yaglioglu, A. Elmali, J. Zhao and M. Hayvali, *J. Mater. Chem. C*, 2014, **2**, 3900–3913.

353 V.-N. Nguyen, Y. Yan, J. Zhao and J. Yoon, *Acc. Chem. Res.*, 2021, **54**, 207–220.

354 Y. Dong, B. Dick and J. Zhao, *Org. Lett.*, 2020, **22**, 5535–5539.

355 G. B. Berselli, N. K. Sarangi, A. V. Gimenez, P. V. Murphy and T. E. Keyes, *Chem. Commun.*, 2020, **56**, 11251–11254.

356 S. Ramadurai, M. Werner, N. K. H. Slater, A. Martin, V. A. Baulin and T. E. Keyes, *Soft Matter*, 2017, **13**, 3690–3700.

357 S. Ramadurai, A. Kohut, N. K. Sarangi, O. Zholobko, V. A. Baulin, A. Voronov and T. E. Keyes, *J. Colloid Interface Sci.*, 2019, **542**, 483–494.

358 S. S. NA Kshirsagar, SK Pandya, BG Kirodian, *J. Postgrad. Med.*, 2005, **51**, 5–15.

359 S. Zununi Vahed, R. Salehi, S. Davaran and S. Sharifi, *Mater. Sci. Eng. C*, 2017, **71**, 1327–1341.

360 L. A. Bagatolli and E. Gratton, *Biophys. J.*, 2000, **78**, 290–305.

361 T. Baumgart, A. T. Hammond, P. Sengupta, S. T. Hess, D. A. Holowka, B. A. Baird and W. W. Webb, *Proc. Natl. Acad. Sci.*, 2007, **104**, 3165–3170.

362 A. Moscho, O. Orwar, D. T. Chiu, B. P. Modi and R. N. Zare, *Proc. Natl. Acad. Sci.*,

1996, **93**, 11443–11447.

363   D. Hirsch-Lerner and Y. Barenholz, *Biochim. Biophys. Acta - Biomembr.*, 1998, **1370**, 17–30.

364   B. P. Gaber and J. P. Sheridan, *Biochim. Biophys. Acta - Biomembr.*, 1982, **685**, 87–93.

365   J. Hernandez-Borrell and K. M. W. Keough, *Biochim. Biophys. Acta - Biomembr.*, 1993, **1153**, 277–282.

366   T. Katsu and K. Nakashima, *Analyst*, 1999, **124**, 883–886.

367   T. Yasuda, N. Matsumori, H. Tsuchikawa, M. Lönnfors, T. K. M. Nyholm, J. P. Slotte and M. Murata, *Langmuir*, 2015, **31**, 13783–13792.

368   M. E. Haque, T. J. McIntosh and B. R. Lentz, *Biochemistry*, 2001, **40**, 4340–4348.

369   V. Gaul, S. G. Lopez, B. R. Lentz, N. Moran, R. J. Forster and T. E. Keyes, *Integr. Biol.*, 2015, **7**, 402–411.

370   Y. Kita, H. Shindou and T. Shimizu, *Biochim. Biophys. Acta - Mol. Cell Biol. Lipids*, 2019, **1864**, 838–845.

371   R. H. Schaloske and E. A. Dennis, *Biochim. Biophys. Acta - Mol. Cell Biol. Lipids*, 2006, **1761**, 1246–1259.

372   J. E. Burke and E. A. Dennis, *J. Lipid Res.*, 2009, **50**, S237–S242.

373   M. Menschikowski, A. Hagelgans, B. Nacke, C. Jandeck, O. A. Mareninova, L. Asatryan and G. Siegert, *Tumor Biol.*, 2016, **37**, 8097–8105.

374   X. Wang, C.-J. Huang, G.-Z. Yu, J.-J. Wang, R. Wang, Y.-M. Li and Q. Wu, *Hum. Pathol.*, 2013, **44**, 2020–2027.

375   T. MIRTTI, V. J. O. LAINE, H. HIEKKANEN, S. HURME, O. ROWE, T. J. NEVALAINEN, M. KALLAJOKI and K. ALANEN, *APMIS*, 2009, **117**, 151–161.

376   N. D. Quach, R. D. Arnold and B. S. Cummings, *Biochem. Pharmacol.*, 2014, **90**, 338–348.

377   R. Verger, M. C. E. Mieras and G. H. De Haas, *J. Biol. Chem.*, 1973, **248**, 4023–4034.

378   M. Grandbois, H. Clausen-schaumann and H. Gaub, *Biophys. J.*, 1998, **74**, 2398–2404.

379   Y. Jin, F. Yang and L. Du, *Colloids Surfaces B Biointerfaces*, 2013, **112**, 421–428.

380   M. J. Barnes, C.-M. Li, Y. Xu, J. An, Y. Huang and J. G. Cyster, *J. Exp. Med.*, 2015, **212**, 1011–1020.

381   D. P. Cherney, G. A. Myers, R. A. Horton and J. M. Harris, *Anal. Chem.*, 2006, **78**, 6928–6935.

382   J. Li, Z. Chen, X. Wang, G. Brezesinski and H. Möhwald, *Angew. Chemie*, 2000, **39**,

1996, **93**, 11443–11447.

363   D. Hirsch-Lerner and Y. Barenholz, *Biochim. Biophys. Acta - Biomembr.*, 1998, **1370**, 17–30.

364   B. P. Gaber and J. P. Sheridan, *Biochim. Biophys. Acta - Biomembr.*, 1982, **685**, 87–93.

365   J. Hernandez-Borrell and K. M. W. Keough, *Biochim. Biophys. Acta - Biomembr.*, 1993, **1153**, 277–282.

366   T. Katsu and K. Nakashima, *Analyst*, 1999, **124**, 883–886.

367   T. Yasuda, N. Matsumori, H. Tsuchikawa, M. Lönnfors, T. K. M. Nyholm, J. P. Slotte and M. Murata, *Langmuir*, 2015, **31**, 13783–13792.

368   M. E. Haque, T. J. McIntosh and B. R. Lentz, *Biochemistry*, 2001, **40**, 4340–4348.

369   V. Gaul, S. G. Lopez, B. R. Lentz, N. Moran, R. J. Forster and T. E. Keyes, *Integr. Biol.*, 2015, **7**, 402–411.

370   Y. Kita, H. Shindou and T. Shimizu, *Biochim. Biophys. Acta - Mol. Cell Biol. Lipids*, 2019, **1864**, 838–845.

371   R. H. Schaloske and E. A. Dennis, *Biochim. Biophys. Acta - Mol. Cell Biol. Lipids*, 2006, **1761**, 1246–1259.

372   J. E. Burke and E. A. Dennis, *J. Lipid Res.*, 2009, **50**, S237–S242.

373   M. Menschikowski, A. Hagelgans, B. Nacke, C. Jandeck, O. A. Mareninova, L. Asatryan and G. Siegert, *Tumor Biol.*, 2016, **37**, 8097–8105.

374   X. Wang, C.-J. Huang, G.-Z. Yu, J.-J. Wang, R. Wang, Y.-M. Li and Q. Wu, *Hum. Pathol.*, 2013, **44**, 2020–2027.

375   T. MIRTTI, V. J. O. LAINE, H. HIEKKANEN, S. HURME, O. ROWE, T. J. NEVALAINEN, M. KALLAJOKI and K. ALANEN, *APMIS*, 2009, **117**, 151–161.

376   N. D. Quach, R. D. Arnold and B. S. Cummings, *Biochem. Pharmacol.*, 2014, **90**, 338–348.

377   R. Verger, M. C. E. Mieras and G. H. De Haas, *J. Biol. Chem.*, 1973, **248**, 4023–4034.

378   M. Grandbois, H. Clausen-schaumann and H. Gaub, *Biophys. J.*, 1998, **74**, 2398–2404.

379   Y. Jin, F. Yang and L. Du, *Colloids Surfaces B Biointerfaces*, 2013, **112**, 421–428.

380   M. J. Barnes, C.-M. Li, Y. Xu, J. An, Y. Huang and J. G. Cyster, *J. Exp. Med.*, 2015, **212**, 1011–1020.

381   D. P. Cherney, G. A. Myers, R. A. Horton and J. M. Harris, *Anal. Chem.*, 2006, **78**, 6928–6935.

382   J. Li, Z. Chen, X. Wang, G. Brezesinski and H. Möhwald, *Angew. Chemie*, 2000, **39**,

3059–3062.

383   S. Yokoyama and F. J. Kézdy, *J. Biol. Chem.*, 1991, **266**, 4303–4308.

384   K. M. Maloney, M. Grandbois, D. W. Grainger, C. Salesse, K. A. Lewis and M. F. Roberts, *Biochim. Biophys. Acta - Biomembr.*, 1995, **1235**, 395–405.

385   W. Schulte, M. Orlof, I. Brand, B. Korchowiec and E. Rogalska, *Colloids Surfaces B Biointerfaces*, 2014, **116**, 389–395.

386   H. P. Vacklin, F. Tiberg, G. Fragneto and R. K. Thomas, *Biochemistry*, 2005, **44**, 2811–2821.

387   Y. Tong, N. Li, H. Liu, A. Ge, M. Osawa and S. Ye, *Angew. Chemie Int. Ed.*, 2010, **49**, 2319–2323.

388   S. Kai, X. Li, B. Li, X. Han and X. Lu, *Phys. Chem. Chem. Phys.*, 2018, **20**, 63–67.

389   L. K. Nielsen, J. Risbo, T. H. Callisen and T. Bjørnholm, *Biochim. Biophys. Acta - Biomembr.*, 1999, **1420**, 266–271.

390   L. K. Nielsen, K. Balashev, T. H. Callisen and T. Bjørnholm, *Biophys. J.*, 2002, **83**, 2617–2624.

391   P. Høyrup, O. G. Mouritsen and K. Jørgensen, *Biochim. Biophys. Acta - Biomembr.*, 2001, **1515**, 133–143.

392   S. Ramadurai, A. Holt, V. Krasnikov, G. van den Bogaart, J. A. Killian and B. Poolman, *J. Am. Chem. Soc.*, 2009, **131**, 12650–12656.

393   M. Poznik, U. Faltermeier, B. Dick and B. König, *RSC Adv.*, 2016, **6**, 41947–41950.

394   T. Andresen, S. Jensen, T. Kaasgaard and K. Jorgensen, *Curr. Drug Deliv.*, 2005, **2**, 353–362.

395   T. L. Andresen, J. Davidsen, M. Begtrup, O. G. Mouritsen and K. Jørgensen, *J. Med. Chem.*, 2004, **47**, 1694–1703.

396   H. Alrbyawi, I. Poudel, M. Annaji, R. D. Arnold, A. K. Tiwari and R. J. Babu, *Pharm. Nanotechnol.*, 2022, **10**, 3–23.

397   H. Kapalatiya, Y. Madav, V. S. Tambe and S. Wairkar, *Drug Deliv. Transl. Res.*, 2022, **12**, 1293–1305.

398   A. S. Alekseeva, P. E. Volynsky, N. A. Krylov, V. P. Chernikov, E. L. Vodovozova and I. A. Boldyrev, *Biochim. Biophys. Acta - Biomembr.*, 2021, **1863**, 183481.

399   R. M. Kramer and J. D. Sharp, *FEBS Lett.*, 1997, **410**, 49–53.

400   A. Dessen, J. Tang, H. Schmidt, M. Stahl, J. D. Clark, J. Seehra and W. S. Somers, *Cell*, 1999, **97**, 349–360.

401   I. Kudo and M. Murakami, *Prostaglandins Other Lipid Mediat.*, 2002, **68–69**, 3–58.

402 E. A. Dennis, J. Cao, Y.-H. Hsu, V. Magrioti and G. Kokotos, *Chem. Rev.*, 2011, **111**, 6130–6185.

403 G. Wiegand, N. Arribas-Layton, H. Hillebrandt, E. Sackmann and P. Wagner, *J. Phys. Chem. B*, 2002, **106**, 4245–4254.

404 F. Abbasi, J. J. Leitch, Z. Su, G. Szymanski and J. Lipkowski, *Electrochim. Acta*, 2018, **267**, 195–205.

405 M. S. Khan, N. S. Dosoky, B. K. Berdiev and J. D. Williams, *Eur. Biophys. J.*, 2016, **45**, 843–852.

406 P. C. Gufler, D. Pum, U. B. Sleytr and B. Schuster, *Biochim. Biophys. Acta - Biomembr.*, 2004, **1661**, 154–165.

407 A. Więckowska, E. Jabłonowska, E. Rogalska and R. Bilewicz, *Phys. Chem. Chem. Phys.*, 2011, **13**, 9716.

408 R. V. Stahelin and W. Cho, *Biochemistry*, 2001, **40**, 4672–4678.

409 J. Shum, P. K.-K. Leung and K. K.-W. Lo, *Inorg. Chem.*, 2019, **58**, 2231–2247.

410 V. W.-W. Yam and K. M.-C. Wong, *Chem. Commun.*, 2011, **47**, 11579.

411 V. Fernández-Moreira, F. L. Thorp-Greenwood and M. P. Coogan, *Chem. Commun.*, 2010, **46**, 186–202.

412 E. Baggaley, J. A. Weinstein and J. A. G. Williams, *Coord. Chem. Rev.*, 2012, **256**, 1762–1785.

413 D.-L. Ma, H.-Z. He, K.-H. Leung, D. S.-H. Chan and C.-H. Leung, *Angew. Chemie Int. Ed.*, 2013, **52**, 7666–7682.

414 A. Li, C. Turro and J. J. Kodanko, *Acc. Chem. Res.*, 2018, **51**, 1415–1421.

415 P. LAINE, S. CAMPAGNA and F. LOISEAU, *Coord. Chem. Rev.*, 2008, **252**, 2552–2571.

416 N. Soliman, G. Gasser and C. M. Thomas, *Adv. Mater.*, 2020, **32**, 2003294.

417 M. R. Gill and J. A. Thomas, *Chem. Soc. Rev.*, 2012, **41**, 3179.

418 F. E. Poynton, S. A. Bright, S. Blasco, D. C. Williams, J. M. Kelly and T. Gunnlaugsson, *Chem. Soc. Rev.*, 2017, **46**, 7706–7756.

419 A. M.-H. Yip and K. K.-W. Lo, *Coord. Chem. Rev.*, 2018, **361**, 138–163.

420 M. Mital and Z. Ziora, *Coord. Chem. Rev.*, 2018, **375**, 434–458.

421 B.-Z. Zhu, X.-J. Chao, C.-H. Huang and Y. Li, *Chem. Sci.*, 2016, **7**, 4016–4023.

422 W. Wu, S. Ji, W. Wu, J. Shao, H. Guo, T. D. James and J. Zhao, *Chem. – A Eur. J.*, 2012, **18**, 4953–4964.

423   A. Cannizzo, F. van Mourik, W. Gawelda, G. Zgrablic, C. Bressler and M. Chergui, *Angew. Chemie Int. Ed.*, 2006, **45**, 3174–3176.

424   A. C. Bhasikuttan, M. Suzuki, S. Nakashima and T. Okada, *J. Am. Chem. Soc.*, 2002, **124**, 8398–8405.

425   D. Escudero, B. Happ, A. Winter, M. D. Hager, U. S. Schubert and L. González, *Chem. - An Asian J.*, 2012, **7**, 667–671.

426   R. R. Islangulov, D. V Kozlov and F. N. Castellano, 2005, **1**, 3776–3778.

427   S. Ji, W. Wu, W. Wu, H. Guo and J. Zhao, *Angew. Chemie Int. Ed.*, 2011, **50**, 1626–1629.

428   W. Wu, J. Sun, X. Cui and J. Zhao, *J. Mater. Chem. C*, 2013, **1**, 4577.

429   J. Zhou, Q. Liu, W. Feng, Y. Sun and F. Li, .

430   S. Bonnet, *Dalt. Trans.*, 2018, **47**, 10330–10343.

431   J. Shen, H.-C. Kim, J. Wolfram, C. Mu, W. Zhang, H. Liu, Y. Xie, J. Mai, H. Zhang, Z. Li, M. Guevara, Z.-W. Mao and H. Shen, *Nano Lett.*, 2017, **17**, 2913–2920.

432   L. Zhu, Z. Kuang, P. Song, W. Li, L. Gui, K. Yang, F. Ge, Y. Tao and W. Zhang, *Nanotechnology*, 2021, **32**, 455103.

433   M. Abrahamsson, H.-C. Becker and L. Hammarström, *Dalt. Trans.*, 2017, **46**, 13314–13321.

434   E. A. Medlycott and G. S. Hanan, *Chem. Soc. Rev.*, 2005, **34**, 133.

435   E. A. Medlycott and G. S. Hanan, *Coord. Chem. Rev.*, 2006, **250**, 1763–1782.

436   L. Hammarström and O. Johansson, *Coord. Chem. Rev.*, 2010, **254**, 2546–2559.

437   V. Gray, D. Dzebo, A. Lundin, J. Alborzpour, M. Abrahamsson, B. Albinsson and K. Moth-Poulsen, *J. Mater. Chem. C*, 2015, **3**, 11111–11121.

438   N. Yanai, K. Suzuki, T. Ogawa, Y. Sasaki, N. Harada and N. Kimizuka, *J. Phys. Chem. A*, 2019, **123**, 10197–10203.

439   M. Abrahamsson, M. Jäger, T. Österman, L. Eriksson, P. Persson, H.-C. Becker, O. Johansson and L. Hammarström, *J. Am. Chem. Soc.*, 2006, **128**, 12616–12617.

440   P. C. Boutin, K. P. Ghiggino, T. L. Kelly and R. P. Steer, *J. Phys. Chem. Lett.*, 2013, **4**, 4113–4118.

441   M. Abrahamsson, M. Jäger, R. J. Kumar, T. Österman, P. Persson, H.-C. Becker, O. Johansson and L. Hammarström, *J. Am. Chem. Soc.*, 2008, **130**, 15533–15542.

442   J. Kübel, R. Schroot, M. Wächtler, U. S. Schubert, B. Dietzek and M. Jäger, *J. Phys. Chem. C*, 2015, **119**, 4742–4751.

443   A. K. Pal, N. Zaccheroni, S. Campagna and G. S. Hanan, *Chem. Commun.*, 2014, **50**, 6846.

444   A. T. Vu, D. A. Santos, J. G. Hale and R. N. Garner, *Inorganica Chim. Acta*, 2016, **450**, 23–29.

445   C. A. Heller, R. A. Henry, B. A. McLaughlin and D. E. Bliss, *J. Chem. Eng. Data*, 1974, **19**, 214–219.

446   K. J. Morris, M. S. Roach, W. Xu, J. N. Demas and B. A. DeGraff, *Anal. Chem.*, 2007, **79**, 9310–9314.

447   K. Maruszewski, D. P. Strommen and J. R. Kincaid, *J. Am. Chem. Soc.*, 1993, **115**, 8345–8350.

448   X. Zhao, Y. Hou, L. Liu and J. Zhao, *Energy & Fuels*, 2021, **35**, 18942–18956.

449   M. A. Argüello Cordero, P. J. Boden, M. Rentschler, P. Di Martino-Fumo, W. Frey, Y. Yang, M. Gerhards, M. Karnahl, S. Lochbrunner and S. Tschierlei, *Inorg. Chem.*, 2022, **61**, 214–226.

450   X. Zhang, Y. Hou, X. Xiao, X. Chen, M. Hu, X. Geng, Z. Wang and J. Zhao, *Coord. Chem. Rev.*, 2020, **417**, 213371.

451   A. Haefele, J. Blumhoff, R. S. Khnayzer and F. N. Castellano, *J. Phys. Chem. Lett.*, 2012, **3**, 299–303.

452   R. Vadrucci, C. Weder and Y. C. Simon, *Mater. Horizons*, 2015, **2**, 120–124.

453   Z. Liang, X. Yan, H. Cui, H. Xie, H. Li, D. Yan, C. Ye, X. Wang and X. Tao, *ChemistrySelect*, , DOI:10.1002/slct.202103851.

454   M. H. Gehlen, *J. Photochem. Photobiol. C Photochem. Rev.*, 2020, **42**, 100338.

455   H. M. Suresh Kumar, R. S. Kunabenchi, J. S. Biradar, N. N. Math, J. S. Kadadevarmath and S. R. Inamdar, *J. Lumin.*, 2006, **116**, 35–42.

456   H. S. Geethanjali, D. Nagaraja and R. M. Melavanki, *J. Mol. Liq.*, 2015, **209**, 669–675.

457   J. R. Lakowicz, in *Principles of Fluorescence Spectroscopy*, Springer US, Boston, MA, 1983, pp. 257–301.

458   H. S. Geethanjali, D. Nagaraja, R. M. Melavanki and R. A. Kusanur, *J. Lumin.*, 2015, **167**, 216–221.

459   S. Raišys, K. Kazlauskas, S. Juršėnas and Y. C. Simon, *ACS Appl. Mater. Interfaces*, 2016, **8**, 15732–15740.

460   S. Ji, W. Wu, J. Zhao, H. Guo and W. Wu, *Eur. J. Inorg. Chem.*, 2012, **2012**, 3183–3190.

461   Y. Y. Cheng, B. Fückel, T. Khoury, R. G. C. R. Clady, N. J. Ekins-Daukes, M. J.

Crossley and T. W. Schmidt, *J. Phys. Chem. A*, 2011, **115**, 1047–1053.

462   D. Dzebo, K. Börjesson, V. Gray, K. Moth-Poulsen and B. Albinsson, *J. Phys. Chem. C*, 2016, **120**, 23397–23406.

463   G. Heinrich, S. Schoof and H. Gusten, *J. Photochem.*, 1974, **3**, 315–320.

464   M. S. Workentin, L. J. Johnston, D. D. M. Wayner and V. D. Parker, *J. Am. Chem. Soc.*, 1994, **116**, 8279–8287.

465   S. Chiantia, P. Schwille, A. S. Klymchenko and E. London, *Biophys. J.*, 2011, **100**, L1–L3.

466   H. Li, T. Zhao and Z. Sun, *Rev. Anal. Chem.*, , DOI:10.1515/revac-2017-0012.

467   M. Jezek and M. R. Blatt, *Plant Physiol.*, 2017, **174**, 487–519.

468   M. Wang and W. Zhan, *Acc. Chem. Res.*, 2016, **49**, 2551–2559.

469   M. Orsi, W. E. Sanderson and J. W. Essex, *J. Phys. Chem. B*, 2009, **113**, 12019–12029.

470   N. J. Yang and M. J. Hinner, 2015, pp. 29–53.

471   C. Bourgaux and P. Couvreur, *J. Control. Release*, 2014, **190**, 127–138.

472   M. Khan, N. Dosoky and J. Williams, *Int. J. Mol. Sci.*, 2013, **14**, 21561–21597.

473   H. Basit, A. Van der Heyden, C. Gondran, B. Nysten, P. Dumy and P. Labbé, *Langmuir*, 2011, **27**, 14317–14328.

474   L. Zhang and S. Granick, *J. Chem. Phys.*, 2005, **123**, 211104.

475   C. Peetla, A. Stine and V. Labhasetwar, *Mol. Pharm.*, 2009, **6**, 1264–1276.

476   A. M. Seddon, D. Casey, R. V. Law, A. Gee, R. H. Templer and O. Ces, *Chem. Soc. Rev.*, 2009, **38**, 2509.

477   L. M. Lichtenberger, Z.-M. Wang, J. J. Romero, C. Ulloa, J. C. Perez, M.-N. Giraud and J. C. Barreto, *Nat. Med.*, 1995, **1**, 154–158.

478   L. Redondo-Morata, R. Lea Sanford, O. S. Andersen and S. Scheuring, *Biophys. J.*, 2016, **111**, 363–372.

479   L. M. Lichtenberger, Y. Zhou, V. Jayaraman, J. R. Doyen, R. G. O'Neil, E. J. Dial, D. E. Volk, D. G. Gorenstein, M. B. Boggara and R. Krishnamoorti, *Biochim. Biophys. Acta - Mol. Cell Biol. Lipids*, 2012, **1821**, 994–1002.

480   M. Darvas, P. N. M. Hoang, S. Picaud, M. Sega and P. Jedlovszky, *Phys. Chem. Chem. Phys.*, 2012, **14**, 12956.

481   G. L. L. Patrick, *OUP Oxford*.

482   T. Yamamoto, Y. Umegawa, H. Tsuchikawa, N. Matsumori, S. Hanashima, M. Murata,

R. Haser, B. J. Rawlings and P. Caffrey, *Bioorg. Med. Chem.*, 2015, **23**, 5782–5788.

483   D. M. Kamiński, D. Pociecha, E. Górecka and M. Gagoś, *J. Mol. Struct.*, 2015, **1082**, 7–11.

484   L. Becucci, M. Innocenti, E. Salvietti, A. Rindi, I. Pasquini, M. Vassalli, M. L. Foresti and R. Guidelli, *Electrochim. Acta*, 2008, **53**, 6372–6379.

485   L. Rose and A. T. A. Jenkins, *Bioelectrochemistry*, 2007, **70**, 387–393.

486   S. Lacour, A. Hammann, S. Grazide, D. Lagadic-Gossmann, A. Athias, O. Sergent, G. Laurent, P. Gambert, E. Solary and M.-T. Dimanche-Boitrel, *Cancer Res.*, 2004, **64**, 3593–3598.

487   C. Nunes, G. Brezesinski, D. Lopes, J. L. F. C. Lima, S. Reis and M. Lúcio, *J. Phys. Chem. B*, 2011, **115**, 12615–12623.

488   A. Rebillard, X. Tekpli, O. Meurette, O. Sergent, G. LeMoigne-Muller, L. Vernhet, M. Gorria, M. Chevanne, M. Christmann, B. Kaina, L. Counillon, E. Gulbins, D. Lagadic-Gossmann and M.-T. Dimanche-Boitrel, *Cancer Res.*, 2007, **67**, 7865–7874.

489   C. L. Armstrong, E. Sandqvist and M. C. Rheinstadter, *Protein Pept. Lett.*, 2011, **18**, 344–353.

490   P. B. Mitchell, *Br. J. Clin. Pharmacol.*, 2001, **52**, 45–54.

491   M. V. Rudorfer and W. Z. Potter, *Cell. Mol. Neurobiol.*, 1999, **19**, 373–409.

492   M. P. Kurpius and B. Alexander, *Pharmacotherapy*, 2006, **26**, 505–510.

493   P. Perry, *J. Affect. Disord.*, 1996, **39**, 1–6.

494   R. G. Robinson, *Biol. Psychiatry*, 2003, **54**, 376–387.

495   S. Silberstein and P. Goadsby, *Cephalalgia*, 2002, **22**, 491–512.

496   M. Namaka, C. R. Gramlich, D. Ruhlen, M. Melanson, I. Sutton and J. Major, *Clin. Ther.*, 2004, **26**, 951–979.

497   P. G. O'Malley, E. Balden, G. Tomkins, J. Santoro, K. Kroenke and J. L. Jackson, *J. Gen. Intern. Med.*, 2000, **15**, 659–666.

498   J. Slatkoff and B. Greenfield, *Expert Opin. Investig. Drugs*, 2006, **15**, 649–667.

499   N. R. Johnson, A. C.-J. Wang, C. Coughlan, S. Sillau, E. Lucero, L. Viltz, N. Markham, C. Allen, A. R. Dhanasekaran, H. J. Chial and H. Potter, *Alzheimers. Res. Ther.*, 2022, **14**, 88.

500   E. Tanaka and S. Hisawa, *J. Clin. Pharm. Ther.*, 1999, **24**, 7–16.

501   P. K. Gillman, *Br. J. Pharmacol.*, 2007, **151**, 737–748.

502   S. Albouz, B. Tocqué, J. J. Hauw, J. M. Boutry, F. Le Saux, R. Bourdon and N.

Baumann, *Life Sci.*, 1982, **31**, 2549–2554.

503   K. Y. Hostetler and Y. Matsuzawa, *Biochem. Pharmacol.*, 1981, **30**, 1121–1126.

504   I. Scuntaro, U. Kientsch, U. N. Wiesmann and U. E. Honegger, *Br. J. Pharmacol.*, 1996, **119**, 829–834.

505   B. Breiden and K. Sandhoff, *Biol. Chem.*, 2019, **401**, 31–46.

506   S. Mukherjee, B. Mukherjee, R. Mukhopadhyay, K. Naskar, S. Sundar, J. C. Dujardin, A. K. Das and S. Roy, *PLoS Negl. Trop. Dis.*, 2012, **6**, e1987.

507   V. V. Andrade-Neto, T. M. Pereira, M. do Canto-Cavalheiro and E. C. Torres-Santos, *Parasit. Vectors*, 2016, **9**, 183.

508   R. Kapoor, T. A. Peyear, R. E. Koeppe and O. S. Andersen, *J. Gen. Physiol.*, 2019, **151**, 342–356.

509   A. Walewska, M. Krajewska, A. Stefanowska, A. Buta, R. Bilewicz, P. Krysiński, P. Bednarczyk, P. Koprowski and A. Szewczyk, *Int. J. Mol. Sci.*, 2022, **23**, 1210.

510   B. R. Cater, D. Chapman, S. M. Hawes and J. Saville, *Biochim. Biophys. Acta - Biomembr.*, 1974, **363**, 54–69.

511   S. J. Fisar Z., Krulik R., Fuksova K., *Gen Physiol Biophys.*, 1996, **15**, 51–64.

512   M. A. Yorek, *CRC Press*.

513   C. B. Fox and J. M. Harris, *J. Raman Spectrosc.*, 2010, **41**, 498–507.

514   M. Lucio, J. L. F. C. Lima and S. Reis, *Curr. Med. Chem.*, 2010, **17**, 1795–1809.

515   J. K. Seydel and M. Wiese, Eds., *Drug-Membrane Interactions*, Wiley, 2002, vol. 15.

516   J. S. Santos, D.-K. Lee and A. Ramamoorthy, *Magn. Reson. Chem.*, 2004, **42**, 105–114.

517   Z. Fisar, *Gen Physiol Biophys.*, 2005, **24**, 161–80.

518   D. Yonar, D. D. Paktaş, N. Horasan, J. Strancar, M. Šentjurc and M. M. Sünnetçioğlu, *J. Liposome Res.*, 2011, **21**, 194–202.

519   H. Osanai, T. Ikehara, S. Miyauchi, K. Shimono, J. Tamogami, T. Nara and N. Kamo, *J. Biophys. Chem.*, 2013, **4**, 11–21.

520   R. Ehsanian, C. Van Waes and S. M. Feller, *Cell Commun. Signal.*, 2011, **9**, 13.

521   T. Herraiz, H. Guillén, D. González-Peña and V. J. Arán, *Sci. Rep.*, 2019, **9**, 15398.

522   S. Kumar, M. Guha, V. Choubey, P. Maity and U. Bandyopadhyay, *Life Sci.*, 2007, **80**, 813–828.

523   E. Kalogera, D. Roy, A. Khurana, S. Mondal, A. L. Weaver, X. He, S. C. Dowdy and V. Shridhar, *Gynecol. Oncol.*, 2017, **146**, 187–195.

524 D. B. Oien, C. L. Pathoulas, U. Ray, P. Thirusangu, E. Kalogera and V. Shridhar, *Semin. Cancer Biol.*, 2021, **68**, 21–30.

525 R. Preet, P. Mohapatra, S. Mohanty, S. K. Sahu, T. Choudhuri, M. D. Wyatt and C. N. Kundu, *Int. J. Cancer*, 2012, **130**, 1660–1670.

526 N. Nagano, Y. Imaizumi and M. Watanabe, *Jpn. J. Pharmacol.*, 1996, **71**, 51–60.

527 M. Inaba, E. Maruyama, *Cancer Res.*, 1988, **48**, 2064–7.

528 U. Pindur, M. Jansen and T. Lemster, *Curr. Med. Chem.*, 2005, **12**, 2805–2847.

529 B. Vaidya, N. S. Kulkarni, S. K. Shukla, V. Parvathaneni, G. Chauhan, J. K. Damon, A. Sarode, J. V. Garcia, N. Kunda, S. Mitragotri and V. Gupta, *Int. J. Pharm.*, 2020, **577**, 118995.

530 K. C. Hwang and D. Mauzerall, *Nature*, 1993, **361**, 138–140.

531 W. E. Ford, J. W. Otvos and M. Calvin, *Proc. Natl. Acad. Sci.*, 1979, **76**, 3590–3593.

532 W. Zhan and K. Jiang, *Langmuir*, 2008, **24**, 13258–13261.

533 K. Jiang, H. Xie and W. Zhan, *Langmuir*, 2009, **25**, 11129–11136.

534 M. Ø. Pedersen, J. Linnanto, N.-U. Frigaard, N. C. Nielsen and M. Miller, *Photosynth. Res.*, 2010, **104**, 233–243.

535 R. E. Blankenship, *Molecular Mechanisms of Photosynthesis*, Wiley, 2002.

536 C. von Ballmoos, A. Wiedenmann and P. Dimroth, *Annu. Rev. Biochem.*, 2009, **78**, 649–672.

537 A. Pannwitz, D. M. Klein, S. Rodríguez-Jiménez, C. Casadevall, H. Song, E. Reisner, L. Hammarström and S. Bonnet, *Chem. Soc. Rev.*, 2021, **50**, 4833–4855.

538 M. Hansen, S. Troppmann and B. König, *Chem. - A Eur. J.*, 2016, **22**, 58–72.

539 J. N. Robinson and D. J. Cole-Hamilton, *Chem. Soc. Rev.*, 1991, **20**, 49.

540 G. B. Berselli, A. V. Gimenez, A. O'Connor and T. E. Keyes, *ACS Appl. Mater. Interfaces*, 2021, **13**, 29158–29169.

541 N. Ikuta, S. Takizawa and S. Murata, *Photochem. Photobiol. Sci.*, 2014, **13**, 691–702.

542 A. Benda, M. Beneš, V. Mareček, A. Lhotský, W. T. Hermens and M. Hof, *Langmuir*, 2003, **19**, 4120–4126.

543 J. Ferté, *Eur. J. Biochem.*, 2000, **267**, 277–294.

544 G. D. Eytan, R. Regev, G. Oren and Y. G. Assaraf, *J. Biol. Chem.*, 1996, **271**, 12897–12902.

545 S. L. Veatch and S. L. Keller, *Biophys. J.*, 2003, **85**, 3074–3083.

546   L. M. Ickenstein, M. C. Sandström, L. D. Mayer and K. Edwards, *Biochim. Biophys. Acta - Biomembr.*, 2006, **1758**, 171–180.

547   K. Hashizaki, H. Taguchi, C. Itoh, H. Sakai, M. Abe, Y. Saito and N. Ogawa, *Chem. Pharm. Bull.*, 2003, **51**, 815–820.

548   T. Tabarin, A. Martin, R. J. Forster and T. E. Keyes, *Soft Matter*, 2012, **8**, 8743.

Appendices A-D

Appendix A

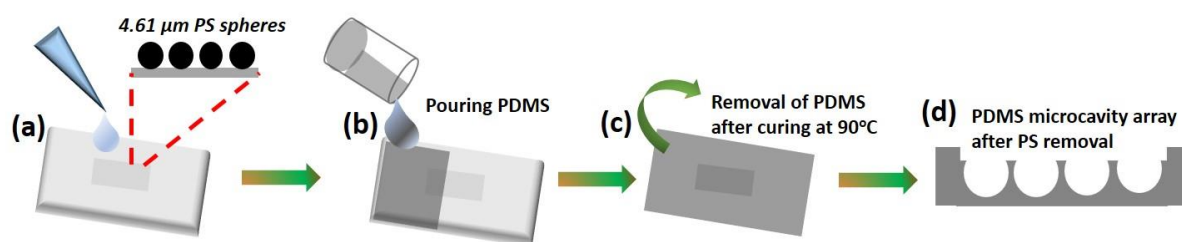**Chapter 2:** BODIPY Charge Transfer Dyad Sensitized Triplet-Triplet Annihilation Upconversion in Solution and Model Membranes

Figure S2.1 Schematic illustration of PDMS microcavity array preparation.
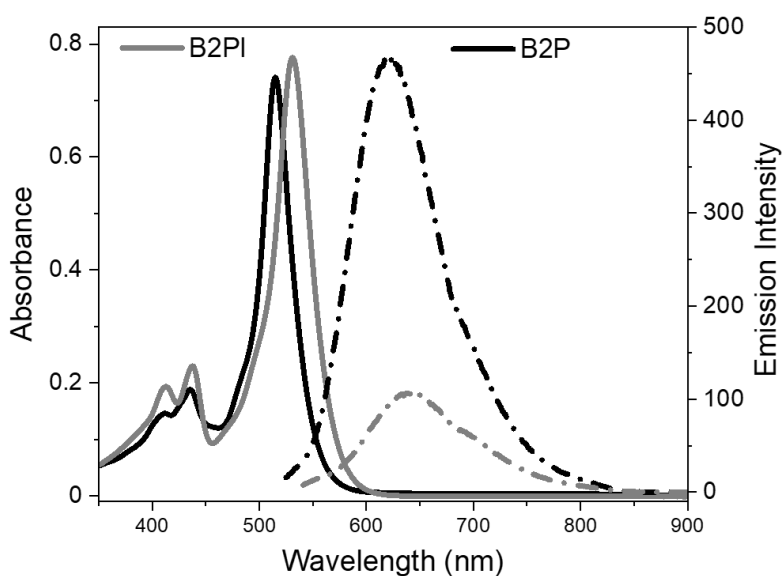
Figure S2.2 Absorption (solid line) and emission spectra (dash dotted line) of 10 µM B2P (black) and B2PI (grey) in dioxane. Emission spectra of B2P, and B2PI were collected by exciting at 517, and 532 nm respectively with 5 nm excitation and emission slit widths.
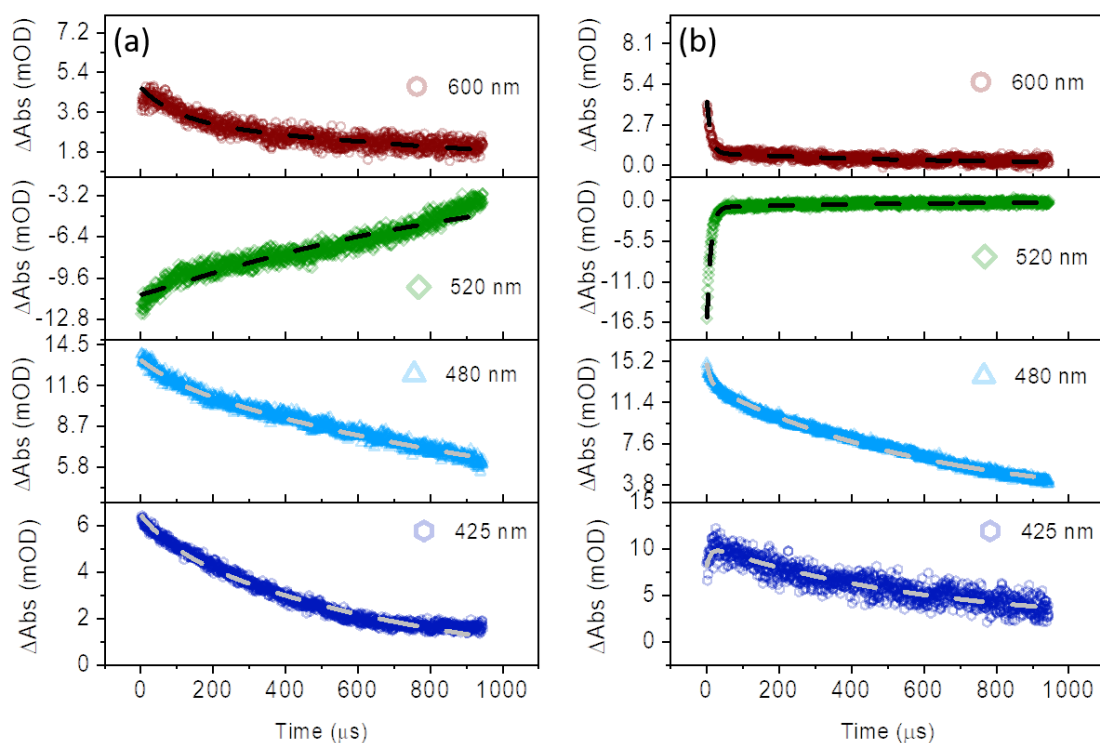
Figure S2.3 Kinetics (symbols) and global fits (dotted lines) of (a) B2P 5 µM (c) B2P 5 µM and perylene 100 µM. Data courtesy of Keshav Kumar Jha (Friedrich Schiller University Jena).
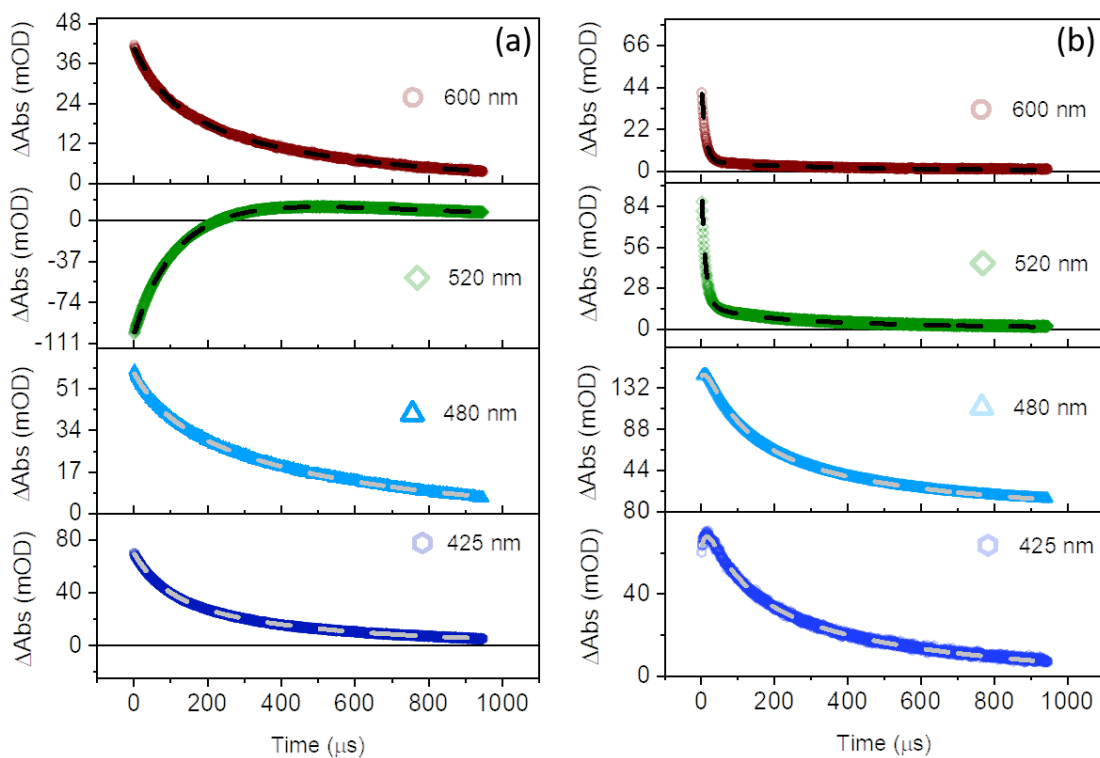
Figure S2.4 Kinetics (symbols) and global fits (dotted lines) of (a) B2PI 5 µM (c) B2PI 5 µM and perylene 100 µM. Data courtesy of Keshav Kumar Jha (Friedrich Schiller University Jena).
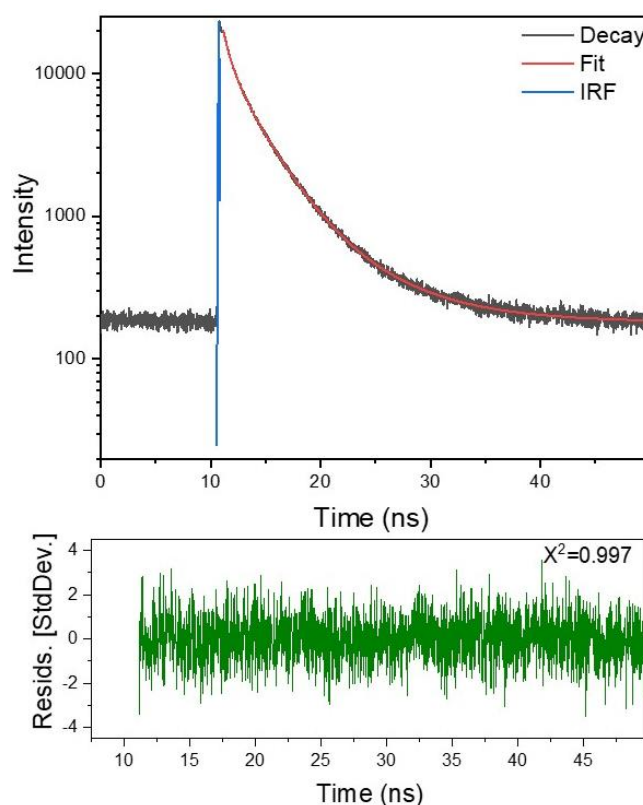
Figure S2.5 Time correlated single photon counting trace of B2P in DOPC spanned MSLB recorded extracted from FLCS data.
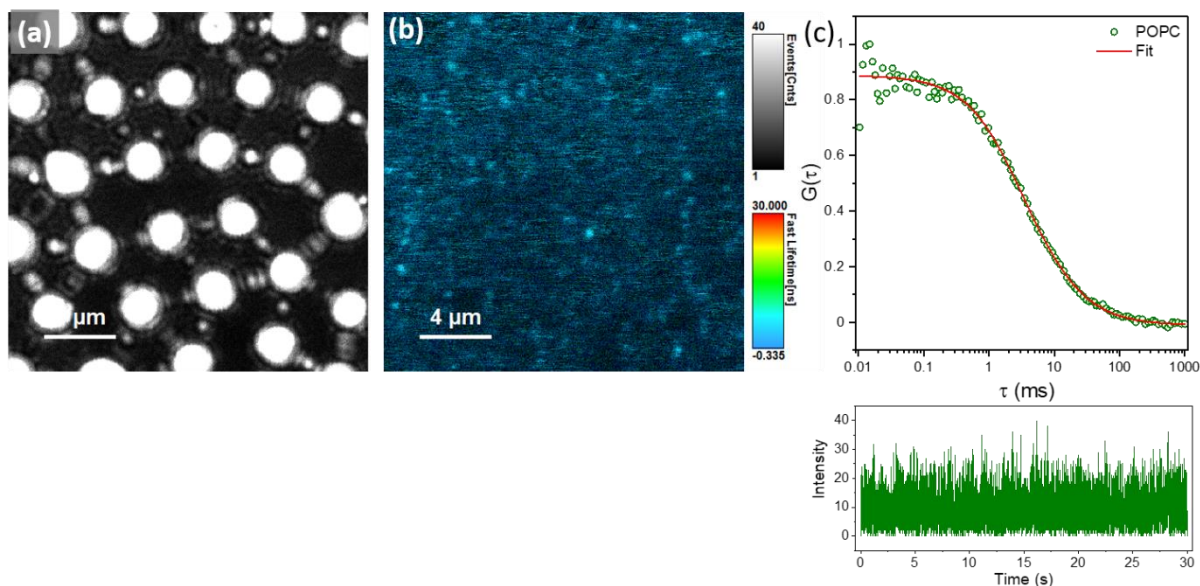
Figure S2.6 (a) Reflectance image and (b) Fluorescence Lifetime Image of POPC lipid spanning cavities labelled with 0.01 mol% DOPE-ATTO655. (c) Representative normalized FLCS autocorrelation curve measured over a single cavity spanned with DOPC bilayer labelled with 0.01 mol% DOPE-ATTO655. Bottom panel shows the corresponding intensity-time trace. FLCS data were collected from 40-50 cavities and the average is shown. The solid lines are the 2D diffusion fit using

equation 2.1 and the diffusion coefficient was calculated to be 8.8 ± 0.52 µm^{2}s^{-1} using equation 2.2. All measurements were carried out in PBS at pH 7.4.
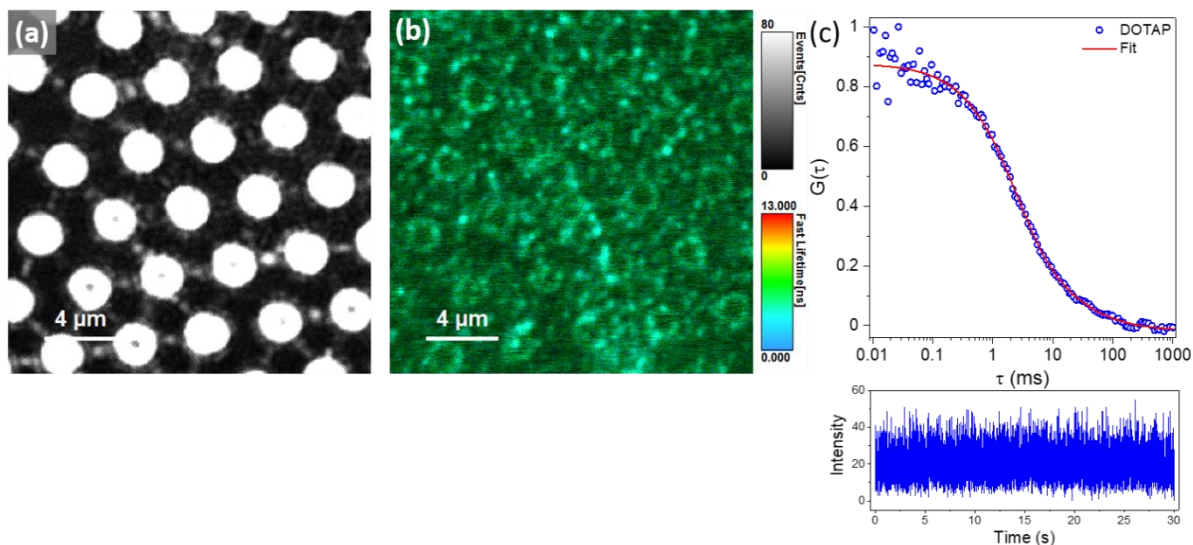

Figure S2.7 (a) Reflectance image and (b) Fluorescence Lifetime Image of DOTAP lipid spanning cavities labelled with 0.01 mol% DOPE-ATTO655. (c) Representative normalized FLCS autocorrelation curve measured over a single cavity spanned with DOPC bilayer labelled with DOPE-ATTO655. Bottom panel shows the corresponding intensity-time trace. FLCS data were collected from 40-50 cavities and the average is shown. The solid lines are the 2D diffusion fit using equation 2.1 and the diffusion coefficient was calculated to be 7.2 ± 0.64 µm^{2}s^{-1} using equation 2.2. All measurements were carried out in PBS at pH 7.4.
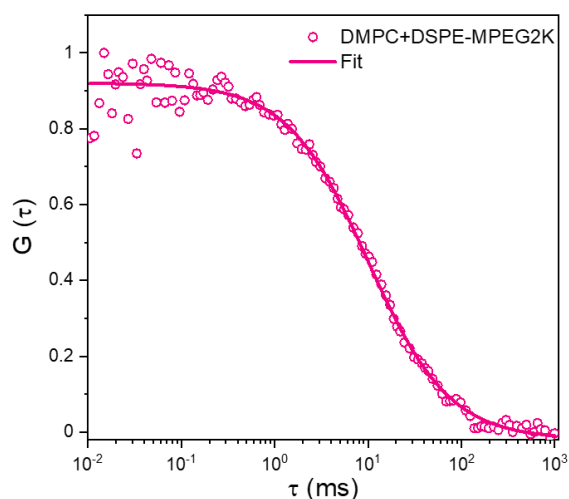
Figure S2.8 Representative normalized FLCS autocorrelation curve measured over a single cavity spanned with DMPC:DSPE-MPEG2000 (100:4 mole ratio) bilayer labelled with DOPE-ATTO655. FLCS data were collected from 40-50 cavities and the average is shown. The solid lines are the 2D diffusion fit using equation 2.1 and the diffusion coefficient was calculated to be 3.66 ± 0.35 µm^{2}s^{-1} using equation 2.2. All measurements were carried out in PBS at pH 7.4.
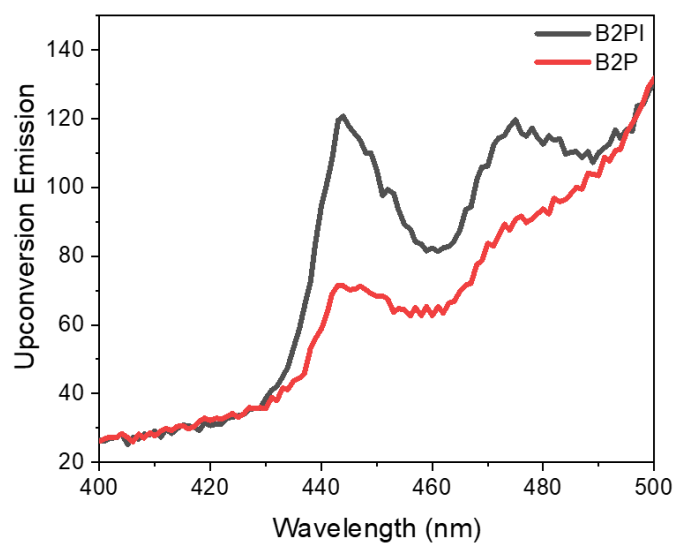
Figure S2.9 TTA-UC in DMPC:DSPE-MPEG2000 (100:4 mole ratio) LUV with 0.25 μM B2PI(black)/B2P(red) and 2.5 μM perylene. All measurements are recorded with 10 nm emission slit width at 532 nm excitation in presence of 20 mM sodium sulfite.

Appendix B

Chapter 3: Role of phospholipase A$_2$ modulating Triplet-Triplet Annihilation Upconversion of B2PI-perylene pair within model biomembrane
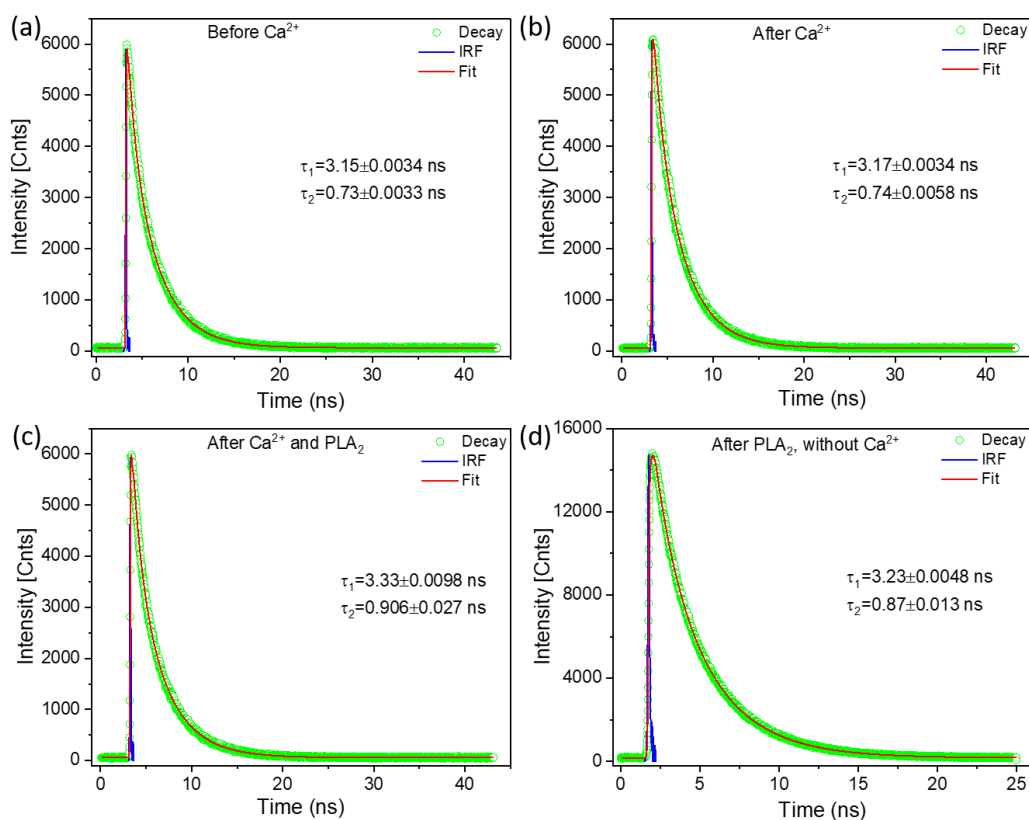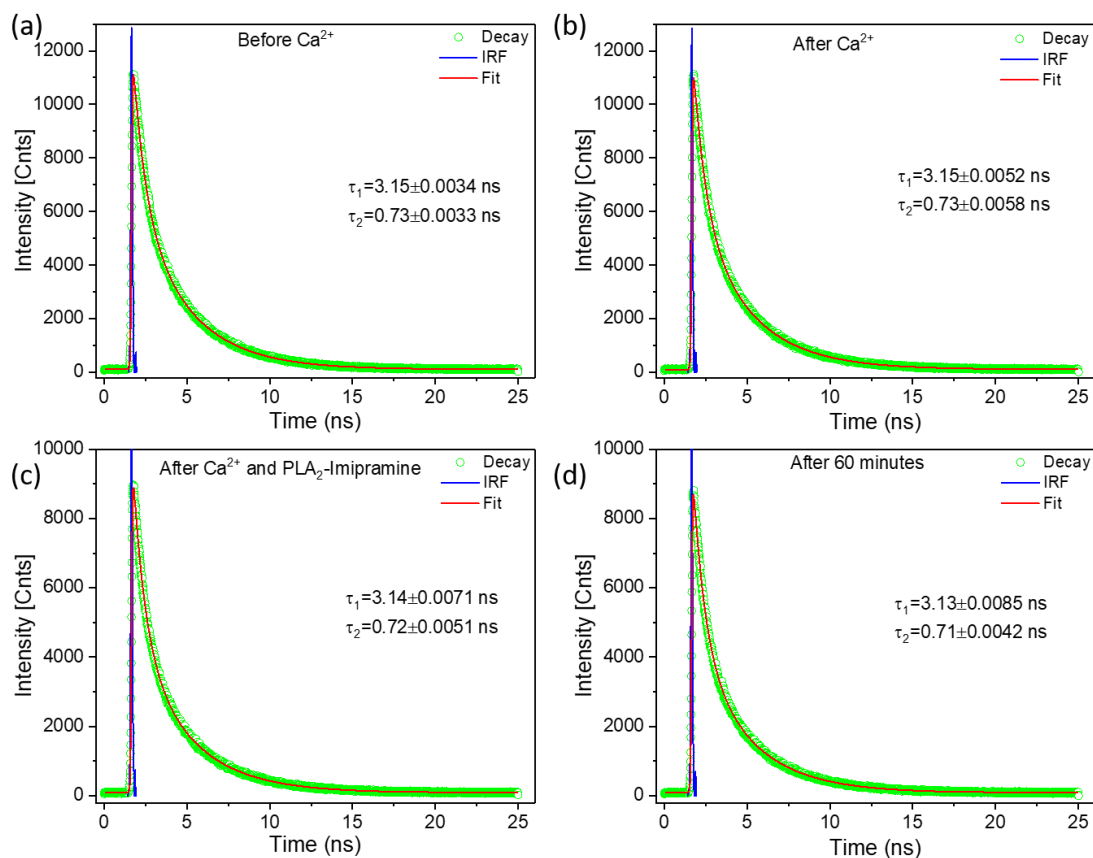

Figure S3.1 Emission decays (green) extracted from FLIM of DOPC MSLBs labelled with 0.01 mol% DOPE-ATTO655 (upper leaflet) (a) before, (b) after the addition of 5 mM Ca^{2+}, (c) after the addition of 5 µM PLA$_2$ in presence of Ca^{2+}, and (d) after the addition of 5 µM PLA$_2$ in the absence of Ca^{2+}. All measurements were carried out in Tris-HCl buffer at pH 7.4. The instrument response function (IRF) is shown in blue and the bi-exponential fit is given in red. The lifetimes are given inside each figure.

Figure S3.2 Emission decays (green) extracted from FLIM of DOPC MSLBs labelled with 0.01 mol% DOPE-ATTO655 (upper leaflet) (a) before, (b) after the addition of 5 mM Ca^{2+}, (c) 10 minutes after the addition of 5 µM PLA_2 pre-incubated with 20 µM imipramine in presence of Ca^{2+}, and (d) after 60 minutes. All measurements were carried out in Tris-HCl buffer at pH 7.4. The instrument response function (IRF) is shown in blue and the bi-exponential fit is given in red. The lifetimes are given inside each figure.
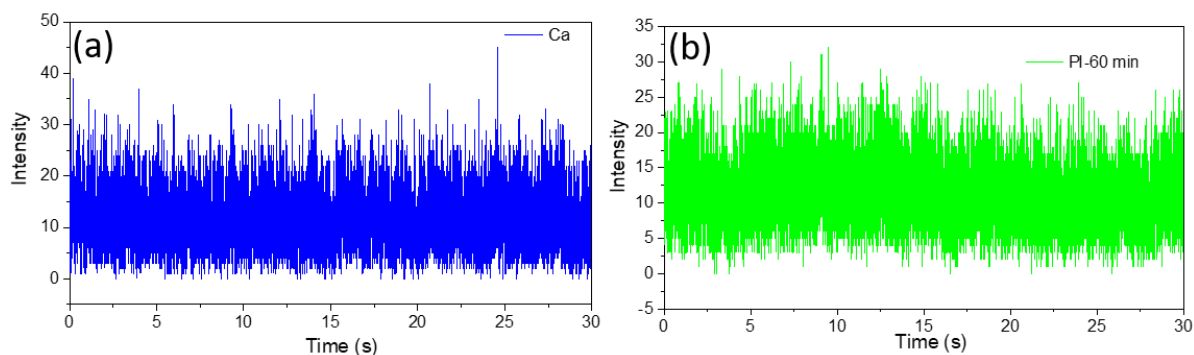
Figure S3.3 Intensity-time traces of FLCS data obtained from DOPC MSLB labelled with 0.01 mol% DOPE-ATTO655 (upper leaflet) (a) after Ca^{2+} addition and (b) after the addition of PLA_2 treated imipramine. PDMS microcavity arrays are filled with Tris-HCl buffer of pH 7.4.

Appendix C

Chapter 4: Ruthenium(II) Polypyridyl Complex Sensitized Triplet-Triplet Annihilation Upconversion
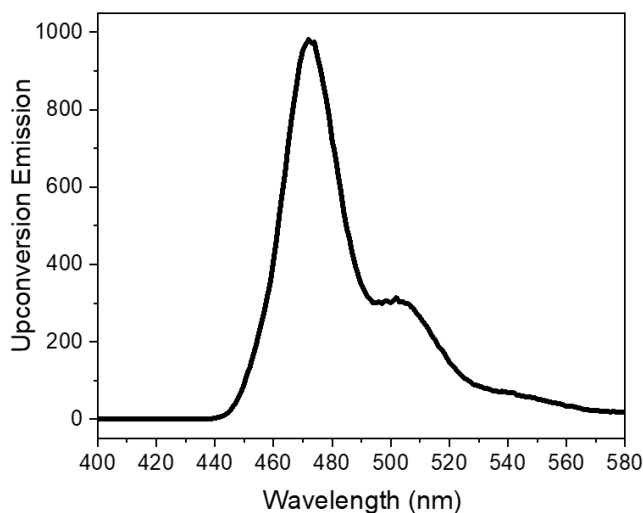

Figure S4.1 Upconverted emission from deaerated toluene containing 10 µM palladium tetraphenyltetrabenzoporphyrin and 200 µM perylene excited with a 630 nm laser of 5 mW power, at 10 nm slit width.
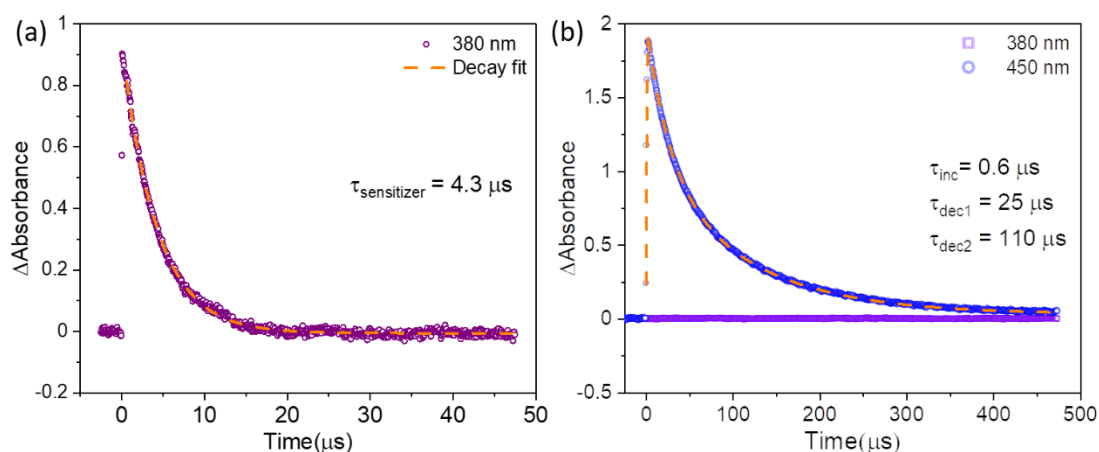

Figure S4.2 Decay transients from nanosecond transient absorption spectra recorded at 380, and 4800 nm are shown and the line and symbol represent the raw data and the dashed line represents the exponential fit. In (a) decay transient recorded at 380 nm for Ru-bqp-oct - 20 µM, and (b) Ru-bqp-oct - 20 µM & DPA 400 µM in deaerated acetonitrile is shown. The dashed line in (a) in orange colour represents the monoexponential decay fit to the spectra at 380 nm. τ represents the triplet lifetime of the individual species as indicated in the subscript and the triplet state lifetime of the sensitizer is 4.3 µs. The dashed line in (b) in orange colour represents the biexponential decay fit to the spectra at 450 nm

(blue). The triplet state lifetimes of the annihilator are decay $\tau_{dec1} = 25$ µs and $\tau_{dec2} = 110$ µs. The maximum error is within 10% of the given value. Data courtesy of Keshav Kumar Jha (Friedrich Schiller University Jena).
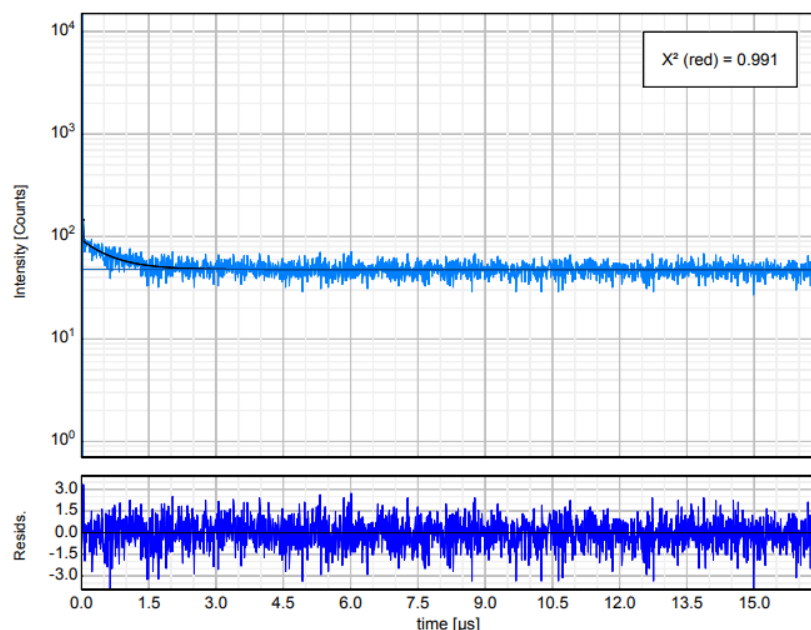

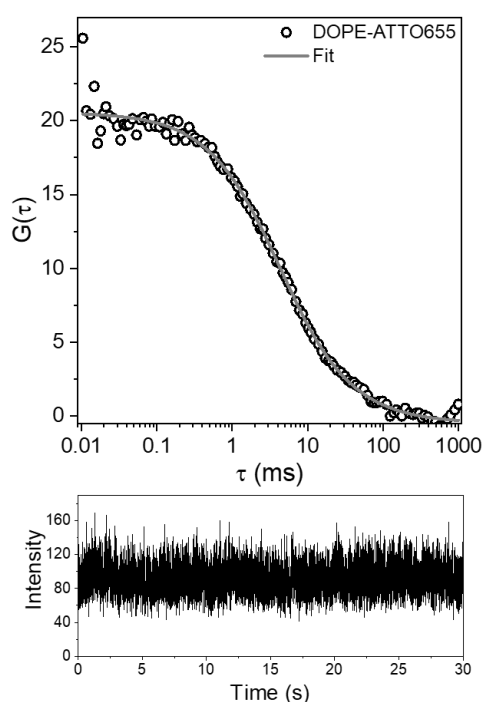**Figure S4.3** Lifetime decay and fit of 5 µM Ru-bqp-oct in DOPC liposomes under 450 nm excitation.

Figure S4.4 (a) Representative fluorescence lifetime correlation spectroscopic (FLCS) autocorrelation function (ACF) of DOPC MSLB labelled with 0.01 mol% DOPE-ATTO655 (upper leaflet) and the (a) corresponding intensity-time trace. FLCS was measured over 40-50 cavities and the average is shown. The solid lines are the 2D diffusion fit using equation 2.1. All measurements were carried out under PBS of pH 7.4.

Appendix D

Chapter 5: Microcavity Supported Lipid Bilayers: Versatile tools for understanding membrane fluidity responses to drug and fluorophores
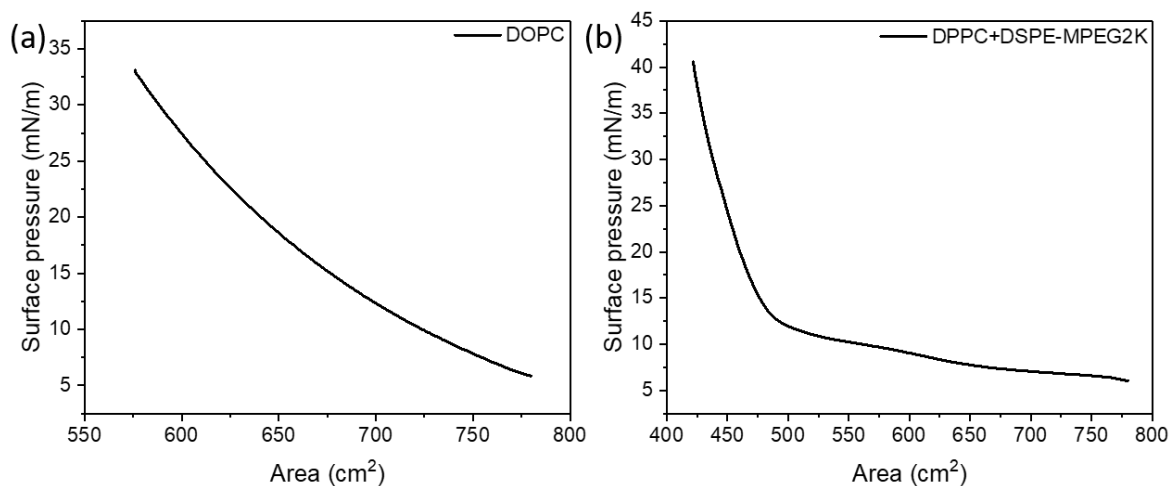

Figure S5.1 Lipid monolayer transfer using Langmuir-Blodgett lipid films. Isotherms of (a) DOPC, and (b) DPPC+DSPE-MPEG(2000).
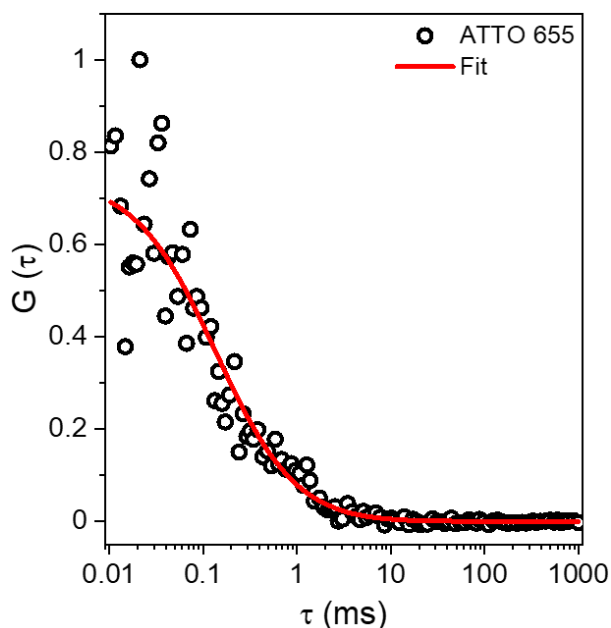

Figure S5.2 (a) Representative fluorescence lifetime correlation spectroscopic (FLCS) autocorrelation function (ACF) of 0.01 mol% ATTO655 in water. The solid lines are the 2D diffusion fit using equation 5.2. This was used for the calibration of FLCS confocal volume. The diffusion coefficient (D) is 426 $\mu m^2 s^{-1}$.